N°d'ordre NNT : 2016LYSEI016

THESE de DOCTORAT DE L'UNIVERSITE DE LYON
opérée au sein de
(L'Institut National des Sciences Appliquées de Lyon)

Ecole Doctorale N° ED162
(Mécanique, Energétique, Génie civil, Acoustique)

Spécialité de doctorat : Mécanique, Energétique, Génie civil, Acoustique

Soutenue publiquement le 22/03/2016, par :
(Sayed Mohamed Baqer Albahrani)

Photoluminescent CdSe/CdS/ZnS Quantum Dots for Temperature and Pressure Sensing in Elastohydrodynamic Contacts

---

Devant le jury composé de :

Guillot, Gérard	Professeur émérite	INL (CNRS-UMR5270)	Président
Glovnea, Romeo	Reader	University of Sussex, United Kingdom	Rapporteur
Ledoux, Gilles	Chargé de Recherche	ILM (UMR5306 - UCB Lyon 1)	Rapporteur
García Solé, Jose	Professeur	Universidad Autónoma de Madrid, Spain	Examinateur
Reiss, Peter	Chercheur CEA HdR	INAC (CEA-UJF-CNRS, SPrAM/LeMOH)	Examinateur
Philippon, David	Maître de conférences	LaMCoS (CNRS-UMR5259)	Examinateur
Vergne, Philippe	Directeur de Recherche CNRS	LaMCoS (CNRS-UMR5259)	Directeur de thèse
Bluet, Jean-Marie	Professeur	INL (CNRS-UMR5270)	Co-directeur de thèse

"الَّذِينَ يَسْتَمِعُونَ الْقَوْلَ فَيَتَّبِعُونَ أَحْسَنَهُ أُولَئِكَ الَّذِينَ هَدَاهُمُ اللَّهُ وَأُولَئِكَ هُمْ أُولُو الْأَلْبَابِ" ـ القرآن الكريم سورة الزمر آية ١٨

*"**Those who listen to the word, and follow the best of it, these are they whom Allah has guided, and these are they who possess intellect**" – Holly Coran, Azzumar, 18*

*« **Ceux qui prête l'oreille à la parole, puis suivent ce qu'elle contient de meilleur, ce sont ceux-là qu'Allah a guidés et ce sont eux les doués d'intelligence** » – Saint Coran, Azzumar, 18*

Département FEDORA – INSA Lyon - Ecoles Doctorales – Quinquennal 2016-2020

SIGLE	ECOLE DOCTORALE	NOM ET COORDONNEES DU RESPONSABLE
CHIMIE	**CHIMIE DE LYON** http://www.edchimie-lyon.fr Sec : Renée EL MELHEM Bat Blaise Pascal 3e etage secretariat@edchimie-lyon.fr Insa : R. GOURDON	M. Stéphane DANIELE Institut de Recherches sur la Catalyse et l'Environnement de Lyon IRCELYON-UMR 5256 Équipe CDFA 2 avenue Albert Einstein 69626 Villeurbanne cedex directeur@edchimie-lyon.fr
E.E.A.	**ELECTRONIQUE, ELECTROTECHNIQUE, AUTOMATIQUE** http://edeea.ec-lyon.fr Sec : M.C. HAVGOUDOUKIAN Ecole-Doctorale.eea@ec-lyon.fr	M. Gérard SCORLETTI Ecole Centrale de Lyon 36 avenue Guy de Collongue 69134 ECULLY Tél : 04.72.18 60.97 Fax : 04 78 43 37 17 Gerard.scorletti@ec-lyon.fr
E2M2	**EVOLUTION, ECOSYSTEME, MICROBIOLOGIE, MODELISATION** http://e2m2.universite-lyon.fr Sec : Safia AIT CHALAL Bat Darwin - UCB Lyon 1 04.72.43.28.91 Insa : H. CHARLES Safia.ait-chalal@univ-lyon1.fr	Mme Gudrun BORNETTE CNRS UMR 5023 LEHNA Université Claude Bernard Lyon 1 Bât Forel 43 bd du 11 novembre 1918 69622 VILLEURBANNE Cédex Tél : 06.07.53.89.13 e2m2@univ-lyon1.fr
EDISS	**INTERDISCIPLINAIRE SCIENCES-SANTE** http://www.ediss-lyon.fr Sec : Safia AIT CHALAL Hôpital Louis Pradel - Bron 04 72 68 49 09 Insa : M. LAGARDE Safia.ait-chalal@univ-lyon1.fr	Mme Emmanuelle CANET-SOULAS INSERM U1060, CarMeN lab, Univ. Lyon 1 Bâtiment IMBL 11 avenue Jean Capelle INSA de Lyon 696621 Villeurbanne Tél : 04.72.68.49.09 Fax :04 72 68 49 16 Emmanuelle.canet@univ-lyon1.fr
INFOMATHS	**INFORMATIQUE ET MATHEMATIQUES** http://infomaths.univ-lyon1.fr Sec :Renée EL MELHEM Bat Blaise Pascal 3e etage infomaths@univ-lyon1.fr	Mme Sylvie CALABRETTO LIRIS – INSA de Lyon Bat Blaise Pascal 7 avenue Jean Capelle 69622 VILLEURBANNE Cedex Tél : 04.72. 43. 80. 46 Fax 04 72 43 16 87 Sylvie.calabretto@insa-lyon.fr
Matériaux	**MATERIAUX DE LYON** http://ed34.universite-lyon.fr Sec : M. LABOUNE PM : 71.70 –Fax : 87.12 Bat. Saint Exupéry Ed.materiaux@insa-lyon.fr	M. Jean-Yves BUFFIERE INSA de Lyon MATEIS Bâtiment Saint Exupéry 7 avenue Jean Capelle 69621 VILLEURBANNE Cedex Tél : 04.72.43 71.70 Fax 04 72 43 85 28 Ed.materiaux@insa-lyon.fr
MEGA	**MECANIQUE, ENERGETIQUE, GENIE CIVIL, ACOUSTIQUE** http://mega.universite-lyon.fr Sec : M. LABOUNE PM : 71.70 –Fax : 87.12 Bat. Saint Exupéry mega@insa-lyon.fr	M. Philippe BOISSE INSA de Lyon Laboratoire LAMCOS Bâtiment Jacquard 25 bis avenue Jean Capelle 69621 VILLEURBANNE Cedex Tél : 04.72 .43.71.70 Fax : 04 72 43 72 37 Philippe.boisse@insa-lyon.fr
ScSo	**ScSo*** http://recherche.univ-lyon2.fr/scso/ Sec : Viviane POLSINELLI Brigitte DUBOIS Insa : J.Y. TOUSSAINT viviane.polsinelli@univ-lyon2.fr	Mme Isabelle VON BUELTZINGLOEWEN Université Lyon 2 86 rue Pasteur 69365 LYON Cedex 07 Tél : 04.78.77.23.86 Fax : 04.37.28.04.48

*ScSo : Histoire, Géographie, Aménagement, Urbanisme, Archéologie, Science politique, Sociologie, Anthropologie

Photoluminescent CdSe/CdS/ZnS Quantum Dots for Temperature and Pressure Sensing in Elastohydrodynamic Contacts

Abstract

Temperature and pressure are two relevant parameters for the optimization of lubrication performance in the elastohydrodynamic lubrication (EHL) regime. To date, various experimental methods have been developed to measure these two parameters with more or less success. In a continuation of these efforts, some investigations are presented in the current work in view of developing a new *in situ* technique allowing for local measurements of these two parameters throughout elastohydrodynamic (EHD) contacts. This technique exploits the photoluminescence (PL) sensitivity of CdSe/CdS/ZnS quantum dots (QDs) to changes in temperature and pressure. In this respect, calibrations have been carried out in order to establish the sensitivity of these QDs to the two parameters. Moreover, the versatility of these QDs for sensing applications have been examined by testing two different lubricants, namely squalane and a mixture of squalane and cyclopentane. Some measurements were also conducted under dynamic conditions, in order to study (i) the influence of the QDs presence on the lubricant rheology and (ii) the influence of shear rate on the PL of QDs. Although these different tests demonstrated the potential of CdSe/CdS/ZnS QDs, they revealed the existence of other parameters that affect, in addition to temperature and pressure, their response. A comprehensive study was thus conducted in order to elucidate the mechanisms behind these findings. More importantly, a methodology was defined in order to minimize these undesired influences and, *in fine*, enable these QDs to be used as reliable nanosensors.

Keywords: Elastohydrodynamic lubrication, *in situ* measurement, photoluminescence, quantum dots, temperature and pressure calibration.

Boîtes Quantiques Photoluminescentes de CdSe/CdS/ZnS pour la Mesure de la Température et de la Pressure dans les Contacts Elastohydrodynamiques

Résumé

La température et la pression sont deux paramètres particulièrement importants pour l'optimisation des performances du régime de lubrification élastohydrodynamique (EHL). A ce jour, différentes méthodes expérimentales ont été développées, avec plus ou moins du succès, pour la mesure de ces deux paramètres. Ce travail présente, en continuité de ces approches, des investigations visant à développer une nouvelle technique *in situ* permettant de mesurer localement ces deux grandeurs dans les contacts élastohydrodynamiques (EHD). Cette technique exploite la sensibilité en photoluminescence (PL) des boîtes quantiques (ou en anglais « quantum dots (QDs)) de CdSe/CdS/ZnS aux variations de température et de pression. A cet égard, des calibrations ont été réalisées afin d'évaluer la sensibilité de ces QDs aux deux paramètres. De plus, la versatilité de ces QDs comme nanosondes a été examinée en testant deux lubrifiants différents : le squalane et un mélange de squalane et de cyclopentane. Des mesures ont été également effectuées sous conditions dynamiques afin d'étudier (i) l'influence de la présence des QDs sur la rhéologie du lubrifiant et (ii) l'influence du taux de cisaillement sur la PL des QDs. Bien que ces différents tests aient prouvé le potentiel des QDs de CdSe/CdS/ZnS, ils ont révélé l'existence d'autres paramètres qui peuvent, tout comme la température et la pression, en modifier la réponse. L'étude a été menée afin d'approfondir la compréhension des mécanismes responsables de tels effets. Plus important encore, une méthodologie a été définie pour minimiser ces effets indésirables, et pour *in fine*, permettre l'usage de ces QDs en tant que nanosondes fiables.

Mots-clés : Lubrification élastohydrodynamique, mesure *in situ*, photoluminescence, boîtes quantiques, calibration en température et pression

Acknowledgements

In the following lines I would like to express my special thanks to all the people who contributed to the accomplishment of my PhD thesis and all those who shared with me all the pleasant years at LaMCoS.

I have to express my gratitude to Institut Carnot for the funding of this project.

Special appreciation goes to my PhD supervisors: Philippe Vergne, David Philippon and Jean-Marie Bluet. Their complementary roles, due to their successful teamwork and their very distinct characters, was crucial for attaining the goals of the work. I will remember you Philippe for your straightforwardness, long-term vision and your exemplary dosage between strictness and kindness accordingly to the requirement of the situation. David, thanks to the uncountable and real scientific discussions and exchanges with you, as well as your continuous availability and your inspiring human qualities, I could surpass many difficulties throughout my thesis. Jean-Marie, owing to your modesty and your confidence in me, I could maintain my self-confidence and courage in explaining my observations.

Many thanks to Pr. Guillot who accepted to be the president of the jury, as well as to the jury members: Dr. Glovnea, Dr. Ledoux, Dr. Reiss, Pr. García Solé, for the time they devoted in examining my manuscript and in assisting to my oral defense. The pertinent questions addressed either before or after the presentation were very helpful in improving the quality of the work and my reflection on the thesis problematics.

I am also grateful to the other persons who contributed in the realization of the project. Special thanks to Michel Querry whose idea on the application of QDs as sensor was actually the seed idea upon which the current project has been initiated. Michel, despite your retirement in my first year of PhD, you did not hesitate to dedicate your time for hours of fruitful discussions whenever you passed to the laboratory. I would like to thank Hamza Hajjaji who participated before me in this project as a PhD student for the synthesis of Si and SiC nanoparticles. I appreciated his role in helping me to launch my PhD work. I had also precious help in experimentations from: Nathalie Bouscharain for the use of the rheometer, Lionel Lafarge in the design of the different apparatus used in my work, Nicolas Devaux for making measurements with the tribometer, Jean-David for numerical computation of the behaviour of the lubricant within EHD contacts. I would like to thank also Hervé Cardon and Gilles Montagnac from ENS de Lyon for the training sessions on the use of the high pressure diamond anvil cells.

During my thesis, I had the opportunity to make many new friends in a rich multi-cultural environment. Thank you Eymard, Serge, Serigne, Jérôme, Jonathan, Stephane, Jean-David, Vincent, Nicolas, Pauline, Camille, Pierrick, Julian, Rudy, Marion, Ghassene, Hassen, Amina, Ayman, Hafed, Hussam, Mirela, Bogdan, Mihaela, Livia, Komla, Ayman, , Giovanna, Elena, Tatiana, Ilaria, Martino, Simona, Jacopo, Davide et Maria-Daniella! I will not forget my pleasant moments with you during lunches, coffee breaks, hikings in the beatuful country-side

of Rhône-Alpes region and outings in city center of Lyon. I will also remember you being by my side during difficult periods and assisting me in overcoming these moments.

Special thanks from all my heart to my Bahraini friends with whom I started my journey and adventure and in France ten years ago. Thank you Hasan Naser, Ahmad Alsatrawi, Mohamed Sabt, Ali Almoosawi, Hussan Rajab, Hasan Almajed and Ahmed Alghanim. During these long and hard years with almost daily struggles, we actually grew up together and my moments with you were the most unforgettable episodes in my life.

No words can express my gratitude to my precious family: my mother and father without whom I could not be who I am today, my dear brother and sisters, whose support is the most sincere and helpful I could ever find.

Table of contents

Nomenclature

Latin letters

a	Contact area (m^2)
a_c	Radius of the cavity in which the fluorophore resides (m)
a_v, a_v^0	Volume deformation potential (eV)
a_P	Pressure-viscosity coefficient (Pa^{-1})
A	Absorbance of a fluorophore
B	Bulk modulus (Pa)
B'	Constant in Murnaghan's equation of state
c	Molar concentration of the QDs ($Mol.m^{-3}$)
c_A	Molar concentration of the acceptors ($Mol.m^{-3}$)
C	Mass concentration of the QDs ($kg.m^{-3}$)
C_0	Mass concentration of the QDs at ambient temperature (298 K) and pressure (0.1 MPa)
C_f	Thermal capacity of the lubricant ($J.K^{-1}$)
D	Diffusion constant ($m^2.s^{-1}$)
D_r	Rotational diffusion constant ($m^2.s^{-1}$)
$-e$	Electron charge (C)
e_{CdS}	Thickness of the CdS shell (m)
e_{ZnS}	Thickness of the the ZnS shell (m)
E	Energy (eV)
E_A	Absorption energy (eV)
E_E	Emission energy (eV)
E_{mean}	Constant in the Gaussian fitting of fluorescence emission: mean emission energy (eV)
E_g	Bandgap energy (eV)
E_g^B	Bulk contribution in the bandgap energy (eV)
$E_g^{B,\circ}$	Bulk contribution in the bandgap energy (eV) at ambient temperature (298 K) and pressure (0.1 MPa)

E_g^Q	Quantum contribution in the bandgap energy (eV)
E_{LO}	LO-phonon energy (eV)
E_1, E_2	Young moduli of contacting bodies (Pa)
E'	Reduced Young modulus of the contacting bodies (Pa)
E^{ET}	Efficiency of energy transfer
E^{RET}	Efficiency of radiative energy transfer
E^{FRET}	FRET efficiency
$f(R)$	Distance distribution (m^{-1})
F_D	Corrected fluorescence intensity of the donor (with the integrated intensity normalized to unity)
h	Film thickness (m)
$\hbar$	Reduced Planck constant ($m^2.kg.s^{-1}$)
h_c	Central film thickness (m)
h_{min}	Minimum film thickness (m)
H, H_0	Gap between the rotating disc and the plate in a rheometer (m)
I	Fluorescence intensity
$I_{baseline}$	Constant in the Gaussian fitting of fluorescence emission: baseline of the fluorescence spectrum
I_{max}	Constant in the Gaussian fitting of fluorescence emission: maximum fluorescence intensity (after substracting the baseline)
I_i	Intensity of the incident light
I_t	Intensity of light transmitting through the absorbing medium
I_{T_R}	Time-resolved intensity
$I^0_{T\_R}$	Time-resolved intensity immediately after an excitation pulse
J^{RET}	Overlap integral for radiative energy transfer
J^{FRET}	Overlap integral for radiative energy transfer
J^{Dexter}	Overlap integral for Dexter effect
$\boldsymbol{J}_{\dot{\gamma}}$	Shear flux vector ($m.s^{-1}$ for each component)
$\boldsymbol{J}_{\eta}$	Viscosity flux vector ($m.s^{-1}$ for each component)
$\boldsymbol{J}_C$	Curvature flux vector ($m.s^{-1}$ for each component)
$\boldsymbol{J}_B$	Brownian flux vector ($m.s^{-1}$ for each component)
k	Wavenumber (cm^{-1})

k_B	Boltzmann constant ($m^2.kg.s^{-2}.K^{-1}$)
k^{Dexter}	Rate of the Dexter effect (s^{-1})
k^{FRET}	Rate of FRET (s^{-1})
k^{RET}	Rate of radiative energy transfer (s^{-1})
k_f	Thermal conductivity of the lubricant ($W.m^{-1}.K^{-1}$)
k_r	Radiative decay rate (s^{-1})
k_{nr}	Nonradiative decay rate (s^{-1})
K	Constant in the rate of dexter effect
$K_{\dot{\gamma}}$	Constant of shear flux
K_η	Constant of viscosity flux
K_C	Constant of curvature flux
K_B	Constant of Brownian flux
l	Distance from the rotating axis in a rheometer (m)
l_A	Thickness of the absorbing medium
L	Radius of the rotating disc in the rheometer (m)
L_B	The average Bohr radius (m)
m_e	Mass of an electron (kg)
m_e*	Effective mass of an electron
m_h*	Effective mass of a hole
MFP	Mean Free Path (nm)
n	The refractive index of the solvent
N_A	Avogadro constant (mol^{-1})
p	Pressure (Pa)
P	Probability
p_{max}	Maximum pressure within a contact (Pa)
Q	Internal quantum yield
Q_D	Internal quantum yield of the donor in the abscence of the acceptor
r	Radius of a particle or a QD (m)
r^*	Apparent radius of the QDs (m)
r_{CdSe}	Radius of the core CdSe (m)
R	Donor-acceptor spacing (m)
R^*	Apparent donor-acceptor spacing (m)

R_{mean}	Mean donor-acceptor spacing (m)
R_{min}	Minimum donor-acceptor spacing (m)
R_0	Förster distance (m)
R_0^*	Apparent Förster distance (m)
R_1, R_2	Curvature radii of the contacting bodies (m)
R'	Reduced curvature radius of the contacting bodies (m)
R_s	Combined surface roughness (m)
S_p	Pressure sensitivity ($eV.Pa^{-1}$)
S_p^B	Pressure sensitivity of the bulk contribution ($eV.Pa^{-1}$)
S_p^Q	Pressure sensitivity of the quantum contribution ($eV.Pa^{-1}$)
S_T	Temperature sensitivity ($eV.K^{-1}$)
S_T^B	Temperature sensitivity of the bulk contribution ($eV.K^{-1}$)
S_T^Q	Temperature sensitivity of the quantum contribution ($eV.K^{-1}$)
S_r^Q	Senstivity to size variation ($eV.m^{-1}$)
SRR	Slip to Roll Ratio
t	Time
T	Temperature (K)
u_1, u_2	Surface velocities of the contacting bodies ($m.s^{-1}$)
u_m	Entrainment velocity at the x direction ($m.s^{-1}$)
V	Solvent volume (m^3)
$V_{Molecule}$	Volume of a solvent molecules (m^3)
V_0	Solvent volume at ambient temperature (298 K) and pressure (0.1 MPa)
$V_{Crystal}$	Volume of a primitive cell of the crystalline structure (m^3)
$V_{Molecule}$	Volume of a solvent molecule (m^3)
v_m	Entrainment velocity at the y direction ($m.s^{-1}$)
w	Normal load (N)
w_L	Normal load per unit length ($N.m^{-1}$)
x	Space coordinate (m)
$x_{Diffusion}^D$	Donor diffusion (m)
$x_{Diffusion}^A$	Acceptor diffusion (m)

X	Fraction of photons emitted by the donors and absorbed by the acceptors
y	Space coordinate (m)
z	Space coordinate (m)

Greek letters

α_1	Constant in Varshni law
α_2	Constant in the linear and quadratic approximation of bandgap energy variation with pressure
a_c	Raidus of the cavity in which the fluorophore resides (m)
α_T	Bulk coefficient of thermal expansion (K^{-1})
α_T^Q	Coefficient of thermal expansion of the QDs (K^{-1})
α_p	Bulk coefficient of compressibility (MPa^{-1})
α_p^Q	Coefficient of compressibility of the QDs (MPa^{-1})
β_1	Constant in Varshni law
β_2	Constant in the quadratic approximation of bandgap energy variation with pressure
$\dot{\gamma}$	Shear rate (s^{-1})
γ^Q	Constant in effective mass approximation ($eV.m^2$)
δ_1, δ_2	Elastic deformation of the contacting bodies
$\delta E_g^{Polarity}$	Shift in emission energy induced by polarity effect (eV)
$\delta E_g^{Q\text{-}ET}$	Shift of the quantum contribution to the bandgap energy due to energy transfer (eV)
δr	Shift of the radius induced by energy transfer (m)
$\delta S_r^{Q\text{-}ET}$	Shift in sensitivity to size variation due to energy transfer (eV/m)
$\delta S_T^{B\text{-}ET}$	Shift of the temperature bulk sensitivity due to energy transfer (eV/K)
δT	Temperature rise induced by shear-heating (K)
Γ	Full Width at Half Maximum or FWHM (eV)
Γ_{inh}	Inhomogeneous broadening (eV)
Γ_{LO}	Exciton-acoustic-phonon coupling coefficient (eV)

Δf	Orientation polarizability
Δr	Thermal expansion of the QDs (m)
ε	Static dielectric constant of the solvent
ε_0	Vacuum permittivity ($F.m^{-1}$)
ε_r	Relative permittivity of QDs material
ε_A	Molar absorption coefficient ($M^{-1}.cm^{-1}$)
η	Lubricant viscosity (Pa.s)
θ_D	Debye temperature (K)
κ^2	Orientation factor
λ	Wavelength (m)
μ_E	Excited state dipole moment (C.m)
μ_G	Ground state dipole moment (C.m)
ν	Frequency (s^{-1})
ν_0, ν_1, ν_2	Frequencies in emission and reabsorption process (s^{-1})
ν_A	Absorption frequency (s^{-1})
ν_E	Emission frequency (s^{-1})
ν^Q	Constant in Effective mass approximation (eV.m)
ν^P_1, ν^P_2	Poisson's ratio of the contacting bodies
σ_E	Constant in the Gaussian fitting of fluorescence emission: Standard deviation of the emission energy
ρ	Lubricant density ($Kg.m^{-3}$)
$\rho_{QD}{}^s$	QDs density ($kg.m^{-3}$)
τ	Lifetime (s)
τ_n	Natural lifetime (s)
τ_D	Lifetime of the donor in the absence of the acceptor
τ_{Relax}	Relaxation time (s)
φ	Angle of the cone in the cone-plate geometry (°)
Φ	Volume fraction of the QDs
Φ_0	Volume fraction of the QDs under steady-state conditions
ω	Angular velocity (rad/s)

Résumé Etendu

Introduction

En régime de lubrification élastohydrodynamique (EHD), le film lubrifiant est soumis à des conditions de sollicitations sévères. Il subit en effet des pressions élevées (quelques GPa), des contraintes de cisaillement allant jusqu'à quelques centaines de MPa. Le frottement entre les couches de fluide conduit à de l'échauffement pouvant atteindre plusieurs dizaines de degrés. Tous ces phénomènes se produisent dans des temps de passage du lubrifiant très courts (< 1 ms) et dans un contact très confiné (quelques centaines de microns de largeur et moins d'un micron d'épaisseur).

Le confinement du fluide est un obstacle pour l'étude expérimentale *in situ* du contact EHD. Cela nécessite de développer de nouvelles techniques de mesure locales et sensibles aux paramètres thermodynamiques et mécaniques des contacts.

L'objectif de cette thèse est de démonter le potentiel d'une nouvelle méthode de mesure *in situ* permettant de mesurer localement la température et la pression dans les contacts élastohydrodynamiques (EHD). Cette technique exploite la sensibilité en photoluminescence (PL) des boîtes quantiques (ou en anglais « Quantum dots (QDs) ») aux variations de température et de pression.

L'étude est présentée en deux parties :

Dans une première partie (Chapitres 1 et 2), les différents paramètres importants à prendre en compte sont identifiés. Cette identification est basée sur les savoirs actuels dans les différents domaines concernés par notre étude, à savoir : le régime de lubrification EHD, la PL et les QDs.

Dans la deuxième partie (Chapitres 3 et 4), les résultats de mesures expérimentales sur des QDs de CdSe/CdS/ZnS sont présentés. Ces mesures ont été réalisées en conditions statiques puis dynamiques. Les tests statiques ont pour objectif principal de calibrer la réponse de ces QDs aux variations de température et de pression. Les tests en conditions dynamiques simples ont été, quant à eux, considérées afin d'évaluer (i) l'influence de la présence des QDs sur la rhéologie du lubrifiant et (ii) l'influence du taux de cisaillement sur la PL des QDs. Une attention particulière a été portée le long de l'étude sur l'influence de tous les paramètres parasites qui peuvent perturber la mesure de la température et la pression.

Première partie : Identification de paramètres importants

Régime de lubrification élastohydrodynamique (EHD)

Le régime EHD est fréquemment rencontré dans les systèmes mécaniques fortement chargés, comme les roulements et les engrenages. C'est un cas particulier du régime hydrodynamique où le lubrifiant forme un film assurant une séparation complète des surfaces en contact. Cette particularité réside dans la concentration de la charge dans une zone très réduite, générant des pressions importantes. Celles-ci sont capables de déformer élastiquement les surfaces en contact et d'induire une augmentation importante de la viscosité du lubrifiant (Figure 1).

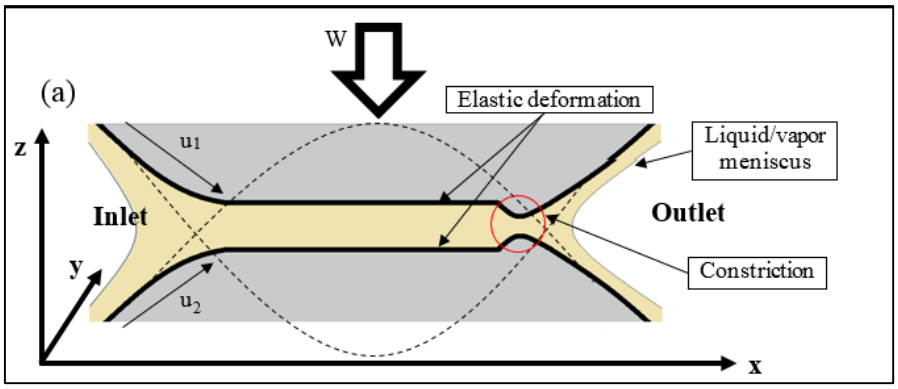

Figure 1. Schéma du lubrifiant et du solide dans le contact élastohydrodynamique, et les différents phénomènes observés.

Le Tableau 1 donne des ordres de grandeurs typiques de quelques caractéristiques physiques et géométriques trouvés dans le régime EHD. Ces conditions extrêmes rendent l'étude de ce régime complexe, tant du point de vue expérimental que numérique.

Caractéristiques	Ordres de grandeur
Epaisseur de film	< 0.5 µm
Diamètre de la zone du contact	≈ 400 µm
Volume du lubrifiant dans le contact	Quelques dizaines de pL
Pression	0.5 – 3 GPa
Déformation élastique	Au moins un ordre de grandeur plus grande que l'épaisseur du film
Augmentation de la viscosité	Quelques ordres de grandeur plus grande que la viscosité à l'entrée du contact
Contrainte du cisaillement	Quelques kPa jusqu'à quelques MPa
Taux du cisaillement	$10^5 – 10^7$ s^{-1}
Augmentation de température	Jusqu'à 100°C
Temps du passage du lubrifiant dans le contact	$10^{-5} – 10^{-3}$ s

Tableau 1. Ordres de grandeur typiques des caractéristiques géométriques et physiques du contact EHD.

Photoluminescence

La photoluminescence (PL) est l'émission de lumière par une molécule (ou toute autre forme de matière) après une excitation par des photons. Elle est donc un processus parmi d'autres, pour la dissipation d'énergie suite à l'absorption d'un photon par la matière. La Figure 2 montre le diagramme de Jablonski nommé en l'honneur du physicien Alexander Jablonski, et qui est utilisé pour illustrer les différents mécanismes de dissipation d'énergie. Dans ce diagramme, les niveaux d'énergie sont représentés par des lignes horizontales. Les lignes les plus épaisses correspondent aux niveaux électroniques (S_0, S_1, S_2, T_1, T_2), tandis que les lignes les plus fines représentent les niveaux vibrationnels (V_0, V_1, V_2, V_3, …) associés à chaque niveau électronique.

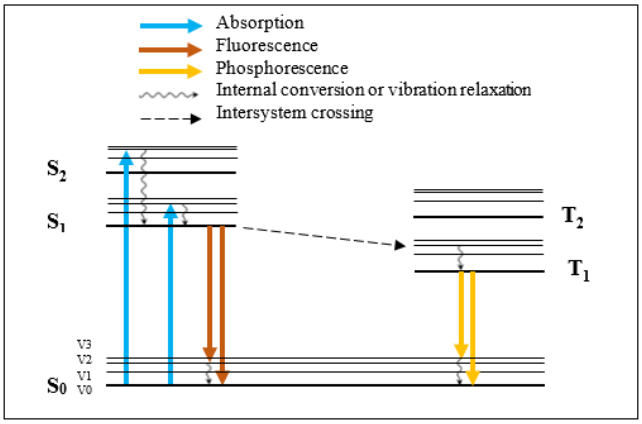

Figure 2. Un diagramme de Jablonski simplifié.

Suite à l'absorption d'un photon, les électrons de la molécule passe de l'état fondamental (S_0) à un état électronique supérieur (S_1 ou S_2), Le retour à l'état fondamental peut s'effectuer par photoluminescence (sous forme de fluorescence ou phosphorescence) ou par dissipation vibrationnelle (sous forme de conversion interne ou conversion intersystème), ou une combinaison des deux processus.

En plus de ces effets internes, les molécules photoluminescentes peuvent interagir avec leur environnement. Des interactions avec les molécules photoluminescentes voisines ou les molécules du solvant (dans le cas de suspensions colloïdales) peuvent avoir lieu. Comme le montre la Figure 3, ces interactions peuvent se produire par l'intermédiaire de photons (interaction radiative) ou sans photons (interaction non-radiative). L'efficacité de chaque interaction dépend fortement de la distance entre les molécules concernées ainsi que leur compatibilité énergétique (chevauchement du spectre d'émission du « donneur » avec le spectre d'émission de l' « accepteur »).

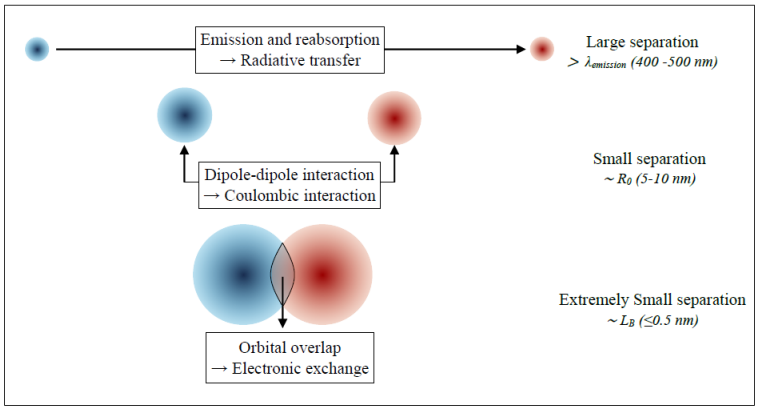

Figure 3. Les différentes natures de transfert d'énergie et leur dépendance entre donneur et accepteur.

Les interactions peuvent être influencées par la distance entre les fluorophores, mais aussi par :

- Des paramètres physiques affectant le mouvement des fluorophores les uns par rapport aux autres (la diffusion par les mouvements Browniens, et éventuellement l'écoulement du lubrifiant) pour l'interaction de type dipôle-dipôle.

– Paramètres dépendant du système de mesure, utilisé comme l'épaisseur du film pour l'interaction radiative.

Boîtes quantiques

Les boîtes quantiques (QDs) sont des nanocristaux de matériaux semiconducteurs. Elles ont été découvertes en 1981 par Ekimov et Onushchenko, et des développements ultérieurs dans la synthèse de ces structures ont permis d'optimiser leurs propriétés. Ces matériaux nanométriques sont connus pour émettre de la lumière dont la couleur varie en fonction de leur taille comme le montre la Figure 4. Ces effets connus sous le nom de confinement quantique, sont dus à la dépendance de l'énergie de la bande interdite E_g de ces matériaux avec leur taille.

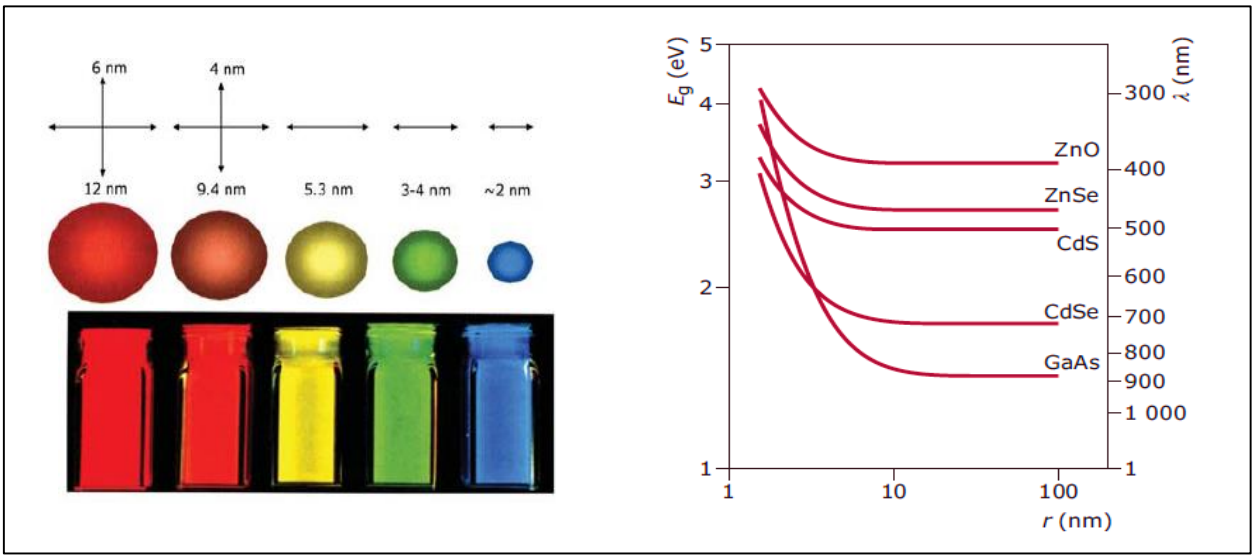

Figure 4. (a) Dépendance de la couleur des QDs avec leur taille; (b) Variation de l'énergie de bandgap ou par conséquent la longueur d'onde d'émission de la taille des QDs.

En effet, selon l'approximation de la masse effective, initialement proposée by Efros et ensuite modifiée par Brus, l'énergie E_g des QDs est déterminée en appliquant un terme correctif (E_g^Q) à l'énergie du matériau massique correspondant (E_g^B) afin de tenir compte du confinement de l'exciton (paire d'électron-trou liée par des forces électrostatiques) dans les QDs :

$$E_g = E_g^B + E_g^Q(r)$$

Pour des QDs sphériques, la correction dû au confinement quantique s'écrit de la façon suivante :

$$E_g^Q(r) = \frac{\gamma^Q}{r^2} - \frac{\nu^Q}{r}$$

Avec :

$$\gamma^Q = \frac{\hbar^2\pi^2}{2}\left(\frac{1}{m_e^* m_e} + \frac{1}{m_h^* m_e}\right)$$

$$\nu^Q = \frac{1.8e^2}{4\pi\varepsilon_r\varepsilon_0}$$

Dans l'expression précédente, $\hbar$ est la constant de Planck réduite (= $h/2\pi$, h étant la constant de Planck), r est le rayon de la BQ, m_e est la masse d'un électron, m_e* est la masse effective d'un électron, m_h* est la masse effective d'un trou, e est la charge d'un électron, ε_r est la permittivité relative de la BQ et ε_0 est la permittivité du vide.

Principe physique de la mesure température et pression

L'énergie d'émission des QDs dépend de la température et la pression pour deux raisons :

- leur *sensibilité massique :* influence de la température et la pression sur la structure cristalline et sur l'interaction exciton-phonon.
- leur *sensibilité quantique :* influence de la température et la pression sur la taille des QDs.

Cette nouvelle technique de mesure proposée dans cette thèse consiste à disperser des QDs de CdSe/CdS/ZnS dans un lubrifiant. Le lubrifiant qui passe dans le contact est illuminé par une source laser afin d'exciter localement ces QDs et leur réponse en PL est détectée. La dépendance de la réponse des QDs avec la température et la pression locale pourra être utilisée pour cartographier ces deux paramètres dans les contacts EHD. L'utilisation d'une seconde famille de QDs pourrait s'avérer indispensable pour découpler chacun des paramètres.

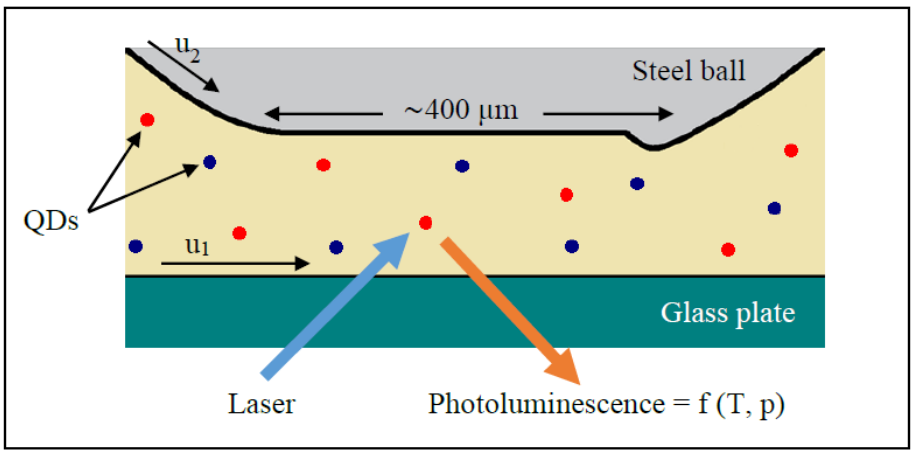

Figure 5. Principe de méthode proposée pour la mesure de la température et la pression dans les contacts EHD (cas avec deux nanosondes).

La Figure 6 montre une représentation schématique des QDs de CdSe/CdS/ZnS utilisées dans notre étude. Comme on peut le constater, ces QDs ont une structure multi-coquilles. En effet ; elles sont constituées d'un cœur de CdSe encapsulé dans deux coquilles en matériaux semiconducteurs (CdS et ZnS), elles-mêmes recouvertes de ligands organiques (à base d'acide stéarique). Les deux coquilles en matériaux semiconducteurs sont utilisées pour la passivation des états de surfaces du cœur, améliorant ainsi le rendement quantique (rapport entre le nombre de photons émis et le nombre de photons absorbés) de ces QDs. De plus, les matériaux

constituant les coquilles ont une énergie de bandgap plus grande que celui du cœur, ce qui assure un meilleur confinement de l'exciton dans le cœur. Les ligands sont utilisés pour (i) passiver les liaisons pendantes à la surfaces des coquilles et (ii) assurer l'affinité des QDs avec leur environnements (hydrophile ou hydrophobe selon les solvants), permettant ainsi la formation de suspensions colloïdales stables.

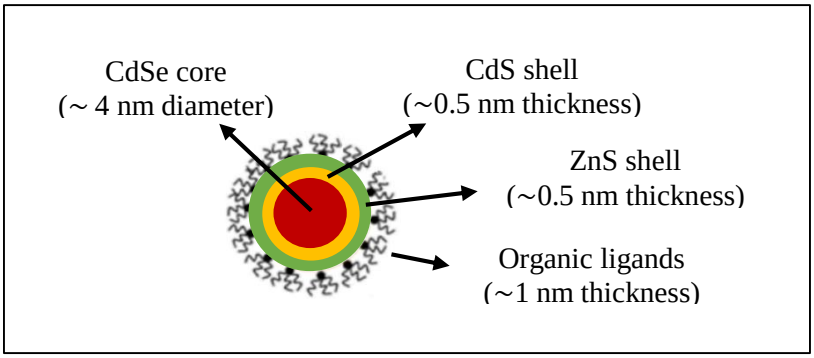

Figure 6. Représentation schématique de la structure multi-coquilles de QDs de CdSe/CdS/ZnS.

Paramètres d'influence

D'après la description présentée ci-dessous, différents paramètres sont à considérer (à des ordres différents) pour la réponse QDs lors de leur passage au contact EHD :

- La température et la pression locales pour leur influence sur la structure, les niveaux vibrationnels activés et la taille des QDs.
- La viscosité du lubrifiant pour son influence sur la diffusion des QDs et par conséquence sur l'interaction entre QDs. La viscosité elle-même est dépendante de la température et la pression.
- L'écoulement du lubrifiant pour son influence sur l'interaction entre les QDs.
- La concentration des QDs pour son influence sur la distance (et donc l'interaction) entre les QDs.
- L'épaisseur de film pour son influence sur les interactions radiatives entre les QDs.

Deuxième partie : étude expérimentale

Etude statique

En vue de l'application finale dans les contacts lubrifiés, il faut dans un premier temps calibrer le déplacement en énergie (ou longueur d'onde) du pic de PL en fonction des paramètres pression et température, c'est-à-dire déterminer la sensibilité des nanosondes étudiées. La calibration a été réalisée dans une cellule haute pression (cellule à enclumes de diamant) régulée en température.

En vue de minimiser les effets parasitiques sur les mesures de pression et température, différents tests statiques ont été réalisés pour étudier :

- L'influence de la concentration des QDs sur leur PL, à température et pression ambiante.

- L'influence de la concentration sur la sensibilité en température des QDs, à pression ambiante.
- L'influence de la température, de la nature du lubrifiant et de la concentration en QDs sur la sensibilité des QDs à la pression.

Le dernier test est le plus important puisqu'il permet de calibrer la réponse des QDs aux variations de la température et la pression. Les deux autres tests ont été réalisés afin de vérifier l'existence et d'évaluer l'influence des paramètres affectant les interactions entre QDs.

La Figure 7 montre la variation de l'énergie d'émission avec la concentration des QDs. On remarque que l'énergie de l'émission diminue de façon importante quand la concentration augmente. Cette dépendance montre clairement un effet d'interaction entre les QDs.

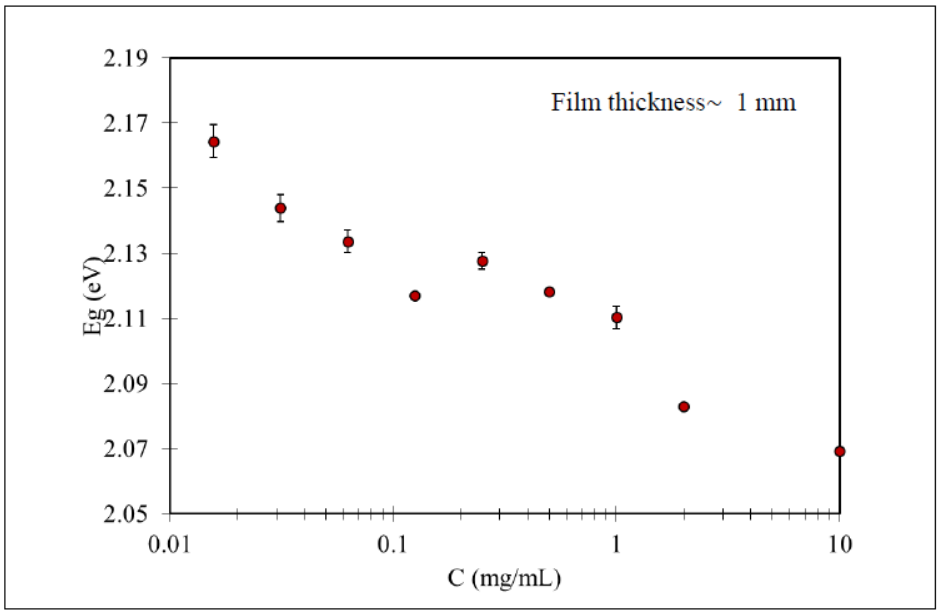

Figure 7. Energie d'émission des QDs de CdSe/CdS/ZnS QDs dispersés dans du squalane en fonction de la concentration. Les mesures ont été effectuées à la température et la pression ambiante.

La Figure 8 montre la variation de l'énergie de PL en fonction de la température pour différentes concentrations en QDs. On peut remarquer une diminution de l'énergie d'émission lorsque la température augmente. Cette observation est compatible avec la dépendance attendue par la contribution massique et quantique de l'émission des QDs avec la température (loi de Varshni et Approximation de la Masse Effective, respectivement).

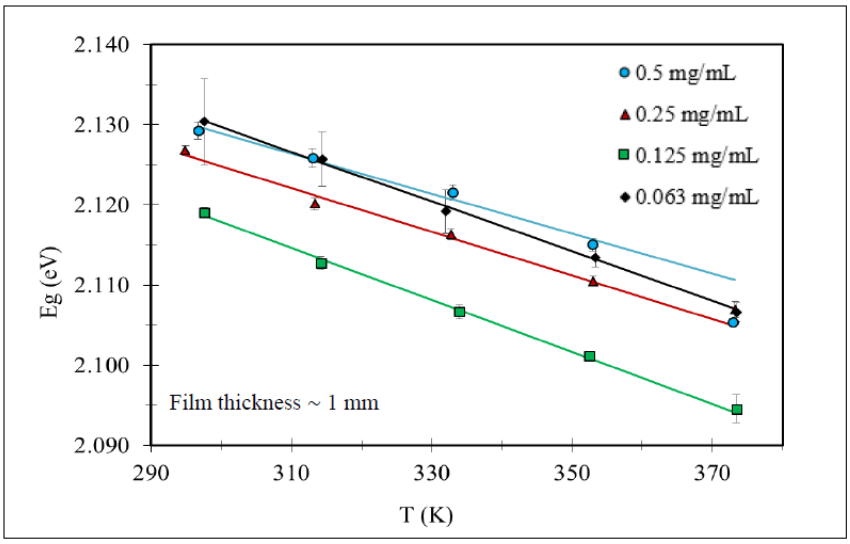

Figure 8. Variation avec la température de l'énergie de l'émission des QDs de CdSe/CdS/ZnS dispersées dans le squalane à différentes concentrations.

Les variations avec la température sont linéaires pour les faibles concentrations. Un écart à la linéarité est observé pour la plus forte concentration (0.5 mg/mL). Les courbes de calibration tracées sur la Figure 8 ont été obtenues en faisant une régression linéaire uniquement dans la gamme de température entre 293 K et 353 K.

D'autre part, on peut remarquer que la sensibilité à la température des QDs varie avec la concentration en QDs : la pente des courbes augmente (en valeurs absolues) lorsque la concentration diminue. Ces variations de sensibilité pourraient être expliquées par les effets d'interaction entre QDs. En effet ; à forte concentration, le transfert d'énergie radiative des plus petites QDs vers les plus grosses masque la contribution des petites QDs dans la réponse en PL de la suspension. Or, les QDs de petites tailles sont plus sensibles aux effets de température et de pression que les plus grosses. La sensibilité qui augmente quand la concentration diminue peut s'expliquer par l'absence d'interaction entre QDs et donc par une forte contribution des petites QDs dans la réponse en PL.

La non-linéarité observée à la plus forte concentration (0.5 mg/mL) ne peut pas être expliquée en considérant uniquement le transfert radiatif entre les petites et les grosses QDs. Une explication possible serait l'effet de la diffusion des QDs. En effet ; l'augmentation de la température et la chute de viscosité qui en résulte favorise le mouvement relatif entre les QDs et le transfert non-radiatif d'énergie entre celles-ci. Par conséquent, une diminution progressive de l'énergie pourrait être attendue à hautes températures.

La Figure 9 montre la variation de l'énergie de l'émission de QDs avec la pression pour différentes conditions (nature du solvant, température et concentration en QDs). Cet effet est intéressant en vue de l'application métrologique. D'une part, on peut remarquer une augmentation linéaire de l'énergie d'émission lorsque la pression augmente. D'autre part, on remarque que la sensibilité à la pression (i) augmente lorsque la concentration diminue, (ii) dépend de la nature du lubrifiant, et (iii) augmente avec la température.

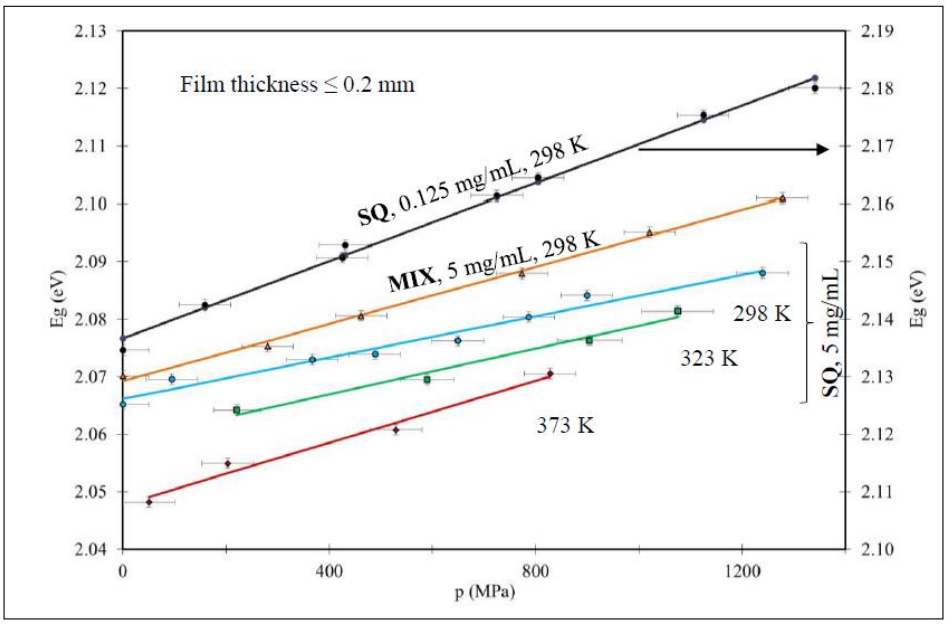

Figure 9. Variation de l'énergie d'émission en fonction de la pression pour des QDs de CdSe/CdS/ZnS dispersées dans le squalane à différentes températures, solvants et concentrations des QDs. SQ: Squalane; MIX: Mélange du squalane (30 vol%) et du cyclopentane (70 vol%).

Les différents tests effectués avec la concentration *de 5 mg/mL*, plusieurs observations montrent l'effet non négligeable de la viscosité sur la sensibilité des QDs à la pression, en particulier :

- La chute de viscosité du squalane induite par l'augmentation de la température est accompagnée par une augmentation de la sensibilité en pression.
- A la température ambiante, les QDs sont plus sensibles à la pression dans le solvant le moins visqueux, c'est à dire le mélange squalane (30 vol%) + cyclopentane (70 vol%).

Afin de confirmer l'influence de la viscosité sur la sensibilité en pression, les valeurs de viscosité ont été calculées pour les deux solvants (le squalane et le mélange) dans les différentes conditions de température et pression. Les résultats sont montrés sur la Figure 10. On note que la squalane à 373 K et le mélange à la température ambiante couvrent le même de domaine de viscosité et donnent lieu à des sensibilités à la pression similaires. Cet effet de viscosité s'explique par la dépendance de l'efficacité du transfert non-radiatif à la diffusion des particules, et la dépendance de la diffusion à la viscosité du solvant.

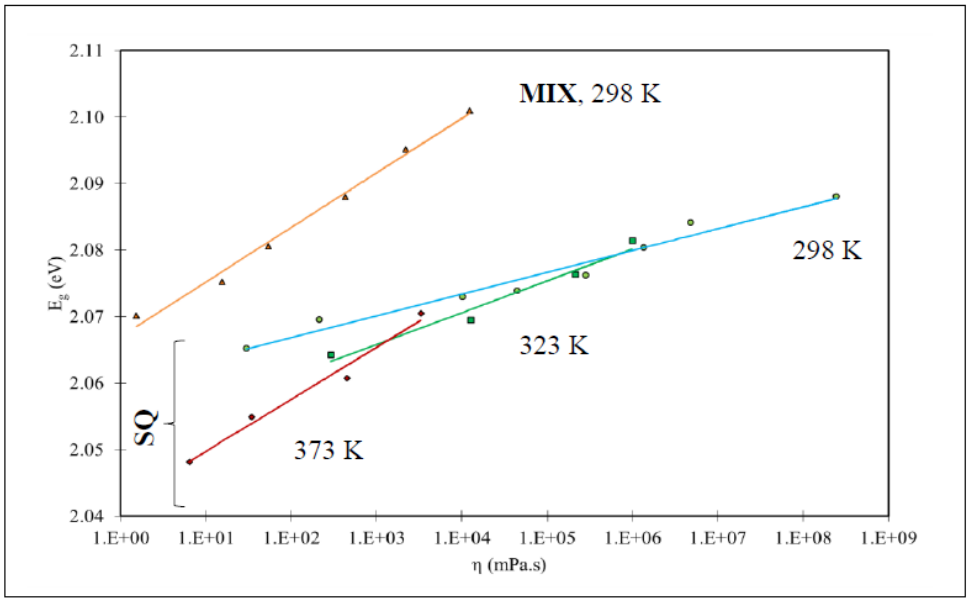

Figure 10. Variation de l'énergie d'émission des QDs de CdSe/CdS/ZnS QDs (C = 5 mg/mL) en fonction de la viscosité du solvant. SQ: Squalane; MIX: Mélange du squalane (30 vol%) et du cyclopentane (70 vol%).

Enfin, sur la Figure 9, en comparant la sensibilité à la pression dans le squalane obtenue pour 5 mg/mL à celle obtenue à 0.125 mg/mL (à 298K), on remarque que la sensibilité augmente en diminuant la concentration. Cet effet est similaire à celui observé pour la sensibilité à la température, et s'explique par l'augmentation de la contribution des petites QDs (ayant une sensibilité plus importante que les grosses particules) dans les solutions diluées.

Le diagramme suivant résume l'effet de la concentration et de la diffusion des particules sur leur sensibilité à la pression. D'une part, la sensibilité augmente en diminuant la concentration, et d'autre part un effet de diffusion est observé, mais celui devient négligeable dans les solutions très diluées.

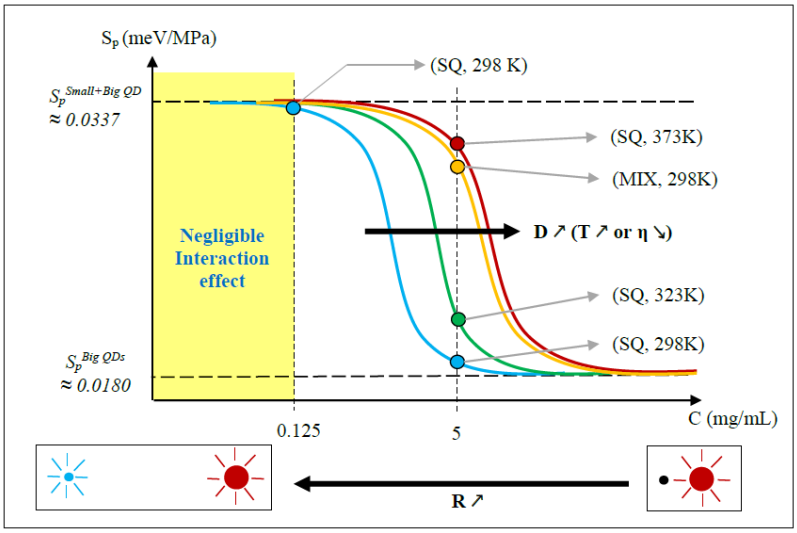

Figure 11. Diagramme pour les différents paramètres influençant la sensibilité en pression des QDs de CdSe/CdS/ZnS. SQ: squalane; MIX: Mélange du squalane (30 vol%) et du cyclopentane (70 vol%).

Les essais en conditions statiques ont montré le potentiel des QDs de CdSe/CdS/ZnS comme nanosondes de pression et température, lorsque les effets d'interactions entre particules sont éludés.

Etude dynamique

Afin de compléter l'étude statique, trois séries de tests ont été réalisées en conditions dynamiques simples. Celles-ci ont été réalisées dans un rhéomètre où le cisaillement et la température peuvent être imposés. Cet appareil travaille à pression ambiante.

Une première série de test a permis de mesurer la viscosité de la suspension colloïdale (squalane avec QDs) pour la comparer à celle du solvant pur (squalane). Une deuxième et troisième série de tests ont permis de mesurer la PL de QDs sous cisaillement afin de répondre à deux questions importantes :

- Est-ce que les QDs sont sensibles au cisaillement ? (deuxième série de tests).
- Est-ce que la réponse de QDs est stable lors de longues périodes de cisaillement ? (troisième série de tests)

La Figure 12 compare les valeurs de viscosité de la suspension colloïdale (squalane avec 0.125 mg/mL de QDs) avec celles du solvant pur (squalane), pour des températures comprises entre 293 et 373 K. Les mesures dans le squalane pur ont été réalisées avec une géométrie de plans en acier parallèles (SPSP) et une géométrie « plan en acier contre plan en verre » (SPGP). Pour le squalane avec QDs, une mesure a été réalisée avec une géométrie SPGP. Ces mesures montrent que les QDs ont un impact négligeable sur la viscosité lorsqu'elles sont présentes à faibles concentrations (≤ 0.125 mg/mL).

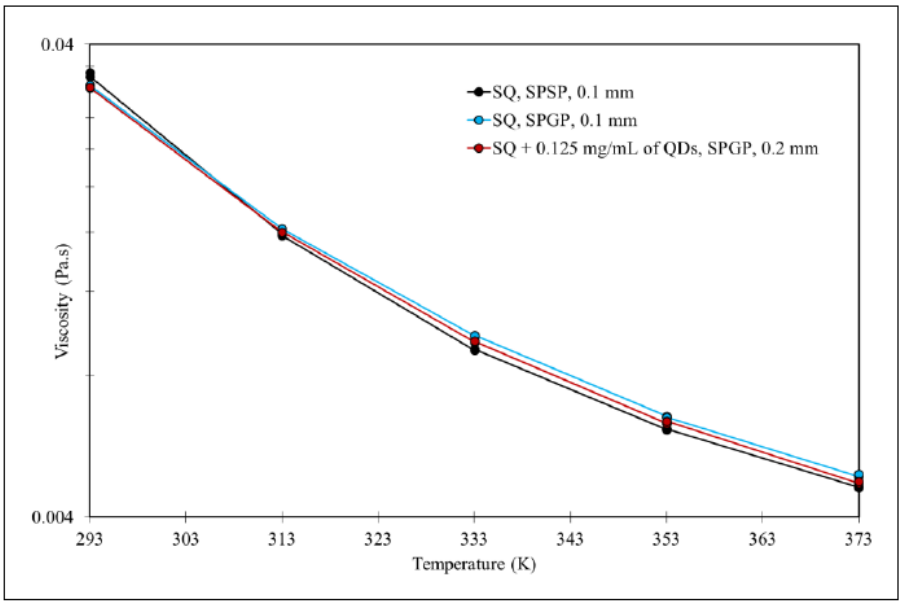

Figure 12. Comparaison entre la viscosité du squalane (SQ) avec et sans QDs.

La Figure 13 montre l'influence du cisaillement sur la réponse des QDs. On remarque que l'énergie d'émission est quasiment indépendante du taux de cisaillement, ce qui est intéressant d'un point de vue métrologique.

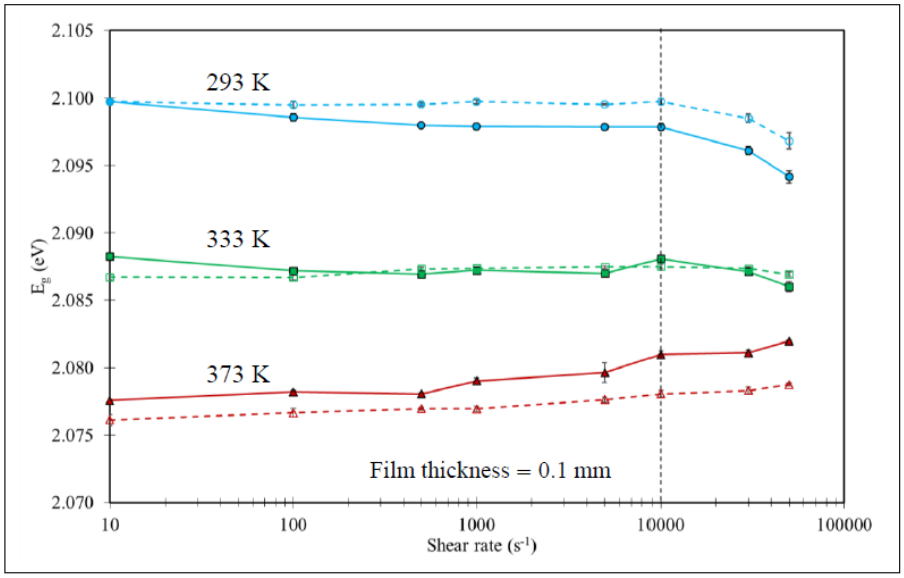

Figure 13. Variation de l'énergie d'émission des QDs de CdSe/CdS/ZnS dispersées dans le squalane en fonction du taux de cisaillement, à différentes températures et pour deux concentrations. (Symboles pleins) 0.125 mg/mL, (Symboles vides) 0.063 mg/mL.

Une certaine variation est pourtant observée aux taux de cisaillement élevés (30000 s^{-1} et 50000 s^{-1}). Les taux de cisaillements élevés s'accompagnent en général d'un auto-échauffement, et ce dernier induit à la fois une chute de viscosité et une diminution de l'énergie d'émission des QDs. Afin de vérifier s'il y a une corrélation entre la viscosité et l'énergie de l'émission, il est utile d'examiner :

- La variation de la viscosité relative η/η_0, avec $\eta_0 = \eta(\dot{\gamma} = 10\ s^{-1})$, en fonction du taux de cisaillement (voir Figure 14).
- La variation de l'énergie d'émission en fonction de la viscosité sous différentes conditions (2 concentrations, 3 températures et taux de cisaillement entre 10 et 50000 s^{-1}) (voir Figure 15).

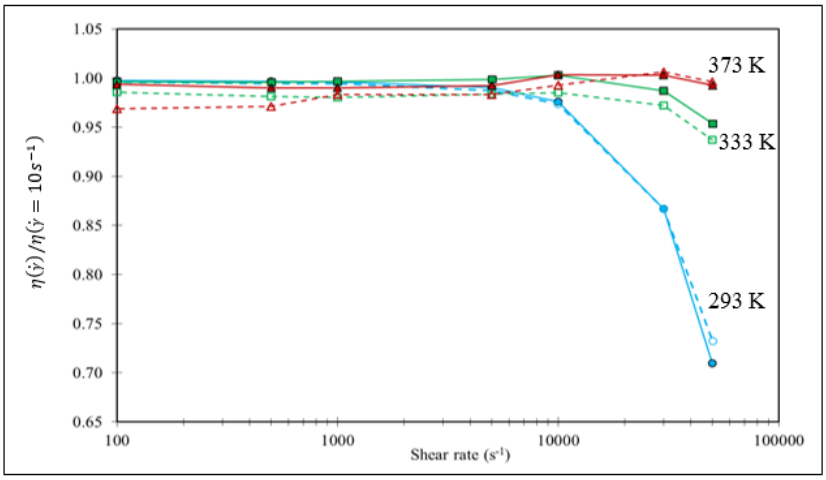

Figure 14. Variation de la viscosité mesurée du squalane en fonction du taux de cisaillement à 3 trois différentes températures et 2 différentes concentrations. (Symboles pleins) 0.125 mg/mL, (Symboles vides) 0.063 mg/mL.

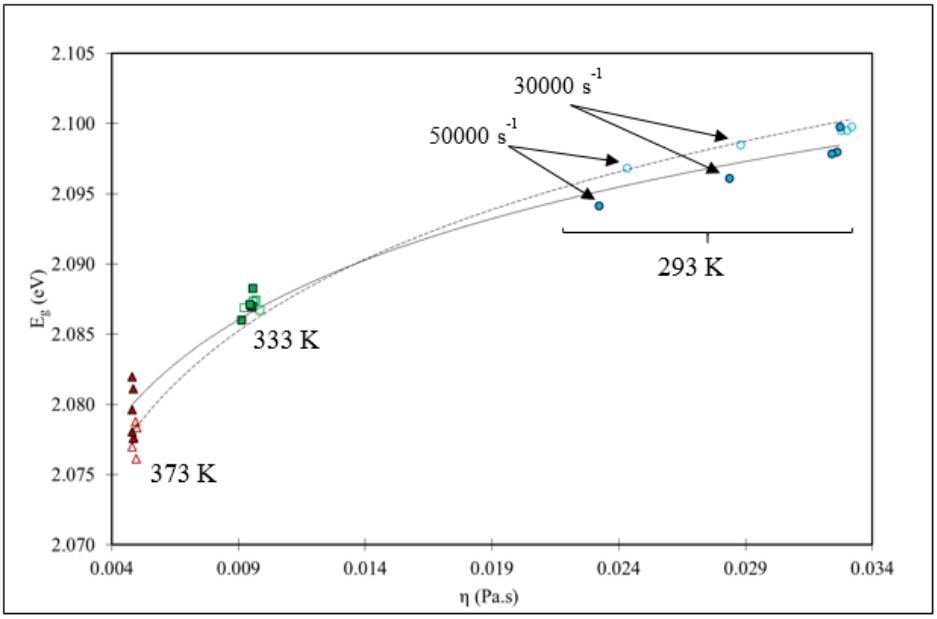

Figure 15. Variation de l'énergie d'émission des QDs de CdSe/CdS/ZnS QDs dispersées dans le squalane en fonction de la viscosité pour 5 taux de cisaillement (de 10s^{-1} à 50000s^{-1}), et à 3 températures différentes et 2 concentrations. (Symboles pleins) 0.125 mg/mL, (Symboles vides) 0.063 mg/mL.

La comparaison entre ces deux figures montre que la variation observée aux forts taux de cisaillement est due à un échauffement par cisaillement. Cet échauffement est à l'origine d'une chute viscosité, et aussi une chute en énergie d'émission (sensibilité des QDs à la température). On voit clairement sur la Figure 15 que les énergies mesurées à 30000 s^{-1} et 50000 s^{-1} suivent bien la ligne reliant les mesures effectuées aux différentes températures, et elle se situe à une viscosité correspondant à une température entre 293 K et 333 K.

Sur la Figure 15, on peut observer également une dépendance au taux de cisaillement même pour des conditions d'isoviscosité (ou conditions d'auto-échauffement négligeable). De plus, cette dépendance semble varier avec la concentration des QDs, ce qui montre que le cisaillement est un paramètre qui peut influencer les interactions entres les QDs. Deux mécanismes pourraient être responsables de ces effets d'interaction :

- L'influence du cisaillement sur le mouvement relatifs entre QDs, et donc sur le transfert d'énergie de petites QDs vers les plus grosses.
- La création d'un gradient de concentration à cause d la migration des particules pendant le cisaillement.

Afin de caractériser la stabilité de la réponse des QDs sous cisaillement, deux types de mesure ont été réalisés à 333 K et avec une concentration en QDs de 0.063 mg/mL dans le squalane. L'une avec une géométrie cône-plan et l'autre avec une géométrie plan-plan. Les spectres d'émission des QDs ont été enregistrés à trois rayons : l_1 = *8.33 mm*, l_2 = *13.33 mm* et l_3 = *18.33 mm*. Le taux de cisaillement dans la géométrie cône-plan est indépendant du rayon (19000s^{-1}), alors qu'en géométrie plan-plan, il est proportionnel au rayon (12500, 20000 et 27500 s^{-1}, respectivement pour les rayons l_1, l_2 et l_3). Les résultats des mesures sont présentés sur la Figure 16.

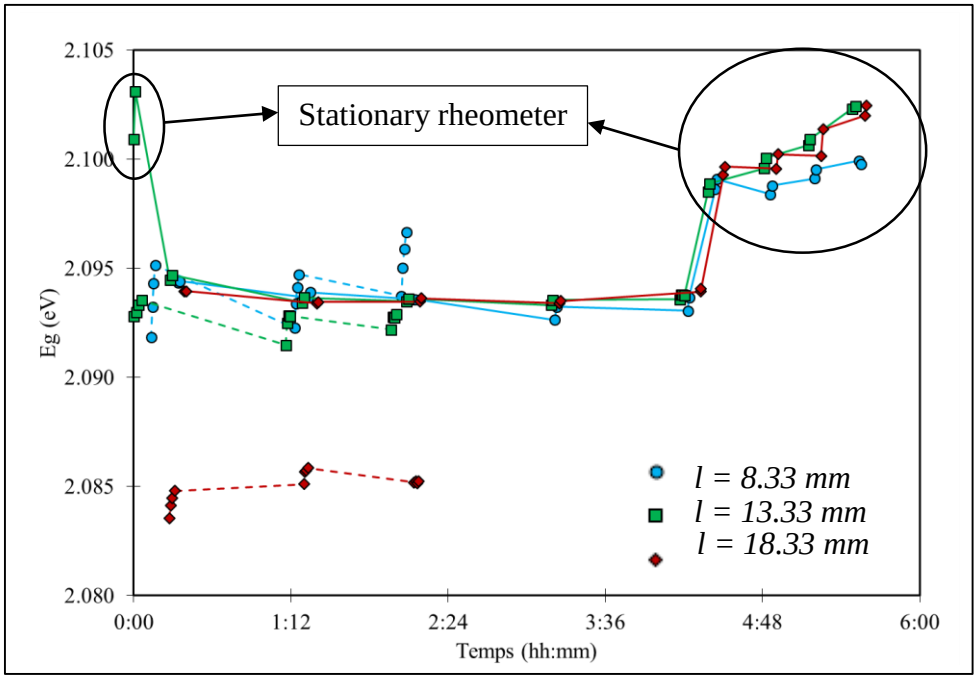

Figure 16. La stabilité de la réponse des QDs de CdSe/CdS/ZnS soumises à longues durées de cisaillement. (Traits pleins) géométrie cône-plane et (Traits en pointillé) géométrie plan-plan.

On peut remarquer tout d'abord que la réponse de QDs reste stable dans le temps sous l'effet du cisaillement quel que soit la géométrie, ce qui est primordial pour l'application visée.

Des mesures ont également été réalisées lorsque le rhéomètre est à l'arrêt avec la géométrie cône-plan (voir les points encadrés sur la Figure 16). On constate clairement que le cisaillement induit un décalage en énergie de PL, mais cet effet est réversible. En d'autres termes, pour l'application finale, la réponse des QDs ne changera en fonction de leurs nombres de passage dans le contact.

Conclusion

Cette étude a été consacrée au développement d'une nouvelle technique de mesure *in situ* permettant de mesurer simultanément la température et la pression dans les contacts élastohydrodynamiques (EHD).

Une étude compréhensive a été menée afin d'identifier les différents paramètres capable d'affecter la PL des QDs. Elles ont été classées en deux groupes (voir la Figure 17) :

- *Paramètres intrinsèques*, dans le sens où ils proviennent de la structure et des propriétés de l'échantillon étudié. Ces paramètres peuvent être reliés aux *paramètres de dimension* et *paramètre d'interaction*.
- *Paramètres extrinsèques*, dans le sens où ils dépendent du système de mesure.

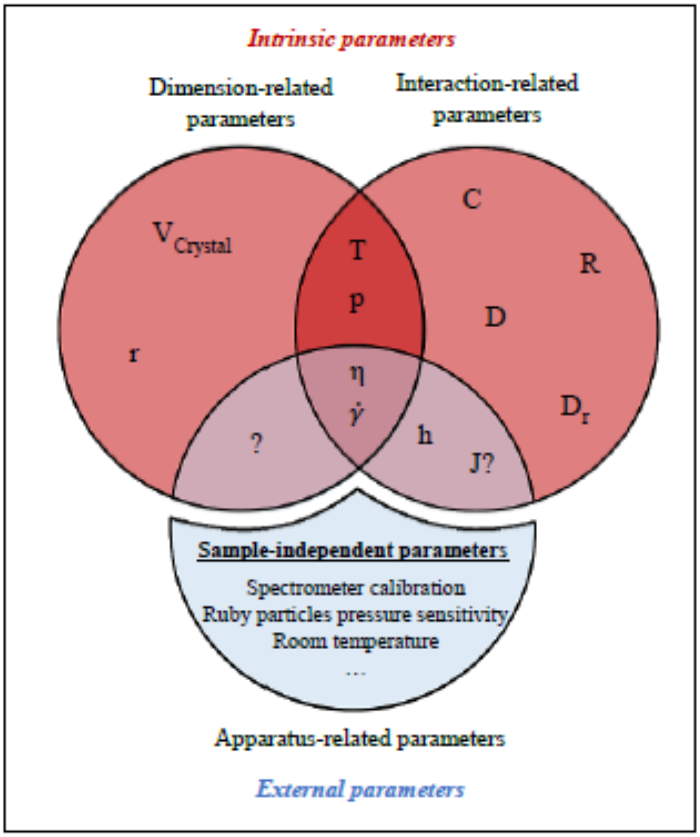

Figure 17. Classification des paramètres d'influence dans la caractérisation des QDs.

Les deux paramètres de dimension fondamentaux sont la structure cristalline (V_{Cryst}) et la taille (r) des QDs. Leur dépendance à la température (T) et la pression (p) est la raison pour laquelle ces nanoparticules ont été choisies en tant que nanosondes.

Les effets d'interaction émergent quand un ensemble de QDs est considéré. L'ampleur de ces effets dépend naturellement de la concentration (C) des QDs, de la distance (R) entre celle-ci, et de leurs mouvements les unes par rapport aux autres. Ces mouvements peuvent être induit par la diffusion Brownienne (D) des QDs, l'écoulement du lubrifiant induit par le cisaillement ($\dot{\gamma}$), et éventuellement la migration des particules (J) induit par différents gradients existant dans le lubrifiant (température, pression, viscosité et taux de cisaillement). Ces mouvements dépendent de la viscosité (η) du lubrifiant, elle-même dépendante de la température et la pression. Les interactions entre les QDs peuvent être influencées aussi par l'épaisseur de l'échantillon (h).

Les effets extrinsèques ou d'appareillage existent dans toutes les mesures expérimentales. Certaines d'entre elles sont indépendantes de l'échantillon étudié (voir Figure 17). D'autres paramètres proviennent de la dépendance de paramètres intrinsèques aux caractéristiques de l'appareil, comme (i) l'auto-échauffement induit par cisaillement qui dépend des propriétés d'isolation thermique de l'appareil, (ii) l'épaisseur du film qui peut varier considérablement d'un appareil à l'autre, (iii) la migration de particules qui dépend fortement de la configuration étudiée.

Dans l'étude que nous menons, l'objectif est de réaliser des mesures précises de température et de pression. Pour cette raison, tous les paramètres parasites, provenant de l'interaction entre

QDs et/ou l'influence de l'appareillage, doivent être identifiés, soit pour minimiser soit pour quantifier leurs effets. Notre choix était de minimiser ces effets en réduisant la concentration des QDs. En effet ; nous avons montré dans l'étude statique que la sensibilité des QDs à la température et la pression devient indépendantes des paramètres d'interaction (la concentration et la diffusion des QDs) dans les solutions fortement diluées.

Introduction

Pressure and temperature are two relevant parameters in the elastohydrodynamic lubrication (EHL) regime. This regime is encountered in many machine components and is characterized by the occurrence of extreme conditions within a very tiny lubricant volume. For instance, the high pressures (up to 3 GPa) result in an important elastic deformation of the rubbing bodies (compared to lubricant film thickness) and induce an important elevation of the lubricant viscosity. In addition, temperature rise can occur due to the sliding motion between the surfaces.

To date, various experimental methods have been developed to measure pressure and temperature within elastohydrodynamic (EHD) contacts, including electrical resistance, infrared emissivity and Raman spectroscopy.

The work presented in this thesis aims at developing a new *in situ* technique for the measurement of these two parameters. This technique exploits the photoluminescence (PL) sensitivity of semiconductor nanocrystals, also called quantum dots (QDs), to changes in pressure and temperature. By monitoring photoluminescence energy variation of QDs dispersed in the lubricant and excited by an appropriate radiation, local measurements could be carried out, allowing the two parameters to be mapped throughout the contact provided that two families of QDs are used. In this work we focus on CdSe/CdS/ZnS QDs.

The manuscript begins in the two first chapters with general reviews on the state of the art on EHL (Chapter I), PL principles and QDs properties (Chapter II). These reviews are needed actually for (i) having a global picture of the different parameters existing in EHD contacts, and (ii) introducing the various parameters to which the QDs could be sensitive.

In the third chapter, calibration tests aiming at evaluating the sensitivity of CdSe/CdS/ZnS QDs to temperature and pressure variations are presented. These calibrations were made in hydrostatic conditions using a diamond anvil cell. The temperature of the cell can be regulated which allows to make coupled temperature and pressure measurements in ranges comparable to those formed in a realistic EHD contact. A particular attention was paid to the influencing parameters in addition to the temperature and the pressure, in order to ensure the reliability of these QDs for local measurements. In particular but not limited to, the effect of the QDs concentration on PL was thoroughly analyzed.

The last chapter deals with simple dynamic conditions imposed with an optical rheometer in which only the temperature and the shear rate can be varied. Measurements allowed to (i) verify if highly diluted QDs suspensions can modify the rheology of the lubricant under investigation (and therefore film and friction generation in EHD contacts) and to (ii) study the influence of shear rate on the PL of QDs.

In the general conclusion, an attempt to sum up all the influencing parameters on the QDs photoluminescence is proposed through a didactic general diagram, and an opening for future investigations and developments of this pioneering work is presented.

I. Context and approach

I.1. Context: Elastohydrodynamic lubrication

I.1.1. Place of elastohydrodynamic lubrication

Before entering in a somehow detailed description of the basics of the elastohydrodynamic (EHD) lubrication problem and its evolution, it is useful to point out its place among the other regimes of lubrication. This could be helpful to underline some of its main features in contrast to the other regimes, and to clarify in this way the context we will be dealing with in our work.

In literature, lubrication regimes have been classified in two different ways: the first being in terms of the friction within the contact, and the other in terms of the behaviour of the solids and the liquid once the contact is established.

I.1.1.1. Classification based on friction value: Stribeck curve

Stribeck performed, between 1900 and 1902, measurements of the value of friction in rolling and sliding bearings under different operating conditions (normal load W and sliding velocity V) and for lubricants with different viscosities η. He obtained[1] what was later called the Stribeck curve which allows three different lubrication regimes to be identified (see Figure I.1). This curve with the "dimensionless lubrication parameter", $\eta V/W$, in abscissa suggests a net friction variation governed by the ratio h_{min}/R_S, with h_{min} being the minimum film thickness and R_S the combined surface roughness of the bounding surfaces. Indeed, when the viscosity or the velocity is decreased or the load is increased, lubrication passes through the following regimes[2]:

- Regime I: hydrodynamic lubrication regime ($h_{min}/R_S >> 3$);
- Regime II: mixed lubrication ($1 \leq h_{min}/R_S < 3$);
- Regime III: boundary lubrication ($h_{min}/R_S < 1$).

In the first regime, the load is entirely carried by the fluid due to the latter's relatively important thickness (compared with roughness) ensuring a full and continuous separation between the two solids. As a consequence, the measured friction originates from the internal friction in the lubricant film. In the second regime, the role of the roughness becomes more relevant and the load will be partially carried by the fluid and partially by the contacting asperities. For the same reason, friction will be shared between the shearing of the lubricant and the deformed surfaces asperities. Finally in the third regime, the bulk lubricant rheology role recedes in favor of solid/solid (asperities) interactions as well as the solid/liquid interfacial interactions. These interactions can in some cases induce some chemical reactions (also called triboreactions).

Elastohydrodynamic lubrication (EHL) is a special case of hydrodynamic lubrication. It is encountered within non-conformal contacts in which the load is concentrated in a very small area. Due to the high-pressure conditions experienced, some very particular features are observed in this regime, which will be the discussion of next paragraphs. It is worthy to note that mixed lubrication is sometimes called partial EHL. This is because away from asperity conjunctions, the lubricant experiences similar conditions encountered in an EHD contact. For this reason, dealing with mixed lubrication requires considering both solid/solid contact and EHD contact (or actually micro-EHD contact, which refers to a contact whereby surface roughness can modify the flow of the lubricant due to the extreme confinement of the fluid film).

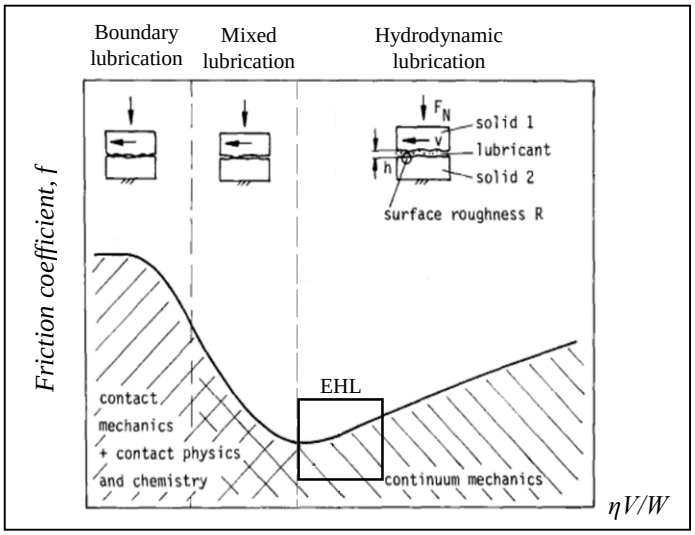

Figure I.1. Stribeck curve (adapted from[3]).

I.1.1.2. Classification based on solid/liquid behaviour

In order to predict flow characteristics when a lubricant passes within a contact, the mechanical behaviour of the liquid and the solids has to be considered. By the 1970s, four lubrication regimes were clearly identified based on liquid/solid behaviour: isoviscous-rigid, isoviscous-elastic, piezoviscous-rigid and piezoviscous-elastic lubrication regimes[4] (see Figure I.2). Indeed, depending on the operating conditions, the properties of the contacting solids and the nature of the lubricant, the following behaviors can be observed:

- The liquid's viscosity is whether pressure-independent (isoviscous) or pressure-dependent (piezoviscous);
- The solid is whether not deformed (rigid) or elastically deformed (elastic).

The high-pressure values encountered in EHL are enough to induce a substantial increase in viscosity and an elastic deformation of the lubricated surfaces. For this reason, EHL is formally classified as the piezoviscous-elastic lubrication regime[4].

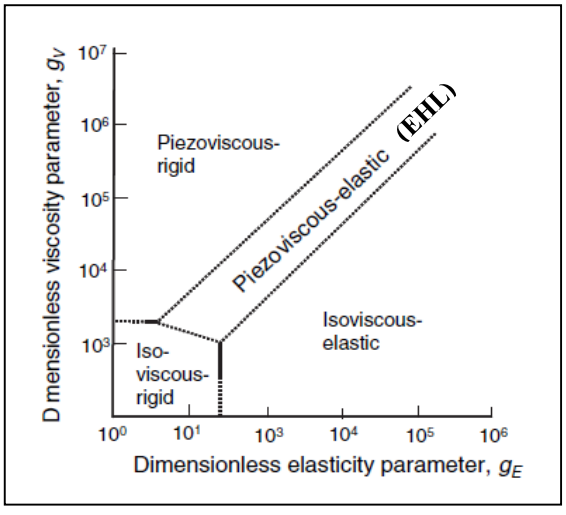

Figure I.2. The four regimes of lubrication in EHD point contact lubrication, from[5], adapted by[4].

I.1.2. Main features of the EHL

Due to the intense research activity on EHL, its main features have been elucidated. Nevertheless, despite all the achievements, the comprehension and the prediction of some important characteristics of EHD contacts has not yet attained an acceptable level. For instance:

- The determination of the lubrication regime under given operating conditions relies on the prediction of the minimum film thickness, which is not yet satisfactory;
- The physical mechanisms responsible of the friction in a thin-film fluid are not clear, and the question is still open to debate[6,7].

Two main reasons can be mentioned. The first is the multi-physics and the multi-scale nature of the EHL. The second is the difficulty of the experimental approach due to the severe confinement and the dynamics of EHD contacts. These facts raise the necessity of the development of techniques providing local measurements of the relevant parameters in these contacts. In the following paragraphs, some of the main characteristics of the EHL will be presented in order to have a better insight of the basic mechanisms involved in this regime of lubrication. In addition, the different characteristics which impede the progress of the experimental approach will be presented. A detailed presentation of the evolution of EHL theory demonstrating its multi-physics and multi-scale nature will be given in the next section. A particular emphasis on the actual and possible contribution of the experimental approach, and in a more specific way on *in situ* methodologies, will be made therein.

I.1.2.1. The different zones in EHD contacts

When two lubricated solids, with non-conformal geometries[*], are brought into contact and animated with the velocities u_1 and u_2 and loaded with a normal force w as shown in Figure I.3 (a), four zones with distinguishable properties are observed (see Figure I.3 (a) to (c)):

- The inlet or the hydrodynamic zone;
- The high pressure central zone;
- The constriction zone;
- The outlet.

The lubricant supply is ensured at the inlet (whose position relative to the contact depends on the magnitude and the direction of u_1 and u_2). Next, the lubricant crosses the high-pressure zone where the solids are elastically flattened and a near constant film thickness is formed. When the lubricant approaches the outlet, the pressure declines towards the atmospheric level. However, the requirement of maintaining the continuity of mass flow implies a local restriction of film thickness in the so-called constriction zone. Such variation in geometrical form between the high pressure central zone and the constriction zone generates a narrow pressure spike[8], known as the Petrusevich spike[9]. In the outlet, the depressurizing continues until the breakdown of the lubricant film and the formation of the liquid/vapor meniscus.

[*] Contacts can be either conformal or non-conformal. In the first case, the two bodies have closely matching curvatures, which results in a relatively large contact area – of the same order of magnitude as the dimensions of the two bodies – and thus low pressures. Examples are journal bearings and seals. In the second case however the curvatures do not match well and consequently the load is concentrated in a small area, resulting in high pressure values. When this "mismatch" is in both principal directions of the surfaces, a point contact is obtained, and when it happens in only one direction, a line contact is obtained. Non-conformal contacts are encountered in rolling bearings, gears, cam and followers, etc.

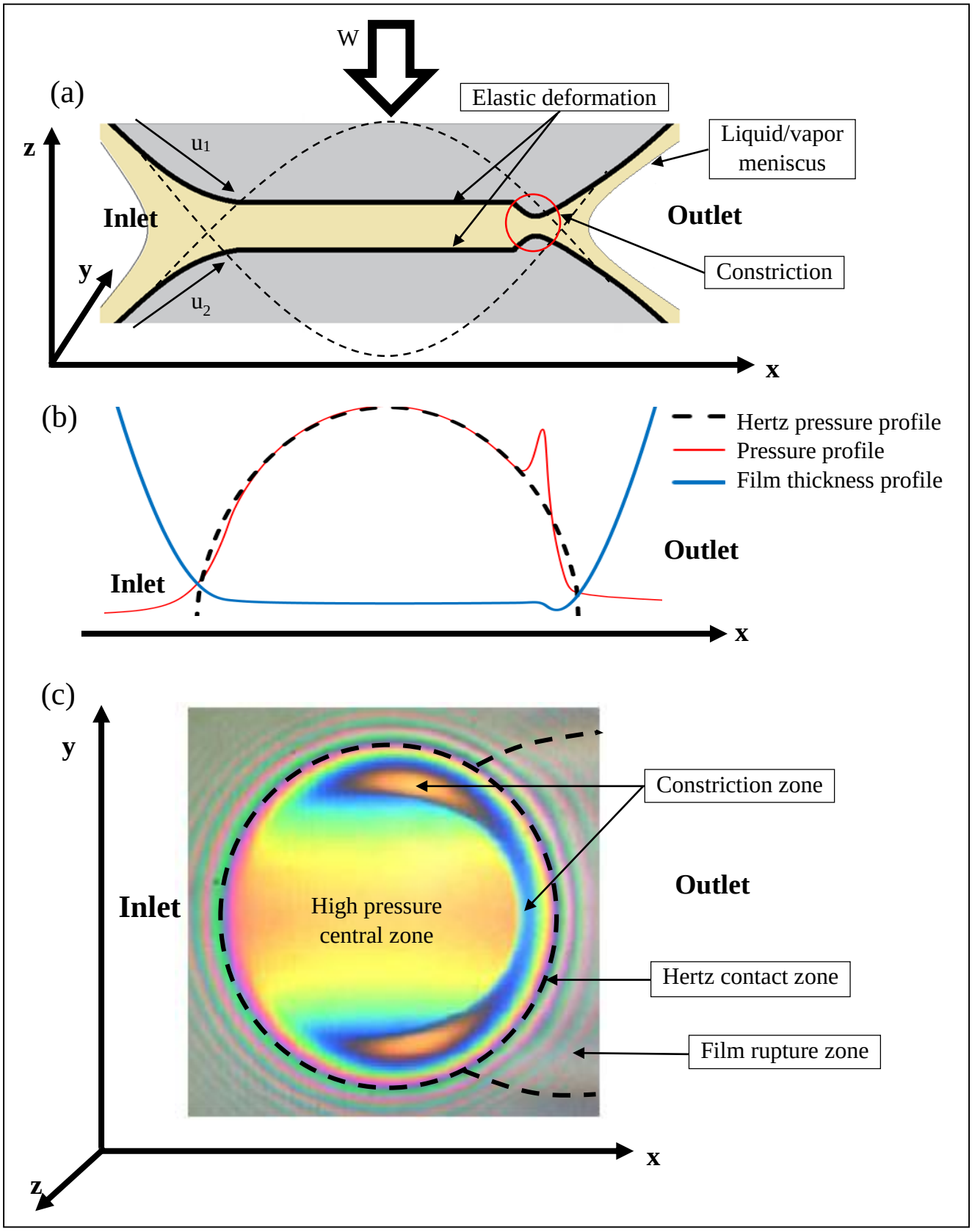

Figure I.3. The different zones of the EHD contact: (a) Schematic of the lubricant and the solid within the contact, and the different phenomena that can be observed, (b) film thickness and pressure profiles (Hertzian pressure profile is included for comparison), (c) The different zones of contact on an interferogram (that can be used to extract film thickness).

This is the most common picture encountered in EHD contacts, but things become more complex under particular conditions (severe sliding conditions or transient effects for instance). Some examples will be given when presenting the evolution of EHL problem.

I.1.2.2. Geometrical and physical characteristics

As mentioned above, performing detailed experimental investigation on EHD contacts is not an easy task because of the extreme conditions encountered in such contacts. Therefore, it is sorely needed to be familiar with these conditions and difficulties before developing any experimental method adapted to the requirements of EHL. Table I.1 gives some typical orders of magnitude of the geometrical and physical characteristics found in these types of contact.

Characteristic	Order of magnitude
Film thickness	< 0.5 µm
Contact zone diameter	≈ 400 µm
Lubricant volume within the contact	Some tens of pL
Pressure	0.5 – 3 GPa
Elastic deformation	At least an order of magnitude larger than film thickness
Viscosity rise	Several orders of magnitude larger than inlet viscosity
Shear stress	Some kPa to some MPa
Strain rate	$10^5 – 10^7$ s^{-1}
Temperature rise	Up to 100°C
Transit time of the lubricant in the contact	$10^{-5} – 10^{-3}$ s

Table I.1. Typical orders of magnitude of the geometrical and physical characteristics in EHL.

First of all, the lubricant is highly confined: given a contact diameter and film thicknesses of about 400 µm and 0.5 µm, respectively, the lubricant volume within the contact is in the order of some picoliters. This implies serious difficulties for (i) getting access to the contact and (ii) performing local measurements of the physical properties which, we know, can vary importantly within the contact. For these reasons, many measurement devices, such as thermometers, can only yield rough estimations, and some parameters, such as friction, have not yet been measured locally (or at least in a direct and a faithful way). Furthermore, in machine components the lubricants are confined between nontransparent solids, which restricts the application of optical methods unless if at least one of the solids are replaced with a transparent object. This is actually very often practiced, but it presents however the inconvenient of working with solids having different properties from those used in real contacts.

The other difficulty is related to the severity of the physical conditions, particularly the pressure. Values of pressure up to 3 GPa can be experienced, and this induces as mentioned above high local deformation of the contacting solids and a substantial increase of the lubricant's viscosity. The deformation can be several orders of magnitude larger than the film thickness, and the viscosity is increased by an order of magnitude every 25 to 250 MPa[10]. Obviously, when it comes to developing a new experimental technique, one must ensure that this technique remains unaffected to such high pressure rises. This is particularly true for the techniques that consist of introducing sensors within the contact.

In some mechanisms, the kinematic conditions induce sliding motion within the contacts, and in such cases the lubricant is highly sheared. Typically, values of shear stress ranging from some KPa to some MPa, and strain rates between 10^5 and 10^7 s^{-1} are obtained. The existence of such high shear stresses (together with the high values of pressure) can increase the severity of the contact and induce temperature rises up to 100 °C. Clearly, under such conditions, the resistance of the experimental techniques becomes again a major issue.

Another characteristic of the contact is the transit time of the lubricant, which is usually in the order of 10^{-5} to 10^{-3} s. Within this short time, the lubricant experiences all the important variations in film thickness, pressure, shear stress, etc. Ultra-fast techniques are thus needed to probe the flow, and for techniques requiring the use of sensors, their responses' timescale has to be shorter than the transit time. The problem becomes more difficult under transient effects, since the timescales offered by experimental methods (sensors and/or capturing apparatus) have to be much shorter than the characteristic times of these effects.

I.1.3. Evolution of the EHD problem and contribution of the experimental approach

I.1.3.1. From Hertzian and hydrodynamic contacts to EHD contacts

From certain viewpoint, EHL can be considered as a combination of Hertzian dry contact and hydrodynamic lubricated contact. Before presenting this viewpoint, a brief description will be given of these two forms of contacts.

In 1881, Hertz presented his well-known theory on static dry contacts[11] that can be considered as the milestone of contact mechanics. His theory could later find its way, due to its simplicity and its acceptable accuracy, to a large number of applications. His calculations were based on the following assumptions:

- Homogeneous, isotropic and elastic materials;
- Continuous, smooth and non-conforming surfaces;
- Zero tangential force (frictionless contact) and negligible adhesion and repulsion forces;
- Small strains.

Based on these assumptions, he could determine the dimensions of the contacting area, the pressure distribution within this area, and the deformation of the solids. In the case of a point contact formed between two spheres of radii R_1 and R_2, and of modulus of elasticity E_1 and E_2, and of Poisson's ratio ν^p_1 and ν^p_2, respectively, the two solids are flattened within a circular contact area. The radius, a, of this area, the pressure distribution, p, and the deformations, δ_1 and δ_2, are respectively given by (see Figure I.4 (a)):

$$a = \left(\frac{3wR'}{2E'} \right)^{1/3} \qquad (I.1)$$

$$p(x,y) = \begin{cases} p_{\max} \left[1 - \dfrac{x^2 + y^2}{a^2} \right]^{1/2}, & for\ x^2 + y^2 \le a^2 \\ 0, & elsewhere \end{cases} \qquad (I.2)$$

$$\delta_i(x,y) = \frac{1-\left(\nu^p{}_i\right)^2}{\pi E_i} \iint_S \frac{p(x',y')\,dx'dy'}{\sqrt{(x-x')^2+(y-y')^2}}, \quad i=1,2 \tag{I.3}$$

Where:

p_{max} is the maximum pressure given by:

$$p_{\max} = \frac{3w}{2\pi a^2} \tag{I.4}$$

R' is the effective radius defined as:

$$\frac{1}{R'} = \frac{1}{R_1} + \frac{1}{R_2} \tag{I.5}$$

E' is the effective Young modulus defined as:

$$\frac{2}{E'} = \frac{1-\left(\nu^p{}_1\right)^2}{E_1} + \frac{1-\left(\nu^p{}_2\right)^2}{E_2} \tag{I.6}$$

Some years later in the same decade, Reynolds published a paper[12] presenting a theoretical analysis on Tower's journal bearing experiment[13]. In this paper, he derived what was later called the Reynolds equation and which actually can be considered as the foundation of thin-film or hydrodynamic lubrication theory. To do so, he applied the general Navier-Stokes equations (describing the motion of fluid in space and time) and the continuity equation to liquids in narrow gaps, or on other terms, to thin liquid films*, and he made several assumptions:

- Laminar and isothermal flow;
- Newtonian fluid;
- Negligible inertia and body forces (compared to viscous forces);
- Negligible through-thickness variation of pressure, viscosity and density;
- Negligible curvature effects (which implies a film thickness much smaller than the dimensions of the contacting solids).

Under stationary conditions, the Reynold's equation can be written in the following way:

$$\frac{\partial}{\partial x}\left[\frac{\rho h^3}{12\eta}\frac{\partial p}{\partial y}\right] + \frac{\partial}{\partial y}\left[\frac{\rho h^3}{12\eta}\frac{\partial p}{\partial x}\right] = \frac{\partial(u_m \rho h)}{\partial x} + \frac{\partial(v_m \rho h)}{\partial y} \tag{I.7}$$

where ρ is the density of the lubricant, η is the viscosity of the lubricant, h is the film thickness, u_m and v_m are the velocities in the x and y directions, respectively. The terms on the left represent the

* This assumption is sometimes called lubrication assumption[22].

pressure-induced flows (Poiseuille flows), whereas the terms on the right describe the shear-driven flows or, in other terms, the flows driven by the moving surfaces (Couette flows).

Reynolds equations have been applied successfully to conformal-contact components (Figure I.4 (b)) working at low pressures (typically between 0.1-10 MPa)[14]. Regarding conformal contacts, an early attempt has been made by Martin in 1916[15] to use Reynold's equation to predict the film thickness in the conjunction between two parallel cylinders (simulating the contact between a pair of gear teeth). In this analysis, Martin made the assumptions of rigid solids and isoviscous Newtonian fluid. Unfortunately for him, the analysis failed because the predicted values were extremely small (in the order of 1-10 nm) and far below the roughness of the surfaces (0.8-0.8 μm) to ensure the full separation between the surfaces (which was already a well-known fact at that time). Further attempts have been made to refine the analysis by assuming elastic-isoviscous[16] (in 1938) or rigid-piezoviscous[17] (in 1945) behaviors, but all failed in predicting a realistic film thickness.

Ertel was the first to incorporate both elastic and piezoviscous effects in the solution of the hydrodynamic problem[18]. The genuine way he approached the problem, albeit imperfect as we will see, demonstrates the viewpoint presented in the beginning of the paragraph considering EHL as a combination between Hertzian dry contact and hydrodynamic lubrication contact. Indeed, while considering a piezoviscous hydrodynamic problem, Ertel assumed an elastic flattening according to Hertz equation for dry contacts, except that here, a thin lubricant film of a constant thickness, h_c, is entrapped between the two surfaces (see Figure I.4 (c)). More formally, he made the assumption of a Hertzian pressure profile within the contact zone ensuring the flattening of the surfaces. On the other hand, he assumed a pressure profile at the inlet of the contact approaching infinity on the edge of the Hertzian zone (see Figure I.4 (c)) and an incompressible fluid in order to allow for the generation of the constant lubricant film within the contact.

Following these assumptions, Ertel could calculate much more acceptable film thicknesses than those predicted by Martin's analysis (one to two orders of magnitude greater values were obtained). It is worth noting that the following equation that he could derive for line contacts is remarkably similar to the EHD regression formulas obtained later *via* numerical methods (such as for example, Dowson and Higginson's equation[19])[4]:

$$h_c = 1.93\left(\eta U a_p\right)^{0.727} R'^{0.364}\left(\frac{E'}{w_L}\right)^{0.091} \text{, from Ertel}^{18} \qquad (I.8)$$

Where a_p is the pressure-viscosity coefficient, w_L is the applied normal load per unit length, U is the entrainment velocity defined as:

$$U = u_1 + u_2 \qquad (I.9)$$

Being aware of the limitations of his theory/model, namely on the shape of pressure distribution, the fluid compressibility and the pressure profile at the inlet, Ertel anticipated the existence of a local reduction in film thickness and a corresponding pressure spike near the outlet of the contact[20]. Ertel's early anticipations have been confirmed later with the full resolution of the EHL problem (Figure I.4 (d)) which actually requires at least the simultaneous consideration of the following equations:

- Elastic deformation of the solids (equation (I.3));

- The flow of the fluid (Reynold's equation (I.7));
- The load balance equation;
- The variation of fluid rheological properties (viscosity and density) with pressure.

A considerable effort has been made during the last seventy years to obtain numerical solutions to the previous equations (and eventually with further complications that can be added to the problem, as we will see in the following paragraphs). The detailed presentation is however beyond the scope of our survey. Interested readers can refer to reviews on the subject, such as those published by Gohar[21], and Lugt and Morales-Espejel[22].

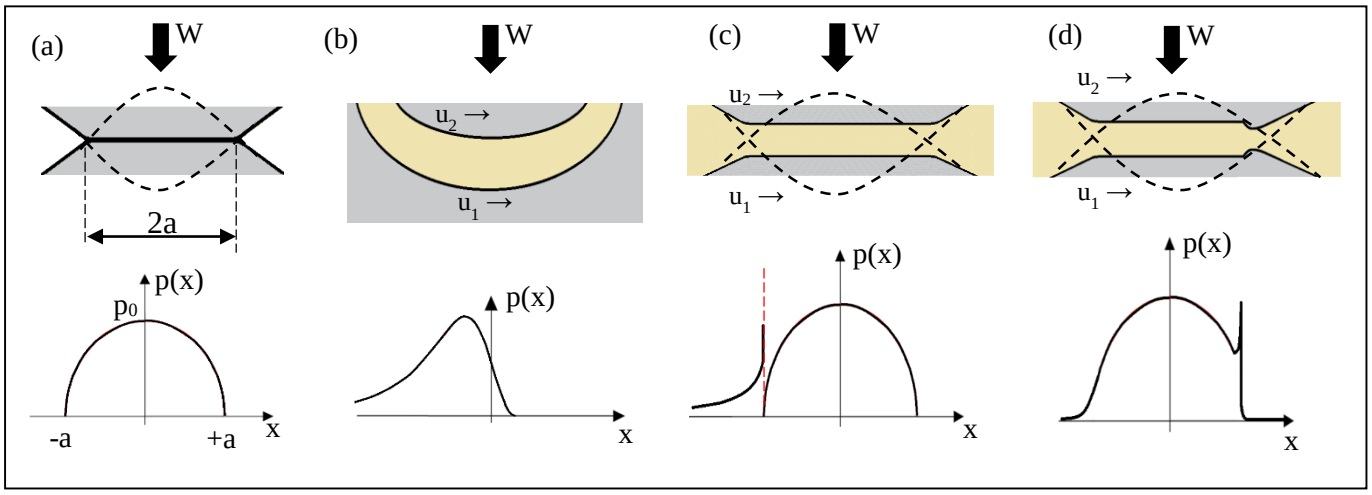

Figure I.4. The shape of solids' surfaces and pressure profiles in the case of: (a) dry Hertzian contact, (b) hydrodynamic contact, (d) EHD contact under Ertel's simplified assumptions and (c) realistic EHD contact. The dotted curves represent the shape of the non-deformed surfaces.

The strong coupling between the different physical parameters reveals also the multi-physics nature of EHL and consequently the necessity of experimental approach. This approach can indeed:

- Assess the validity of the numerical predictions;
- Improve these predictions by verifying or refining the basic assumptions on which they rely;
- Supply the numerical models with the accurate experimental data needed for calculations, such as those on boundary conditions or on the rheological properties of the fluids.

Some concrete examples will be given on the two last points in the next sections. As for the first point, we can mention two examples on experimental approaches confirming basic theoretical predictions:

- Optical interferometry[23,24] and electrical capacitance[25,26] methods confirmed the theoretical predictions of shape of the film thickness and its dependence on the operating conditions and the rheological properties of the fluids;
- Pressure profile within the contact, and more particularly, the existence of a pressure spike upstream the contact have been confirmed by using evaporated manganin pressure electrical gauge[27];

A more detailed description of these methodologies (and others) and their contribution can be found in the review published by the author and co-workers on the *in situ* methodologies applied for studying EHL[28].

I.1.3.2. From film thickness prediction to friction control

In the early years of the development of the EHL theory, most attention was placed on the prediction of film thickness. The main purpose was to obtain a sufficient film thickness ensuring the full separation between the solids in order to reduce wear and, consequently, to prevent the failure of the mechanical components. However, these predictions were in general made upon basic assumptions such as: Newtonian behaviour for fluids and isothermal conditions within the contact[8]. Given the fair agreement between theory and experiment, further refinement seemed unnecessary at that time.

Things changed greatly when power efficiency *via* friction (or traction) control became the priority in the design of tribological machine components. Searching for a better comprehension of friction, it quickly became apparent that the above-mentioned assumptions were not always satisfactory. Figure I.5 shows a typical traction curve exhibiting three different tendencies depending on the value of the Slip to Roll Ratio (*SRR*) defined as:

$$SRR = \frac{\Delta u}{\bar{u}} = \frac{u_2 - u_1}{\left(u_2 + u_1\right)/2} \qquad (I.10)$$

- In zone I, the traction increases linearly with slip, indicating the Newtonian behaviour of the lubricant (or shear-independent viscosity);
- In zone II, a slow-down in the rate of increase followed by the stabilization of the traction is observed. Such variation reveals a particular non-Newtonian behaviour characterized by the stabilization of friction beyond a given slip value corresponding to a certain shear stress value commonly called the Limiting Shear Stress (LSS);
- In zone III, thermal effects become important due to the high slip values leading to the decrease of the friction of the fluid.

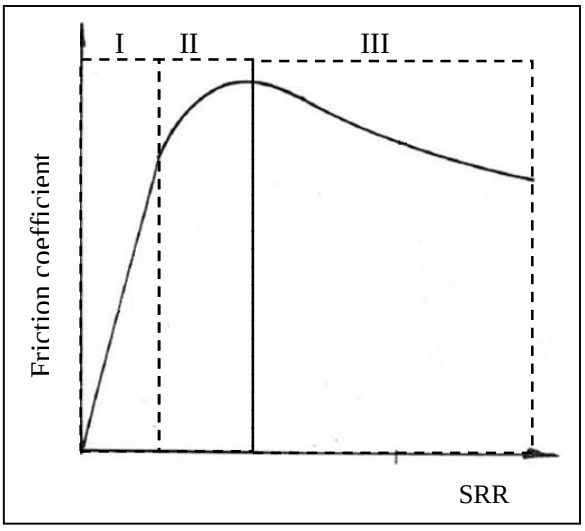

Figure I.5. An example of traction curve.

Furthermore, it is now accepted that the film thickness is determined by the properties of the fluid at the inlet region of the contact, but when it comes to predicting friction, the high-pressure central zone has the dominant influence. The two zones are actually decoupled[4]; the shift from the former to the latter is nevertheless not trivial neither experimentally nor numerically. Indeed, the values of the maximum pressure in the inlet region are around 70 MPa[4], and the shear rates encountered at this region can be easily reproduced outside the contact (for the need of establishing the rheological properties of the fluid for example). Conversely, the current knowledge on fluid friction mechanism is relatively poor because of the extreme conditions at the central region involving (i) a more complex rheology (high-pressure and eventually high-stress rheology, and the coupling between the two), (ii) thermal effects and eventually (iii) phase transformation. Reproducing such extreme conditions, individually or together, in a controlled way outside the contact with the aim of decoupling the influence of each parameter and observing each phenomenon, is not always possible (to this day). This demonstrates the importance of developing *in situ* local measurements, allowing the investigation of such phenomena and mechanisms in realistic conditions.

A brief description of the possible complications that has to be taken into account in predicting friction, with a special emphasis on the actual or possible contribution of the experimental approach, is given below.

Limiting shear stress

The concept of LSS was first proposed by Smith[29] to describe the stabilization of the friction at high slips in terms of the maximum value of shear stress that a lubricant can sustain (under given operating conditions). The physical origin of the LSS is far from being completely clear. Two main methods have been used to shed some light on this phenomenon:

- High-pressure rheology (different apparatus have been designed to this purpose, such as: high-pressure chamber[30], Hopkinson torsion bars[31], plate impact tests[32], Kolsky bars[33], and bouncing ball apparatus[34]);
- Friction measurement in EHL contacts (using disc machines[35] or, later, ball-on-disk tribometers).

As stated by Bair and McCabe[36] in a paper published in 2004 on this subject, "Ideally, after 40 years, the two methods … should have converged. Such is not the case". The question is thus still open to debate. The reason relies on the limitations of each method. The rheological measurements offer a precise estimation of shear stress – provided that thermal effects are minimized or controlled. They are, however, to date incapable of reproducing high values of pressure and shear stress simultaneously and within short duration, as it is the case for the fluid attaining its limiting shear stress while transiting the high-pressure central zone of EHD contacts.

Conversely, friction measurements are performed under realistic conditions, but here only the mean value of friction from all over the contact area is obtained. Such evaluation might be misleading since friction can vary considerably across the contact due to the important temperature and pressure gradients. To date, different mechanisms have been suggested to explain this intriguing phenomenon:

- Evans and Johnson[37] proposed the shear localization mechanism according to which only certain zones of the lubricant are sheared;

- Kaneta *et al.*[38] suggested that the lubricant solidifies in the contact and slips at or close to the contacting surfaces;
- Ehret proposed the "plug flow model"[39] which supposes that the lubricant solidifies, except to a thin layer of lubricant (of macromolecular dimensions) close to the solids' surfaces which remains in the liquid state and undergoes the shear stress.

More or less plausible arguments have been used to support these different interpretations. We are not aiming to discuss the validity of these interpretations and their respective arguments in our brief presentation. It should be noticed however that some of these explanations can challenge basic assumptions in EHL theory, namely the fluid-state of the lubricant during its whole transit in the contact, the linear velocity profile and the zero-slip condition presumed in Reynold's equation. This explains the important effort made currently on the development of new *in situ* techniques in order to examine such assumptions. We can for example mention the work of Ponjavic *et al.*[40] published in 2014 using Fluorescence Recovery after Photobleaching (FRAP) aiming at measuring the through-thickness velocity and the slip at the lubricant/solid boundary. On the other hand, local measurements of shear stress and ultimately of friction throughout the contact is highly desired to establish a more solid theoretical foundation for the LSS. It is with this perspective that Spikes *et al.*[41] tried to derive temperature maps obtained by Infrared thermography to shear stress and friction maps, but the approach and the assumptions are not straightforward and may be subject to criticism.

Thermal effects

Severe operating conditions, such as high sliding, important entrainment speed and also heavy loads can involve substantial temperature rises. Further increases are obtained for the lubricants of high viscosity or viscosity-pressure dependencies due to the viscous friction heating.

Including thermal effects in the analysis of EHD contacts increases considerably the complexity of the problem. Moreover, the accurate prediction of both friction and film thickness becomes critical. There is actually an important coupling between friction and temperature; friction can induce shear-heating within the lubricant and also the two surrounding bodies, while the temperature determines the rheological properties of the fluid and thus friction.

Furthermore, when the two solids are heated, they will alter the lubricant temperature and therefore its rheological properties at the inlet region of the contact. As a consequence, film thickness can also change significantly. In order to account for temperature rising in the prediction of film thickness, the energy equation has to be added to the basic equations of the EHL[42,43]:

$$\rho C_f \left(u_m \frac{\partial T}{\partial x} + v_m \frac{\partial T}{\partial y} \right) - k_f \frac{\partial^2 T}{\partial z^2} = -T \frac{1}{\rho} \left(\frac{\partial \rho}{\partial T} \right)_p \left(u_m \frac{\partial p}{\partial x} + v_m \frac{\partial p}{\partial y} \right) + \eta \left[\left(\frac{\partial u_m}{\partial z} \right)^2 + \left(\frac{\partial v_m}{\partial z} \right)^2 \right] \qquad (I.11)$$

Where T, C_f and k_f are respectively the temperature, the thermal capacity and the thermal conductivity of the lubricant. The first and the second terms on the left represent the heat transfer by convection and conduction, respectively. On the right, the first term represents the compressive heating of the film, and the second term expresses the shear dissipation within the lubricant.

In addition, it is necessary to include the temperature-dependence of the rheological properties (density and viscosity) of the lubricant wherever they appear in the different equations. Figure I.6 shows an extreme case presented by Guo *et al.*[44], who made numerical calculations taking into account the thermal effects present at *SRR = 255 %*. One can see its profound influence on the shape of film thickness, temperature and pressure distributions.

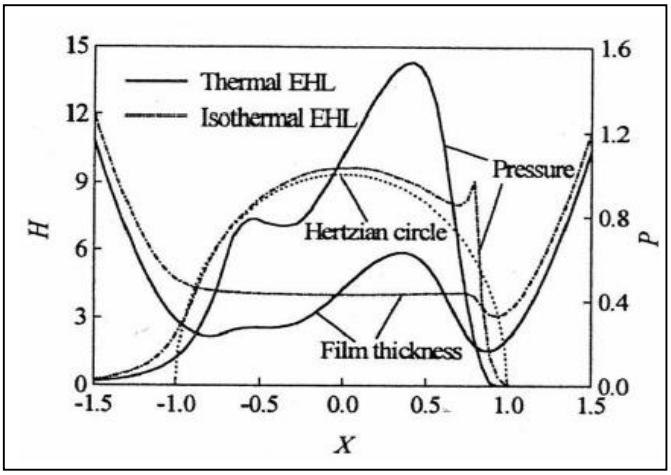

Figure I.6. Numerical simulations of thermal effects at high SRR (255%)[44].

Predicting friction is even more complex for the reasons we already mentioned, that is to say: the non-availability of experimental data of the lubricants' rheological properties covering all the range of temperature, pressure and shear stress experienced in the high-pressure central zone of (thermal-) EHD contacts. Added to this is the non-availability of local measurements of friction allowing for a true validation or fitting of the theoretical models[45].

It is however possible to compare the numerical predictions on the distribution of shear stress throughout the contacts[46] with the experimental measurement of friction which is nothing more than the integral of shear stress over the contact area. The major drawback of this approach resides in the fact that the numerical predictions make use of rheological models established over a given range of conditions. This means that extrapolation becomes inevitable whenever the investigations are extended beyond this range. However, if the lubricant behaviour is obtained from independent measurements, a full picture of the EHD friction regimes can be established. Based on the respective values of dimensionless parameters, a quantitative delineation of the friction regimes can be thus proposed[2].

Dimple formation

One of the first indirect observation of dimples dates back to 1950s when Cameron investigated pure sliding conditions (u_1 and u_2 at opposite directions) and found out that values of friction corresponding to hydrodynamic lubrication are attained at higher sliding speeds[47].

Such behaviour was later found to be linked to the punctual increase of film thickness: first from electrical resistance measurement by El-Sisi *et al.*[48,49], and then by electrical capacitance measurement by Dyson *et al.* [50]. This was augmented by a series of interferometric observations under simple sliding conditions (u_1 or $u_2 = 0$) conducted by Kaneta's group[51–53]. They reported the existence

of a deep conical depression or dimple in the high-pressure central region instead of the flat plateau expected by the EHL theory (see Figure I.7 (a) and (b)). More exotic features have also been observed by Kaneta and his co-workers such as: the formation of three dimples in elliptical contacts, or the instability and the cyclic movement of dimples (that they captured by a high-speed camera).

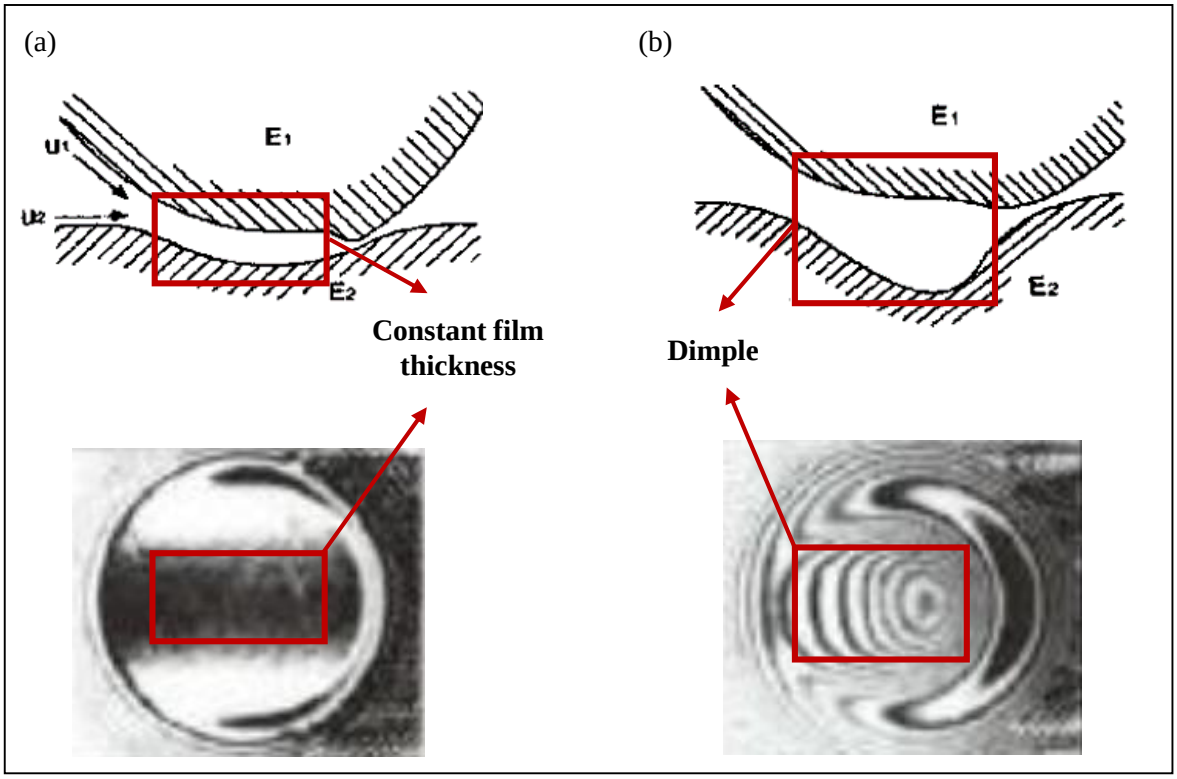

Figure I.7. Comparison between an EHD contact, (a) without and (b) with dimple, from[51].

Different mechanisms have been suggested to explain the formation of dimples, such as:

- The phase transition of the lubricant (or the plug model) as proposed by Eret *et al.*[39];
- The viscosity wedge action as advocated by Cameron[47], and which considers the through-thickness variation of viscosity due to temperature gradient between the two surrounding surfaces;
- The limiting shear stress and the wall slip as suggested by Zhang and Wen[54].

These mechanisms were all capable of reproducing the dimple numerically, it is therefore difficult to make a judgement on their validity without a solid experimental evidence. In this context, Yagi *et al.*[55] pointed out the necessity of (i) examining the lubricant phase change, (ii) mapping the temperature across and along the lubricant film and (iii) measuring the slippage at the interface between the surfaces and lubricant. Following these recommendations, they reported on the application of IR thermography for performing three-dimensional temperature measurements to examine the idea of viscosity wedge. In more recent publications, different methods were reported on the measurement of "slip-length", such as optical interferometry by Guo and Wong[56] or fluorescence imaging by Ponjavic *et al.*[40]. Finally, one can consider the application of Raman[57,58] or Infrared spectroscopy[59] for investigating the eventual phase transition within the contact.

Micro-elastohydrodynamics

As one can notice from the Stribeck curve (Figure I.1), friction decreases in the elastohydrodynamic lubrication by approaching the mixed lubrication regime. Minimizing film thickness while ensuring a full separation between the contacting surfaces can thus be regarded as an ideal situation allowing to extend the lifetime of the mechanical components and to improve their performance by reducing power losses. In this sub-regime of lubrication, called micro-EHL by some authors[60], the ratio h/R_S is decreased, which means that the influence of surface roughness is no more negligible. This effect has thus to be considered in the prediction of both film thickness and friction. This situation can also be encountered with rough[61] or artificially textured[62,63] surfaces.

I.1.3.3. From stationary conditions to transient conditions

Until today, most investigations in EHL dealt with stationary conditions. However, real machine components work rarely under fully steady-state conditions. They are actually subjected to transient conditions either in terms of load (gears and rolling element bearings), speed (reciprocating seals and bearings from stepper motors), geometry (cams and followers) or environment (uncontrolled vibrations). When considering transient effects, the Reynolds equation has to be completed with a transient term:

$$\frac{\partial}{\partial x}\left[\frac{\rho h^3}{12\eta}\frac{\partial p}{\partial y}\right]+\frac{\partial}{\partial y}\left[\frac{\rho h^3}{12\eta}\frac{\partial p}{\partial x}\right]=\frac{\partial\left(u_m \rho h\right)}{\partial x}+\frac{\partial\left(v_m \rho h\right)}{\partial y}+\frac{\boldsymbol{\partial}\left(\boldsymbol{\rho h}\right)}{\boldsymbol{\partial t}} \qquad (I.12)$$

A severe example of non-steady state conditions is the one encountered at the so-called impact EHD contact or pure squeeze lubrication. This extreme state of transient condition is obtained when for example a ball or a cylinder is vertically dropped on a plane solid. The pioneering studies on these contacts dates back to the 1960s, and they revealed both numerically[64] and experimentally[65] the formation of a central dimple entrapping a very highly pressurized lubricant. Figure I.8 (a) shows an interferogram and the corresponding film thickness profile as obtained by Dowson and Jones[65]. By decreasing the initial impact gap, Guo *et al.*[66] obtained circumferential dimple. Safa and Gohar[67] revealed a striking feature of impact EHD contacts using a manganin pressure transducer. This feature was, by the way, later demonstrated theoretically by Dowson and Wang[68]. The pressure variation against time was found to be remarkably similar to the pressure profile across stationary EHD contacts (Figure I.8 (b)).

The variation of entrainment speed is another subject that has been also considered. Examples of investigated situations are the start-up[69] or start-stop[70] of motion and step[71] or reversal[72,73] of entrainment speed. In all these situations, the steady-state approximation induces a non-negligible error. In some mechanisms, entrainment and squeeze-film actions are combined. For the sake of briefness, it should just be emphasized that, in addition to the dynamic conditions of load, speed or conjunction geometry, these contacts involve important shear rates, pressures and temperatures. It is therefore necessary, as Dowson and Ehret[8] highlighted in their review on EHL, to "consider carefully not only the dynamic conditions experienced by the conjunction but also the thermal conditions, and the rheological characteristics of the lubricant".

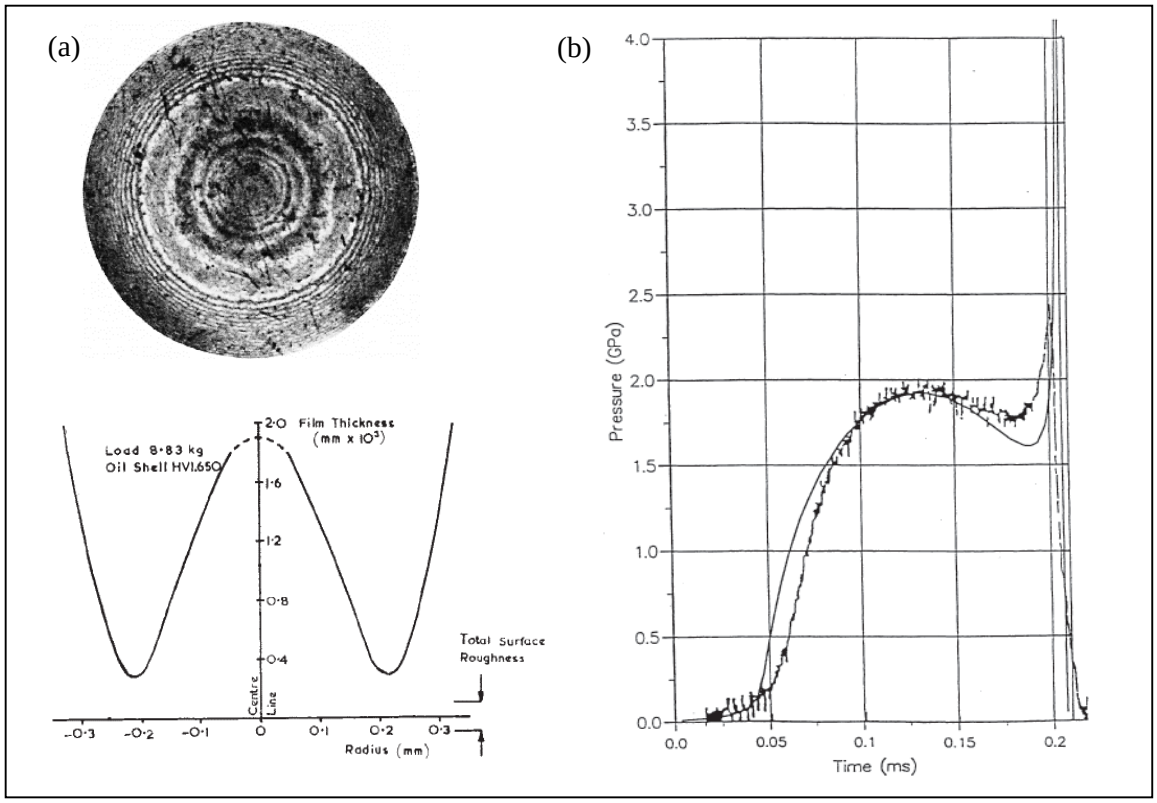

Figure I.8. (a) A central dimple as obtained by Dowson and Jones[65]; (b) Time variation of the central pressure during impact measured with manganin pressure transducer[67].

I.1.3.4. Other possible complications

The major complications have been briefly presented in the previous paragraphs. These complications can be related to (i) the contact geometry, (ii) the kinematics of the contacting bodies, (iii) the lubrication conditions and (iv) the environment.

In addition to the classical geometries found in literature, i.e. circular and line contacts, other geometries exist in real machine components (due the geometry of the contacting surfaces or the loading), such as: elliptical and toroidal contacts. Skewing and spinning and are some examples of complex kinematic conditions. And finally, many tribological systems can work under starved lubrication conditions. All these systems have been studied both numerically and experimentally, but we will skip them in our presentation for sake of briefness and because they are not for the time being considered of high priority for the current study.

I.1.4. Conclusion on the contribution of the experimental approach

The past 60 years have witnessed a growing research effort in developing *in situ* techniques adapted to the EHD contact problem. These techniques, together with theoretical and numerical analysis, have been of crucial importance for achieving our current understanding of the multi-scale and multi-physics nature of the EHL. They have contributed largely in elucidating a number of basic features of EHL, but also revealed the existence of more complex phenomena. Much hope is however being placed on the development of such techniques for gaining a better understanding of the EHL in all its complexity. Interested readers can refer to the review of Spikes[74] and more recently of Albahrani *et*

al.[28] for more details. Table I.2 summarizes the actual and the possible contributions that have been mentioned before.

Assumption or phenomena	Electrical methods			Optical methods					Acoustic methods
	Voltage discharge	Electrical capacitance	Electrical resistance	X-rays	Optical interferometry	Infrared	Raman	Fluorescence	Ultrasonic reflection
Film thickness	75,76	77	-	-	25,26	23,24	-	-	78
Pressure	-	-	27,63	-	-	-	79,80	-	-
Temperature	-	-	81	-	-	41,55,82	-	-	-
Friction	-	-	-	-	-	41	-	-	-
Limiting shear stress	-	-	-	-	-	-	-	83	-
Dimple formation	-	-	-	-	51–53	-	-	-	-
Velocity profile	-	-	-	-	-	-	-	40,84	-
Wall slip assumption	-	-	85	-	-	-	-	-	-
Viscosity wedge	-	-	86	-	-	55	-	-	-

Table I.2. The actual and possible contributions of the in situ approach to EHL.

I.2. *In situ*, local and simultaneous measurement of temperature and pressure

I.2.1. Temperature and pressure measurement: Importance and existing methods

In the discussion on the different aspects of the EHD problem, we showed that the two key parameters in designing tribological components are film thickness and friction. On one hand, film thickness should be predicted and thereafter controlled in a reliable and accurate manner in order to ensure a full separation between the surfaces in contact. On the other hand, however, energy loss by friction has to be generally minimized in order to enhance the efficiency of the mechanisms using such tribological components. As we underlined before, film thickness and friction are decoupled in the sense that they are determined by the rheological properties of the lubricant and all the other factors in two distinct regions in the contact: the inlet and the high-pressure central zone, respectively. The rheological properties at each point of the contact are, in turn, intimately related to the local temperature and pressure. Given all this, the precise and detailed knowledge of temperature and pressure is of crucial importance in extending the lifetime and optimizing the performance of the tribological systems.

At a more fundamental level, we should say that despite all the achievements, the full picture of friction in EHL is not yet elucidated because of the severity of the physical conditions and the extreme confinement of the lubricant. The limiting shear stress, phase transition and dimple formation are some examples among others which attest the importance of the live measurement of determining parameters such as the temperature and the pressure.

To date, various experimental methods have been developed with more or less success to measure pressure and temperature within EHD contacts, including electrical resistance, infrared emissivity, and Raman spectroscopy[28]. The long term aim of this work is to introduce or apply nanotechnology as an alternative solution for having access to these physical parameters within EHD contacts, eventually with enhanced resolution and accuracy. A brief discussion on nanotechnologies will be given in the next section before presenting globally the technique we have developed.

I.2.2. Nanotechnologies

Nanotechnology was first proposed, as a concept, by the Nobel Prize laureate in physics, Richard Feynman. In a lecture entitled "There is *Plenty* of Room at the Bottom" in an American Physical Society meeting at Caltech on December 29, 1959, he described the field without using explicitly the term:

> "I would like to describe a field, in which little has been done, but in which an enormous amount can be done in principle. [...] Furthermore, a point that is most important is that it would have an enormous number of technical applications. What I want to talk about is the problem of manipulating and controlling things on a small scale. […] It is a staggeringly small world that is below".

It is now recognized, in agreement with Feynman vision, that nanotechnologies have a huge potential. This is further confirmed by looking at the increasing investments, from governments and private sectors around the world, attracted by this field. Table I.3, extracted from the study published by Roco[87], shows six indicators pointing out the development of nanotechnologies research and industry.

Year	Indictors					
	People primary workforce	SCI papers	Patent applications	Final products market	R&D funding public + private	Venture capital
2000 (actual)	~ 60,000	18,085	1,197	~ $30 B	~ $1.2 B	~ $0.21 B
2008 (actual)	~ 40,000	65,000	12,776	~ $200 B	~ $15 B	~ $1.4 B
2000-2008 (average growth)	~ 25%	~ 23%	~ 35%	~ 25%	~ 35%	~ 30%
2015 (2000 estimate)	2,000,000			~ $1,000 B		
2020 (extrapolation)	6,000,000			~ $3,000 B		

Table I.3. Impact of nanotechnologies based on six indicators: (i) the number of researchers and workers involved, (ii) the number of Science Citation Index (SCI), (iii) the number of patents filed in the top 50 depositories, (iv) the value of products incorporating nanotechnologies as the key component, (v) the annual investment on R&D from private and public sources, (vi) the global venture capital investment.

Nanotechnologies deal with objects and phenomena at very small scales, typically between 1-100 nm. It is actually in this range that materials exhibit properties fundamentally different from those found at larger scales. These differences arise from several reasons, the most important are:

- **Surface-to-volume ratio effect**: when the size of an object is decreased, the surface-to-volume ratio decreases. For spherical particles, this ratio is equal to *1/r*, with *r* being the radius of the sphere. This ratio is an important factor for the chemical reactivity. It indicates actually the number of the molecules found at the surface of the object, and which are thus capable of interacting with the surrounding molecules. For instance, given spherical particles of 30, 10 and 3 nm radius, the proportion of molecules at their surfaces is respectively about 5, 20 and 50 %. Furthermore, many properties, such as the cohesion, melting temperature and ionization potential display an approximate linear variation with *1/r*. At macroscopic scale, the ratio *1/r* approaches zero, implying a negligible size effect. When it comes to nanometric scales

however, important variations are observed with size owing to the large surface-to-volume ratio;

- **Quantum effects**: these effects, generally associated to atoms and molecules, appear at the nanoscale. Again, the smaller the size of the particles, the more influential they become;
- **Random motion**: the random motion of small particles due to their kinetic energy is a well-known fact. Since these motions occur at the same scale as the size of the particles, their influence on the behaviour of nano-objects can be considerable;
- **Influencing forces**: gravitational forces become negligible regarding the extremely small mass of nanometric objects. However, the electromagnetic forces are unaffected by mass since they are only function of charge and distance between particles. These forces are thus very strong and even predominant at this scale. In addition, at nanoscales, the inertial forces become negligible in comparison to surface tension.

Naturally, all these features have to be considered in the design, characterization and manufacture of structures, systems and – maybe in the future – devices functioning or operating at the nanoscale. Despite the fact that nanotechnologies are still at their infancy, the applications are wide. In a report published by the Royal Society and Royal Academy of Engineering's nanoscience and nanotechnologies in 2004[88], the applications or uses of nanotechnology were divided in four categories:

- **Nanomaterials**: globally speaking, the term "nanomaterial" encompasses all materials that have at least one of their dimensions in the range between 1-100 nm. Following this definition, nanomaterials can be divided in three types: materials with one (nanolayers), two (nanowires or nanotubes) or three (nanoparticles) nanometric dimensions. These structures can be considered as the building blocks that can be assembled together and/or with other materials in order to create materials with innovative properties. The main challenge in developing such materials resides in (i) understanding the properties and the behaviour of materials at the nanoscale, and (ii) controlling the structure of these materials. Many experts in the field believe that such process would be a revolution in materials, industry and even in civilization[89,90];
- **Electronics, optoelectronics and Information and Communication Technology (ICT)**: nanotechnology have a huge impact in this field, in particular in improving data storage capacity, transfer and computation. This is actually achieved by miniaturizing the electronic components. Obviously, controlling materials properties at the nanoscale is a prerequisite for such a process;
- **Bio-nanotechnology and nanomedicine**: the discussion about this category is fascinating, and the applications are promising. They include tissue and cellular engineering scaffolds, drug delivery and discovery, diagnostic and therapeutic techniques and imaging at cellular scales (and below). However, according to many experts, it is a longer-term prospect since it requires many fundamental aspects to be investigated in the first place[88];
- **Nanometrology**: nanometrology is defined as the science of measurement at nanoscale. It includes the measurement of size, force, mass, electrical and optical properties, etc.

The above-mentioned categories can of course overlap in some applications. Concerning the objective of our study, we should say that it is at the frontier between nanomaterials and nanometrology. This because (i) it aims at *measuring locally* the physical properties of confined fluid films, (ii) the lubricant film that we are trying to investigate can be of *nanometric thickness* and (iii) the materials

that we will characterize for this purpose need to be *nano-sized* for getting inside the contact and to remain as minimally invasive as possible.

I.2.3. Quantum dots as temperature and pressure sensors

Nanomaterials have been proposed in the literature as candidates for temperature and/or pressure sensors[91–95]. For our study, we should ensure that the nanomaterials are adapted to (i) the context we are dealing with, i.e. EHD contacts, (ii) the available instrumentations and (iii) the required measurement quality (resolution, precision, etc.). The selection can be done according to several criteria illustrated in Figure I.9.

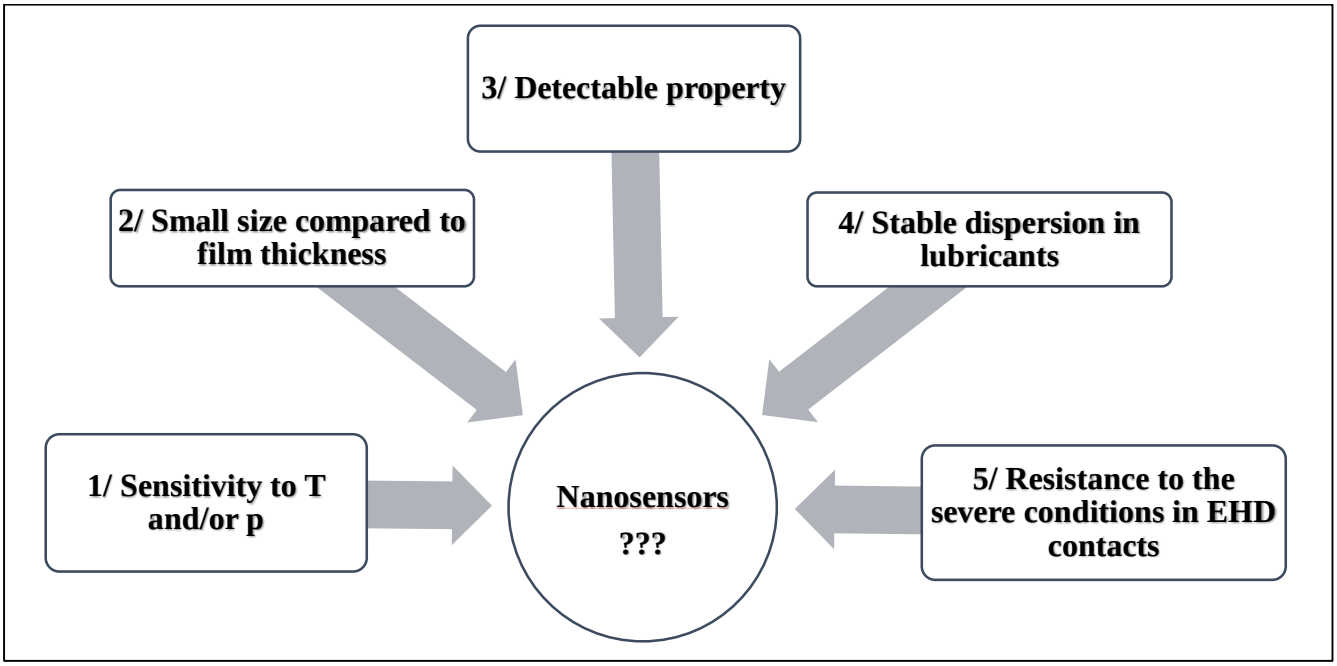

Figure I.9. Criteria for the selection of the nanosensors.

The choice that we made in our work was to explore a particular class of nanoparticles called quantum dots (QDs), and more particularly CdSe/CdS/ZnS QDs. QDs are constituted of semiconductor molecules, and due to their nanometric size they exhibit unique properties. They are also a part of photoluminescent materials which upon light excitation, emit photons before returning to the ground (or the unexcited) state. More on the physics of QDs and photoluminescence (PL) will be given in the next chapter. Here, CdSe-based QDs have been preferred mainly for their higher PL efficiency, which allows to use them at low concentrations. The small size distribution of these QDs, obtained by bottom-up chemical synthesis, is also an important parameter. The critical importance of these two latter parameters (concentration and size distribution) will be thoroughly evidenced in the next chapters.

Regarding the adaptability of CdSe/CdS/ZnS QDs to the above-mentioned criteria, the following points should be retained here:

– The PL of these QDs is sensitive to temperature and pressure variations (criterion n°1);

- Their mean diameter is lower than 10 nm and thus a big range of film thicknesses can be studied (criterion n°2);
- They are capable of absorbing and emitting efficiently in the visible range, which is adapted to the instrumentations available and to the systems that are usually used for simulating EHD contacts (discs transparent to visible radiation) (criterion n°3);
- They are covered by organic ligands that allow them to form a stable colloidal dispersion within usual lubricants in order to make local measurements in EHD contacts (criterion n°4);
- The resistance of these QDs to the severe conditions encountered in EHL has to be verified in further studies (criterion n°5).

Regarding this latest criterion, a previous pioneer study on robust covalent Si and SiC QDs has been realized[96].

The basic idea in the technique we are aiming to develop is to disperse CdSe/CdS/ZnS QDs with eventually another family of QDs (InP for instance) within the lubricant. Once the lubricant enters in the contact, a laser beam is used to excite locally the QDs, and their PL is detected. Since the response of each QD is dependent on its local environment, particularly on the local temperature and pressure, the detected PL signal can be used to map the temperature and pressure throughout the contact (see Figure I.10). In this work we focus on the characterization of CdSe/CdS/ZnS QDs.

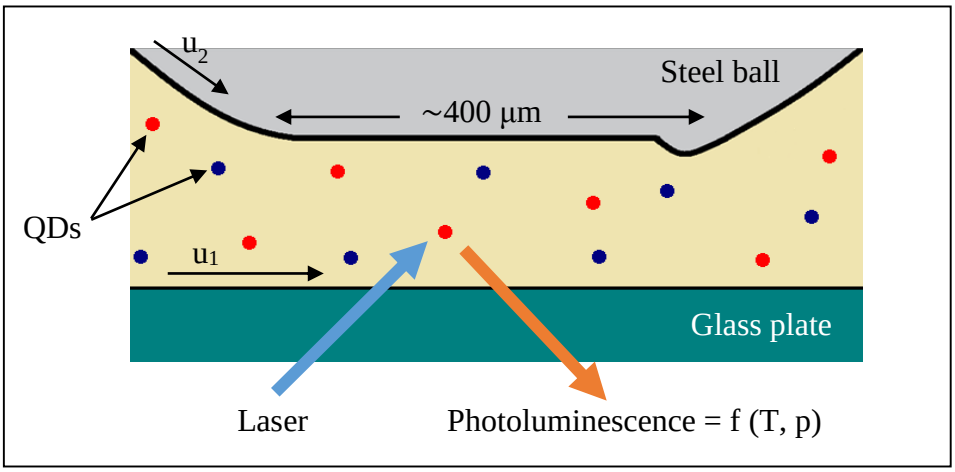

Figure I.10. Principle of the new proposed technique of temperature and pressure measurement: Two different families of QDs are dispersed within the lubricant in an EHD contact, and their PL, after laser excitation, is detected and could be used to make local estimations of temperature and pressure.

I.3. Organization of the manuscript

In the next chapter, a brief literature review will be given on the PL phenomena and the properties of QDs. This review is actually necessary to establish the list of parameters susceptible of influencing the response of the QDs for further characterizations.

In the third chapter, the response of the QDs to temperature and pressure variations will be calibrated under static conditions. The empirical laws established from these calibrations can be used in realistic

EHD contacts to yield local temperature and pressure measurements. Furthermore, the influence of other parameters, listed in the second chapter, will be evaluated and discussed.

Unlike in calibration measurements, the lubricant is not static in an operating machine element. For this reason, the last chapter deals with dynamic conditions. Results obtained under simple dynamic conditions produced with an optical rheometer will be presented. These conditions will allow to (i) observe the eventual influence of shear stress on the fluorescence emission of QDs and to (ii) verify if highly diluted QDs can modify the rheology of the lubricant under investigation.

II. Photoluminescence and Quantum Dots

II.1. Introduction

In the previous chapter, the context of our work, i.e. EHL regime, was presented. This description was useful for being prepared to the difficulties that can be encountered in probing this regime, and more importantly for the identification of the parameters imposed in such a context. We should name in particular: film thickness, viscosity, temperature, pressure, flow, and shear stress.

In this chapter we will try to find out the parameters to which the quantum dots (QDs) could be sensitive. To achieve this, we need to go through the physics of photoluminescence (PL) and QDs. Indeed, while some properties of the QDs arise from them being photoluminescent species, other properties are unique and require a specific treatment. It should be however noticed that in such a study experiment is the veritable guide. It was actually through experiment that we could extract the parameters that need to be considered, and in the future, other parameters could be revealed when examining more complex situations.

II.2. Photoluminescence*

II.2.1. Position of photoluminescence in matter-light interaction and light emission

PL is light emission by a molecule (or by any form of matter) after being electronically excited with photons. As illustrated in Figure II.1, the position of PL can be regarded from two view angles: the first is in the frame of light-matter interaction and the other is the nature or the cause of the light emission or luminescence.

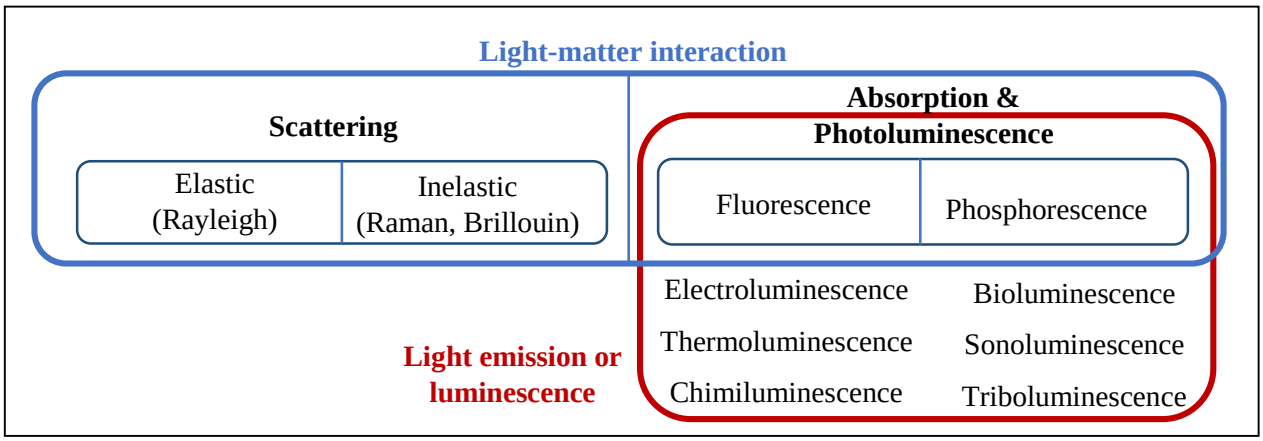

Figure II.1. Position of photoluminescence.

The illumination of a sample is followed by different processes:

- A part of the light is reflected or transmitted (if the sample is thin enough) without any light-matter interaction;
- A small fraction of the light is scattered in all directions, without any change in energy (elastic or Rayleigh scattering), or with some change in energy (inelastic scattering, such as Raman and Brillouin scattering);

* Much of the information given in this section is classical, and have been extracted from reference textbooks on the subject such as[98,101].

– Light can also be absorbed and this absorption can be followed by a light emission or photoluminescence, in form of fluorescence or phosphorescence[*].

However, luminescence can be induced by other effects without prior interaction with light. Examples are bioluminescence, chemiluminescence, electroluminescence, etc.

II.2.2. Photoluminescence: A mechanism of energy dissipation

Figure II.2 shows a simplified form of Jablonski diagram[97], named in honor of the polish physicist Alexander Jablonski, and which can be used to illustrate the different forms of PL and the other possible mechanisms of energy dissipation in the case of molecules and molecular structures. In this diagram, the energy levels are schematically depicted as horizontal lines. The thicker lines in Figure II.2 are representations of the limits of electronic energy states (S_0, S_1, S_2, T_1, T_2)[†] whereas the thinner lines represent the multiple vibrational states (V_0, V_1, V_2, V_3, …) associated to each electronic state. Again, each vibrational state can be further subdivided into rotational energy levels, but those are generally omitted in typical Jablonski diagrams.

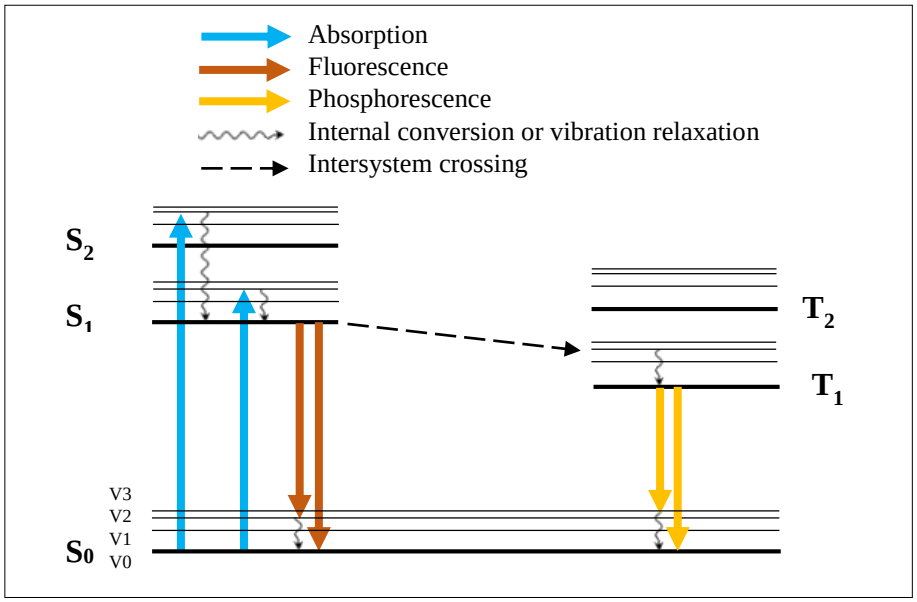

Figure II.2. A simplified Jablonski diagram.

Following light absorption, an electron of the molecule is excited from ground state S_0 to one of the vibrational levels of the first or the second electronic levels, S_1 and S_2. This transition occurs in about 10^{-15} s, which can be considered almost instantaneous compared to nuclei motion (Frank-Condon principle). The relaxation of this electron to its ground state is accompanied by energy dissipation following different mechanisms or channels. The competition between these channels of dissipation is governed by the time scales corresponding to each one of them. Table II.1 gives some orders of magnitude of the basic transition mechanisms. The shorter is the timescale of the transition (or dissipation) by a mechanism, the higher the likelihood of this mechanism to occur or dominate the others. It is, therefore, imperative to have an idea of the timescale of a process in order to know if it is more or less likely to happen.

[*] The difference between fluorescence and phosphorescence will be explained in the next paragraphs.
[†] *S* for singlet and *T* for Triplet energy state.

Phenomenon	Time scale (s)
Absorption	10^{-15}
Vibrational Relaxation or internal Conversion	$10^{-13} – 10^{-11}$
Fluorescence	$10^{-9} – 10^{-7}$
Intersystem Crossing	$10^{-8} – 10^{-3}$
Phosphorescence	$10^{-4} – 10^{-1}$

Table II.1. Orders of magnitude for different transition mechanisms, from[98].

II.2.2.1. Vibrational relaxation and internal conversion

As we can see through the time scales, the first way for energy dissipation is by vibrational relaxation, which is a nonradiative process in that it does not imply the emission of a photon. The excess of energy is given away as kinetic energy during the collision of the excited molecules to the surrounding solvent molecules[*]. In general, this transition occurs between vibrational levels, and the molecule does not change its electronic state. However, as the electronic energy level increases, the vibrational energy levels can strongly overlap electronic ones, and in this case, it is possible to get a transition between a vibrational level in an electronic state to another vibrational level in a lower electronic state. This process, called internal conversion, occurs in the same timescale as a typical vibrational relaxation. It happens generally in electronic levels higher than the first excited state S_1 where there is a sufficient overlap between electronic and vibrational states. Conversely, in the ground state S_0, due to the lack of such an overlap, and the relatively large energy difference between the states S_0 and S_1, the dissipation by internal conversion becomes very slow, allowing other energy dissipation mechanisms to compete with, such as fluorescence, intersystem crossing and phosphorescence.

II.2.2.2. Fluorescence

As the fluorescence is a relatively slow process, it is not a very likely path for energy dissipation, especially for electronic states higher than the first excited state S_1. For this reason, fluorescence is mostly observed between the energy states S_1 and S_0, where it becomes able, in regard to timescales, to compete with kinetic energy dissipation. It is also for this reason that fluorescence emission characteristics depend generally weekly on the excitation energy. This property of fluorescence is known as Kasha's rule[99]. Indeed as mentioned above, if the molecule is excited to an energy state higher than S_1, the excess of energy is rapidly dissipated through vibrational relaxation and internal conversion to the lowest vibrational state associated to S_1 before fluorescence. Generally, the molecule conserves some amount of energy after fluorescence, or in other terms, it returns to an excited vibrational level of the ground electronic state S_0. This excess amount of vibrational energy is quickly dissipated kinetically.

It is worthy to note that due to the kinetic energy dissipation prior to fluorescence, and sometime after emission, the energy of the emitted photon is generally less than the one of the exciting one. This phenomenon was first observed by G. Stokes in 1852[100], and was thus named after him: Stokes Shift. Resonant fluorescence occurs, in contrary, when the emitted photons have the same energy as the exciting ones. Stokes shift is a valuable feature for spectroscopic studies since it allows the separation of the excitation background from emission band (using appropriate filters) without reducing the sensitivity of fluorescence-based techniques.

[*] In crystalline materials, this vibrational relaxation occurs via phonon propagation. For QDs, which are an intermediate state between molecules and crystals, both collisional dissipation and phonon propagation coexist.

II.2.2.3. Intersystem crossing and phosphorescence

If the vibrational relaxation is slow enough, electrons in the S_1 state can undergo a spin conversion, leading to unpaired electrons. This change of spin multiplicity from an excited singlet state S_1 to an excited triplet state T_1 (see Figure II.2) is called intersystem crossing and is a forbidden transition if strictly and only based on electronic selection rules (Pauli Exclusion Principle). It becomes, though, "slightly" allowed by coupling vibrational factors into the selection rules mentioned above (more precisely, due to the so-called spin-orbit coupling[*]). Being almost forbidden, this process is one of the slowest processes in the Jablonski diagram.

The molecule stabilizes (through vibrational relaxation) to the lowest vibrational level of T_1. As the transition from the triplet and the singlet excited states is again forbidden (as it implies a new spin conversion), return to the ground state S_0 occurs generally through vibrational relaxation. There are some molecules, however, which exhibit a radiative emission in their route to the ground state S_0. This process is called *phosphorescence* and its timescale is some orders of magnitude smaller than the one of fluorescence.

In our work however, we will study the fluorescence of QDs, and therefore, the words *fluorescence* and *photoluminescence* will be used interchangeably. The word *fluorophore* will be used to describe any fluorescent substance.

In addition to the above-mentioned channels of energy dissipation which we can qualify as internal[101], other processes can also lead to the return to the ground state through the interaction of the fluorophore with the other molecules. We can call them intermolecular-interaction channels for energy dissipation. These processes may induce further Stokes shift since they can compete with fluorescence. These channels of energy dissipation will be next described, but before, it is useful to introduce some notions about the characterization of fluorophores.

II.2.3. Characterization of fluorophores: Concepts and measurements

The characterization of fluorophores are made using spectroscopic tools. These tools can be classified based on the following criteria:

- Depending on whether one is interested in the dependence of the efficiency of light absorption on excitation energy, or in the emission probability associated to the different energy levels, one obtain the *emission spectrum* or the *absorption spectrum* of the fluorophore, respectively;
- Depending on the timescale (or time window) of measurement, it is possible to perform either *steady-state* or *time-resolved measurements*.

In the following paragraphs, the difference between these tools, the relation between them, and the measured characteristics are briefly presented.

[*] Spin-orbit coupling can be understood as the interaction between two magnetic moments: one generated by the rotation of an electron around the nucleus (nuclear magnetic field), and the other generated by the rotation of the electron around its own axis (electron spin).

II.2.3.1. Absorption spectrum and emission spectrum

The efficiency of light absorption by an absorbing medium at any wavelength λ (or energy) can be characterized by the absorbance *A*, defined as:

$$A(\lambda) = \log\left(\frac{I_i(\lambda)}{I_t(\lambda)}\right) \qquad (II.1)$$

Where I_i and I_t are, respectively, the intensity of the incident light and the intensity of light transmitting through the absorbing medium.

For fluorophore molecules dissolved in a solvent, the absorbance can be calculated by Beer–Lambert Law:

$$A(\lambda) = \varepsilon_A(\lambda) l_A c \qquad (II.2)$$

Where ε_A is the molar absorption coefficient which expresses the ability of a molecule to absorb light in a given solvent, l_A is the thickness of the absorbing medium, *c* is the molar concentration of the fluorophore molecules.

An absorption spectrum is the plot of either the absorbance or the molar absorption coefficient as a function of wavelength λ (or any equivalent physical quantity such as energy *E*, frequency *v* or wavenumber *k* [*]). Conversely, the emission spectrum of a fluorophore is obtained by recording the variation of its emission intensity (in arbitrary units) against wavelength. Figure II.3 (a) and (b) shows two examples of absorption and emission spectra: one obtained from Perylene and the other from Quinine. One can clearly observe two common features in the two examples:

- A shift between emission and absorption spectra;
- A mirror symmetry between emission and absorption spectra.

The shift is actually the Stokes shift mentioned earlier partly due to the vibrational relaxation and internal conversion. It can be further enhanced by other nonradiative mechanisms capable of competing fluorescence, namely those induced by molecular-interaction effects that will be presented later. There is an overlap between the two spectra that could be perceived as a departure from Stokes shift or, more importantly, to be contradictory to the principle of energy conservation. Such is actually not the case because this overlap is due to the existence of a small fraction of molecules within a vibrational state higher than V_0 (the equilibrium state) of the energy state S_0 before excitation. The mirror symmetry, called mirror-image rule, is due to two reasons: (i) the same energy levels are involved in both processes (absorption and emission), and (ii) the vibrational energy levels in S_0 and S_1 are similar (see the illustration of the band diagrams in Figure II.3 (a)).

[*] The relation between these different parameters is found in Appendix A.

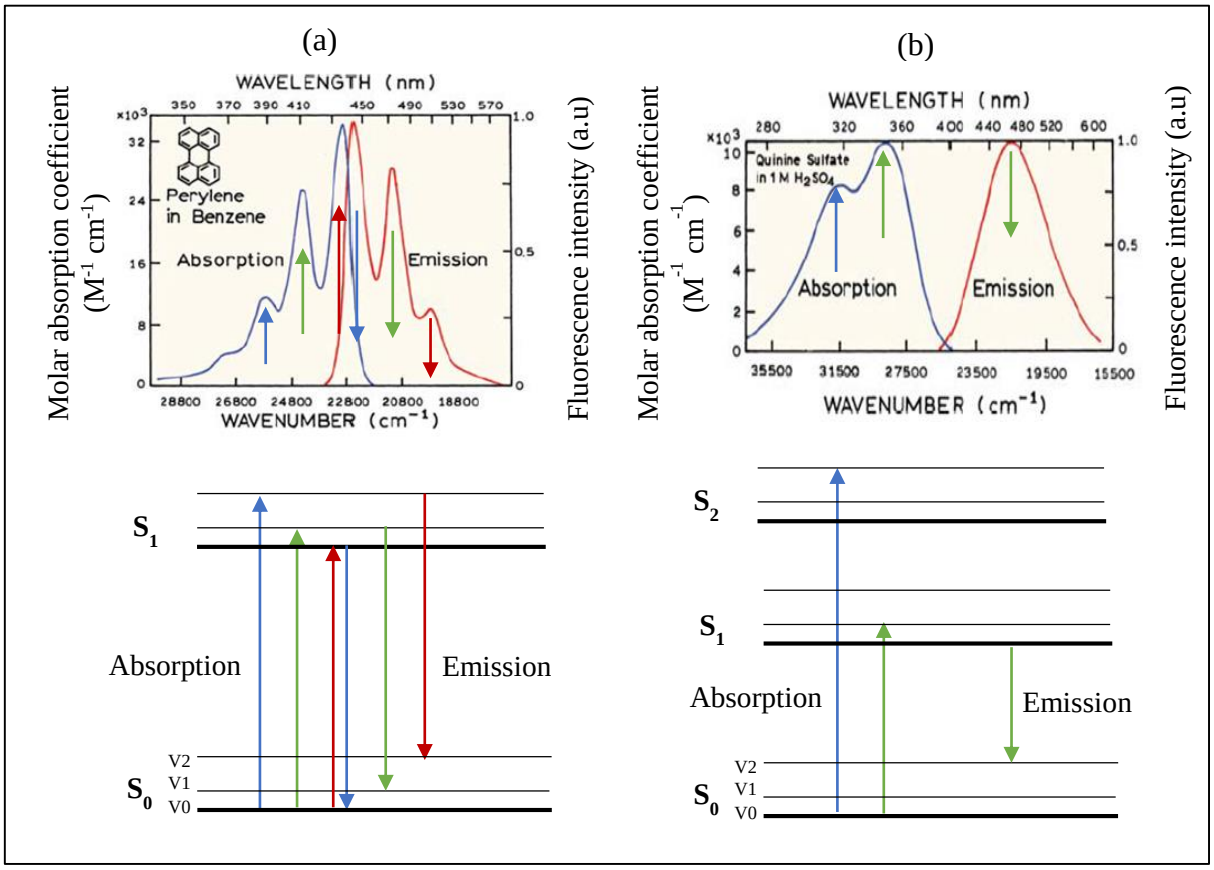

Figure II.3. Emission spectra, absorption spectra and the electronic and vibrational energy levels involved in (a) Perylene and (b) Quinine, adapted from[102].

In the case of Quinine (Figure II.3 (b)) however, there are two peaks for the absorption, while only one peak is obtained in the emission spectrum. This difference is due to what was mentioned earlier, i.e. fluorescence corresponds a $S_1 \rightarrow S_0$ transition, and even though the molecule is excited to higher energy levels (S_2 for example), it relaxes to S_1 *via* nonradiative processes before fluorescing. Conversely, absorption spectrum gives a picture of the all energy levels to which the molecules within the sample can be excited. It is thus a valuable tool for identifying the electronic structure and the vibrational modes of the matter. Another difference between absorption and emission is related to the sensitivity to the local environment of the atoms. Both are actually sensitive to the microenvironment of the absorbing or emitting molecule, but emission yields more information about molecular dynamics. Indeed, due to the quasi-instantaneous feature of absorption (10^{-15} s), the fluorescent molecule is exposed to the same local environment in the ground and the excited states (just before and just after excitation). For this reason, time-dependent effects such as the diffusion of fluorescent molecules or the surrounding solvent molecules cannot alter the absorption spectrum. Only information about the average ground-state of the molecule is obtained from the absorption spectrum, and only the solvent molecules immediately adjacent to absorbing molecule can have some influence on it. Emission is also an ultra-fast process, but before emitting, the molecule remains in the excited state in a relatively long time (10^{-8} s, typically). During this time, the molecule is exposed to the local environment, and it can thus interact with other molecules as it diffuses within the solvent and as the solvent molecules diffuse around the excited molecule. The emission spectrum of fluorophores is therefore a valuable tool for probing the local environment and molecular dynamics.

II.2.3.2. Steady-state measurement and dynamic measurements

Prior to the return to the ground state, the molecule remains in the excited state for a certain time. When considering an ensemble of atoms, the process of depopulation is random, and in the simplest cases, it can be described by a single-exponential decay law of the time-resolved intensity $I_{T\text{-}R}$ of fluorescence (see Figure II.4 (a)):

$$I_{T-R}(t) = I_{T-R}^{0} e^{-t/\tau} \qquad (II.3)$$

Where $I^{0}_{T\text{-}R}$ is the intensity of light emitted immediately after an excitation pulse ($t = 0$), τ is called lifetime or decay time and it represents the average time the molecule spends in the excited state before returning to the ground state. Following the previous equation, 63% of the molecules decay before $t = \tau$ and *37%* decay after. In the case of single-exponential decay, lifetime is related to radiative decay rate (k_r) and nonradiative decay rate (k_{nr}) with the following expression (Figure II.4 (b)):

$$\frac{1}{\tau} = k_r + k_{nr} \qquad (II.4)$$

With:

$$k_r = \frac{1}{\tau_n} \qquad (II.5)$$

Where τ_n is called the intrinsic or natural lifetime, and is defined as the lifetime of the fluorophore in the absence of nonradiative processes.

Since the nonradiative channels of relaxation are the signature of the interaction of the fluorescent molecule with its microenvironment, the measurement of lifetime can yield precious information about such interactions, and hence about the microenvironment of the fluorophores. For the same reason, lifetime can give an idea of the efficiency of the fluorophore, or its internal quantum yield *Q*. Indeed, the latter is defined as the ratio of the number of emitted photons relative to the number of absorbed photons[*] and it is equal to:

$$Q = \frac{k_r}{k_r + k_{nr}} = k_r \tau \qquad (II.6)$$

When the decay is more complex than a single-exponential (multi- or non-exponential decays), it is possible to use the general expression of the average time during the excited-state:

$$< t > = \frac{\int_0^{\infty} t I_{T-R}(t)\, dt}{\int_0^{\infty} I_{T-R}(t)\, dt} \qquad (II.7)$$

[*] The internal quantum yield is always bigger than the external quantum yield which is defined as the ratio of the number of emitted photons relative to the number of incident photons.

In these cases also, this average time as well as the exact shape of the decay can be used to extract structural and dynamic information about the fluorophores.

In order to perform time-resolved measurements, the sample is excited with a pulse of light with a duration made as short as possible (Figure II.4 (a)). The intensity decay of a fixed emission energy is then recorded as a function of time (Figure II.4 (a)) using a time-resolved fluorometer. These measurements have been made possible by high repetition rate illumination sources and fast-response photomultipliers, allowing time resolutions down to the femtosecond to be achieved. By combining the fluorometer with a monochromator, it is also possible to obtain time-resolved emission spectra and eventually extract the variation of fluorescence energy (or wavelength) with time (Figure II.4 (c)). In opposition, steady-state measurements are performed with continuous wave (CW) excitation. Due to the long response time of most available instrumentations compared to the nanosecond timescale of fluorescence, steady-state measurements are the most common type.

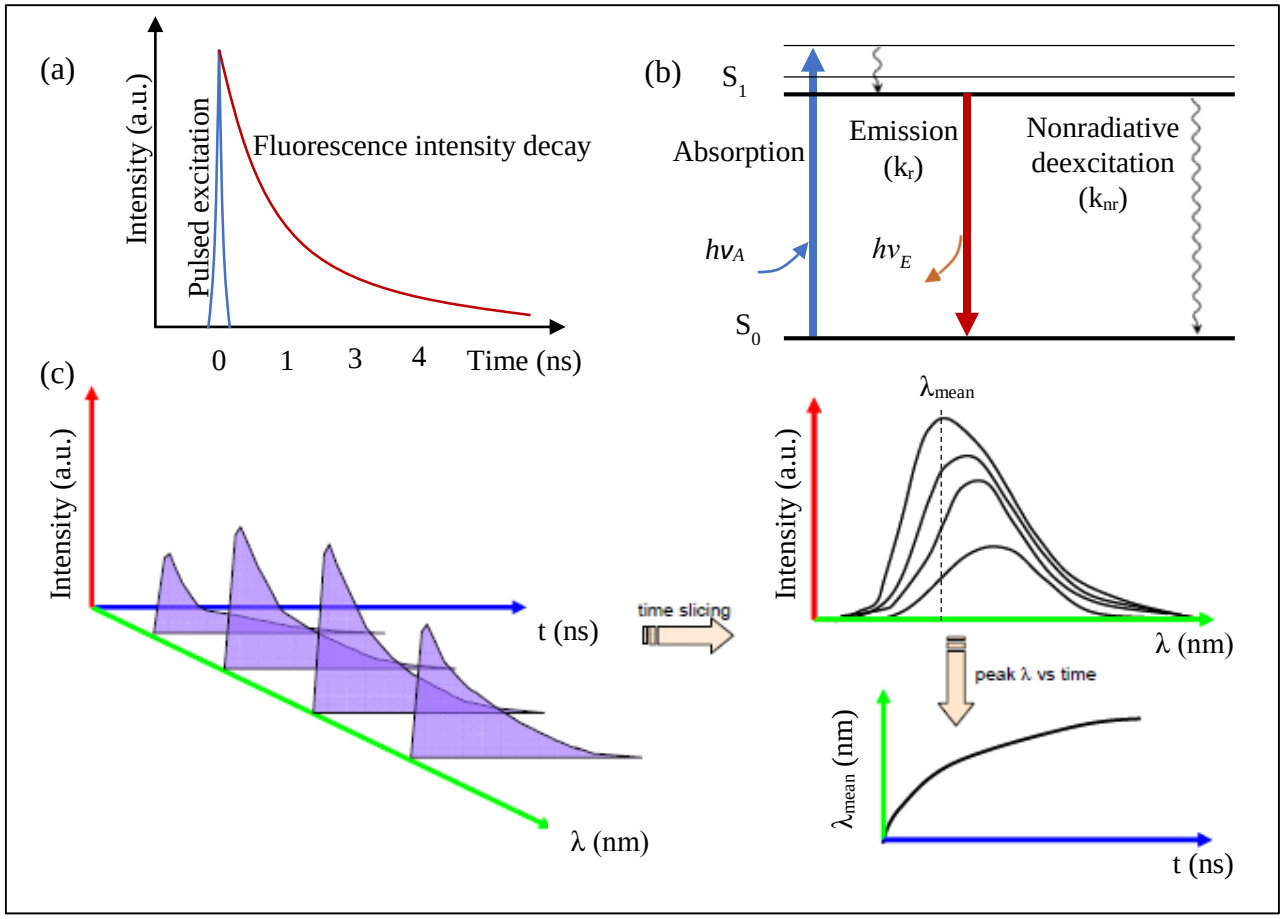

Figure II.4. (a) Pulsed excitation and time-resolved measurement of emission intensity; (b) Radiative and nonradiative channels of deexcitation, (c) time-resolved emission spectra, from[103].

Time-resolved and steady-state measurements are nevertheless related, since the latter is nothing else than the average of the former over the intensity decay time of the sample:

$$I_{S-S}(\lambda) = \int_0^\infty I_{T-R}(\lambda, t)\, dt \qquad (II.8)$$

From this statement, it follows that much of the molecular information is lost in steady-state measurements. However, even though molecular dynamic effects can be monitored only in time-resolved measurements, they maintain their influence on steady-state measurements. Such is the case because the dynamic effects can influence the overall weight of nonradiative paths in the deexcitation process and consequently modify the resulting emission spectrum.

In our study, we will use steady-state emission spectra of the QDs for temperature and pressure calibrations.

II.2.4. Intermolecular-interaction channels for energy dissipation

As mentioned above, the paths of deexcitation of the fluorophores can be either internal or induced by the interaction between couples of fluorophores or between the fluorophores and their surrounding microenvironment. In the following paragraphs, we will discuss briefly the mechanisms leading to such interactions.

II.2.4.1. Radiative energy transfer: Emission & Reabsorption or trivial energy transfer

Radiative energy transfer is commonly called the *trivial energy transfer* due to the simplicity of the phenomenon from the conceptual point of view, and its dependence on trivial factors such as the size of the sample container, the path length, the absorbance of the sample, and the geometric arrangement of the excitation and emission light paths[98]. As illustrated in Figure II.5, this process involves four main steps:

- A first fluorophore, called *donor (D)*, is excited by a photon of energy $h\nu_0$;
- The donor emits after a delay (corresponding to its lifetime) a photon with an energy $h\nu_1 < h\nu_0$;
- Another fluorophore, called *acceptor (D)*, is excited by the photon emitted by the donor;
- The acceptor emits a photon with an energy $h\nu_2 < h\nu_1$.

The inequalities $h\nu_2 < h\nu_1 < h\nu_0$ arise from the Stokes shifts. Furthermore, from the previous description, the emission of the donor and the absorption of the acceptor need to be at least of equal energies, or in other term, the emission spectrum of the donor have to overlap the absorption spectrum of the acceptor* (as we will see shortly).

In colloidal systems where donors and acceptors are randomly dispersed within a solvent, the efficiency of radiative energy transfer is doubly affected by the distances between donors and acceptors. Firstly because the rate of radiative energy transfer k^{RET} between a donor and an acceptor increases nearly as $1/R^2$, where R is the donor-acceptor spacing[101,104,105]. Secondly, the probability of having an acceptor in the path of a photon emitted by a donor increases with number or the concentration of the acceptors within the solvent. The fraction X of photons emitted by the donors and absorbed by the acceptors is given by:

$$X = \frac{1}{Q_D}\int_0^\infty F_D(\lambda)\left(1-10^{-\varepsilon_A(\lambda)c_A l_A}\right)d\lambda \qquad (II.9)$$

* In the case of QDs, the absorption and emission spectra are strongly dependent on their size, and the inequalities $h\nu_2 < h\nu_1 < h\nu_0$ imply the transfer of the energy from smaller to bigger QDs.

where Q_D is the internal quantum yield of the donor in the absence of the acceptor, F_D is the corrected fluorescence intensity of the donor (with the integrated intensity normalized to unity), ε_A is the molar absorption coefficient of the acceptor, c_A is the molar concentration of the acceptors and l_A is the thickness of the absorbing medium. When absorbance A ($= \varepsilon_A(\lambda)c_A l_A$) is not too large, the previous expression simplifies to:

$$X = \frac{2.3}{Q_D} c_A l_A J^{RET} \qquad (II.10)$$

where J^{RET} is the overlap integral for radiative energy transfer, given by:

$$J^{RET} = \int_0^{\infty} F_D(\lambda)\varepsilon_A(\lambda)d\lambda \qquad (II.11)$$

Since the concentration of the donors and the mean distance between donors and acceptors in colloidal solutions are related, the fraction X and thus the probability of radiative energy transfer increase with decreasing mean distance R_{mean} between fluorophores.

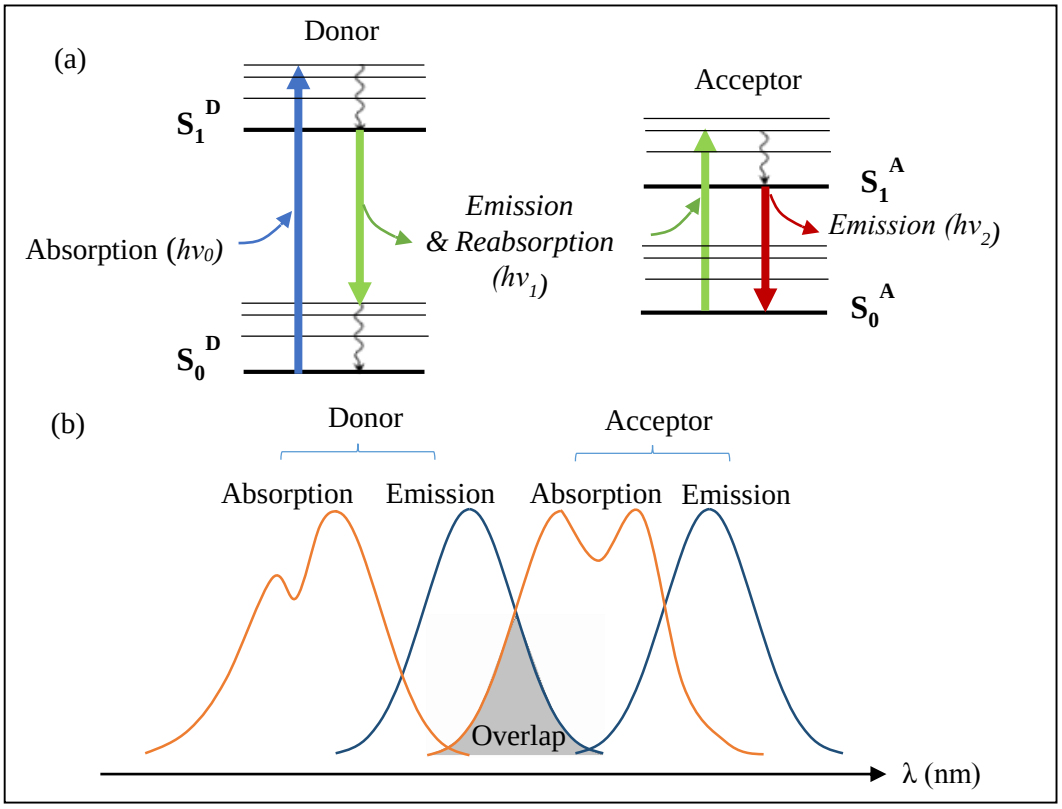

Figure II.5. Radiative energy transfer: (a) mechanism and (b) the condition of overlap between the emission spectrum of the donor and the absorption spectrum of the acceptor.

II.2.4.2. Nonradiative energy transfer

Förster resonance energy transfer

Förster Resonance Energy Transfer (FRET) is a physical process whereby a fluorophore in its excited state (the *donor*) transfers its energy nonradiatively to another molecule in its ground state (the *acceptor*), which can be either fluorescent or not. In the well-established theory proposed by Förster[106], the fluorophore is regarded as an oscillating dipole which transfers its energy to another dipole having a similar resonance frequency[107]. The excitation induces a dipole moment within the donor, this dipole moment induces another within the acceptor, creating in this way a Coulomb interaction between the two dipoles. This dipole-dipole interaction implies the simultaneous deexcitation of the donor and the excitation of the acceptor (see Figure II.6 (a)).

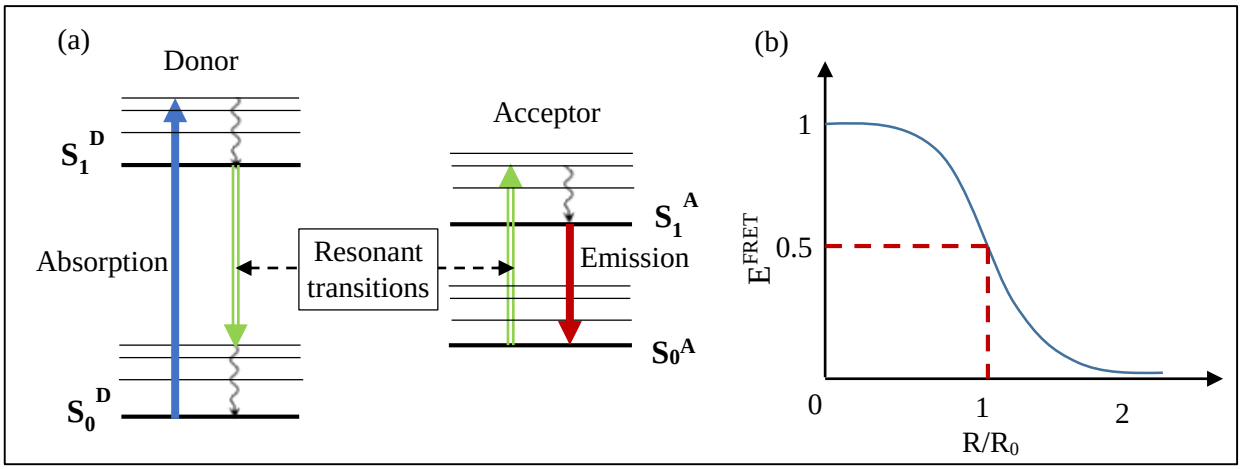

Figure II.6. Nonradiative energy transfer: (a) mechanism and (b) distance-dependency.

Considering a donor and an acceptor separated by a distance R, the rate k^{FRET} and the efficiency E^{FRET} of the nonradiative energy transfer are, respectively, given by:

$$k^{FRET}(R) = \frac{1}{\tau_D}\left(\frac{R_0}{R}\right)^6 \qquad (II.12)$$

$$E^{FRET}(R) = \frac{R_0^6}{R_0^6 + R^6} \qquad (II.13)$$

where τ_D is the lifetime of the donor in the absence of the acceptor, and R_0 is called Förster distance. This latter distance yields, regarding equation (II.13), a transfer efficiency of 50 % (see Figure II.6 (b)), and is given by:

$$R_0 = \frac{9000(\ln 10)\kappa^2 Q_D}{128\pi^5 N_A n^4} J^{FRET}(\lambda) \qquad (II.14)$$

where κ^2 is a factor that describes the relative orientation in space of the transition dipoles of the donor and acceptor, Q_D is the internal quantum yield of the donor in the absence of acceptor, n is the refractive index of the medium, N_A is the Avogadro constant and $J^{FRET}(\lambda)$ is the overlap integral for nonradiative energy transfer:

$$J^{FRET}(\lambda) = \int_0^{\infty} F_D(\lambda)\varepsilon_A(\lambda)\lambda^4 d\lambda \qquad (II.15)$$

Equations (II.12) to (II.15) show that two conditions have to be satisfied for the transfer to take place: first a spectral overlap between the donor emission and the acceptor absorption*, and second a close proximity between the donor and the acceptor.

Electron exchange: Dexter effect

Dexter effect occurs for distances extremely small, sufficient for overlap between the molecular orbitals† of the donor and the acceptor (usually smaller than 0.5 nm). This process implies a synchronous dual exchange of electrons[108], and its rate obeys an exponential decay with distance:

$$k^{Dexter} = \frac{2\pi}{h} K J^{Dexter} e^{\frac{-2R}{L_B}} \qquad (II.16)$$

where L_B is the average Bohr radius, and J^{Dexter} is the integral overlap for Dexter effect which is given by:

$$J^{Dexter}(\lambda) = \int_0^{\infty} F_D(\lambda)\varepsilon_A(\lambda) d\lambda \qquad (II.17)$$

II.2.4.3. Distinction between the mechanisms of energy transfer

As one can notice, there are many similarities between radiative and nonradiative energy transfer. Both processes increase with the proximity between donors and acceptors, and both require an overlap between the emission spectrum of the donor and the acceptor. They can be separated however by considering:

- **The dependency on donor-acceptor separation**: while the efficiency of radiative energy transfer is nearly proportional to $1/R^2$, FRET's efficiency varies as $1/R^6$ ‡, and Dexter effect decays exponentially with R;
- **The range of efficient energy transfer**: Dexter effect requires extremely reduced distances between molecules. For distances about or less than 10 nm, FRET is the dominant mechanism for energy transfer, and for bigger distances, the radiative energy transfer prevails[109];
- **Lifetime of the donors**: The nonradiative processes can compete with fluorescence and thus reduce the lifetime of the donors. Radiative energy transfer, however, takes place in a serial fashion prior to the final emission without competing the latter[107]. The lifetime of the donor is therefore lengthened in contrary to what happens in the case of nonradiative energy transfer.

* In the case of QDs, an overlap exist between the emission spectrum of smaller particles and the absorption spectrum between bigger QDs. This overlap implies the energy transfer from smaller to bigger QDs.

† Or more specifically in the case of QDs, the overlap of the wavefunction of the excited electrons.

‡ A full classical model of energy transfer is presented in[101] allowing the description of the radiative energy transfer and Förster energy transfer in a unified way, and shows that there is a transition between $R<<\lambda_{emission}$ *and* $R>>\lambda_{emission}$.

II.2.4.4. Which parameters could influence energy transfer?

As it can be noticed from the abovementioned description of energy transfer, the donor-acceptor spacing has a crucial role in determining the efficiency of energy transfer and, more importantly, the nature of the transfer (radiative, Förster or electron energy transfer). Figure II.7 illustrates the different natures of energy transfer and gives the orders of magnitude of donor-acceptor spacings required for the energy transfer to occur efficiently. The distances between adjacent molecules are governed by their concentration.

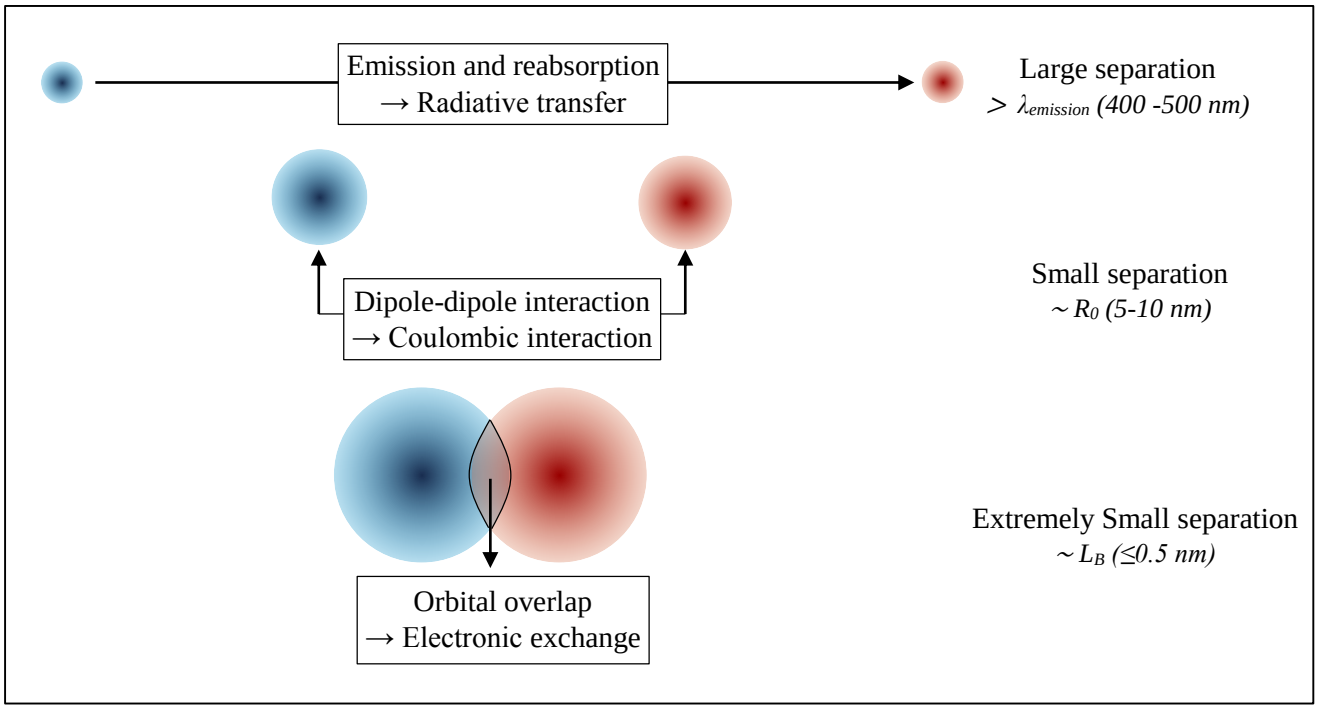

Figure II.7. The different natures of energy transfer depending on the separation between the donor and the acceptor. The distances are based on reference [110] *(section 3.6).*

In addition to the concentration, which acts directly on the distance distribution between donors and acceptors, other parameters can act indirectly on energy transfer efficiency through their influence on the motion of the molecules within the solvent.

For instance, the particles can diffuse within the solvent due to the Brownian motion*. The average distance traveled by a moving particle during a time period *t*, also known as the Mean Free Path (MFP), is given by:

$$MFP = \sqrt{< x^2 >} = \sqrt{6Dt} \qquad (II.18)$$

where *D* is the (transitional) diffusion coefficient of molecules given by Einstein-Stokes equation:

* Brownian motion is a random motion of particles suspended in a fluid as a result of their collisions with the surrounding molecules.

$$D = \frac{k_B T}{6\pi\eta r} \qquad (II.19)$$

Where k_B is the Boltzmann constant, T is the temperature, r is the radius of the particle and η is the viscosity of the solvent.

For the very fast radiative energy transfer mechanism, the diffusion of the molecules will have no influence, but in the case of Förster mechanism, given the excited state lifetime is sufficiently long, donor and acceptor molecules can move to get closer.

It is worth noticing that the expression of D indicates the dependence of diffusion on parameters such as the temperature and the viscosity, with the latter being itself dependent on the temperature and the pressure. The influence of these different parameters has thus to be kept in mind when considering non-radiative energy transfer mechanisms.

The molecules can also move relative to each other under dynamic conditions. Dynamic conditions can be generated under rolling or sliding conditions. The shear rate and the entrainment speed may therefore modify the balance between the different mechanisms of energy transfer. Finally, the radiative energy transfer depends, as mentioned earlier, on the thickness of the absorbing media, with the latter being itself dependent on the apparatus employed for studying the fluorophores.

II.2.4.5. Polarity effect

The polarity effect is sometimes termed as the general solvent effect since it is formalized independently of the chemical properties of the fluorophore and the solvent, and without considering eventual chemical interactions between them. These latter effects, called specific effects, include hydrogen bonding, complex formation and quenching, and they can have considerable influence on the emission of the fluorophores. Such effects are however excluded from our system as we will explain it later when discussing the properties of the QDs. As a consequence, we will restrict our discussion in this paragraph on the general solvent effect.

Polarity effect is described by Lippert-Mataga equation[111,112] in which the fluorophore is regarded as dipole interacting with a continuous medium of uniform dielectric constant. Following this equation, such interactions affect the energy difference between the ground and the excited states (see Figure II.8 (a)):

$$E_A - E_E = 2\Delta f \frac{\left(\mu_E - \mu_G\right)^2}{a_c^3} + \text{constant} \qquad (II.20)$$

where E_A and E_E are the energy of the absorption and emission, respectively, a_c is the radius of the cavity in which the fluorophore resides, and μ_E and μ_G are, respectively, the excited- and ground-state dipole moments. The constant value represent the Stokes shift without polarity effect (induced by the vibrational relaxations). Δf is the orientation polarizability and it is defined as:

$$\Delta f = \frac{n^2 - 1}{2n^2 + 1} - \frac{\varepsilon - 1}{2\varepsilon + 1} \qquad (II.21)$$

where n and ε are the refractive index and the static dielectric constant of the solvent, respectively.

The polarity effect is intimately linked to the rotational motion or diffusion of the solvent molecules around the fluorophores. When fluorophores are excited, their dipole moment is generally increased ($\mu_E > \mu_G$). If these fluorophores are dispersed in a polar environment ($n^2 > \varepsilon$), the solvent molecules will reorient around the fluorophores. The reorientation results in a *relaxed state* since it lowers the energy of the excited state and increases the energy of the ground state when compared to the *Franck-Condon state*, corresponding to non-oriented solvents molecules (see Figure II.8 (a)). Such energy changes enhance the Stokes shift of the emission spectrum relatively to the absorption spectrum (resulting in a difference E_A - E_E bigger than the constant shift induced only by vibrational relaxations) as it can be seen in Figure II.8 (a) and (b).

Solvent relaxation is a fast process (10^{-10} to 10^{-11} s) when compared to typical values of the lifetime of the excited state (10^{-8}-10^{-9} s) but quite slow when compared to the quasi-instantaneous transitions between electronic levels (10^{-15} s). As a result of such timescales:

- The molecules can have enough time to reorient during the lifetime of the excited state;
- During the transition from the ground state to the excited state or *vice-versa*, the position of solvent molecules is unchanged (Franck-Condon principle), and these molecules remain non-oriented during the absorption and oriented during the emission (see Figure II.8 (a)).

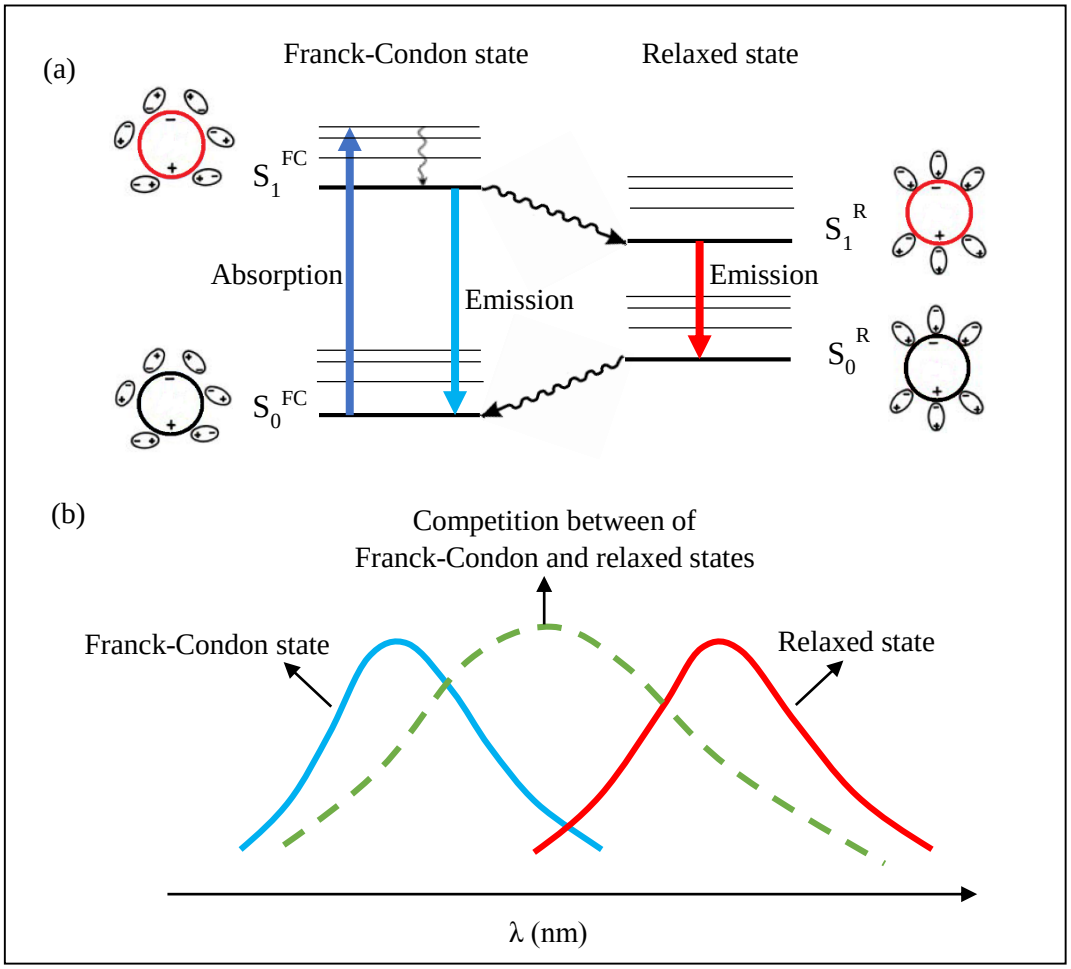

Figure II.8. (a) Jablonski diagram of the polarity effect; (b) effect of solvent polarity on the fluorophore emission spectra.

To estimate the likelihood of solvent molecules relaxation during the lifetime of the excited state, one has to consider carefully the relaxation time τ_{relax}, which is inversely proportional to the rotational diffusion coefficient D_r, given by:

$$D_r = \frac{k_B T}{V_{Molecule}\eta} \qquad (II.22)$$

where k_B is the Boltzmann constant, T and η are respectively the temperature and the viscosity of the solvent, and $V_{Molecule}$ is the volume of a solvent molecule.

At law values of D_r, the relaxation time is long and the solvent molecules remain at the Franck-Condon state, and they will relax in the opposite case. At intermediate values of D_r, however, the relaxation competes with the emission, and an emission spectrum with intermediate stokes shifts (between Franck-Condon and relaxed state) is obtained as shown in Figure II.8 (b).

II.2.5. Photoluminescence and sensing

The characteristics of PL, such as lifetime, quantum yield and the steady-state emission spectrum, are highly affected by the interaction of the fluorophores with their local environment during their excited state. Some examples have been given in or can be deduced from our brief description on PL, including:

- The polarity of the solvent through its influence on the Stokes shift;
- The viscosity of the solvent through its influence on (i) the transitional diffusion of the fluorophores within the solvent and (ii) the rotational diffusion of the solvent molecules around the fluorophores;
- The local temperature through its influence on (i) the active vibrational energy states of the solvent molecules and the fluorophores and (ii) the viscosity of the solvent;
- The local pressure through its influence on the viscosity for example;
- Eventually, the flow of the solvent through its influence on energy transfer between donors and acceptors;
- The apparatus employed for the study of the fluorophores, through its influence on the thickness of the solvent.

Some other effects can arise from structural parameters of the microenvironment. An important example is the strong distance-dependence of the FRET. This mechanism of energy transfer being highly sensitive to variations of distances within nanometric scales, it has been described as "spectroscopic ruler"[113,114], and various techniques based on FRET are commonly applied in order to measure microscopic distances and infer structural information about macromolecules such as proteins[115] and DNA[116]. The influence of some chemical effects was pointed out in our survey, but those are not a concern in our study. Examples are the influence of the pH of the solvent[117], the presence and the concentration of quenchers (hydrogen molecules for example[118]), the rate of chemical reactions[119], to mention few.

These multiple effects of fluorescence present numerous opportunities for probing the local microenvironment surrounding the fluorophores. Added to these prospects are the high temporal and spatial resolution offered by PL-based measurement techniques. Time-resolved measurements can be performed with resolutions below the picosecond. They might consequently offer interesting possibilities for studying transient effects in EHD contacts, even though as a first tentative, this is not

our immediate goal! The spatial resolution is theoretically related to the diffraction limit imposed by the excitation wavelengths being employed (in the order of 400-600 nm for visible radiation). Measurements yield usually through-thickness-averaged measurements as it the case for our measurements, but one can consider fluorescence microscopy in confocal configuration or with a two photon excitation to enhance the resolution in the direction of film thickness.

There are, nevertheless, two main difficulties in performing such measurements.

First; the multiple microenvironment-related effects raise the issue of the interpretation of PL characteristics. Indeed, the mechanisms involved are complex, and the effects may act simultaneously and/or synergistically. Therefore, in order to avoid misleading conclusions, it is very important to (i) be aware of the parameters imposed by the system under investigation, (ii) have a global picture of the possible effects related to the local environment, (iii) make a proper selection of the probe by considering its predominant sensitivity to the parameter(s) of interest and (iv) minimize the influence of the other parasitic parameters on the response of a given probe or at least (v) have a quantitative estimation of their influence if such effects are inevitable.

The other difficulty is related to the perturbation induced by the probe on the microenvironment of each fluorophore, and the global behavior of the solvent containing a system of fluorophores. These perturbations can be of physical and even chemical nature, and much attention has to be paid on the size, shape, quantity and the chemical nature of the probe in order to minimize their effect on the behavior and the properties of the solvent.

II.3. Quantum dots*

Quantum dots (QDs) are fluorescent nanosized crystals made of semiconductor materials. They can be either:

- Simple like pure silicon (Si) QDs;
- Or compound, such as those composed of elements of the groups II and VI of the periodic table (alternatively called II-VI semiconductors, such as CdSe and CdS QDs), and those composed of elements of the groups III and V (III-V semiconductors, such as GaAs QDs).

As mentioned earlier, the QDs have properties arising from them being fluorescent species (see the description of PL in the previous paragraphs), but they have unique properties due to their composition of semiconductors and their nanometric size. The two last features of the QDs will be discussed in the following paragraphs.

II.3.1. QDs as semiconductor materials: Bandgap energy

II.3.1.1. Concept of the Bandgap energy

A semiconductor is a material that possesses an electrical conductivity falling between that of conductors (metals for example) and insulators (such as most polymers), and can exhibit insulator-like or metal-like conductivity by simply increasing their temperature. These properties of semiconductor materials arise from the fundamental concept of bandgap.

* Interested readers can refer to the book of Gaponenko on the optical properties of QDs[181].

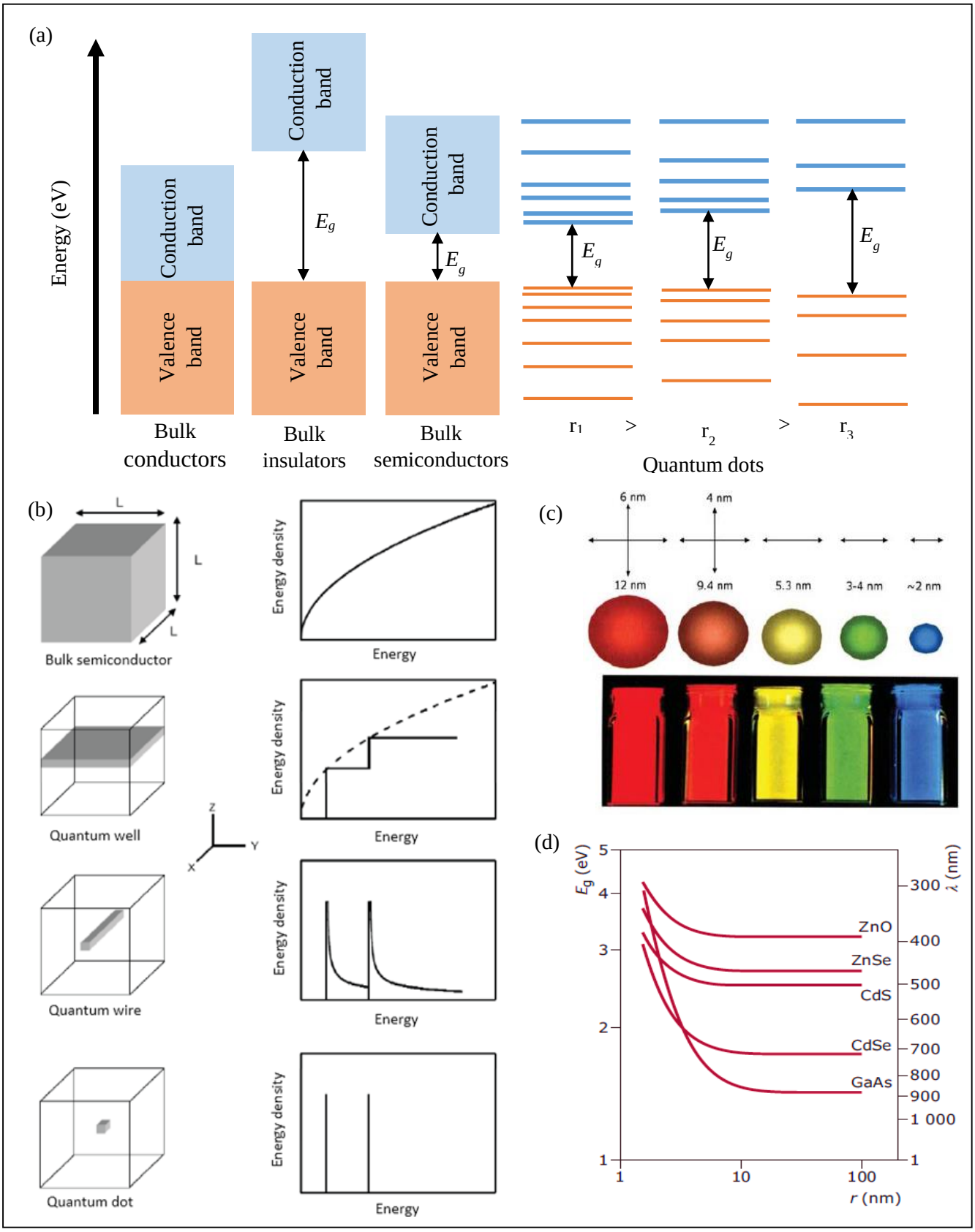

Figure II.9. (a) Electronic structure in bulk conductors, bulk insulators, bulk semiconductors and QDs of Bulk semiconductors and QDs of different diameters; (b) Degrees of confinement and the resulting density of electronic energy states; (c) Color-tenability of QD by size variations; (d) Variation of the emission energy or wavelength with the size of the QDs[120].

The bandgap corresponds to values of energy whereby no electronic energy levels can exist, or equivalently, it is the zone of forbidden energies. This zone is contained between two bands: valence band and the conduction band. The bandgap energy E_g refers to the energy difference between the top of the valence band and the bottom of the conduction band (see Figure II.9 (a)). The larger the bandgap energy, the more energy is required for an electron to migrate from the valence to the conduction band, and the more resistive is the material.

As illustrated in Figure II.9 (a):

- The bandgap of conductor materials is zero, whereas the insulators have large bandgaps, which explain the important difference between their electrical resistances;
- Semiconductor materials have a band structure similar to that of insulators, but the bandgap energy is much smaller, and is sensitive to temperature, which explains their intermediate and temperature-dependent electrical resistance.

Similar differences between these materials (conductors, insulators and semiconductors) are observed for the transition between the energy levels *via* absorption or emission of photons. At the ground state, the valence band is filled, whereas the conduction band is empty. Following the excitation of a semiconductor material with an illumination source (laser for example) of an excitation energy $h\nu_E > E_g$, an electron moves from the valence band into the conduction bands, leaving a *hole* behind. This hole behaves as being a particle with a positive charge $+e$ and an effective mass m_h* capable of migrating within the material. An electron and hole bound together with the electrostatic Coulomb force is called an exciton. The relaxation or the recombination of the exciton to the ground state is accompanied with a light emission of energy E_g.

II.3.1.2. Sensitivity of the bandgap energy to temperature and pressure variations

The sensitivity of the bandgap energy of semiconductor bulk materials E_g^B to temperature and pressure variations is a well-documented phenomenon. These variations arise essentially from the influence of these parameters on (i) the crystalline lattice of semiconductor materials and (ii) the interaction of the exciton with the lattice (electron-phonon interaction). Without getting into deeper considerations, some important results will be presented herein.

Concerning the sensitivity of semiconductor materials to temperature, Varshni law is the more commonly used one. In his work in 1967, Varshni[121] considered theoretical treatments (References 1,2, 4-9 in his paper) which showed that:

$$\Delta E_g^B \propto \begin{cases} T^2, \ if \ T \ll \theta_D \\ T, \ if \ T \gg \theta_D \end{cases} \qquad (II.23)$$

Where θ_D is the Debye temperature.

He proposed an equation consistent which such variations with the following form:

$$E_g^B(T) = E_g^B(0) - \frac{\alpha_1 T^2}{(T + \beta_1)} \qquad (II.24)$$

where $E_g^B(0)$ is the bandgap energy at *0 K*, α_1 is a constant and β_1 is a temperature close to the Debye temperature θ_D.

On the other hand, in order to compute the sensitivity of the bandgap energy to pressure variations, the volume deformation potential a_V is introduced:

$$a_V = \frac{\partial E_g^B}{\partial \ln V_{Crystal}} \qquad (II.25)$$

Where $V_{Crystal}$ is the volume of a primitive cell of the crystalline structure.

This quantity is related to the pressure sensitivity through the bulk modulus:

$$\frac{\partial E_g^B}{\partial p} = -\frac{a_V}{B} \qquad (II.26)$$

with the bulk modulus being defined as:

$$B = -\frac{\partial p}{\partial \ln V_{Crystal}} \qquad (II.27)$$

B can be computed as a function of pressure using Murnaghan's equation of state[122]:

$$B(p) = B(0) + B' p \qquad (II.28)$$

Linear and quadratic variations for the $E_g(p)$ are commonly used in literature[123]. Such choices can be justified by experimental and numerical treatments showing that E_g has almost a linear variation with respect to $dlnV_{Crystal}$[124,125]. Such a behaviour implies that:

$$\frac{\partial E_g^B}{\partial p} = -\frac{a_v^0}{B(0) + B' p} \qquad (II.29)$$

Where a_v^0 is the constant deformation potential.

When the bulk compressibility is approximated with Taylor's expansion to the first order or second order, linear or quadratic expressions are obtained, respectively:

$$E_g^B(p) = E_g^B(0.1MPa) + \alpha_2 p : \text{linear approximation} \qquad (II.30)$$

$$E_g^B(p) = E_g^B(0.1MPa) + \alpha_2 p + \beta_2 p^2 : \text{quadratic approximation} \qquad (II.31)$$

In these expressions, α_2 and β_2 are constants.

The proper approximation is chosen depending on the material and the range of the considered pressures.

II.3.2. QDs as nanosized objects: Quantum confinement effect

QDs have been first discovered in 1981 by Ekimov and Onushchenko[126], and further developments in synthesis procedures have followed one another aiming to optimize their properties for

optoelectronic device technologies (photovoltaic cells[127], light emitting diodes or LEDs[128,129]and QDs lasers[130]) and sensing applications (biological labels and *in vivo* imaging[131,132], temperature probes[133,134] and strain gauges[135]).

These nanosized materials are known to exhibit a spectacular variation of the color (absorbance spectrum) as well as the PL by simply tuning their size (Figure II.9 (c) and (d)). These size-dependent optical properties are due to the so-called quantum confinement effect. Indeed, when at least one of the dimensions of the semiconductor material is reduced to very small values (smaller than exciton Bohr radius), the continuity of energy conduction and valence bands in a bulk semiconductor material is broken up. Quantum well, quantum wires and quantum dots are obtained when the exciton is confined in one, two or three dimensions, respectively (Figure II.9 (b)). In the particular case of QDs, quantum confinement effect results in two properties of major importance. The first is the atomic-like, discrete and well separated electronic energy states (Figure II.9 (a)), and the second is the size-dependent separation between electronic energy levels, and particularly the size-dependent bandgap energy E_g (Figure II.9 (a), (c) and (d)).

These effects can only be described by quantum mechanics, i.e. through the resolution of Schrödinger equation. The theoretical treatment can however be conducted *via* two approaches:

- In the first approach, the kinetic energy of all the nucleus, electrons and holes, and the potential energy of all the interactions are considered;
- In the second approach, it is not the number of particles or quasi-particles (nucleus, electrons and holes) that accounts, but the size of the QD. The QD is actually considered as a box in which electron-hole pairs are combined *via* Coulombic interaction to form excitons, and the excitons are confined within the dimensions of the QD (i.e., the frontiers of the QD of infinite potential constitute the boundary conditions of Schrödinger equation).

The first approach is very complex, and even after many simplifications numerical resolutions are required. We will consider in our work the second approach which, albeit approximate, is commonly used for the investigation of systems of QDs, and allows to reproduce well the experimental observations. This approach, firstly proposed by Efros[136] and later modified by Brus[137], is known as the effective mass approximation (EMA). It stipulates that QDs have the same crystalline structure as the corresponding bulk materials, but their bandgap energy is shifted from ${E_g}^{\mathrm{B}}$ with a quantity ${E_g}^{Q}$ arising from the (quantum) confinement of the excitons:

$$E_g = E_g^B\left(V_{Crystal}\right) + E_g^Q\left(r\right) \qquad (II.32)$$

This assumption yields, when applied to a spherical QD, the following expression:

$$E_g^Q\left(r\right) = \frac{\gamma^Q}{r^2} - \frac{\nu^Q}{r} \qquad (II.33)$$

where:

$$\gamma^Q = \frac{\hbar^2\pi^2}{2}\left(\frac{1}{m_e^* m_e} + \frac{1}{m_h^* m_e}\right) \qquad (II.34)$$

$$\nu^Q = \frac{1.8e^2}{4\pi\varepsilon_r\varepsilon_0} \qquad (II.35)$$

In the previous expressions, $\hbar$ is the reduced Planck constant (= $h/2\pi$, with h being the Planck constant), r is the radius of the QD, m_e is the mass of an electron, m_e^* is the effective mass of an electron, m_h^* is the effective mass of a hole, e is the charge of an electron, ε_r is the relative permittivity of the QDs material and ε_0 is the vacuum permittivity. As it can be noted from Equation (II.33), the shift E_g^Q is the sum of two contributions. The first term, proportional to $1/r^2$, takes into account the confinement effect, and the second term, proportional to $1/r$, is a Coulomb interaction energy. The combination of the two terms leads to a significant increase in the bandgap energy with decreasing size, especially for sizes of QDs between 1-10 nm (see Figure II.9 (d)).

II.3.2.1. Temperature/pressure sensitivity

Size-independent bulk contribution, thermal expansion and compression

To compute the sensitivity of QDs to temperature or pressure variations, the expression of the bandgap energy has to be differentiated with respect to these two parameters:

$$\frac{\partial E_g}{\partial T} = \frac{\partial E_g^B\left(V_{Crystal}\right)}{\partial T} + \frac{\partial E_g^Q(r)}{\partial T} = \frac{\partial E_g^B\left(V_{Crystal}\right)}{\partial T} + \frac{\partial E_g^Q}{\partial r}\frac{\partial r}{\partial T} \qquad (II.36)$$

$$\frac{\partial E_g}{\partial p} = \frac{\partial E_g^B\left(V_{Crystal}\right)}{\partial p} + \frac{\partial E_g^Q(r)}{\partial p} = \frac{\partial E_g^B\left(V_{Crystal}\right)}{\partial p} + \frac{\partial E_g^Q}{\partial r}\frac{\partial r}{\partial p} \qquad (II.37)$$

Or in a more compact way:

$$S_T = S_T^B\left(V_{Crystal}\right) + S_T^Q(r) = S_T^B\left(V_{Crystal}\right) + S_r^Q(r)\frac{\partial r}{\partial T} \qquad (II.38)$$

$$S_p = S_p^B\left(V_{Crystal}\right) + S_p^Q(r) = S_p^B\left(V_{Crystal}\right) + S_r^Q(r)\frac{\partial r}{\partial p} \qquad (II.39)$$

The terms S_T denotes the global temperature sensitivity of the QDs, S_T^B and S_T^Q stand for the bulk and the quantum contributions, respectively. The terms S_p, S_p^B and S_p^Q denote the pressure sensitivity of the QDs, and the bulk and the quantum contributions, respectively. These different notations will be used mainly in the following chapters to describe the variation of the QDs response to temperature and pressure variations.

The bulk-related terms (S_p^B and S_T^B) are related to the crystalline structure of the QDs (symbolically represented by the volume of a primitive cell $V_{Crsytall}$). They can be obtained by differentiating the expression of E_g^B (in Equations (II.24), (II.31) and (II.32)) with respect to the temperature or the pressure. The quantum-related terms (S_p^Q and S_T^Q) are size-dependent. They arise from the temperature- or pressure-induced size variations ($\partial r/\partial T$ and $\partial/\partial p$, respectively), and the variation of the bandgap energy with size of the QDs ($\partial E_g^Q/\partial r = S_r^Q$). The sensitivity of the QDs to size variations S_r^Q is given by:

$$S_r^Q(r) = \frac{\partial E_g^Q(r)}{\partial r} = \frac{\nu^Q}{r^2} - \frac{2\gamma^Q}{r^3} \qquad (II.40)$$

This expression implies (as it can be clearly noticed in Figure II.9 (d)) an increase of the sensitivity of the QDs to size variations with decreasing size.

The thermal expansion $\partial r/\partial T$ and the compression $\partial r/\partial p$ of the QDs can be deduced from the coefficients of thermal expansion α_T^B and compressibility α_p^B defined as:

$$\frac{V(T,p)}{V(T_0,p_0)} = \frac{V(T,p)}{V(T,p_0)}\frac{V(T,p_0)}{V(T_0,p_0)} = \left(1-\alpha_p^B(T,p)\times(p-p_0)\right)\left(1+\alpha_T^B\times(T-T_0)\right) \qquad (II.41)$$

where T_0 and p_0 denote the ambient temperature (298 K) and the ambient pressure (0.1 MPa), respectively. For spherical QDs with a radius r_0 at ambient temperature and pressure, the previous equation becomes:

$$\frac{r(T,p)}{r_0} = \left(\left(1-\alpha_p^B(T,p)\times(p-p_0)\right)\left(1+\alpha_T^B\times(T-T_0)\right)\right)^{1/3} \qquad (II.42)$$

The influence of temperature and pressure can be written more explicitly as following:

$$E_g(T) = E_g^B(0K) + E_g^Q\left(r(T)\right) - \frac{\alpha_1 T^2}{T+\beta_1} \qquad (II.43)$$

$$E_g(p) = E_g^B(0.1MPa) + E_g^Q\left(r(p)\right) + \alpha_2 p + \beta_2 p^2 \qquad (II.44)$$

The sensitivity of some QDs to temperature and pressure variations has been reported in literature[138,139]. An example of CdSe/ZnS QDs is shown in Figure II.10 (a) and (b).

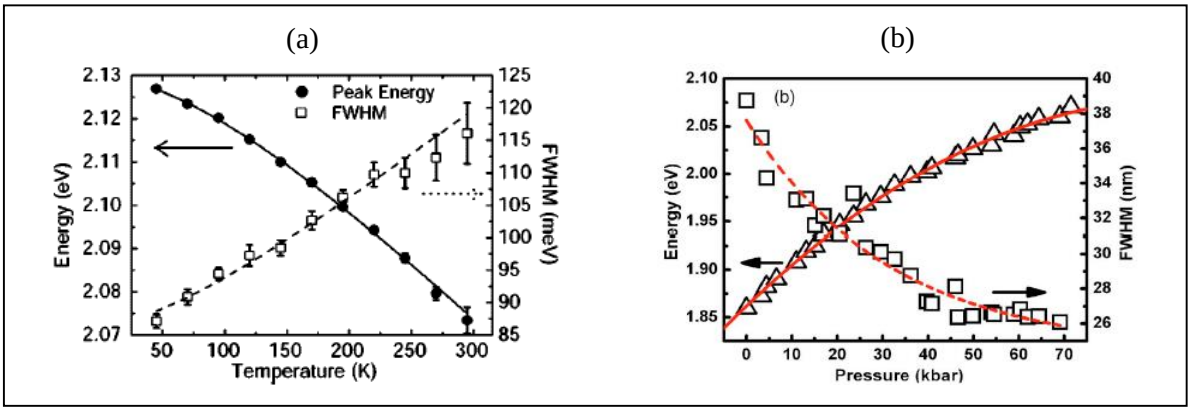

Figure II.10. Variation of the energy of the bandgap and the FWHM of CdSe/ZnS with (a) temperature[138] and (b) pressure[139].

Size-dependent bulk contribution, thermal expansion and compression

The Effective Mass Approximation (EMA) is essentially used to evaluate the bandgap energy of a system of QDs synthesized with a given mean radius *r*. It yields satisfactory predictions by assuming (i) a bulk contribution independent from the size of the QDs and (ii) a quantum contribution as a corrective term taking into account the confinement of the exciton within the dimensions of the QD. However, when it comes to evaluating the variation of the bandgap energy with temperature or pressure, the following questions are raised:

- Are the thermal expansion and the compressibility of nanosized objects the same as the corresponding bulk material?
- Is the influence of temperature and pressure on exciton-phonon interactions the same when considering nanosized (finite) crystals and bulk (infinite) crystals? In other terms, are the interactions between the vibrational modes of crystals and the exciton energy (and the resulting shift in the bandgap energy) independent from the size of the crystal?

The thermal expansion and the compressibility of nanosized objects is more important than of the bulk material due to the important surface effect. For instance, Kůsová *et al.*[140] assumed a thermal expansion of Silicon nanocrystals three time larger than for the corresponding bulk material, in order to account for PL measurements. Freitas Neto *et al.*[141] measured the thermal expansion of 2 nm radius CdS QDs using Raman measurements, and found a thermal expansion coefficient twice the value found for bulk CdS. The dependence of the exciton-phonon interaction on the size of the QDs was reported in many studies[142–146]. In a study conducted by Olkhovets *et al.*[144] on PbS and PbSe QDs, a size-dependent term $(\partial E_g/\partial T)_{el\text{-}ph}$ (el-ph: electron-phonon coupling) was introduced to account for the variation of the temperature sensitivity with the size of the QDs.

Based on these findings, a more accurate expression of temperature and pressure sensitivities can be written as following:

$$S_T = S_T^B\left(r, V_{Crystal}\right) + S_r^Q\left(r\right)\frac{\partial r}{\partial T}\left(\alpha_T^Q\right) \qquad (II.45)$$

$$S_p = S_p^B\left(r, V_{Crystal}\right) + S_p^Q\left(r\right)\frac{\partial r}{\partial p}\left(\alpha_p^Q\right) \qquad (II.46)$$

Where $\alpha_T{}^Q$ and $\alpha_p{}^Q$ are the thermal expansion and the compressibility coefficients of the nanosized crystals, respectively.

More explicitly, we can assume that the coefficients for temperature and pressure dependence vary with the size of the QDs:

$$E_g\left(T\right) = E_g^B\left(0K\right) + E_g^Q\left(r\left(T\right)\right) - \frac{\left(\alpha_1 + \delta\alpha_1\left(r\left(T\right)\right)\right)T^2}{T + \beta_1 + \delta\beta_1\left(r\left(T\right)\right)} \qquad (II.47)$$

$$E_g\left(p\right) = E_g^B\left(0.1MPa\right) + E_g^Q\left(r\left(p\right)\right) + \left(\alpha_2 + \delta\alpha_2\left(r\left(p\right)\right)\right)p + \left(\beta_2 + \delta\beta_2\left(r\left(p\right)\right)\right)p^2 \qquad (II.48)$$

Where $\delta\alpha_1$, $\delta\beta_1$, $\delta\alpha_2$, $\delta\beta_2$ are corrective terms taking into account the influence of size on the bulk temperature and pressure sensitivities. These terms tend to zero when $r \rightarrow \infty$. In the case of many QDs, including those we will consider in our study (CdSe-based QDs), this size dependence implies an increase in temperature and pressure sensitivity with decreasing size.

II.3.2.2. Other features of the emission spectrum of QDs

Up to now, we have considered the energy of the bandgap of the QDs which is not the only information contained in the emission spectrum. Generally speaking, the emission spectrum of QDs contains different features that can be used to extract structural information about the QDs as well as information about the local environment surrounding the QDs. For many QDs and under various conditions, the emission spectrum is almost symmetrical and a Gaussian distribution is commonly used to fit the energy spectrum. This distribution can be written as:

$$I = I_{baseline} + I_{\max} \exp\left(\frac{-1}{2}\left(\frac{E - E_{mean}}{\sigma_E} \right)^2 \right) \qquad (II.49)$$

In this expression (see Figure II.11):

- $I_{baseline}$ is the baseline intensity of the emission spectrum, and it is generally subtracted from the emission spectrum *prior to* fitting;
- I_{max} is the maximum emission intensity obtained after subtracting the baseline, and it corresponds to the energy of the bandgap;
- E_{mean} or the energy at maximum emission corresponds to the mean value bandgap energy of the QDs.
- σ_E is the standard deviation of emission spectrum.

An alternative to σ_E is the Full Width at Half Maximum (FWHM) Γ which is the width of the emission spectrum at $I_{max}/2$ (after subtracting the baseline). The two quantities are actually related:

$$\Gamma = 2\sqrt{2\ln(2)}\sigma_E \approx 2.33\sigma_E \qquad (II.50)$$

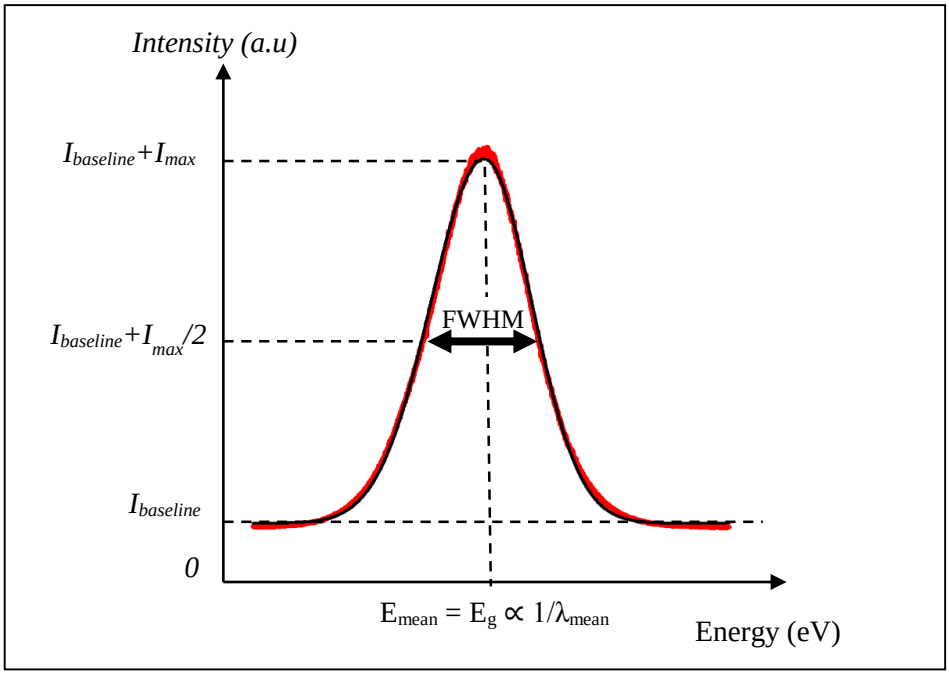

Figure II.11. Emission spectrum (black curve), fitting using a Gaussian distribution (red curve) and the characteristics of the Gaussian distribution.

Even through the intensity of the PL is commonly used for sensing applications[133,147], it is less suitable for our investigation. This is because it depends on other parameters that are either (i) not perfectly adjusted, such as excitation power, or (ii) not constant in the contact such as film thickness in EHD contacts (the intensity being proportional to the number of fluorophores, and thus to the film thickness). For these reasons, this parameter will not be considered in our study.

The width of the emission spectrum is more interesting despite its more complex origin than the single value of the energy at the maximum emission. Indeed, the broadening of the emission spectrum (and also the absorption spectrum) is the result of two effects: homogenous and inhomogeneous broadening. The first effect arises from the existence of an active set of vibrational states associated to each electronic state (exciton-phonon interactions). The second effect is due to the distribution or the fluctuations of the size, shape, composition, crystalline structure, surface defects, microenvironment, etc. of the QDs. We shall insist here on the influence of the size distribution. As a result to the quantum-confinement effects, QDs of smaller size have larger bandgap energies compared to bigger ones (see Figure II.9 (d)). Consequently, the size distribution of a system of QDs results in a distribution in the activated electronic states, with the smaller QDs located toward higher energies (or shorter wavelengths) of the emission spectrum, and the bigger QDs toward lower energies (or higher wavelengths).

The following expression has been proposed for the temperature dependence of the broadening in bulk semiconductors[148]:

$$\Gamma(T) = \Gamma_{inh} + \sigma T + \frac{\Gamma_{LO}}{e^{E_{LO}/k_B T} - 1} \qquad (II.51)$$

In this expression, Γ_{inh} is the inhomogeneous broadening and the two last terms represent the homogeneous broadening. Without describing the physical significance of the different parameters, σ, Γ_{LO} and E_{LO} are respectively called: the exciton-acoustic-phonon coupling coefficient, the exciton-LO-phonon (Longitudinal Optical phonon) coupling coefficient and the LO-phonon energy. Equation (II.51) applies for QDs[138,149], but not necessarily with same values for the different parameters owing to the boundary conditions associated to these nanosized objects. Figure II.10 (a) shows an example for the variation with temperature of the FWHM in the case of CdSe/ZnS QDs.

The variation of Γ with pressure has been reported in literature (see Figure II.10 (b) for an example on CdSe/ZnS QDs[139]) but the underlying mechanism is unclear. In an investigation on CdSe/ZnS, Fan *et al.* suggested that the pressure reduces the surface defects induced by the interfacial mismatch (between the CdSe core and the ZnS shell). As the decrease of the defect states narrows electron population[150], the width of the emission is decreased.

In order to measure simultaneously pressure and temperature, one approach is to analyze different spectroscopic characteristic of one family of QDs. Another approach consists of using only peak position (for instance) of two families of QDs. In this work we will consider the second approach. The first step is to investigate the feasibility of temperature or pressure measurement with one family of QDs.

II.3.3. Structure of the selected probe: CdSe/CdS/ZnS QDs

In our work we have chosen to calibrate CdSe-based QDs for temperature and pressure measurements.

Figure II.12 (a) to (d) shows a schematic representation of the CdSe/CdS/ZnS QDs* (with the dimension of each of its components), a representative TEM image of the QDs, a histogram representing their size distribution and an example of their emission spectrum. As one can see, these QDs have a multi-shelled (or core-shell-shell) structure.

They are constituted of a core of CdSe nanocrystals, encapsulated within two shells of semiconductor materials (CdS and ZnS), themselves recovered by organic ligands (made of stearic acid). The semiconductor shells are used to enhance the quantum yield of the QDs by passivating the core surface states. The shell material have a larger bandgap, in order to ensure a better confinement of the exciton within the core. Ligands are used, in turn, to (i) passivate the dangling bonds that could be found in the surface of the shell, and to (ii) ensure the affinity of QDs with different environments (hydrophilic and hydrophobic environments for example), allowing the formation of a stable colloidal dispersion of QDs.

* The QDs were kindly provided by P. Reiss, and more details about their synthesis, structure and PL are found in[151,182].

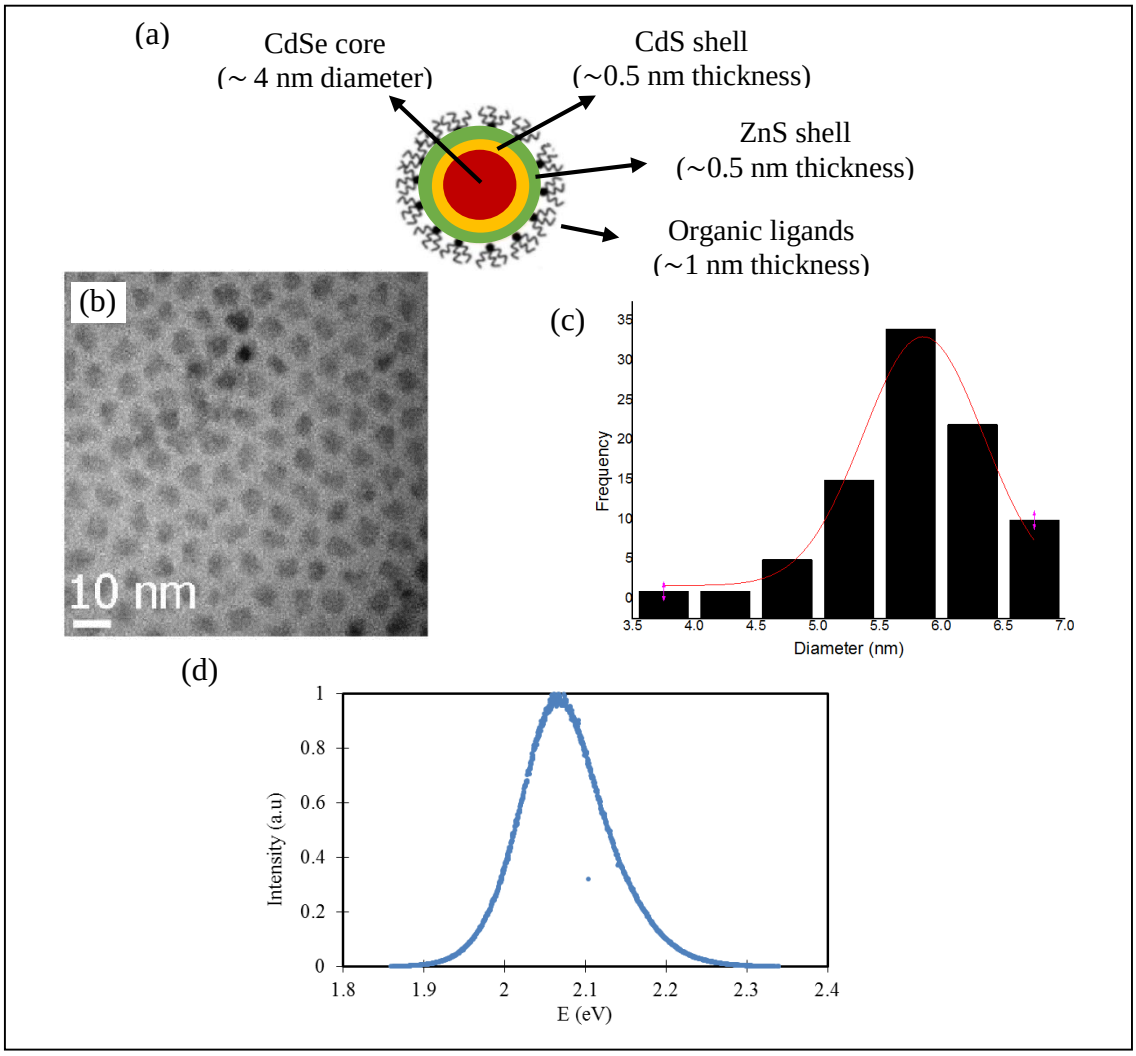

Figure II.12. CdSe/CdS/ZnS QDs: (a) A schematic representation of the multi-shell structure; (b) a TEM image (c) a histogram of size distribution[151] *and (d) an example of the emission spectrum.*

II.4. Conclusion on sensitivity of the QDs

The description of the photoluminescence and quantum dots physics showed the existence of many parameters that could affect the response of the QDs. The two most important for our investigation are naturally the temperature and the pressure. The sensitivity of the QDs to these two parameters can arise from their photoluminescent nature, chemical composition, crystalline structure and nanometric size. The influence of other parameters, such as QDs concentration, the polarity, the viscosity and eventually the flow of the solvent might be non-negligible and should therefore be fully examined.

We pointed out the existence of some special effects arising from the chemical nature of the fluorophores and the solvent molecules and the possible chemical reactions within the system. These effects are fortunately not present in our systems for two main reasons. First, as mentioned earlier, the surface of the CdSe/CdS/ZnS QDs have been passivated during the chemical synthesis, and secondly because there is no tribochemical reactions under the conditions we are considering in EHL.

In the next chapter, we will investigate a static system of QDs dispersed within some lubricants for temperature/pressure calibration purposes. Moreover, as emphasized above, the influence of the eventual parasitic parameters will be examined. In chapter 4, we will get through dynamic studies using a rheometer in order to (i) investigate the influence that the probes could have on the behaviour of the lubricants and (ii) examine in which extent the flow of the solvent and the dynamic-induced constraints (shear stress) could alter the intermolecular-interaction channels of energy dissipation and subsequently the emission of the QDs.

III. Static study – Temperature and pressure calibrations

III.1. Introduction

In the two previous chapters, a list of parameters has been identified through the comparison between (i) the conditions imposed by EHD contacts and (ii) the factors susceptible of modifying the emission of the QDs. It is possible to classify these parameters into two groups. The first group, that we will term as *dimension-related parameters*, include all those capable of changing (i) the bulk properties of the QDs related to their crystalline structure (symbolized by $V_{Crystal}$) or (ii) the radius r of the QDs. Temperature and pressure are the most important dimension-related parameters encountered in EHD contacts. The second group, that we will term as *interaction-related parameters*, include again the temperature and the pressure, but also other parameters such as the concentration of the QDs, the thickness of the light pass through the sample and the viscosity and the polarity of the solvent. These parameters are capable of affecting the interaction between the QDs themselves, and the interactions between the QDs and the solvent molecules.

In this chapter, some results on the calibration of the CdSe/CdS/ZnS QDs response to temperature and pressure variations under static conditions will be presented. A particular attention will be paid to the interaction-related effects. More precisely, the following questions will be addressed:

- Is the response of the CdSe/CdS/ZnS QDs in agreement with the *dimension-related effects*?
- Is the influence of the *interaction-related parameters* significant? If yes, can these parasitic effects be minimized or even suppressed?

The reason of qualifying the interaction-related effects as parasitic is that they may invalidate the *T/p* calibration curves established within a given lubricant, when the QDs are dispersed in another lubricant or when they pass through an EHD contact. Temperature and pressure may alter the response of the QDs through their influence on intermolecular interactions. At first glance, one may think that this latter effect could enhance the sensitivity of the QDs to temperature or pressure variations. It is however not desirable since its magnitude may differ from one lubricant to another. The viscosity and its *T/p* dependence can vary considerably from one lubricant to another, and it is affected by the operating conditions. The influence of the viscosity on the diffusion of the QDs and thus the interaction between them, may result in a "deformed" emission spectrum and a different *T/p* sensitivity. The same remark can be made on the polarity effect since it depends on the rotational diffusion of the solvent molecules around the QDs. We should emphasize however that most lubricants and those considered in our work are not polar. Therefore, polarity-induced variations are *a priori* negligible. Polarity effect has, nevertheless, to be borne into mind because (i) laser excitation may polarize the solvent to some extent, and (ii) polar lubricants or additives are used in some applications. For all these reasons, we should verify if some corrections are needed to be applied to the measurements in order to isolate the dimension-related variations induced by temperature and pressure.

III.2. Methodology

The tests will be presented from more simple to more complex situations, namely on the influence of:

- The QDs concentration on the emission spectrum at ambient temperature and pressure;
- The QDs concentration on the temperature sensitivity at ambient pressure;
- The temperature, the nature of the solvent and the QDs concentration on the pressure sensitivity.

The most important test is the last one since it allows the calibration of the QDs response to *T/p* variations. The other tests were performed in order to verify the existence and evaluate the influence of interaction-related parameters. The conditions are summarized in Table III.1. For the first test, a stock solution with 10 mg/mL of CdSe/CdS/ZnS QDs in squalane was used to prepare serial dilutions. The emission spectra of these samples were recorded at ambient temperature and pressure. In the second test, some of the previous dilutions were used to calibrate the response of the QDs to temperature variations. Finally, pressure calibrations were conducted at three different temperatures, in two solvents and with two QDs concentrations. The description of the different experimental apparatus and the rheological properties of the lubricants are found in appendices B and C, respectively.

A particular attention was paid to ensure a constant film thickness in a given experimental apparatus (as we will see in the following paragraphs on the three series of tests). This is actually necessary since, as explained in the previous chapter, film thickness can affect the radiative energy transfer between QDs and therefore their emission spectrum.

	Parameters				
Test on:	Concentration of the QDs (mg/mL)	Nature of the solvent	Temperature (K)	Pressure (MPa)	Film thickness (mm)
Emission spectrum	10 – 0.016	Squalane	298	0.1	~ 1
Temperature sensitivity	0.5 – 0.063	Squalane	298 – 373	0.1	~ 1
Pressure sensitivity	5	Squalane	298, 323, 373	0.1 – 1400	≤ 0.2
		Squalane (30 vol%) + Cyclopentane (70 vol%)	298		
	0.125	Squalane	298		

Table III.1. Summary of the conditions in the different static tests on CdSe/CdS/ZnS QDs solutions.

As explained in the previous chapter, only two characteristics of the PL can be used for *T/p* measurements. The first is the energy at the maximum emission (which corresponds to the mean bandgap energy of the QDs assembly), and the second is the width of the emission spectrum (which represents the distribution of the bandgap energy and the associated vibrational levels)[*]. It should be noted that due to the rich information contained in the width of emission spectra, the interpretation of this parameter is more difficult[†]. The analysis of the emission width is therefore beyond the scope of this first study, and the discussion will concentrate on the energy at the maximum emission.

The spectral resolution of the spectrometers used in this study is of 0.20 meV/pixel or 1.06 meV/pixel, as explained in Appendix C.II. Using a fitting function improves the precision in determining the emission energy. A Gaussian function (Equation (II.49)) was used to extract the characteristics of the spectra. The error associated to the estimation of the mean emission energy with this function was actually found to vary from 0.1 to 0.2 meV. However, the uncertainty in determining the emission energy can depend on other known or unknown random physical parameters. Therefore, the

[*] As explained in the previous chapter, the emission intensity is not adapted since it depends on film thickness and excitation power.

[†] We will return briefly to the complexity of the analysis of the emission spectrum at the end of this chapter.

uncertainty was evaluated statistically in the different tests. More details on the evaluation of the uncertainty of the emission energy will be given in the corresponding paragraphs.

III.3. Experimental results and general analysis

III.3.1. Concentration effect on emission energy*

Measurements were conducted in a sample holder made of aluminum, presented in Appendix C.III. Using this configuration, the solution forms a capillary bridge between the sample holder and the cover-glass plate above, ensuring a constant film thickness of about 1 mm. For each sample, the objective was focused in the middle of the capillary bridge, and measurements were made at four positions and repeated twice at each position. These different measurements (8 for each concentration) were used to estimate the mean emission energy of the QDs and the standard deviation represented in Figure III.1.

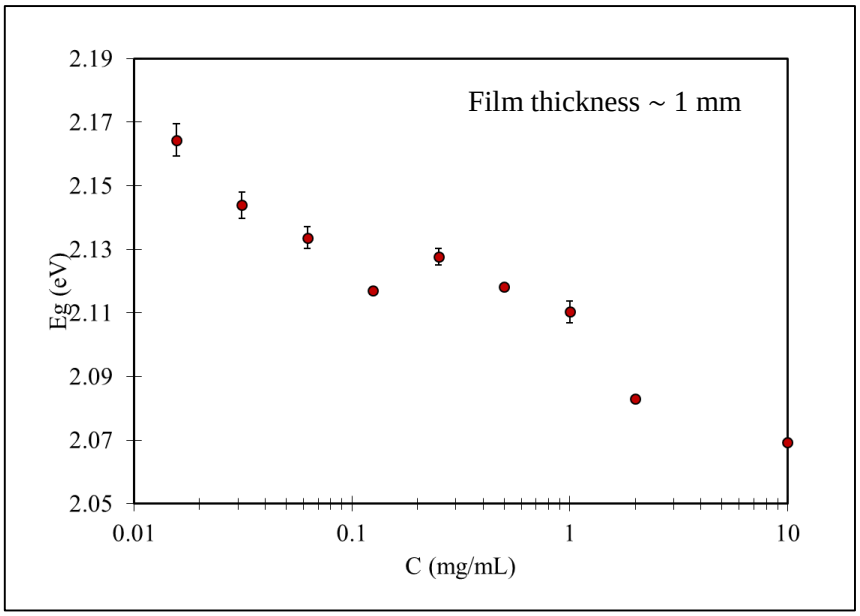

Figure III.1. Emission energy of CdSe/CdS/ZnS QDs dispersed in squalane as a function of the concentration. The measurements were made at ambient temperature and pressure.

It can be noticed that:

- The mean value of emission energy is equal to 2.12 eV;
- The emission energy decreases globally with increasing concentration;

The emission energy of the bulk CdSe E_g^B at ambient temperature and pressure is equal to 1.73 eV [152,153]. The difference between this latter value and the mean emission energy arises from the quantum contribution E_g^Q to the bandgap energy that becomes significant at the nanoscale ($E_g = E_g^B + E_g^Q$). The Effective Mass Approximation (EMA) can be applied to compute the mean size of the QDs yielding such a shift in emission energy. When this approximation is applied, with the values of the different constants reported in Table III.2, a radius r = 2.6 nm (~ 5.2 nm diameter) is obtained.

* For simplicity, the term *emission energy* will be used to denote the *energy at maximum emission*.

$E_g^{B\ (*)}$	ħ (J.s)	e (C)	m_e (kg)	m_e*	m_h*	ε_0 (F/m)	ε_r
1.73	1.0546×10^{-34}	1.602×10^{-19}	9.1×10^{-31}	0.13	0.45	8.854×10^{-12}	4.6

(*) at ambient T and p

Table III.2. The values of the constants used in the EMA. The properties of CdSe molecules (E_g^B, m_e, m_h*, ε_r) are from* [152,153].

This value is larger than the 2 nm radius expected from the TEM measurements ((Figure II.12 (c)), which gives a mean diameter of 6 nm corresponding to a CdSe core of 4 nm in diameter (assuming that the global CdS and ZnS shell have a nominal thickness of 1 nm). The difference comes mainly from wavefunction extension of the exciton in the shell which was not taken into account[151].

The variation of emission energy with the concentration and thus the number of QDs is indicative of an interaction between them. As we will see, excitation energy can transfer, either radiatively or nonradiatively, from smaller QDs (of higher bandgap energy) to larger ones (of lower bandgap energy). Consequently, in very high concentrations, only the larger QDs emission (of lower energy) is detected, while in highly diluted solutions, the emission from all the QDs, whatever their size, is observed. The emission spectrum of concentrated solutions is thus shifted toward lower energies compared to the emission of diluted ones.

III.3.2. Temperature sensitivity

The results presented in the previous paragraph demonstrate the necessity of considering the influence of QDs concentration in calibration measurements. For this reason, several concentrations were studied to calibrate the response of the QDs to temperature variations. Low concentrations ($C \leq 0.5$ *mg/mL*) were used in order to reduce as much as possible the interaction-related effects.

Measurements were conducted also in the sample holder presented in Appendix C.III. More details about the coupling of the sample to the optical system (microscope and spectrometer) and the heating system (voltage source) are presented in Appendix C.IV. Four emission spectra were recorded at different positions in the middle of the capillary bridge. These measurements were used to estimate the mean emission energy and the standard deviation around the mean value as displayed in Figure III.2. Due to the high boiling point of squalane (623 K at ambient pressure), it cannot evaporate in the range of temperature considered here (298 – 373 K). Even with some small evaporation, the formation of the capillarity bridge ensures a constant film thickness.

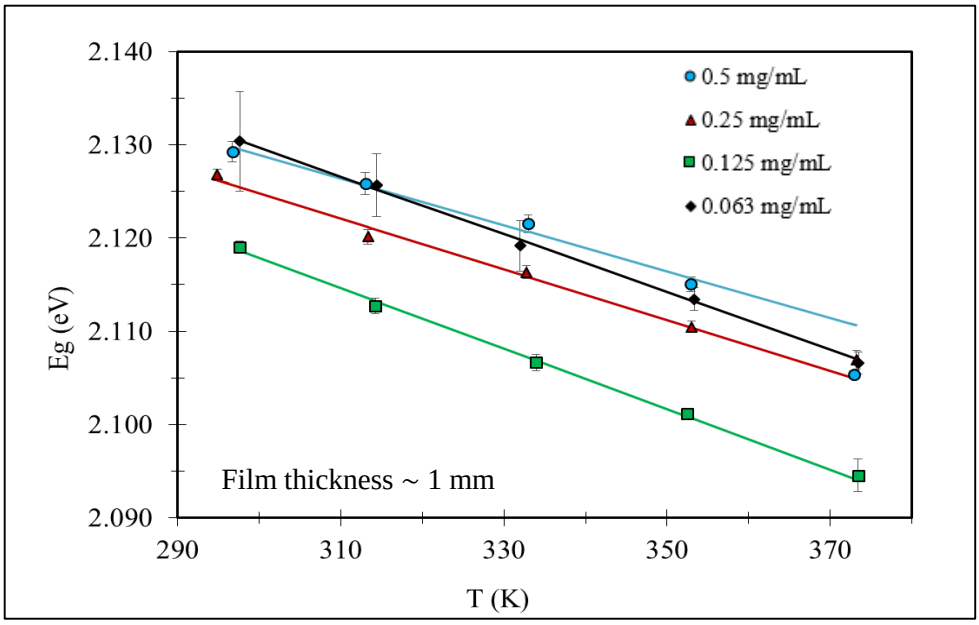

Figure III.2. Temperature variation of the emission of CdSe/CdS/ZnS QDs dispersed in squalane for different concentrations.

One can notice a decrease in emission energy with increasing temperature for all the concentrations. This decrease is compatible with the temperature dependence of both contributions to emission energy: the bulk contribution (Varshni law) and the quantum contribution (Effective Mass Approximation).

As it can be observed, this decrease obey a linear law for the lower concentrations and deviates from it at the higher concentration (0.5 mg/ml). The calibration curves shown in Figure III.2 were then obtained by fitting the experimental data with linear expressions between 293 K and 353 K. The values are reported in Table III.3.

Concentration (mg/mL)	Temperature sensitivity (meV/K)
0.5	-0.25 ± 0.01
0.25	-0.27 ± 0.01
0.125	-0.32 ± 0.01
0.063	-0.31 ± 0.04

Table III.3. Values of temperature sensitivity of CdSe/CdS/ZnS QDs obtained at different concentrations.

One can notice an increasing sensitivity with decreasing concentration. This dependence on concentration can be explained by the fact that (i) the contribution of the smaller QDs decreases with increasing concentration (due to the radiative energy transfer from smaller to bigger QDs) and that (ii) smaller QDs are more sensitive to dimension-related effects than bigger ones (as explained in the previous chapter).

Nevertheless, the nonlinearity obtained at the highest concentration (0.5 mg/mL) is not explained considering only radiative energy transfer. One explanation could be the influence of QDs diffusion. Unlike the concentration which is practically unchanged with temperature, the influence of the

diffusion is not trivial and has to be regarded with caution. Indeed, the temperature rise and the resulting viscosity drop both contribute in enhancing the diffusion of the QDs (see Equation (II.18)). Furthermore, the diffusion enhances the movement of the QDs relative to each other and may favor in this way the energy transfer from smaller to bigger QDs. Therefore, emission energy decreases due to the progressive increase of diffusion with temperature (in addition to the energy decrease induced by the thermal expansion of the QDs). The possible role of this effect will be discussed in section III.4. As a temperature increase corresponds to a viscosity reduction when considering diffusion, a series of experiments have been conducted on suspension of QDs in different viscosities liquids obtained from squalane and cyclopentane mixtures. In order to observe possible diffusion effects, the experiment was conducted for high concentration (5 mg/ml) and for important excitation volume (fluorimeter measurements using a cuvette, see Appendix D). The results presented in Appendix D, clearly show that temperature sensitivity is increased when viscosity is reduced.

The value of temperature sensitivity in the most diluted solutions (*C = 0.125* and *C = 0.063*) stabilizes since the interaction-related effects tend gradually to zero with decreasing concentration. It is only in such a situation that the measured temperature sensitivity can be compared with dimension-related prediction:

$$E_g(T) = \underbrace{E_g^{B,0} - \frac{\alpha_1 T^2}{(T+\beta_1)}}_{\text{Varshni law}} + \underbrace{\frac{\gamma}{r_0^2}\left(1+\alpha_T(T-T_0)\right)^{-2/3}}_{\text{Quantum confinement}} - \underbrace{\frac{\nu}{r_0}\left(1+\alpha_T T(T-T_0)\right)^{-1/3}}_{\text{Colomb interaction}} \qquad \textit{(III.1)}$$

Bulk contribution

Quantum contribution
(Effective Mass Approximation)

Where $E_g^{B,0} = E_g^{B}(T = 0K, p = 0.1\ MPa)$.

Equation (III.1) was used to fit the experimental data obtained for the concentrations *C = 0.125* and *0.063 mg/mL*. The values α_T *and* $E_g^{B,0}$ where fixed to those found for bulk CdSe*, *i.e.* 7.4×10^{-6} K^{-1} [154] and 1.84 eV [152,153], respectively. The other parameters were free to vary for the fitting process. The best regression values are listed in Table III.4.

Concentration (mg/mL)	r_0 (nm)	α_1 (meV/K)	β_1 (K)
0.125	2.77	0.36	180
0.063	2.73	0.35	179

Table III.4. Regression parameters for temperature sensitivity of CdSe/CdS/ZnS QDs dispersed in squalane using dimension-related predictions.

The values of α_1 and β_1 in Table III.4 are consistent with (i) the values of α_1 *= 0.28-0.41 meV/K* and θ_D *= 181-315 K* † known in literature[155] (ii) the values α_1 *= (0.32±0.02) meV/K* and β_1 *= 220±30 K* reported by Valerini *et al.*[138] for colloidal CdSe/ZnS QDs of 2.5 nm radius embedded in an inert polystyrene matrix (for the range of temperatures between 45 and 295 K).

* Bulk values is assumed because of the lack of reliable data for nanosized CdSe structures.
† The Debye temperature θ_D is used as a reference, since according to Varshni analysis, the value of β_1 is close to θ_D.

It should be noted that when the bulk coefficient of thermal expansion used in the regression procedure, it yields negligible size variations. Therefore, the bulk contribution to the temperature sensitivity is dominant under this assumption[*].

As CdSe QDs may degrade for temperature higher than 100°C (*a fortiori* under illumination) the hysteresis with temperature variations was examined in a fluorimeter using quartz cuvette (see Appendix D) and a sample of 5 mg/mL of QDs dispersed in a mixture of squalane (83 vol%) and cyclopentane (17 vol%). Similar tests were performed in an optical rheometer (described in Appendix C.VI), using a sample of 0.063 mg/mL of QDs dispersed in squalane. The optical rheometer was used because of the better temperature regulation ensured by a Peltier devices (yielding a precision of 0.03 °C). In addition, the rheometer was rotating at a very low velocity (1 revolution per minute) throughout the tests (except for the measurement of the PL) in order to enhance the temperature regulation. The values of temperature sensitivities are reported in Table III.5:

Operation	S_T (meV/K)	
	Fluorimeter	Rheometer
Heating (298 → 373 K)	-0.31 ± 0.01	-0.35 ± 0.01
Cooling (373 → 298 K	-0.30 ± 0.01	-0.35 ± 0.01
Heating 2 (298 → 373 K)	-0.29 ± 0.01	-0.32 ± 0.01

Table III.5. Values of temperature sensitivity of CdSe/CdS/ZnS QDs obtained in a fluorimeter (using a sample of 5 mg/mL of QDs dispersed in a mixture of squalane (83 vol%) + cyclopentane (17 vol%), and an optical rheometer (using a sample of 0.063 mg/mL of QDs dispersed in squalane).

III.3.3. Pressure sensitivity

The results presented in the previous paragraphs demonstrate the necessity of considering the influence of both the concentration and the diffusion of the QDs for calibration tests. For comparison purposes and in order to elucidate the contribution of interaction-related effects, the pressure sensitivity of the QDs was measured at two different concentrations, two different natures of lubricants, and three different temperatures.

The diamond anvil cell used in this study is presented in Appendix C.V. In all the tests, the sample was confined in a hole (500 μm in diameter) of a nickel gasket, itself compressed between two diamonds. The initial thickness of all the samples (before compressing) was equal to the thickness of the gasket, *i.e.* 0.2 mm. Using such a closed system impedes the evaporation of the liquid during the tests. Here again, the evaporation was not a concern for squalane since its boiling point is of 623 K at ambient pressure, and the maximum temperature tested was of 373 K. The boiling point of cyclopentane is however much lower (322.3 K). For this reason, the mixed solution of squalane and cyclopentane, as well as the pressure cell were cooled before depositing the solution and closing the cell.

The uncertainty of the emission energy of the QDs in the pressure cell was evaluated statistically. Emission spectra were measured at 10 different x,y and z positions within the squalane + cyclopentane mixture at ambient temperature and at 1280 MPa. The standard deviation of these

[*] According to some results in literature, the QDs have coefficients of thermal expansion and compressibility larger than those of the corresponding bulk materials. This implies that the quantum contribution is underestimated when bulk coefficients are assumed.

measurements was applied to all the tests. This uncertainty is related to the possible small deviations from hydrostatic pressure throughout the sample.

The results, plotted in Figure III.3, are globally in agreement with dimension-related effects which predict that emission energy increases with pressure and decreases with temperature.

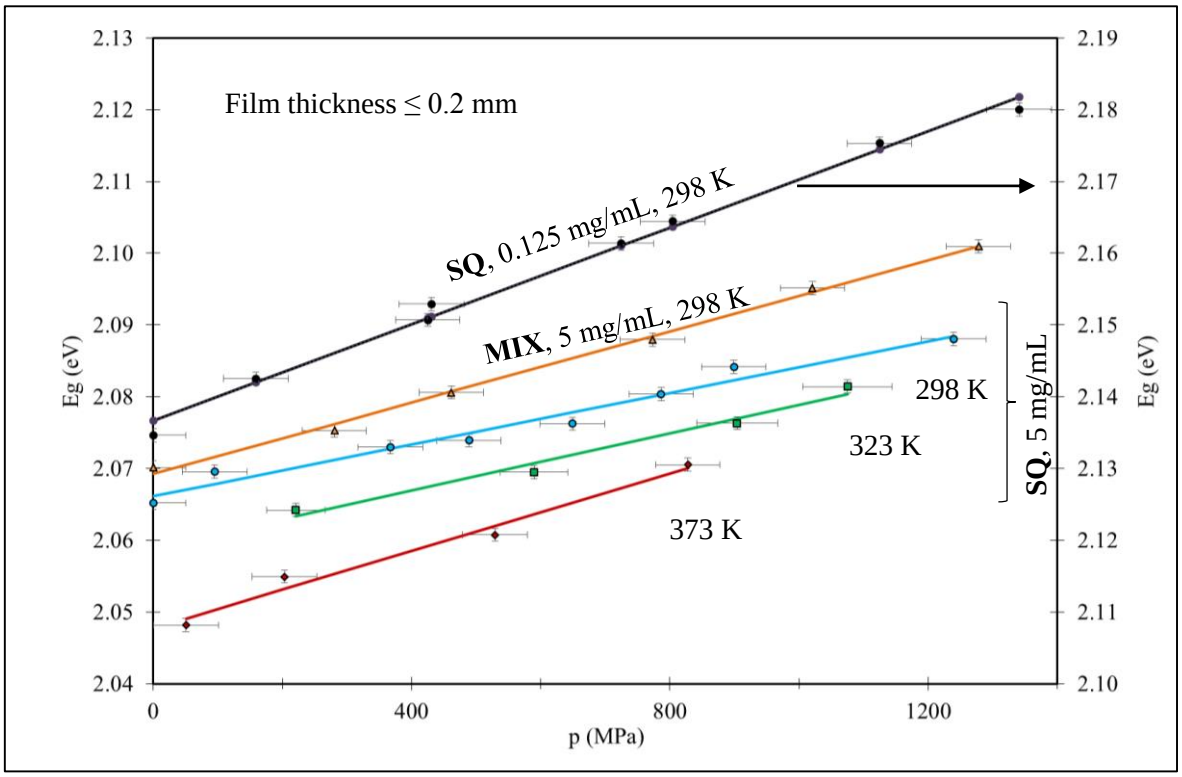

Figure III.3. Pressure sensitivity of CdSe/CdS/ZnS QDs emission energy obtained for different temperatures, solvent natures and QDs concentrations. SQ: Squalane; MIX: Mixture of squalane (30 vol%) and cyclopentane (70 vol%). Film thickness ≤ 0.2 mm.

For a more quantitative analysis, emission energy variation with pressure was fitted using linear approximation. The values of the pressure sensitivity are listed in Table III.6.

Concentration (mg/mL)	Solvent	Temperature (K)	S_p (meV/MPa)
5	Squalane	298	0.018 ± 0.001
		323	0.020 ± 0.002
		373	0.027 ± 0.003
5	Mixture	298	0.025 ± 0.001
0.125	Squalane	298	0.034 ± 0.001

Table III.6. Sensitivity of the QDs to pressure variations obtained at different concentrations, solvents and temperatures.

The reported values in literature of pressure sensitivity for bulk or CdSe QDs vary between 0.027 and 0.058 meV/MPa[123,156,157], which is consistent with our results. Nevertheless, the reported values depend on whether photoluminescence or absorption measurements are used, and also on the

crystalline structure (hexagonal or zinc-blend) formed by CdSe. Consequently, comparison with literature absolute values cannot be considered as a decisive criterion. Then, in the following, our discussion will consider mainly the dependence of the pressure sensitivity on the temperature, the solvent nature and the QDs concentration.

One can notice that the pressure sensitivity S_p (i) increases with decreasing concentration, (ii) depends upon the nature of the lubricant, and (iii) increases with increasing temperature. Such noticeable dispersion in pressure sensitivity S_p cannot be explained purely and simply by dimension-related effects. The influence of the concentration on S_p is similar to its influence on S_T, and can be explained by the difference of pressure sensitivity between smaller and bigger QDs. When the concentration is lowered, the interaction (mainly radiative energy transfer) is minimized and the smaller QDs, which are more sensitive to *T/p* variations, regain their contribution in the emission spectrum.

Looking now at the different samples with *C = 5 mg/mL*, different observations indicate an important role of viscosity in the value of pressure sensitivity. In particular:

- The temperature-induced viscosity drop is accompanied by an increased pressure sensitivity;
- At ambient temperature, the QDs exhibit a higher pressure sensitivity in the mixture, given that the latter has a smaller viscosity compared to squalane;
- The pressure sensitivity in squalane approaches, when its temperature is increased to 373 K, the one obtained for the mixture at ambient temperature.

In order to confirm further the influence of viscosity on pressure sensitivity, viscosity values were estimated for the two solvents under the different *T/p* conditions tested in calibration measurements. The rheological laws used for these computations are presented in Appendix B. The results are displayed in Figure III.4.

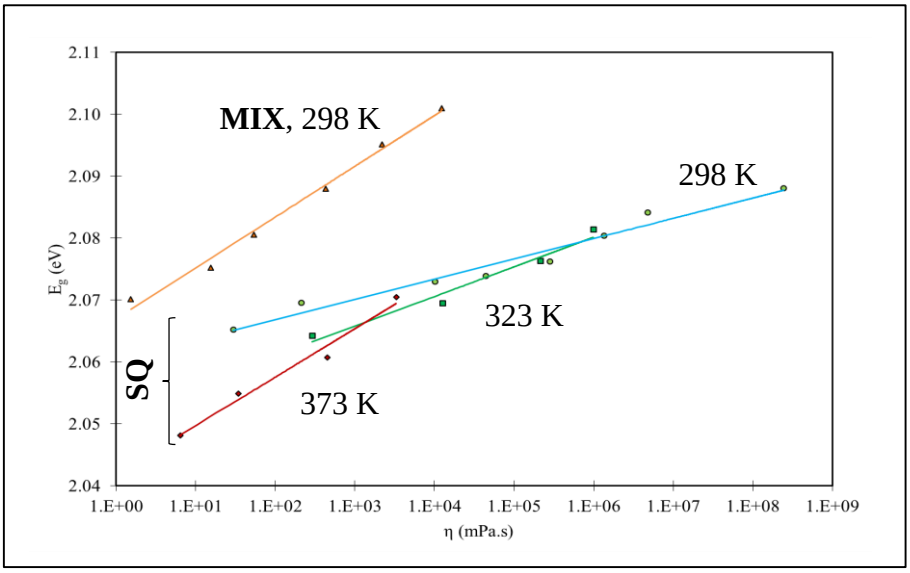

Figure III.4. Variation of the emission energy of CdSe/CdS/ZnS QDs (C = 5 mg/mL) as a function of viscosity at different solvent temperatures. SQ: Squalane; MIX: Mixture of squalane (30 vol%) and cyclopentane (70 vol%).

It can be clearly seen that: (i) squalane at 373 K and the mixture at ambient temperature cover similar ranges of viscosity and yield comparable variations in terms of emission energy, and (ii) squalane viscosity decreases with increasing temperature, and yields smaller variation in terms of emission

energy with increasing viscosity. The analysis of the diffusion influence on pressure sensitivity is rather complex due to its dependence on the temperature and the viscosity of the solvent, and the dependence of the viscosity, in turn, on the temperature and the pressure (Equation (II.19)). A more detailed treatment of concentration and diffusion effect will be provided in paragraph III.4.

The predictions based on dimension-related effects apply only when the interaction between QDs is insignificant – in highly diluted solutions for example. Temperature- and pressure- induced variations are independent[158], and the variations with respect to the pressure are linear. Therefore, we can write:

$$E_g^B(T,p) = E_g^B(T, p = 0.1MPa) + \alpha_2 p \qquad (III.2)$$

$$E_g^B(T,p) = E_g^B(T = 0K, p) - \frac{\alpha_1 T^2}{(T+\beta_1)} \qquad (III.3)$$

Hence:

$$E_g^B(T,p) = E_g^{B,\circ} - \frac{\alpha_1 T^2}{(T+\beta_1)} + \alpha_2 p \qquad (III.4)$$

with $E_g^{B,\circ} = E_g^B(T=0K, p=0.1MPa)$. If we assume a constant compressibility ($\alpha_p(T,p) = \alpha_p$), the full expression of the bandgap energy becomes:

$$E_g(T,p) = E_g^{B,0} - \frac{\alpha_1 T^2}{(T+\beta_1)} + \alpha_2 p + \left((1-\alpha_p\Delta p)(1+\alpha_T\Delta T)\right)^{-2/3}\frac{\gamma}{r_0^2} - \left((1-\alpha_p\Delta p)(1+\alpha_T\Delta T)\right)^{-1/3}\frac{\nu}{r_0} \qquad (III.5)$$

Equation (III.5) was used to measure the sensitivity of the QDs to pressure and/or temperature variations for the sample with *C = 0.125 mg/mL*. The values α_T, α_p *and* $E_g^{B,0}$ where fixed to those found for bulk CdSe*, *i.e.* 7.4×10^{-6} K^{-1} [154], 0.018 GPa^{-1} [159] and 1.84 eV [152], respectively. The other parameters were varied to yield the best regression for the experimental data. The results are reported in Table III.7.

r_0 (nm)	α_1 (meV/K)	β_1 (K)	α_2 (meV/MPa)
2.74	0.31	177	0.028

Table III.7. Regression parameters for the pressure sensitivity of CdSe/CdS/ZnS QDs dispersed in squalane using dimension-related predictions.

By comparing with the values obtained from temperature calibration with the same concentration (Table III.4), one can see the close proximity for the values of r_0 in the two measurements. The parameters α_1 and β_1 are also very close, and the *slight* difference may be attributed to the fact that only one temperature was used in the fitting process. It should be noted that the bulk compressibility

* Bulk values are assumed because of the lack of reliable data for nanosized CdSe structures.

coefficient is used in the regression procedure yields little size variations. Therefore, the bulk contribution to the pressure sensitivity is dominant under this assumption*.

In order to investigate the hysteresis of the QDs response with pressure variations, a cycle of pressurizing (0.1 → 1280 MPa), depressurizing (1280 MPa → 0.1 MPa) and a second pressurizing (0.1 MPa → 1209 MPa) was performed on the same sample of QDs dispersed in the mixture of squalane and cyclopentane. The values of pressure sensitivity and the emission energy were found to be stable.

Operation	Eg at ambient pressure (eV)	Eg at the highest pressure (eV)	S_p (meV/MPa)
Pressurizing 1	2.0701	2.1010	0.025 ± 0.001
Depressurizing 1	2.0679	=	0.026 ± 0.001
Pressurizing 2	=	2.0984	0.025 ± 0.001

Table III.8.Values of pressure sensitivity of CdSe/CdS/ZnS QDs dispersed in the mixture of squalane (30 vol%) and cyclopentane (%70) with a concentration of 5 mg/mL. These sensitivities were obtained in a series of pressurizing and depressurizing.

A negligible hysteresis of the QDs for temperature and pressure cycling, together with the linear dependence of the CdSe/CdS/ZnS QDs response to temperature and pressure variations demonstrates their potential for the measurement of these parameters in combination with another family of QDs.

III.4. Analysis of interaction-related effects

In the next paragraphs, a more quantitative analysis of the influence of interaction-related parameters (concentration and diffusion of the QDs) will be presented. To do so, we will:

- Present the consequences of the different possible mechanisms of interaction.
- Identify the influence of the concentration and the diffusion of the QDs on the efficiency of these mechanisms.
- Evaluate the likelihood of these mechanisms by computing the distance distribution between the QDs and the magnitude of diffusion.
- Propose a model accounting for interaction-related effects.

These different points will be discussed in two paragraphs. The first one will cover the three first points, and the last one will be discussed in the second paragraph.

* According to some results in literature, the QDs have coefficients of thermal expansion and the compression larger than those of the corresponding bulk materials. This implies that the quantum contribution is underestimated when bulk coefficients are assumed.

III.4.1. Identification of the mechanisms of interaction

III.4.1.1. Consequences of energy transfer – Concentration and diffusion effect*

Radiative energy transfer

The occurrence of radiative energy transfer in a system of QDs has already been reported in literature[105,160–162]. As a result of the inequality $h\nu_2 < h\nu_1 < h\nu_0$ required for radiative energy transfer (see Chapter II), the excitation energy transfers from a smaller (of larger energy) to bigger QDs (of lower energy). Such energy transfer can occur even in monodisperse systems, such as the one considered in our study, owing to the random size distribution around the mean value (see Figure II.12 (c)).

Naturally when such a transfer occurs, the emission of the smaller QDs quenches whereas that of the bigger ones increases. Consequently, the overall emission spectrum (of the system of the QDs) shifts towards lower energies. In addition, it was shown in the previous chapter that the smaller QDs are more sensitive to size, temperature and pressure variations than the bigger ones. Such difference signifies that interacting QDs exhibit lower sensitivity.

The influence of the concentration on the energy transfer efficiency can be explained by the density of the QDs found at high distances. This can be seen by the presence of the molar concentration of the acceptors c_A in the expression of fraction X of photons emitted by the donors and absorbed by the acceptors (Equation (II.9) or (II.10)).

Förster energy transfer

The other mechanism that seems to be plausible to explain the interaction between the QDs is FRET. This mechanism needs (i) a vibrational energy level in the acceptor resonant with the emission of the donor, and (ii) a lower electronic energy state in the acceptor capable of trapping the excitation (see Figure II.6). These requirements imply again, as it was the case in radiative energy transfer, the migration of the energy from smaller to bigger QDs (owing to their electronic structure modulated by the quantum confinement effect[163]). Kagan *et al.* were the first to report such energy transfers in both polydisperse and monodisperse systems of QDs[163,164]. In the case of CdSe-based QDs, theoretical values between 5-6 nm and experimental ones between 8-9 nm were reported[165] for the Förster distance R_0 (defined as the distance yielding a FRET efficiency of 50 %).

The implications of FRET on the emission energy and the sensitivity to size variations are similar to those indicated in the case of radiative energy transfer, because both processes imply the deactivation of smaller QDs in favor of larger ones.

The dependence of FRET efficiency on the concentration of the QDs, stems from its dependence on the separation between QDs (Equation (II.13)).

As for diffusion, one may think, at first glance, that it cannot change the interaction between QDs. Indeed, the diffusion of the QDs cannot modify the distance distribution between them (since it brings two QDs closer in the same time it brings two others apart). FRET was found, however, to be

* As we will see from the distribution of distances between neighboring QDs (see paragraph III.4.1.2), electron exchange by Dexter effect is not likely to occur. Therefore, for sake of briefness we will consider here only the radiative and the Förster energy transfer.

enhanced with diffusion in many studies[166,167]. This actually occurs because the closely-spaced pairs (those separated by a distance in the order of Förster distance R_0) are continuously replenished due to the random motion of the QDs, and more and more small QDs are therefore deactivated. This phenomenon is illustrated in Figure III.5 (a) and (b). It can be noted in this figure that when the concentration is increased, R_{mean} becomes close to R_0 and the number of deactivated small QDs (the black circles in Figure III.5) increases. One can also notice that the number of replenished couples rises when diffusion is significant, which implies again the increase of the number of deactivated small QDs.

The analysis of the diffusion-enhanced FRET is a complex problem due to (i) its dynamic nature, (ii) the QDs random size distribution and (iii) the random separation between QDs. The problem can be considered *via* two approaches depending on either the *real distance distribution R, or* the *real Förster distance* R_0 is used:

- The first approach considers that measuring Förster distance in a system of diffusing particles yields an *apparent value* $R_0^* > R_0$ when the real distance distribution between the QDs is assumed for the computations[168–171]. Based on this approach, particles spaced at higher distances than R_0 can interact thanks to their diffusion.
- The second approach considers instead that measuring the distance distribution between diffusing QDs leads to some apparent values $R^* < R$, when the real Förster distance R_0 is assumed[166,172]. The particles can thus interact as they were spaced at lower distances.

The second approach will be considered in the current study. For a given couple of QDs separated at a given distance R, one should examine if diffusion can bring the two QDs sufficiently close for efficient FRET. In other terms, the following inequality has to be satisfied:

$$R_{\min} = R - \left(x^D_{Diffusion} + x^A_{Diffusion} \right) \leq R_0 \qquad \textit{(III.6)}$$

Where $x_{Diffusion}{}^D$ and $x_{Diffusion}{}^A$ are the diffusion of the donor and the acceptor, respectively.

In a system constituted of large number of randomly distributed QDs, the distance R can be substituted by R_{mean} (being the most representative distance and an averaging value for smaller and bigger distances). The distance travelled by the donor and the acceptor during the lifetime of the excited state *via* diffusion can be estimated by the so-called mean free path MFP (see Figure III.6):

$$MFP = \sqrt{6D\tau} \qquad \textit{(III.7)}$$

where τ is the lifetime of the QDs and D is the diffusivity of QDs given by (k_B is being Boltzmann constant):

$$D = \frac{k_B T}{6\pi\eta(T,p)r} \qquad \textit{(III.8)}$$

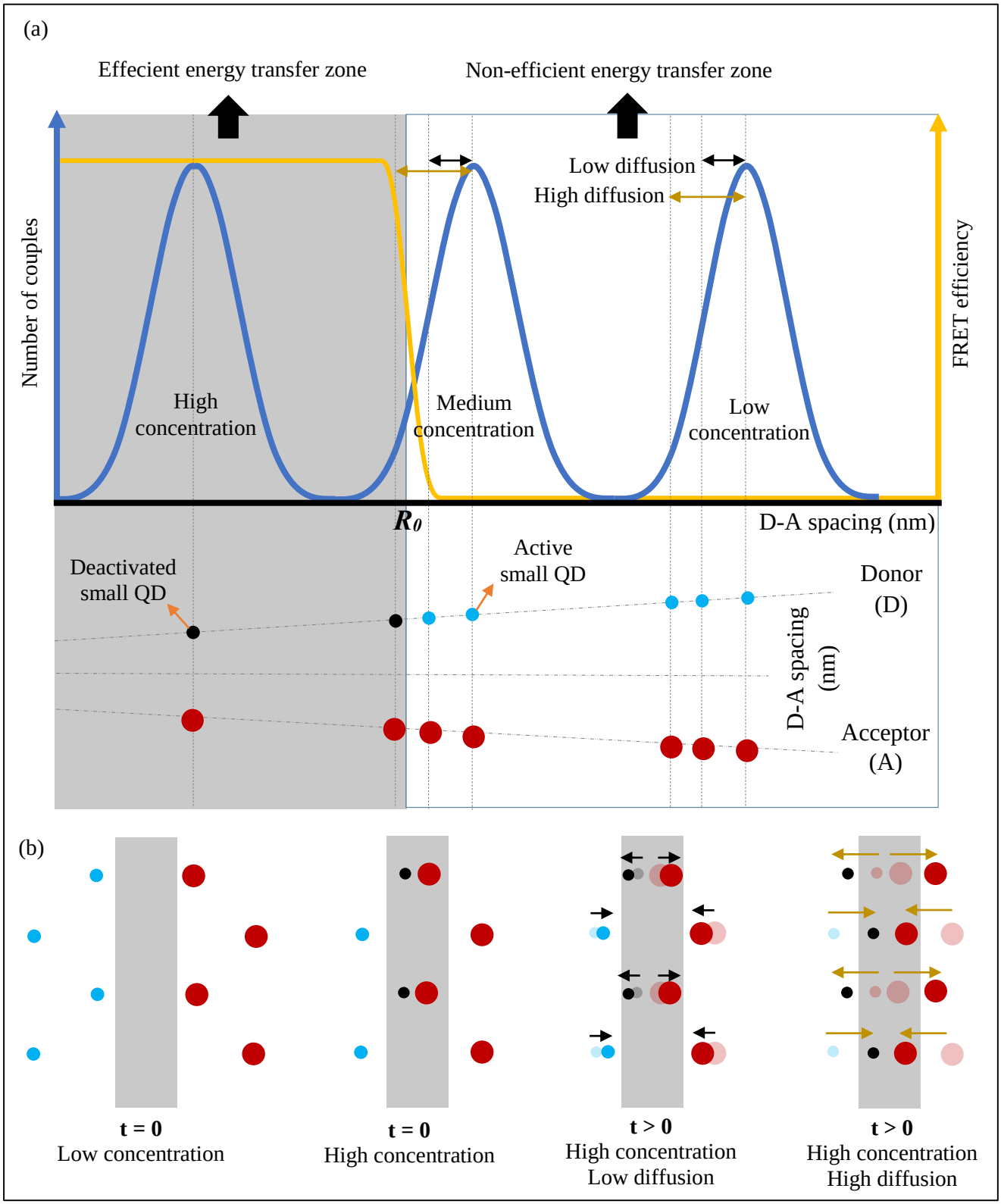

Figure III.5. Influence of the concentration and the diffusion FRET efficiency: (a) FRET efficiency dependence on D-A spacing and diffusion; (b) Special illustration of the different configurations (the grey zone represents donor-acceptor spacings resulting in efficient FRET).

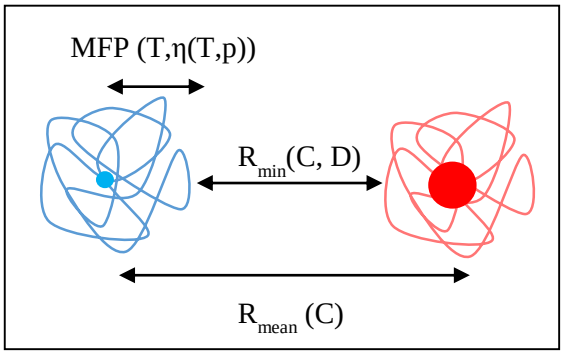

Figure III.6. Notion of the minimum distance between QDs.

Concentration-limited diffusion influence

Although diffusion can enhance the efficiency of energy transfer, this effect is limited by the concentration of the QDs as illustrated in Figure III.7. In the case of FRET, this limitation is described implicitly in the definition of R_{min}. The enhancement of the efficiency of energy transfer can be considerable when $R_{mean} \sim R_0$. The efficiency is almost unaffected by diffusion when $R_{mean} >> R_0$.

Concerning radiative energy transfer, it is unaffected – as mentioned above – by the diffusion of the particles.

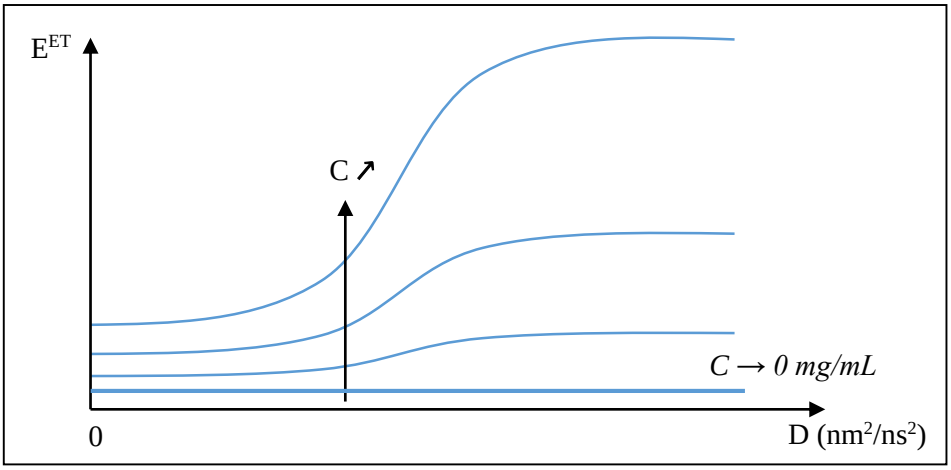

Figure III.7. The concentration-limited diffusion effect.

III.4.1.2. Computation of the distance distribution and the diffusion

Nearest-neighbor distance

A relevant parameter for the analysis of the energy transfer is the distribution of nearest-neighbor distance. For a system of QDs randomly dispersed within a solvent, this distance is described by the distribution *f(R)*, given by[173]:

$$f(R) = \exp\left(\frac{-4\pi R^3 n}{3}\right) 4\pi R^2 n \qquad (III.9)$$

Where *n* denotes the average number of particles per unit volume. The mean distance R_{mean} between nearest-neighbors is simply given by:

$$R_{mean} = \int_0^\infty R\, f(R)\, dR \qquad (III.10)$$

or, after some elementary operations:

$$R_{mean} = \Gamma\left(\frac{4}{3}\right)\left(\frac{4\pi}{3}n\right)^{-1/3} = 0.55396 n^{-1/3} \qquad (III.11)$$

where Γ is the gamma function ($\Gamma(4/3) = 0.892979$). When the average number of QDs per unit volume *n* is substituted with its expression as a function of the mean distance, the distribution *f(R)* becomes:

$$f(R) = 3\Gamma^3\left(\frac{4}{3}\right)\frac{1}{R}\left(\frac{R}{R_{mean}}\right)^3 \exp\left(-\Gamma^3\left(\frac{4}{3}\right)\left(\frac{R}{R_{mean}}\right)^3\right) \qquad (III.12)$$

Figure III.8 shows the distributions *f(R)* for different values of R_{mean}. One can note that when R_{mean} increases, the distribution shifts to higher values of *R*, decays and becomes wider.

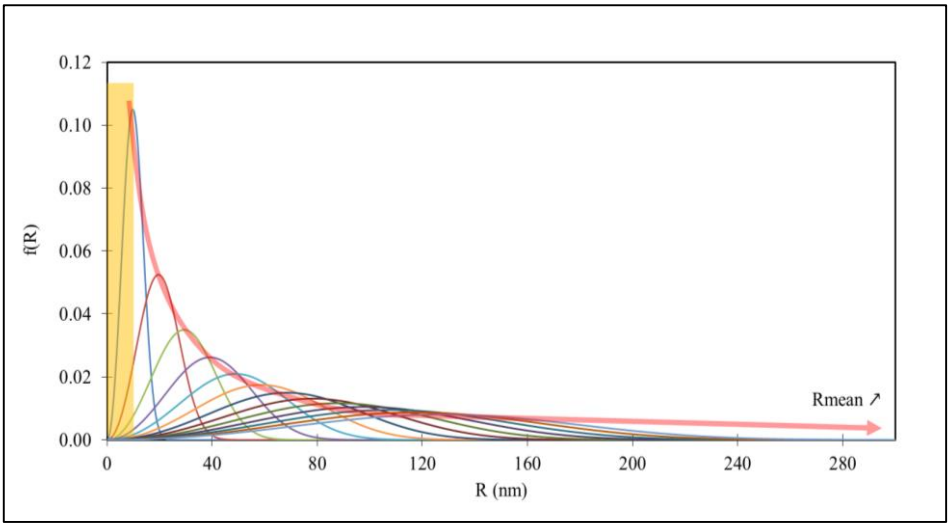

Figure III.8. Distance distribution of the nearest-neighbor f(R) obtained at different mean distances R_{mean}. The yellow zone corresponds to the couples of particles separated at a distance R < 10 nm.

Now in order to estimate the mean distance R_{mean} between CdSe/CdS/ZnS QDs, the expression of the average number of QDs per unit volume *n* has to be written explicitly. It can be written as function of the density ρ_{QDs} mean radius *r*, and the concentration *C* of the QDs:

$$\frac{1}{n} = \left(\frac{\rho_{QDs}}{C} + 1\right)\frac{4\pi}{3}r^3 \qquad (III.13)$$

Therefore, R_{mean} can be written as following:

$$R_{mean} = \Gamma\left(\frac{4}{3}\right)\left(\frac{\rho_{QDs}}{C}+1\right)^{1/3} r \qquad (III.14)$$

Figure III.9 gives the value of R_{mean} with varying concentrations for CdSe/CdS/ZnS QDs of 3 nm radius ($r = r_{CdSe} + e_{CdS} + e_{ZnS}$) and a density ρ_{QDs} *of 4911 mg/mL* (see Appendix E for the estimation of ρ_{QDs}).

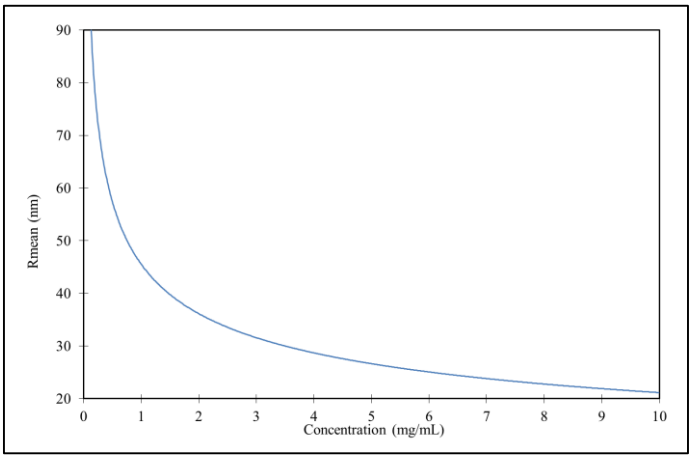

Figure III.9. Mean distance R_{mean} between CdSe/CdS/ZnS QDs obtained at different concentrations at ambient temperature and pressure.

The value of C changes due to the compressibility and the thermal expansion of the solvent*:

$$C(T,p) = \frac{m_{QPs}}{V(T,p)} = \frac{m_{QPs}}{V_0}\frac{V_0}{V(T,p)} = \frac{V_0}{V(T,p)}C_0 \qquad (III.15)$$

Where V_0 and C_0 denote, respectively, the solvent volume and the QDs concentration at ambient temperature (298 K) and pressure (0.1 MPa). The correcting factor $V_0/V(T,p)$ can be computed using the rheological properties of the fluid (the variation of the density with temperature and pressure: see Appendix B). Figure III.10 shows the variation of R_{mean} in the different samples and under the conditions in T/p conditions tested in calibration measurements. One can notice that the variation of the QDs concentration is insignificant.

* The thermal expansion and the compressibility of the QDs have negligible impact on the concentration of the QDs.

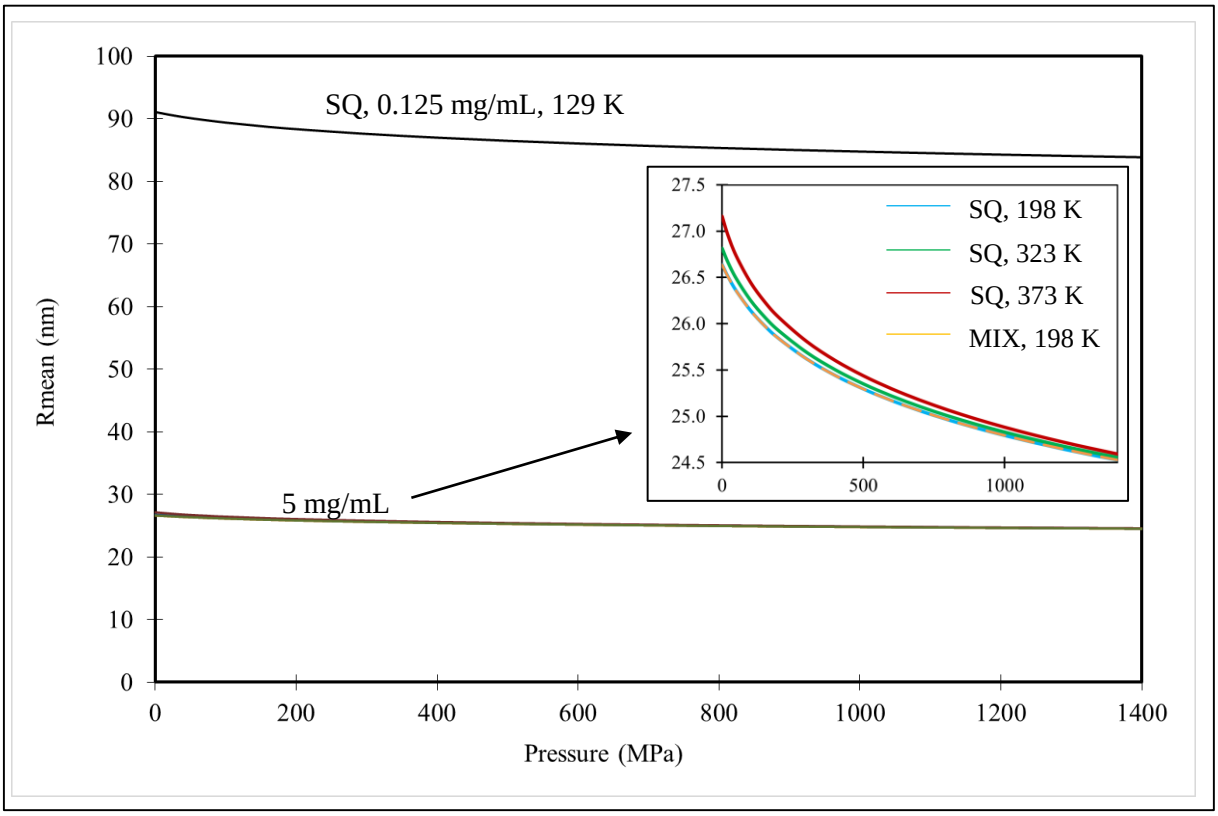

Figure III.10. Variation of the mean distance R_{mean} between CdSe/CdS/ZnS QDs as a function of pressure, at different concentrations and temperatures. SQ: Squalane; MIX: Mixture of squalane (30 vol%) and cyclopentane (70 vol%).

The probability of finding couples of QDs with a spacing $R \leq R_{max}$ can be computed by integrating the distribution over this range of distances:

$$P(R \leq R_{max}) = \int_0^{R_{max}} f(R)\,dR \qquad (III.16)$$

Figure III.11 shows the value of this probability when R_{max} = *10 nm*.

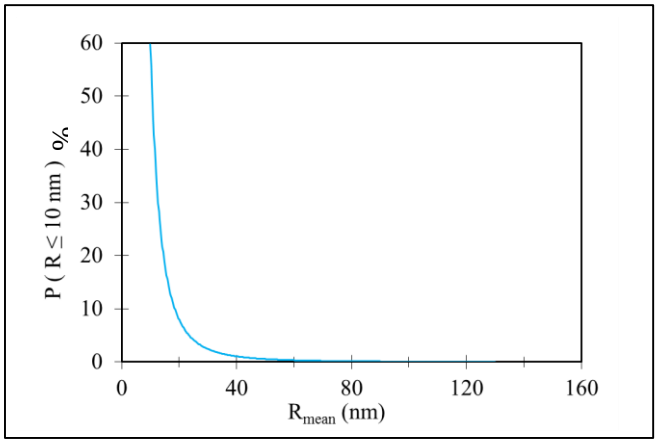

Figure III.11. Probability of finding a nearest-neighbor at $R \leq 10$ nm. This probability shows the population of the QDs couple located at the yellow zone in Figure III.8.

P(R ≤ 10 nm) can gives an idea of the probability of FRET (which is efficient at distances of about 10 nm). One can note that for mean distances larger than 20 nm, this probability is smaller than 10%, and tends quickly to zero. Of course, this estimation is exclusively based on distance distribution considerations, and FRET can be enhanced with the movement of the particles relative to each other (induced by the random diffusion for instance).

The Diffusion and the MFP

The diffusion and the MFP of CdSe/CdS/ZnS QDs are plotted for the samples and conditions tests in the temperature calibrations and the temperature/pressure calibrations in Figure *III.12* (a) and (b), respectively. For the computation of the MFP, the value of the lifetime was fixed at $\tau = 60\ ns$ measured by time-resolved spectroscopy (not shown).

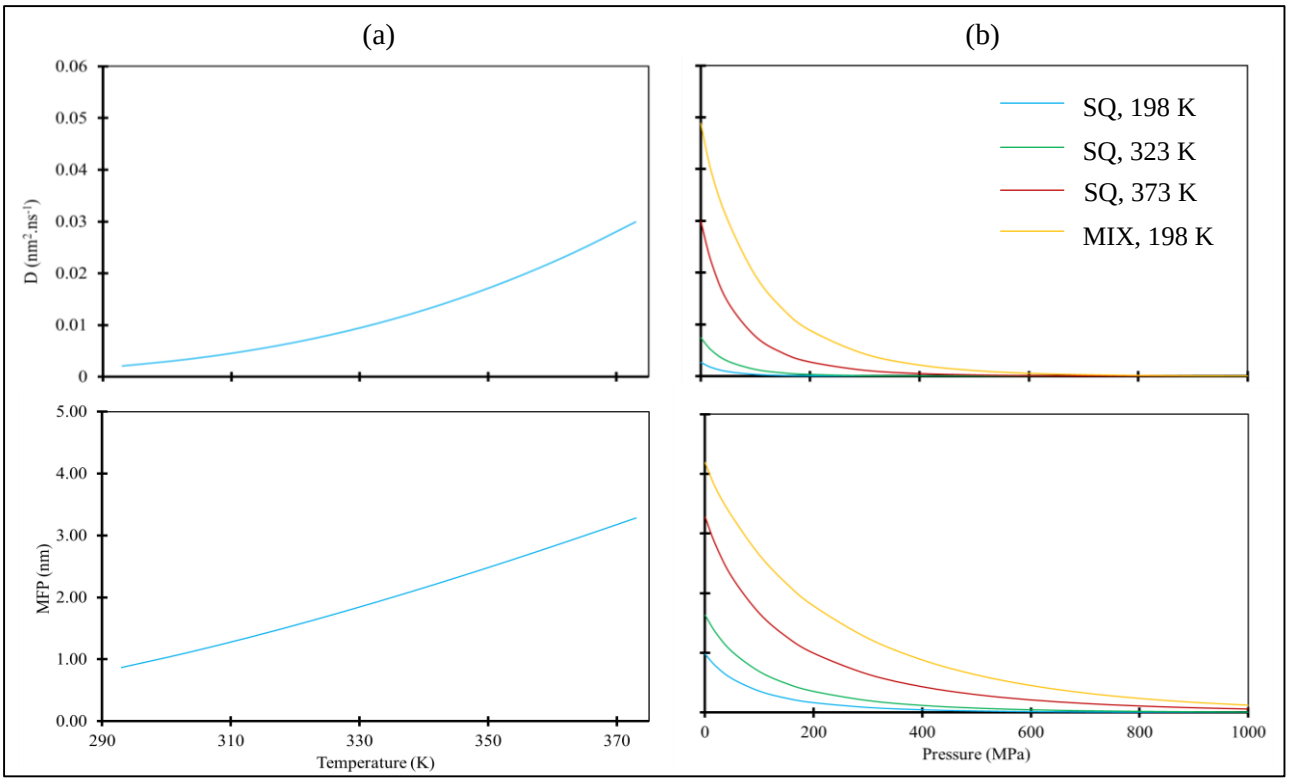

Figure III.12. Variation of the diffusion and the MFP of CdS/CdS/ZnS QDs with (a) temperature and (b) pressure. SQ: Squalane; MIX: Mixture of squalane (30 vol%) and cyclopentane (70 vol%).

III.4.1.3. Which mechanism of interaction?

The influence of the concentration on the emission energy (Figure III.1), the temperature sensitivity (Figure III.2) and the pressure sensitivity (Figure III.3) of the QDs demonstrates incontestably the interaction between them. It is however not trivial to separate the contribution of the different possible mechanisms of energy transfer. Indeed, radiative energy transfer and FRET have similar effects on steady-state measurements. Both mechanisms can lead to (i) an increase of the contribution of the bigger QDs in the emission spectrum, (ii) the shift of the emission spectrum to lower energies and (iii) the decrease of the QDs sensitivity to temperature and pressure variations.

Having recourse to time-resolved measurements can be enlightening. They have been used to distinguish these two mechanisms and to quantify the contribution of each one[105]. Despite the

valuable information that such measurements can bring, their application is not within the scope of our work. It is possible however, based on the calculated distance distributions and the diffusion in the system of the QDs, as well as some findings in literature, to suggest the following assumptions:

First assumption: Concentration effect via reabsorption

Considering exclusively the mean distances between QDs, reabsorption is more likely to occur than FRET. Indeed, the highest concentrations tested in our work yield mean distances is around 27 nm (Figure III.9 and Figure III.10), which is much bigger than the Förster distance R_0 (between 5-10 nm). Reabsorption can thus explain the effect of concentration on the emission energy (Figure III.1), the temperature sensitivity (Figure III.2) and the pressure sensitivity (Figure III.3) of the QDs.

Second assumption: diffusion effect via FRET

The contribution of FRET is more important than when considering exclusively the mean distances between QDs, for the following reasons:

- When considering the nearest-neighbor distance distribution, a proportion of the particles are found to be separated at a distance ≤ 10 nm, as shown in Figure III.11 (see the yellow zone).
- FRET between couples of QDs separated by $R \sim R_0$ can be enhanced by the diffusion of the particles. Therefore, values of probability higher than those shown in Figure III.11 are obtained.

FRET can be further enhanced by radiative energy transfer. As shown in Figure III.13, excitation energy can transfer many times through successive emissions and reabsorptions, before arriving radiatively or nonradiatively to a final acceptor and escaping from the sample. This process has been reported in the literature (in a system of CdSe/ZnS QDs for instance[162]) and is called energy migration. It allows a nonradiative coupling to occur, even when the first donor and the final acceptor are highly separated. This effect is characterized by a diffusion length which is defined as the mean distance between the first donor and the final acceptor particle. This distance is decreasing with increasing absorption coefficient, itself increasing with concentration. A value of 125 µm has been measured in[162] for a concentration of 5 mg/ml and QDs of 4 nm in diameter (samples very similar to ours).

Therefore, FRET can assist in some little amount the radiative energy transfer in explaining the influence of concentration on temperature and pressure sensitivity of the QDs (see Figure III.2 and Figure III.3, respectively). More importantly, FRET can explain some effects related to diffusion, namely: the influence of temperature and the solvent viscosity on the pressure sensitivity of the QDs observed with *C = 5 mg/mL* (Figure III.3) and possibly the nonlinearity observed in temperature calibration with *C = 0.5 mg/mL* (Figure III.2).

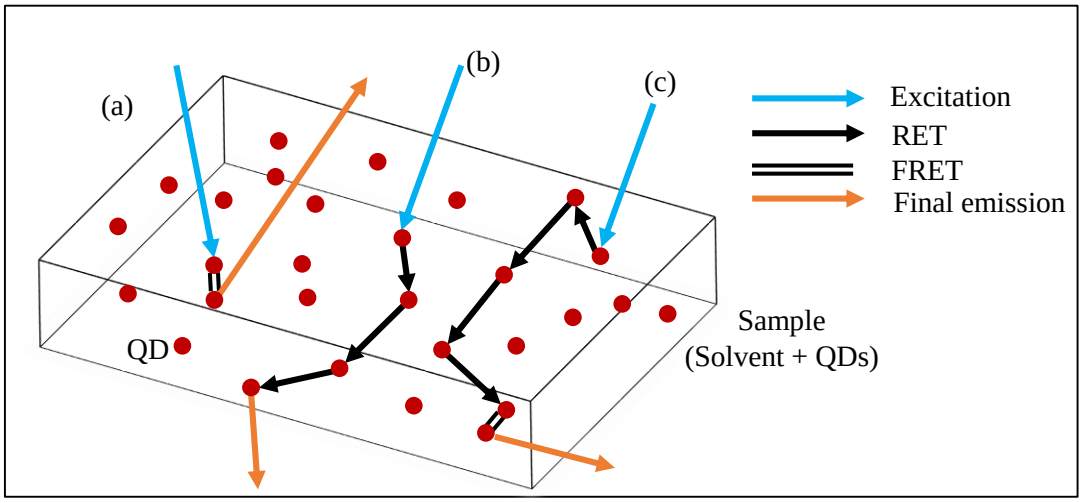

Figure III.13. Illustration of the energy migration in a system of QDs. The excitation energy enters the sample, and before escaping the sample, it can transfer either radiatively or nonradiatively from smaller to bigger QDs. All the QDs are represented with the same size for simplicity. Possible forms of energy migration are represented: (a) FRET; (b) successive emissions and reabsorptions and (c) successive emissions and reabsorptions ending by a FRET. For 5 mg/mL, the diffusion length is around 125 µm[162].

III.4.2. Modelling of the influence of interaction-related parameters

III.4.2.1. The notion of the apparent size of the QDs

A more quantitative evaluation of the response of the QDs requires the following question to be addressed: how dimension-related effects (resulting from the dependence of the bandgap on the crystalline structure and the size of the QDs) and interaction-related effects (resulting from the spacing between QDs and their diffusion) can be combined?

The approach chosen here is to introduce an *apparent radius* r^* defined as the mean radius of the fluorescent or active QDs (in the sense that they participate in the emission spectrum). This radius is larger than the radius r defined as the radius of all the QDs present in the solvent. Indeed, both radiative and nonradiative energy transfer lead to the deactivation of smaller QDs, which implies the shift of the mean radius r^* of active QDs to higher values compared to r. Therefore, for a given energy transfer efficiency, E^{ET}, we can write:

$$r^*\left(E^{ET}\right) = r + \delta r\left(E^{ET}\right) \qquad (III.17)$$

Where δr expresses the shift of the radius of the fluorescent QDs under the effect of energy transfer. E^{ET} combines the efficiencies of both radiative and nonradiative energy transfer:

$$E^{ET}(C,D) = f\left(E^{RET}(C), E^{FRET}(C,D)\right) \qquad (III.18)$$

As it can be noticed in the previous expression, the radiative energy transfer is affected only by QDs concentration, whereas FRET depends on both concentration and the diffusion of the QDs.

The diffusion *D* depends on the temperature, pressure and the viscosity of the solvent: $D(T,p,\eta(T,p))$. However, the concentration is almost unchanged under the various *T/p* conditions: $C(T,p) = C_0$.

III.4.2.2. Influence of the concentration on the emission energy

By substituting *r* by r^*, the equation of the bandgap energy becomes[*]:

$$E_g = E_g^B\left(V_{Crystal}\right) + E_g^Q\left(r^*\right) \qquad (III.19)$$

The quantum-related contribution can be computed using the Effective Mass Approximation (EMA). Using Taylor's expansion to the first order, the following expression is obtained:

$$E_g^Q\left(r^*\right) \approx E_g^Q\left(r\right) - \delta E_g^{Q-ET}\left(r,\delta r\right) \qquad (III.20)$$

where:

$$\delta E_g^{Q-ET}\left(r,\delta r\right) = \left(2\frac{\gamma^Q}{r^2} - \frac{\nu^Q}{r}\right)\frac{\delta r}{r} \qquad (III.21)$$

The apparent shift δr in QDs radius increases with increasing concentration due to the enhanced energy transfer from smaller to bigger QDs. The effect can thus explain the decrease of emission energy with increasing concentration shown in Figure III.1. At highly diluted solutions, δr tends to zero ($r^* \rightarrow r$), which explains the proximity between the theoretical mean emission energy (**Erreur ! Source du renvoi introuvable.**) and the mean emission energy obtained at low concentrations (Figure III.1).

III.4.2.3. Influence of the concentration and diffusion on temperature sensitivity

The variation of the bandgap energy with temperature can be expressed in the following way:

$$E_g\left(T\right) = \left(E_g^B\left(0\right) + E_g^Q\left(r^*\right)\right) - \frac{\left(\alpha_1 + \delta\alpha_1\left(r^*\right)\right)T^2}{T + \beta_1 + \delta\beta_1\left(r^*\right)} \qquad (III.22)$$

With:

$$r^* = r\left(T\right) + \delta r\left(T\right) = r_0 + \Delta r\left(T\right) + \delta r\left(T\right) \qquad (III.23)$$

Where $\Delta r(T)$ is the thermal expansion of the QDs.

The following cases can be distinguished:

[*] The Effective Mass Approximation (EMA) assumes a size-independent bulk contribution to estimate the emission energy. Acceptable results are obtained at ambient temperature and pressure. However, when it comes to evaluating the temperature and pressure sensitivity (see next paragraphs), size-dependent bulk temperature $S_T^B(r)$ and pressure $S_p^B(r)$ sensitivities, thermal expansion coefficient ($\alpha_T(r)$) and compressibility ($\alpha_p(r)$ need to be considered.

- **Case n°1**: negligible thermal expansion and energy transfer:

$$E_g(T) = E_g^B(0) + E_g^Q(r_0) - \frac{\left(\alpha_1 + \delta\alpha_1(r_0)\right)T^2}{T + \beta_1 + \delta\beta_1(r_0)} \qquad (III.24)$$

- **Case n°2**: non-negligible thermal expansion and negligible energy transfer:

$$E_g(T) \approx E_g^B(0) + E_g^Q(r_0) + \Delta r\, S_r^Q(r_0) - \frac{\left(\alpha_1 + \delta\alpha_1(r_0 + \Delta r)\right)T^2}{T + \beta_1 + \delta\beta_1(r_0 + \Delta r)} \qquad (III.25)$$

- **Case n°3**: negligible thermal expansion and non-negligible energy transfer:

$$E_g(T) \approx E_g^B(0) + E_g^Q(r_0) + \Delta r\, S_r^Q(r_0) - \frac{\left(\alpha_1 + \delta\alpha_1(r_0 + \Delta r)\right)T^2}{T + \beta_1 + \delta\beta_1(r_0 + \Delta r)} \qquad (III.26)$$

- **Case n°4**: non-negligible thermal expansion and energy transfer:

$$E_g(T) \approx E_g^B(0) + E_g^Q(r_0) + (\Delta r + \delta r) S_r^Q(r_0) - \frac{\left(\alpha_1 + \delta\alpha_1(r_0 + \Delta r + \delta r)\right)T^2}{T + \beta_1 + \delta\beta_1(r_0 + \Delta r + \delta r)} \qquad (III.27)$$

In these expressions, S_r^Q is the sensitivity to size variations (= $\partial E_g^Q/\partial r$).

The comparison between the different cases can be helpful in understanding the observations:

- **Cases n°1 and 2**: The quantum contribution enhances the temperature sensitivity of the QDs through the term $\Delta r(T) S_r^Q(r_0)$. In addition, the presence of the term $\Delta r(T)$ in the expression $\delta\alpha_1$ implies a lower temperature sensitivity with increasing temperature. This latter effect seems to be negligible since it is not observed at the lowest concentrations with negligible energy transfer (*C = 0.125* and *0.063 mg/mL*).
- **Cases n°2 and 3**: The role of $\delta r(T)$ is similar to the role of $\Delta r(T)$ since energy transfer can induce an *apparent thermal expansion* of the QDs. Energy transfer is enhanced with increasing concentration and diffusion (itself enhanced by increasing temperature and decreasing viscosity): $\delta r = \delta r(C,D(T,\eta(T))$. This can explain the non-linearity effect, i.e. the gradual temperature sensitivity increase with increasing temperature (and the resulting viscosity drop), observed at the highest concentration (*C = 0.5 mg/mL*). At low concentrations, however, diffusion effects become negligible, in agreement with the observations (all the curves were found to be linear). In addition, the dependence of the apparent thermal expansion on the concentration $(\delta r = \delta r(C))$ implies a decreasing temperature sensitivity with increasing concentration, in agreement with the observations.
- **Cases n°3 and 4**: The presence of the term $\delta r(T)$ together with $\Delta r(T)$ enhances further the quantum contribution in the temperature sensitivity. Again, the term $\delta r(C)$ appears also in the expression of $\delta\alpha_1$, and implies a decrease of the temperature sensitivity with increasing concentration.

The influence of diffusion can be visualized better by writing the full expression of the temperature sensitivity S_T. It is obtained simply by differentiating the energy of the bandgap with temperature (after replacing *r* by *r** to account for interaction effects):

$$S_T(T) = S_T^B\left(V_{Crystal}(T), r^*(T)\right) + S_{r^*}\left(r^*(T)\right)\frac{\partial r^*(T)}{\partial T} \qquad (III.28)$$

Or after some considerations detailed in Appendix F:

$$\begin{aligned} S_T = {} & S_T^B\left(V_{Crystal}, r\right) - \delta S_T^{B-ET}\left(V_{Crystal}, \delta r\left(C_0, D\right)\right) \\ & + \left[S_r(r) - \delta S_r^{Q-ET}\left(r, \delta r\left(C_0, D\right)\right)\right] \\ & \times \left[\frac{\partial r}{\partial T} + \underbrace{\frac{\partial(\delta r)}{\partial E^{ET}}\frac{\partial E^{ET}\left(C_0, D\right)}{\partial D}\frac{\partial D}{\partial T}}_{\partial(\delta r)/\partial T}\right] \end{aligned} \qquad (III.29)$$

This expression should be compared to the one obtained without energy transfer:

$$S_T = S_T^B\left(V_{Crystal}(T), r(T)\right) + S_r\left(r(T)\right)\frac{\partial r}{\partial T} \qquad (III.30)$$

The presence of opposite-signed interaction-related terms in the Equation (III.29) signifies that, for a given concentration C_0, the diffusion D acts on temperature sensitivity by two competing mechanisms:

- It weakens the temperature sensitivity by reducing the *apparent bulk temperature sensitivity* ($S_T^B - \delta S_T^{B\text{-}ET}$) and the *apparent sensitivity to size variations* ($S_r^Q - \delta S_r^{Q\text{-}ET}$)*. This is because: (i) the temperature rise and the resulting viscosity drop lead to a higher diffusion and (ii) the diffusion enhances the energy transfer (or δr) and hence the shifts $\delta S_r^{Q\text{-}ET}$ and $\delta S_T^{B\text{-}ET}$.
- It enhances the temperature sensitivity by increasing the *apparent thermal expansion* ($\partial r/\partial T + \partial(\delta r)/\partial T$) of the QDs. This is because both r and δr increase with temperature.

At the highest concentration (0.5 mg/mL), experimental measurements showed that S_T increases with increasing temperature. This observation suggests that the diffusion acts mainly *via* the second mechanism.

Now if the QDs are separated *via* dilution, i.e. the concentration C_0 is decreased, the terms $\delta S_T^{B\text{-}ET}$ and $\delta S_r^{Q\text{-}ET}$ decrease resulting in a higher temperature sensitivity. In addition, the influence of the diffusion decreases with dilution because the term $\partial E^{ET}(C_0)/\partial D$ tends to zero at low concentrations (see Figure III.7). Therefore, the term $\partial(\delta r)/\partial T$ tends to zero with decreasing concentration. These effects combined explain – as illustrated in Figure III.14: (i) the maximization of the sensitivity of the QDs, (ii) the disappearance of diffusion non-linearity effects, and (iii) the stabilization of temperature sensitivity with decreasing concentration.

* The term $\delta S_r^{Q\text{-}ET}$ does not appear in Equations (III.25) and (III.26) obtained using a first order Taylor expansion. This signifies that its effect on the temperature sensitivity is not of first-order importance.

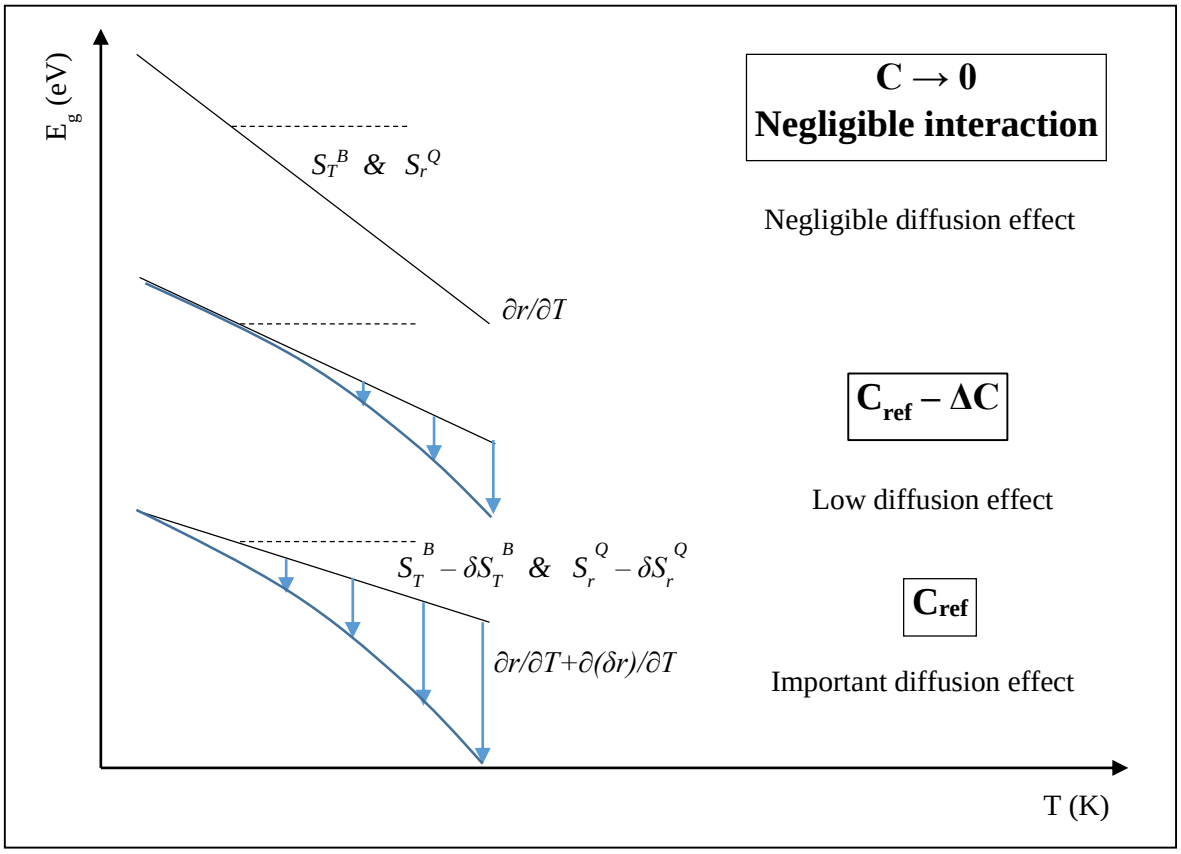

Figure III.14. Illustration of the variation of temperature sensitivity $S_T = \partial E_g/\partial T$ with the concentration and the diffusion of the QDs. The value of emission energy at the lowest temperature is chosen in an arbitrary way for simplification (only the values of the slope, or the temperature sensitivities, have to be considered in the different cases).

III.4.2.4. Influence of the concentration and diffusion on pressure sensitivity

The variation of the bandgap energy with pressure, at a given temperature *T*, can be expressed in the following way:

$$E_g(T,p) = E_g^B(T) + E_g^Q(r^*) + \left(\alpha_2 + \delta\alpha_2(r^*)\right)p \qquad (III.31)$$

With:

$$r^* = r(T,p) + \delta r(T,p) = r(T,p_0) + \Delta r(T,p) + \delta r(T,p) \qquad (III.32)$$

Where *Δr(p)* expresses the compression of the QDs.

The most general case, *i.e.* the one with non-negligible compressibility and energy transfer yields:

$$\begin{aligned} E_g(T,p) &\approx E_g^B(T) + E_g^Q\left(r(T,p_0)\right) \\ &+ (\Delta r + \delta r) S_r^Q\left(r(T,p_0)\right) + \alpha_2\left(r(T,p_0) + \Delta r + \delta r\right)p \end{aligned} \qquad (III.33)$$

Similarly to the discussion presented for temperature sensitivity, we can notice that energy transfer induces an *apparent compression* to the QDs. Indeed, the apparent size increase induced by diffusion is limited when high pressures are applied (due to the important viscosity rises): $\delta r(D(\eta(p))$. Furthermore, the diffusion of the QDs is enhanced when pressure calibrations are conducted at higher temperatures, within solvents of lower viscosity or with high QDs concentrations: $\delta r(D(T,\eta(T,p))$. This explains the increase of pressure sensitivity with increasing temperature or decreasing viscosity observed at highest concentration ($C = 5\ mg/mL$). At lower concentrations however, diffusion effects become negligible.

The influence of diffusion can be visualized better in the full expression of the pressure sensitivity S_p:

$$S_p(p) = S_p^B\left(V_{Crystal}(p), r^*(p)\right) + S_{r^*}\left(r^*(p)\right)\frac{\partial r^*}{\partial p} \qquad (III.34)$$

After some considerations (similar to those detailed in Appendix F for temperature sensitivity S_T), the previous expression becomes:

$$\begin{aligned} S_p = {} & S_p^B\left(V_{Crystal}, r\right) - \delta S_p^B\left(V_{Crystal}, r, \delta r\left(C_0, D\right)\right) \\ & + \left[S_r^Q(r) - \delta S_r^{Q-ET}\left(r, \delta r\left(C_0, D\right)\right)\right] \\ & \times \Bigg[\underbrace{\frac{\partial r}{\partial p} + \frac{\partial(\delta r)}{\partial E^{ET}}\frac{\partial E^{ET}\left(C_0, D\right)}{\partial D}\frac{\partial D}{\partial p}}_{\partial(\delta r)/\partial p}\Bigg] \end{aligned} \qquad (III.35)$$

At highly diluted solutions all the interaction-related terms (*i.e.* δr and $\partial E^{ET}/\partial D$) tend to zero, and the expression of the pressure sensitivity reduces to the one obtained via dimension-related effects:

$$S_p = S_p^B\left(V_{Crystal}(p)\right) + S_r^Q\left(r(p)\right)\frac{\partial r}{\partial p} \qquad (III.36)$$

In this case, the pressure sensitivity stabilizes to its maximum value, and exhibit no dependence on the diffusion of the QDs and, therefore, on the temperature of sample and the viscosity variations (see Figure III.15). At higher concentrations, however, the influence of diffusion is not negligible.

A careful examination of the values of the diffusion in Figure *III.12* (b) as well as the form of the Equation (II.35) can give some insight of the resulting pressure sensitivities. Figure *III.12* shows that the term $\partial D/\partial p$ (i) increases with temperature for a given solvent (squalane), (ii) is bigger in the mixture compared to its value in the squalane at ambient temperature, (iii) has comparable values in the mixture at ambient temperature and the squalane at 373 K and (iv) tends to zero beyond a threshold pressure $p_{thresold}$ whose value decreases with temperature and with solvent's piezo-viscosity (pressure-viscosity coefficient). These variations imply an increase of S_p when the temperature is increased or a less viscous or piezo-viscous solvent is used in the calibrations (see Figure III.15). All this reasoning holds if we suppose an important diffusion effect on the *apparent compressibility* ($\partial r/\partial p + \partial(\delta r)/\partial p$), and a negligible diffusion effect on the *apparent sensitivity to size variation* ($S_r^Q - \delta S_r^{Q\text{-}ET}$). This seems to be the case by referring to the experimental calibration curves.

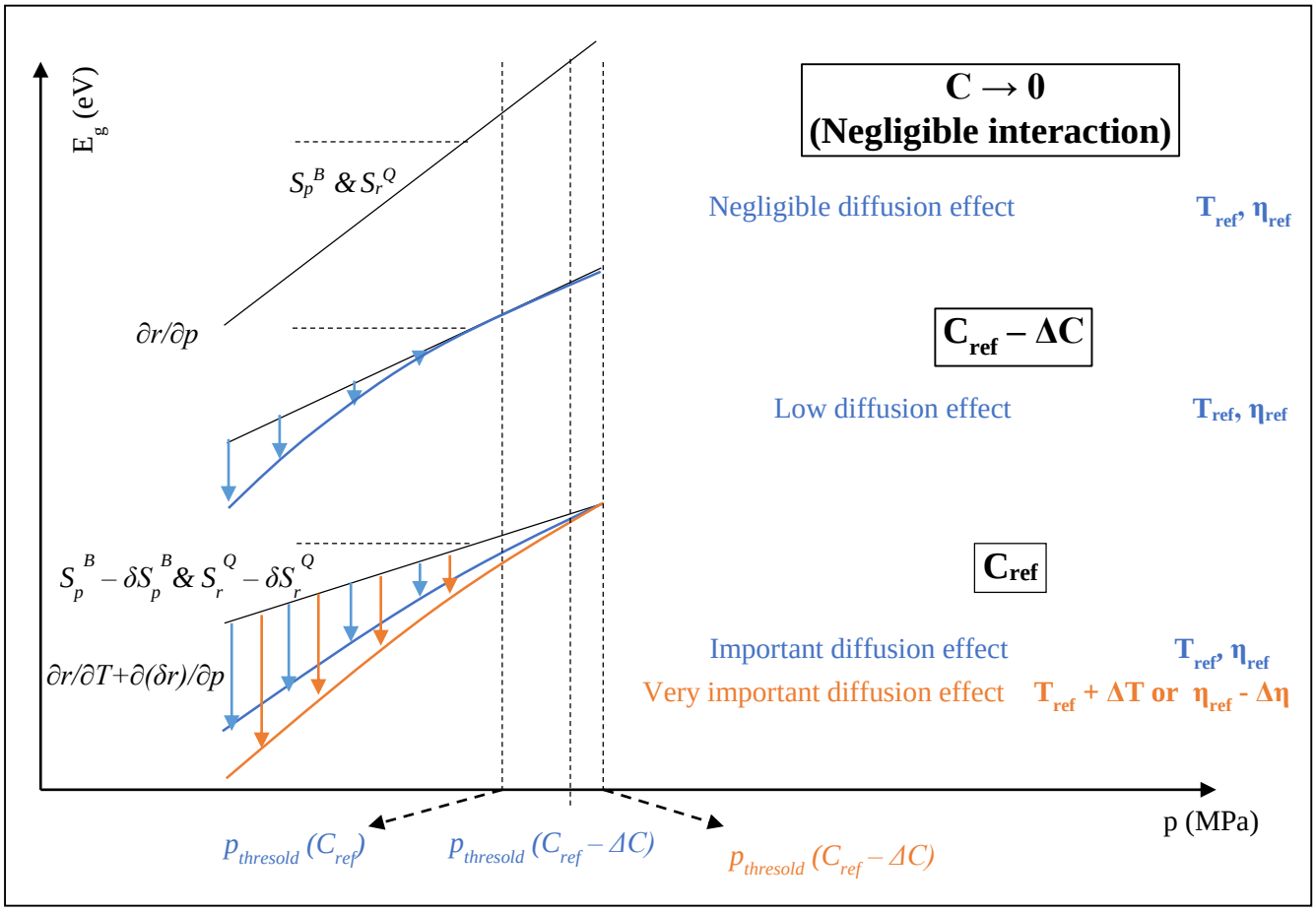

Figure III.15. Illustration of the variation of pressure sensitivity $S_p = \partial E_g/\partial p$ with concentration and the diffusion of the QDs. The value of emission energy at the lowest pressure is chosen in an arbitrary way for simplification (only the values of the slope, or the pressure sensitivities, have to be considered).

Figure III.16 is a diagram summarizing the influence of the different parameters on the pressure sensitivity of QDs. It shows in particular:

- The evolution of pressure sensitivity between two asymptotic values. The lower value obtained at concentrated solutions corresponds to the sensitivity of the bigger QDs, whereas the higher value, obtained in diluted solutions, corresponds to the sensitivity of all the QDs (small and big);
- The enhancement of the measured sensitivity with increasing temperature or decreasing viscosity, which was explained by the pressure-dependent shift in PL spectra induced with these two parameters. These enhancements are stabilized at highly diluted solutions.

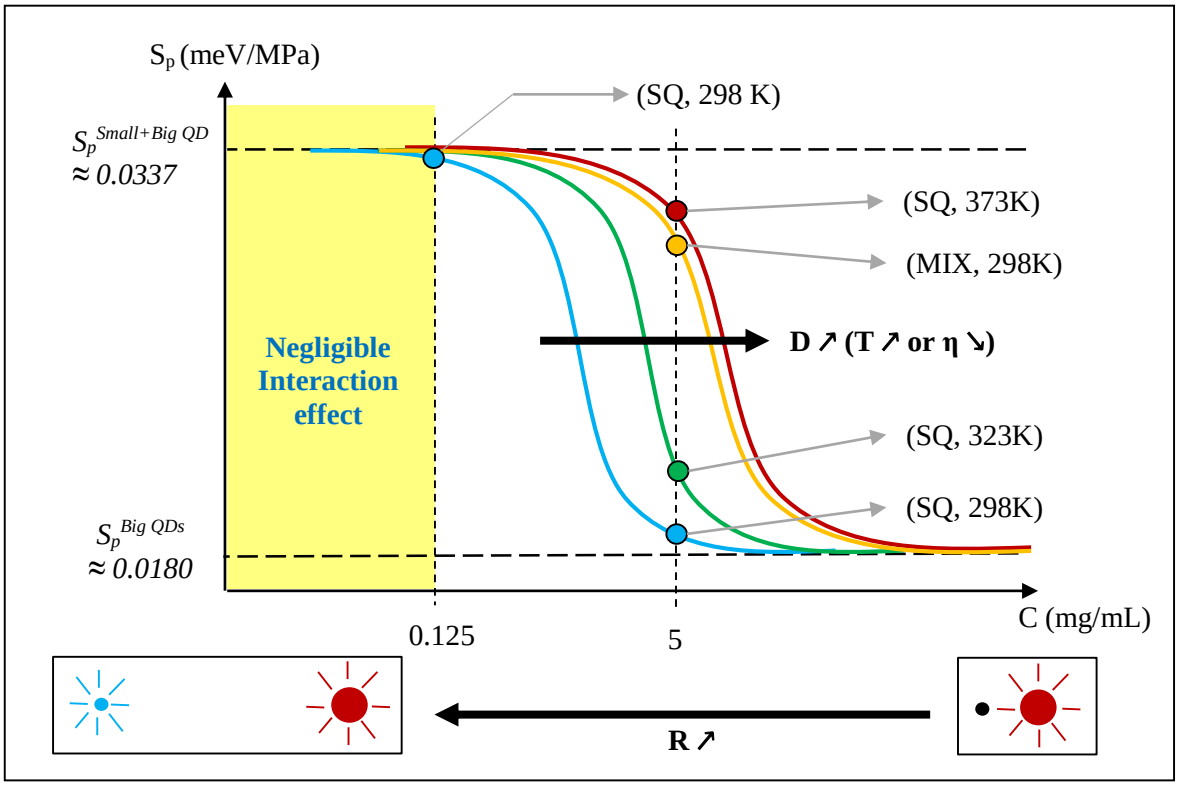

Figure III.16. Diagram for the different parameters that affect the pressure sensitivity of CdSe/CdS/ZnS QDs. SQ: squalane; MIX: mixture of squalane (30 vol%) and cyclopentane (70 vol%).

III.4.2.5. Polarity effect?

The polarity effect leads a shift $\delta E_g^{Polarity}$ in emission energy to lower values:

$$E_g = E_g^{Bulk}\left(V_{Crystal}\right) + E_g^{Quantum}\left(r^*\right) - \delta E_g^{Polarity}\left(\tau_{Relax}\right) \qquad (III.37)$$

A higher shift is obtained for shorter relaxation times, τ_{Relax} (see Figure III.17).

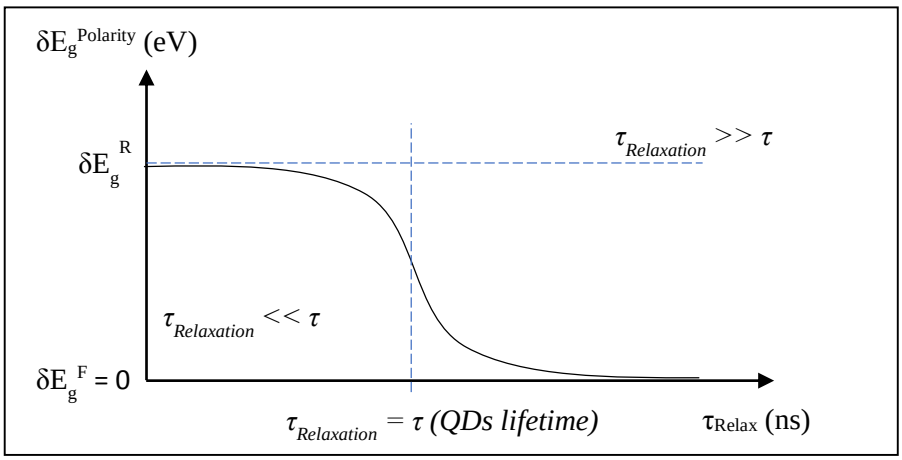

Figure III.17. Variation of the polarity-induced shift with the relaxation time. δE_g^F and δE_g^R are the shifts obtained at the Frack-Condon state and the relaxed state, respectively.

The temperature sensitivity is obtained by differentiating the previous expression with respect to *T*, we get:

$$S_T = S_T^B\left(V_{Crystal}\left(T\right)\right) + S_{r^*}^Q\left(r^*\left(T\right)\right)\frac{\partial r^*\left(T\right)}{\partial T} - \frac{\partial\left(\delta E_g^{Polarity}\right)}{\partial \tau_{Relax}}\frac{\partial \tau_{Relax}}{\partial \eta}\frac{\partial \eta}{\partial T} \qquad (III.38)$$

Squalane is nonpolar solution, the term is $\delta E_g^{Polarity} \approx 0$. Even though it is polarized with the laser excitation, the effects seems to be negligible. Indeed, Equation (III.38) implies some nonlinearity in the variation of the bandgap energy with temperature with all the concentrations. Nonlinear variation is obtained however only at the highest concentrations.

III.5. Analysis of the width of the emission spectrum

The analysis presented in the previous paragraphs show the complexity of the physical phenomena that could perturb the response of the QDs under various conditions. The analysis of the variation of the width of the emission spectrum is even more complex, since it requires the convolution of all the distributions leading to the dispersion of the emission around the mean value. The most important are:

- The distribution of the size of the QDs;
- The distribution of the vibrational energy levels associated to each value of the bandgap;
- The distribution of the distance distribution of the QDs;
- The distribution of the diffusion of the QDs.

These distributions change obviously with the concentration and the diffusion of the QDs as well as with the temperature and the pressure. The combination between these distributions is not trivial either. For example, (i) the energy transfer can occur only from smaller to bigger QDs and not inversely, (ii) the size difference between QDs has to correspond to an energy difference superior to some amount to achieve an efficient energy transfer[174] and (iii) the interaction between the QDs and the vibrational energy of the solvent molecules can depend on the size of these QDs. The quantitative approach consists of (i) identifying these distributions, (ii) evaluating their dependence on the different parameters (*C, T, p, η, …*) and (iii) convoluting properly their interacting effects. Due to the lack of the data for each distribution, the contribution of each mechanism of energy transfer and a satisfying model combining all these effects, this analysis was not covered in this first study.

III.6. Conclusion on the static study

In summary, our calibration tests showed that both temperature and pressure affect the PL energy of CdSe/CdS/ZnS QDs in reversible way and with linear sensitivities provided that the concentration is sufficiently low (<0.125 mg/ml). This confirms their potentiality for sensing applications when used with another family of QDs in order to uncouple the temperature the pressure influence.

Unlike the order of the presentation from more simple to more complex conditions, measurements were first conducted to evaluate the pressure sensitivity of the QDs at 5 mg/mL. The only reason behind this choice was to insure sufficient PL intensities for spectral analysis. The results obtained at

this concentration were less encouraging from the metrological point of view because of the variation of pressure sensitivity with temperature and, more importantly, with the nature of lubricant. Indeed, this latter drawback is constraining since it implies the necessity of other *T/p* calibrations whenever a new lubricant is to be studied. These results motivated to overstep the parametric study aiming at measuring *T/p* sensitivities of the QDs and to lead a more comprehensive investigation.

This investigation first confirmed that energy transfer between QDs is behind the above-mentioned problem, and second it permitted to define a procedure to overcome it, i.e., through minimization of the QDs concentration. Temperature calibrations were made at different concentrations, and showed that for concentrations $C \leq 0.125$ *mg/mL*, the influence of energy transfer on temperature sensitivity becomes negligible. Based on this finding, a more judicious choice of the concentration for *T/p* calibration curves than the initially chosen one (5 mg/mL) was made. The concentration *C = 0.125 mg/mL* was used to perform another pressure calibration on the CdSe/CdS/ZnS QDs. Interestingly, the value of the pressure sensitivity was shown to increase following this minimization, which signifies an improved sensing quality.

Furthermore, a model was proposed combining both dimension- and interaction-related effects. This model, based on the notion of the apparent radius r^* of the QDs (or the radius of the active QDs, preferentially bigger ones), could yield results consistent with the experimental observations.

For practical reason, the film thickness was not the same from an apparatus to another which implies that the obtained threshold concentration of 0.125 mg/ml is valid only for a given apparatus. Such is the case since the efficiency of energy transfer depends on the product of the concentration of the acceptors and the thickness of the absorbing media. Nevertheless, this value was derived from the measurements in temperature cell yielding a film thickness of 1 mm. Consequently, for all measurements conducted with a concentration inferior to 0.125 mg/ml and thickness inferior to 1 mm interaction related effects on the sensitivity of the QDs will be also minimized. This is the case in the pressure cell, and this will be the case for dynamic conditions studies in the next chapter and ultimately in EHD contacts. Nevertheless, for this last case, the signal issue related to the number of QDs has to be considered. Indeed, for thicknesses above 0.1 mm, the intensity of the emission spectrum obtained at 0.125 mg/mL was sufficient owing to the high quantum yield of CdSe/CdS/ZnS QDs. Film thicknesses found in EHD contacts are however orders of magnitude smaller than the thickness of the film in pressure calibrations. This issue can fortunately be overcome since only steady-state EHD contacts are considered in our study. In these contacts, the physical parameters are constant in time, and thus the response of the QDs can be accumulated over the time needed for obtaining a measurable signal.

The other advantage of working with low concentrations is the minimization of the perturbations induced by the QDs to the flow of the lubricant and thus the generation of film thickness and friction in EHD contacts. Such perturbations can be perceived through the increase of the viscosity of the lubricant due to the presence of QDs. Measurements showed however that this increase in insignificant with *C = 0.125 mg/ml* (see next chapter).

Despite the above-mentioned advantages, two important issues have to be addressed.

First of all, pressure calibrations at 0.125 mg/mL were only made for squalane, at ambient temperature. Increasing the temperature or decreasing the viscosity enhances the efficiency of energy transfer, which means that the concentration has to be further reduced in order to compensate this effect. On the other hand, the diffusion is limited when the pressure is increased (due to the pressure-

induced viscosity rise), which extends the range of concentrations with reduced energy transfer effect. A partial response was given in the temperature calibrations, which showed that temperature sensitivity stabilized in squalane for concentrations below 0.125 mg/mL (concentration and diffusion effects became negligible). Other pressure calibration tests are required to verify the stability of the pressure sensitivity of the QDs for $C = 0.125\ mg/mL$, especially at higher temperatures and with solvents with lower viscosities.

The other issue is related to the absolute value of emission energy. The emission energy was found to decrease at the lowest tested concentrations (Figure III.1) and did not attain a plateau as it was the case to the sensitivity of the QDs to temperature variations. Temperature/pressure calibrations at low concentrations can be used to measure the variation of these two parameters in EHD contacts. However, for the measurement of the absolute value of these two parameters, a reference emission energy need to be recorded in proper conditions, since it can be affected with interaction-related parameters. In particular, it has to be measured (i) in the same apparatus simulating EHD contacts (EHD tribometer) to ensure comparable film thicknesses and (ii) for each sample in order to avoid deviations induced by little differences in sample preparation such as small concentration variations.

IV. Dynamic study – Rheology and Photoluminescence

IV.1. Introduction

The rheological properties of the lubricant affect considerably film and friction generation in EHD contacts as shown in the first chapter. These properties can be altered when other species, such as additives or sensors, are present within the lubricant. The perturbations induced by sensors, or QDs in our case, are obviously not desired. Therefore, an important question addressed in this chapter is to what extent the QDs can modify the rheological behaviour of the lubricant, and consequently the characteristics of the EHD contact.

Moreover, in addition to the temperature and the pressure gradients found in EHD contacts, the lubricant flows continuously and may undergo important shear stresses due to the movement of the solid surfaces. Therefore, the other question raised in this chapter is whether or not the flow and the shear rate can change the response of the QDs when flowing through EHD contacts (found in mechanical components or simulated in a tribometer). This question is all the more important, given that the calibration tests were performed under static conditions and that the literature is lacking experimental or theoretical analysis of the QDs PL under dynamic conditions (to the best of the author's knowledge).

To bring some answers to the above-mentioned questions, some tests were performed in a rheometer allowing the effect of flow to be isolated. Indeed, in this apparatus, the pressure is close to the ambient pressure and only the temperature and shear rate can be varied.

IV.2. Methodology

Three kinds of test were performed for the dynamic study. In the first series, the viscosity of the solution (squalane with QDs) was compared to the viscosity of the solvent (squalane). In the other tests, the PL of the QDs experiencing different dynamic conditions was collected in order to answer the following questions:

- Are the QDs sensitive to the shear rate?
- Are the QDs response stable under long periods of shearing?

The different samples and conditions are summarized in Table IV.1. All the tests were realized on CdSe/CdS/ZnS QDs dispersed in squalane. The two concentrations which were shown to yield stabilized temperature sensitivity (see Chapter 3), i.e. *C = 0.125 and 0.063 mg/mL* were examined. A rheometer with three interchangeable geometries was used to simulate the shearing of the solutions:

- Steel plate against steel plate (SPSP);
- Steel plate against glass plate (SPGP);
- Steel cone against glass plate (SCGP).

Some technical information about the rheometer, the geometries, and the coupling of the rheometer with the optical system is presented in Appendix C.VI.

The major difference between the parallel-plates geometry and the cone-plate geometry is the dependence of the shear rate on the distance *l* from the rotating axis. In the first geometry, the gap is constant ($H = H_0$), resulting in a shear rate varying linearly with the distance *l:*

$$\dot{\gamma}(l) = \frac{l\omega}{H_0} \qquad (IV.1)$$

Where ω is the angular velocity of the rotating steel plate.

In the cone-plate geometry, however, the angle φ of the cone allows maintaining a constant shear rate along *l*:

$$\dot{\gamma}(l) = \frac{l\omega}{H(l)} = \frac{l\omega}{l\tan\varphi} = \frac{\omega}{\tan\varphi} \qquad (IV.2)$$

The values of shear rate given in Table IV.1 correspond to (i) the value obtained with $l = 2/3\ L$, with *L* being the radius of the rotating disc (*20 mm*) for the plate-plate geometry and (ii) the constant value of shear rate in the cone-plate geometry. More justification on the choice of the concentration, geometry, and shear rate used at each test will be given in the corresponding paragraphs.

Tests	Parameters			
	Geometry	Concentration of the QDs (mg/mL)	Temperature (K)	Shear rate (s^{-1})
1. Viscosity measurement	SPSP or SPGP	0, 0.125	293 – 373	10 – 10000
2. Influence of shear rate on emission spectrum	SPGP	0.125, 0.063	293, 333, 373	10 – 50000
3. Stability of the response of the QDs under long periods of shear rate	SCGP	0.063	333	19000
	SPGP	0.063	=	20000

Table IV.1. Different dynamic tests on CdSe/CdS/ZnS QDs, and corresponding conditions (geometry of the rheometer, concentration, temperature and shear rate).

IV.3. Rheological study

In Figure IV.1 the values of viscosity of the colloidal suspension (squalane with 0.125 mg/mL of CdSe/CdS/ZnS QDs) are compared with the viscosity of pure squalane for temperatures between 293 and 373 K. The measurements for the colloidal solution were made in SPGP geometry, whereas measurements for pure squalane were made using SPSP and SPGP geometries. The gap was fixed at 0.2 and 0.1 mm for the SPSP and SPGP geometries, respectively. Smaller gaps were chosen for the measurement with glass in order to extend the range of shear rate for the subsequent rheology-PL measurements. Measurements of viscosity are made with 2% of uncertainty.

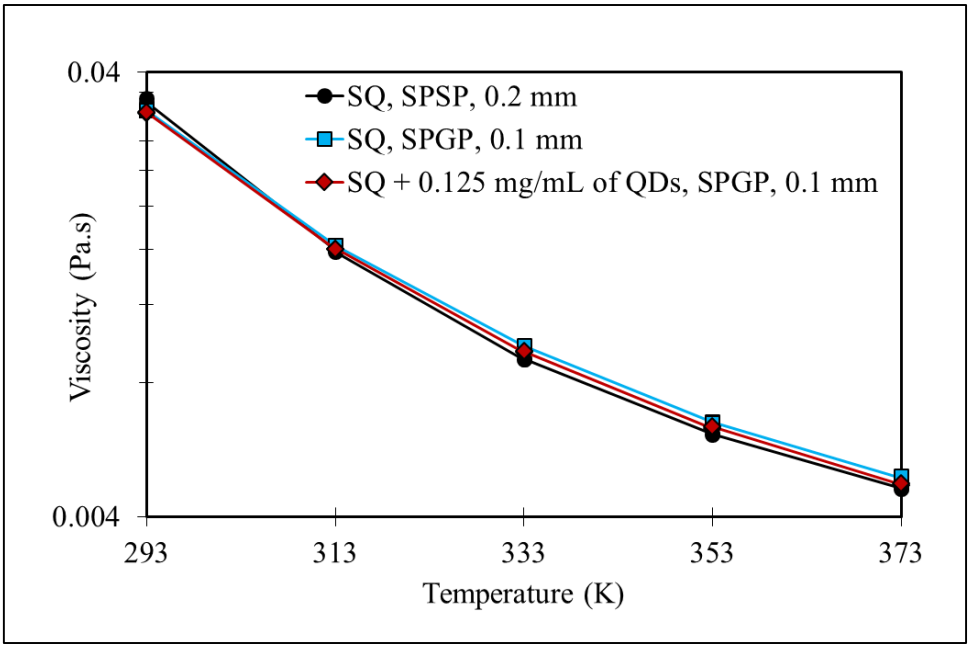

Figure IV.1. Comparison of the viscosity of squalane (SQ) with or without QDs.

Very close values were obtained in all the cases, and the slight differences cannot induce significant perturbation in the characteristics of the lubricant when flowing through EHD contacts. These differences arise probably from the less accurate thermal regulation when one of the surfaces is made of glass, because of the poor thermal conductivity of the latter. At low temperatures, shear-heating can occur because of the higher viscosity of the solution. At higher temperatures, however, the fluid can be partly ejected from the gap because of the lower viscosity, and this effect can be enhanced by the little temperature rise induced by the shearing of the solution. These effects may explain the small drop in viscosity observed in the SPGP geometry compared to the values found in the SPSP at lower temperatures, and the low increase in viscosity observed for higher temperatures.

IV.4. Rheology-PL study

IV.4.1. Dependence of the QDs response on shear rate

Figure IV.2 shows the variation of the emission energy with shear rate of CdSe/CdS/ZnS QDs dispersed in squalane with two concentrations (0.125 and 0.063 mg/mL) and at three temperatures (293, 333 and 373 K). The gap was fixed at 0.1 mm, and the PL spectra were collected at $l = 2/3\ L$. At each condition, measurements were repeated four times to estimate the mean emission energy and the standard deviation presented in Figure IV.2. It can be noticed that the error bars are remarkably small, when compared with those obtained with the temperature cell. This can be explained by three factors: (i) the precise temperature regulation in the rheometer, (ii) the temperature homogenization due to the movement of the sample and (iii) the averaging of the emission spectrum over a large volume of the solution due the rotation of the latter.

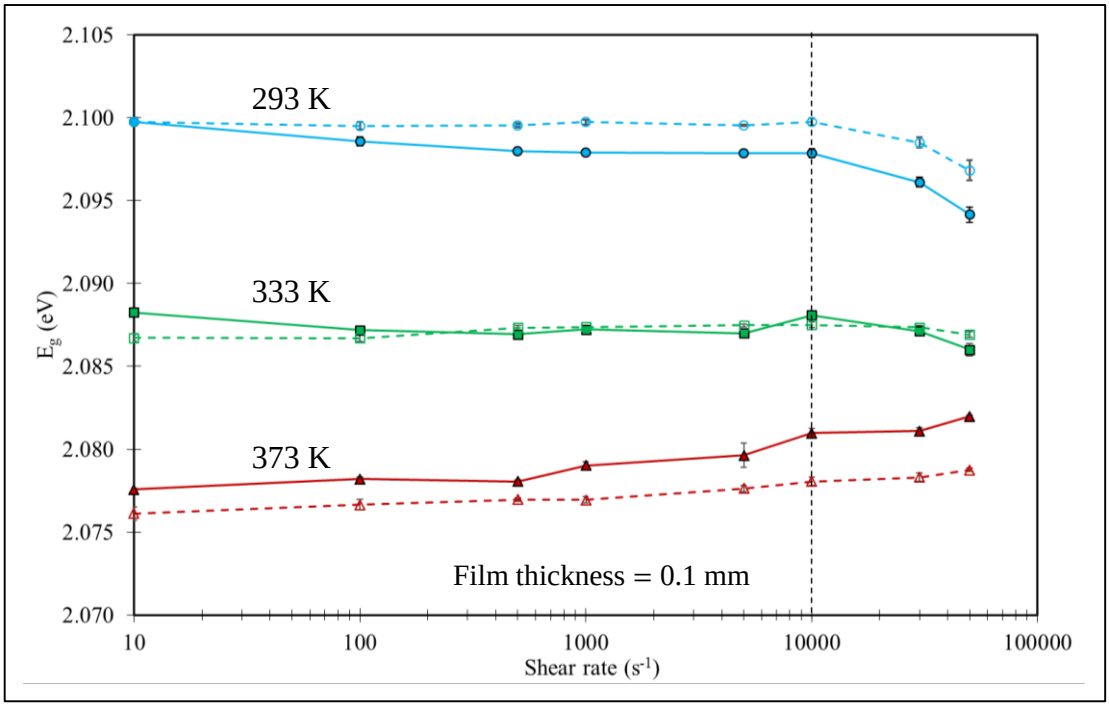

Figure IV.2. Variation of the emission energy of CdSe/CdS/ZnS QDs dispersed in squalane as a function of shear rate, at different temperatures and for two concentrations. (Filled symbols) 0.125 mg/mL (Open symbols) 0.063 mg/mL.

Figure IV.2 show that the QDs response is almost unaffected by shear rate. In addition, the variation of emission energy with temperature is close to those measured in the static study. Indeed, values of temperature sensitivity of -0.28 and -0.30 meV/K is obtained for the concentrations 0.125 and 0.063 mg/mL respectively.

This result is important since it discards the effect of flow or shear rate from the list of parameters encountered in EHD contacts and to which the QDs are sensitive for concentrations below 0.125 mg/mL.

Some little variations are however observed at the highest shear rates. High shear rates can induce some heating within liquids resulting in: (i) a viscosity drop and (ii) decrease in emission energy. In order to verify this, and if there is a correlation between viscosity and emission energy, it is informative to plot:

- The variation of the ratio η/η_0, where $\eta_0 = \eta(\dot{\gamma} = 10\ s^{-1})$, as a function of shear rate (see Figure IV.3).
- The variation of emission energy as a function of the viscosity, under the different conditions (2 concentration, 3 temperatures and shear rates from 10 to 50000 s^{-1}) (see Figure IV.4).

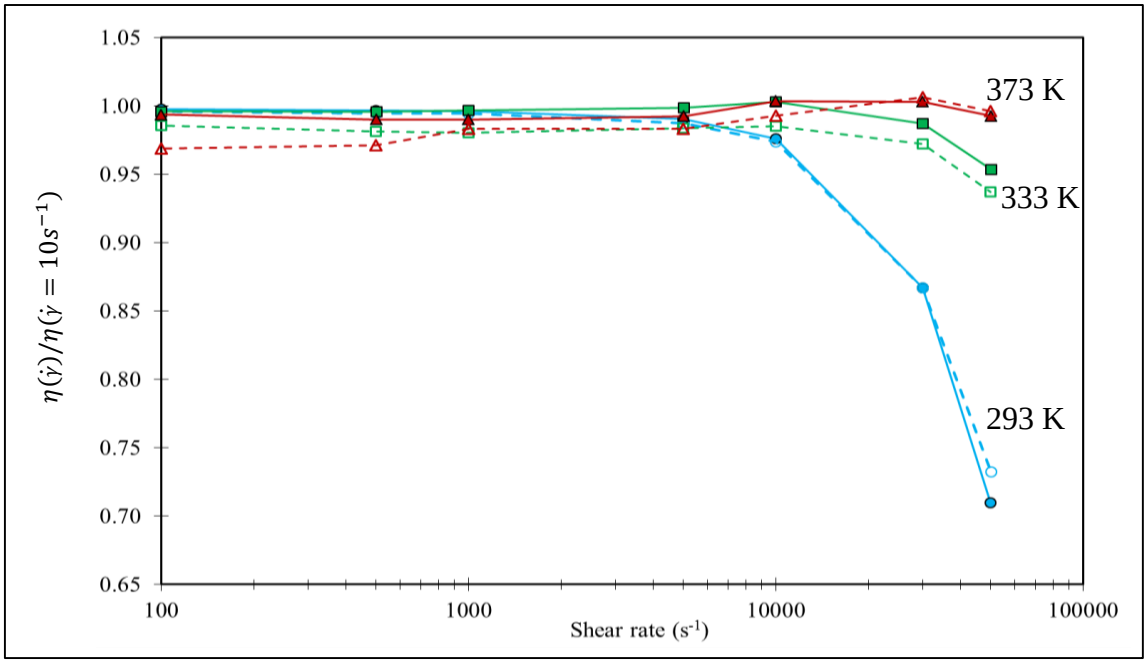

Figure IV.3. Variation of the measured squalane viscosity as a function of the shear rate for the 3 different temperatures and the 2 different concentrations. (Filled symbols) 0.125 mg/mL (Open symbols) 0.063 mg/mL.

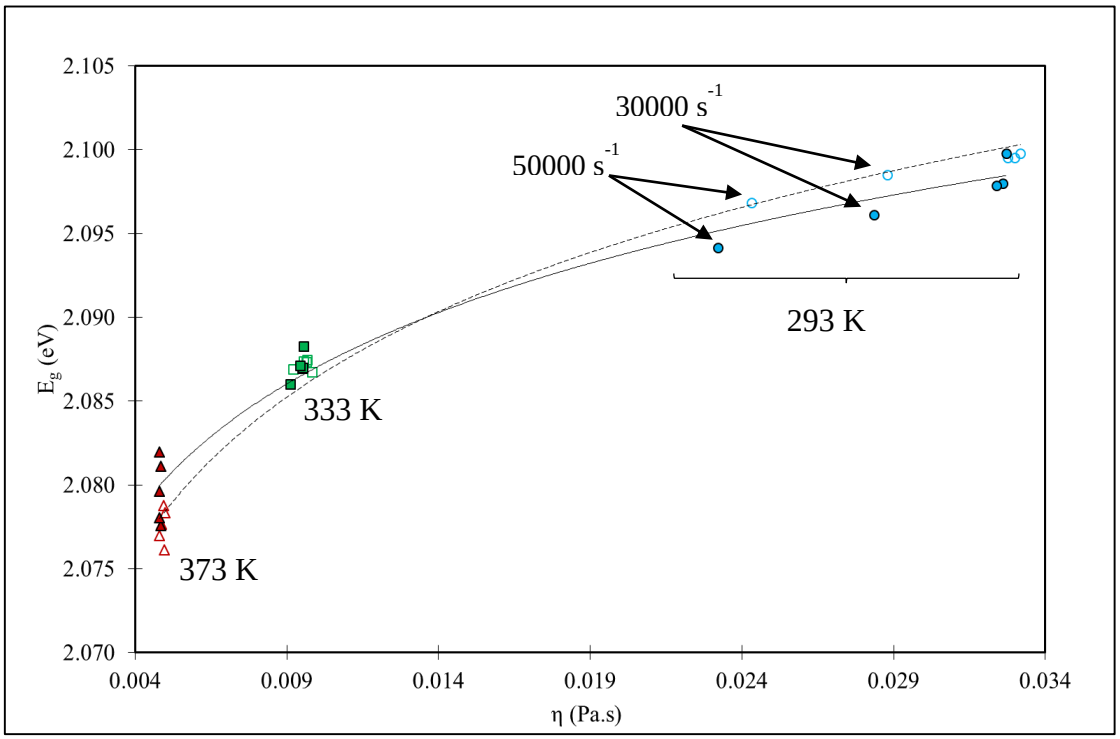

Figure IV.4. Variation of the emission energy of CdSe/CdS/ZnS QDs dispersed in squalane as a function of the measured viscosity for five imposed shear rates (from $10s^{-1}$ to $50000s^{-1}$) at three different temperatures, and for two concentrations. (Filled symbols) 0.125 mg/mL (Open symbols) 0.063 mg/mL.

Several observations can be made:

- At high shear rates (*30000 and 50000 s^{-1}*), the viscosity varies considerably at *T = 293 K*, at *T = 333 K*, rather low changes are obtained whereas for *T = 373 K* it is almost constant (Figure IV.3);
- At T = 293 K, and for both *C = 0.125* and *0.063 mg/mL*, the points *(E_g, η)* measured at high shear (*30000 and 50000 s^{-1}*) are spaced from the others obtained at the same temperature (Figure IV.4). The drop in viscosity is accompanied by a shift in the emission energy to lower values. It can be however noticed that these points follow particularly well the fitting curves linking the measurements made at different temperatures.
- At *T = 373 K*, only a dispersion in emission energy is found for approximately the same values of viscosity (or actually temperature) (Figure IV.4);

Figure IV.5 (a) to (c) shows that there is some correlation between shear rate and the dispersions observed under isoviscous (or isothermal) conditions at two concentrations. In particular:

- At *C = 0.125 mg/mL*, the sensitivity of the QDs to viscosity (or temperature) variations decreases (Figure IV.5 (a)). This effect of shear rate on the sensitivity is attenuated with decreasing concentration (Figure IV.5 (a) and (b)).
- For *C = 0.125 mg/mL*, the energy shifts to lower values at *T =293 K* with increasing shear rate, while shifting to higher values at *T = 373 K* (Figure IV.5 (a));
- For *C = 0.063 mg/mL* however, only the shift to higher values at *T = 373 K* is observed with increasing shear rate. (Figure IV.5 (b));
- At high shear rates, the sensitivity of the QDs to the viscosity (or the temperature) is lowered with increasing concentration (see continuous lines in Figure IV.5 (c)).

The viscosity drop observed in Figure IV.3 may arise from the self-heating of the lubricant at high shear rates. Self-heating is more pronounced when the viscosity of the sample is high (at low temperatures). This is consistent with the magnitude of viscosity drop found at each temperature (the most important drop is found at *T = 293 K* as shown in Figure IV.3). The position of the points *(E_g, η)* at high shear rates (*30000 and 50000 s^{-1}*), particularly at low temperatures (*T = 293 K*), as shown in Figure IV.4, confirms further that both emission energy decrease and the viscosity drop arise mostly from shear-heating. It should be noted that a logarithmic equation was used to fit the variation of the emission energy with the viscosity. This is actually justified by the fact that emission energy varies linearly with temperature (as shown in the previous chapter), and that the viscosity varies nearly exponentially with temperature.

In the next paragraph, we will discuss more deeply the dispersion of the emission energy at isoviscous (or isothermal) conditions.

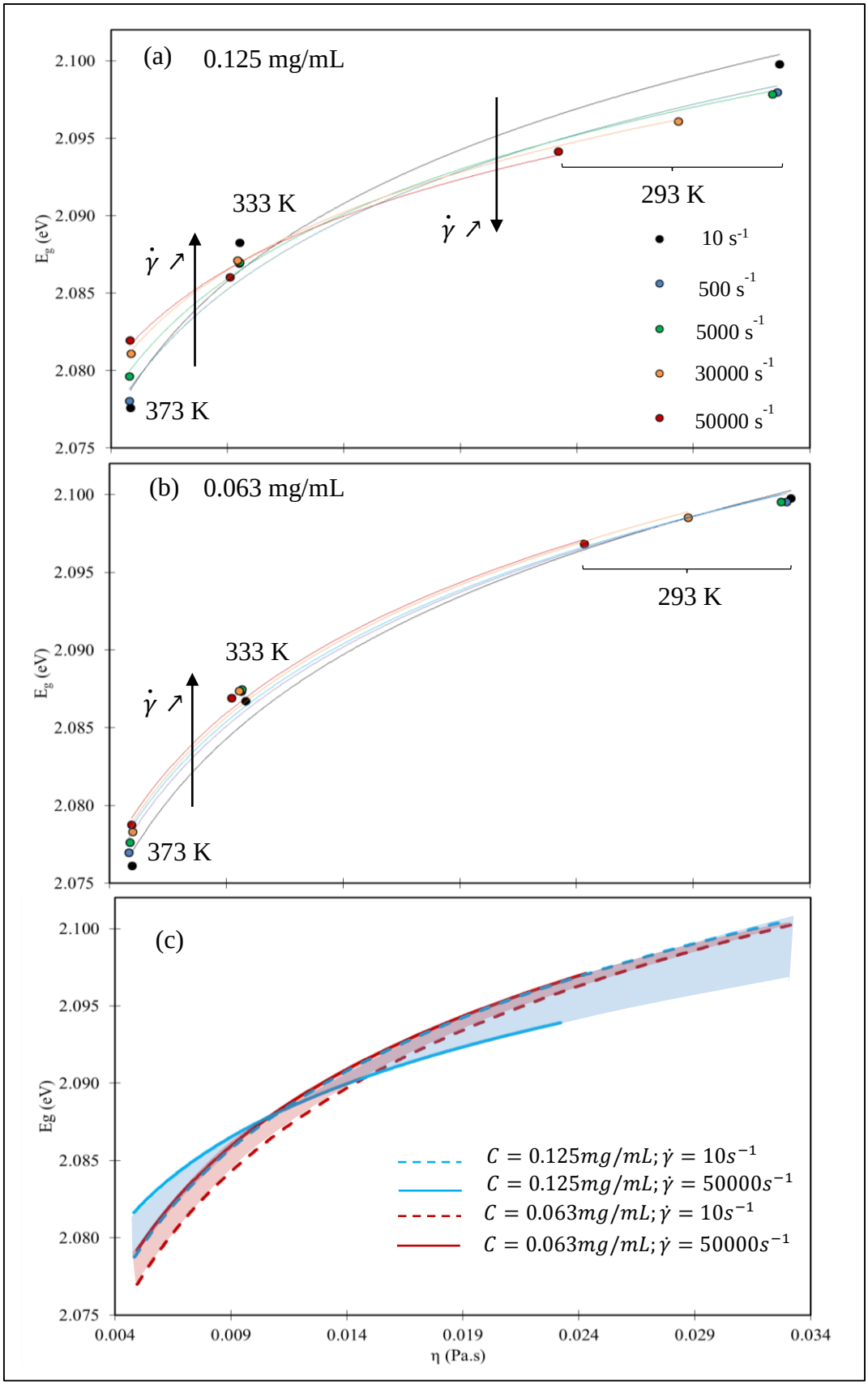

Figure IV.5. Variation of the emission energy of CdSe/CdS/ZnS QDs dispersed in squalane as a function: (a) 0.125 mg/mL; (b) 0.063 mg/mL; (c) 0.125 and 0.063 mg/mL.

IV.4.1.1. Influence of shear rate – Which mechanisms?

Although the variations of emission energy are small, some correlation seems to exist between them and the values of shear rate and the concentration of the QDs. The dispersions in emission energy observed at isoviscous (or isothermal) conditions indicate the existence of other mechanisms, indirectly induced by shear rate, which can alter the response of the QDs. These mechanisms (i) decrease the emission energy at the lowest temperature (298 K), (ii) can increase the emission energy at the highest temperature (373 K) and (iii) have less effect at the lowest concentration (0.063 mg/mL).

The dependence of the above-mentioned dispersions on concentration demonstrates that these mechanisms are the consequence of some residual interaction effects (which seem to persist despite the minimization of the concentration of the QDs, as presented in the previous chapter). On the other hand, the opposite variations at low and high temperatures is indicative of the competition between different mechanisms. In what follows, the implications on the response of the QDs og the different interaction-related parameters will be examined one by one, provided that these parameters satisfy the following conditions:

- They can exist in a parallel-plates geometry;
- They can be enhanced with shear rate under isoviscous and isothermal conditions.

Flow-enhanced energy transfer

As presented in chapters II and III, the diffusion of the particles can enhance the efficiency of FRET. This statement could be generalized to any parameter capable of accelerating the movement of the particles relative to each other, such as the laminar or turbulent flow of the solution (induced by the angular velocity ω). When the efficiency of energy transfer is enhanced, the contribution of the smaller QDs to the emission spectrum reduces, which leads to a lower emission energy and QDs sensitivity to temperature variations (or viscosity variations). These effects may explain partly the decrease of temperature sensitivity with increasing shear rate as well as the decrease in emission energy at 293 K for the highest concentration (0.125 mg/mL). Based on this analysis, the apparent increase in emission energy with increasing shear rate at $T = 373\ K$ is due to the lower temperature (or viscosity) sensitivity, and it is nothing else than a smaller energy decrease with increasing temperature (or viscosity).

The turbulence is more likely to occur at high shear rates and temperatures, and when it occurs, it generally leads to an overestimation of the viscosity. Such is not the case referring to the viscosity measurements (see Figure IV.3), which demonstrates that the flow remains laminar under the different conditions.

Energy transfer limitation by film thickness: Influence of solution ejection

As mentioned in the previous chapters, film thickness is one of the trivial parameters upon which the efficiency of energy transfer depends. Furthermore, as the nonradiative energy transfer can be enhanced by radiative energy transfer through excitation migration process (see Figure III.13), the efficiency of FRET also decreases with decreasing film thickness. Consequently, when film thickness

is reduced, both radiative and nonradiative energy transfer efficiencies decrease, resulting in the shift of emission energy to higher values.

In a rheometer, the lubricants of low viscosity can be ejected, especially at high shear rates. For squalane some ejection can exist at high temperature. The ejection is however negligible referring to the viscosity measurements at the highest temperature and shear rates (see Figure IV.3).

Viscosity gradient- and shear-rate gradient-induced concentration fluctuation

Many theoretical and experimental studies have been reported in the last decades on the migration of the particles in colloidal suspensions. Most of these studies considered micro-sized particles, or more precisely, non-Brownian particles, in which the Brownian motion has negligible effect[175,176]. Recently, more interest has been accorded to the so-called nanofluids, owing to their excellent thermal conductivity. They are defined as suspensions of particles significantly smaller than 100 nm. The migration of the particles in nanofluids have also been reported[177]. In these fluids, the self-diffusion of the particles due to the Brownian motion has to be taken into account in addition to the other mechanisms of migration (reported earlier in literature for non-Brownian particles). In what follows, a framework for quantitative analysis applied on both parallel-plates (in this paragraph) and cone-plate geometries (in paragraph IV.4.2, when discussion the stability of QDs response) will be presented.

The total flux $\boldsymbol{J}$ of the Brownian particles is the sum of different terms: the shear-rate flux $\boldsymbol{J}_{\dot{\gamma}}$, the viscosity flux $\boldsymbol{J}_{\boldsymbol{\eta}}$, the curvature flux $\boldsymbol{J}_{\boldsymbol{C}}$ and the Brownian flux $\boldsymbol{J}_{\boldsymbol{B}}$ [175–177]:

$$\boldsymbol{J} = \boldsymbol{J}_{\dot{\gamma}} + \boldsymbol{J}_{\eta} + \boldsymbol{J}_{C} + \boldsymbol{J}_{B} \qquad (IV.3)$$

$$\boldsymbol{J}_{\dot{\gamma}} = -K_{\dot{\gamma}} r^2 \left(\Phi^2 \nabla\dot{\gamma} + \Phi\dot{\gamma}\nabla\Phi \right) \qquad (IV.4)$$

$$J_{\eta} = -K_{\eta} r^2 \Phi^2 \frac{\dot{\gamma}}{\eta} \nabla\eta \qquad (IV.5)$$

$$J_{B} = -D\nabla\Phi = -\frac{k_B T}{6\pi\eta r^4} \nabla\Phi \qquad (IV.6)$$

Where Φ is the volume fraction of the particles.

In a rotational symmetry (such as the one found in parallel-plates and cone-plate geometries), the curvature flux is given by:

$$J_{C} = K_{C} r^2 \dot{\gamma} \Phi^2 \frac{1}{l} \qquad (IV.7)$$

These different terms imply the migration of the particles from the zones of higher shear rate, viscosity, streamlines curvature and concentration to zones of lower shear rate, viscosity, streamlines curvature and concentration, respectively[177]. Indeed, the general diffusion equation is written in the following form:

$$\frac{\partial \Phi}{\partial t} = -\nabla . \boldsymbol{J} \qquad (IV.8)$$

In particular, in rotational symmetry and under steady-state conditions ($\partial\Phi/\partial t = 0$), the diffusion equation becomes:

$$\underbrace{\left(\underbrace{K_{\dot{\gamma}}\,\dot{\gamma}\frac{1}{\Phi}}_{\text{Shear gradient flux}} + \underbrace{\frac{k_B T}{6\pi\eta r^4}\frac{1}{\Phi^2}}_{\text{Brownian diffusion flux}} \right)}_{\text{Mechanisms reducing concentration gradient}} \frac{\partial \Phi}{\partial l} = \underbrace{K_C \dot{\gamma}\frac{1}{l}}_{\text{Curvature gradient flux}} + \underbrace{K_{\dot{\gamma}}\frac{\partial \dot{\gamma}}{\partial l}}_{\text{Shear gradient flux}} + \underbrace{K_\eta \frac{\dot{\gamma}}{\eta}\overbrace{\frac{\partial \eta}{\partial (\delta T)}}^{\partial\eta/\partial l}\frac{\partial (\delta T)}{\partial \dot{\gamma}}\frac{\partial \dot{\gamma}}{\partial l}}_{\text{Viscosity gradient flux}} \qquad (IV.9)$$

Mechanisms enhancing concentration gradient

It can be noticed that by increasing the sum of the terms on the right, the volume fraction gradient $\partial\Phi/\partial l$ is enhanced, and that increasing the terms on the left of $\partial\Phi/\partial l$ leads to smaller gradients (or the redistribution of particles). The different signs of the terms on the right determine whether the corresponding mechanism leads to an outward (positive sign) or inward (negative sign) migration. In this equation, we assumed that the viscosity-gradient $\partial\eta/\partial l$ is induced by the shear-heating δT of the solvent

[I].

The shear rate flux induces opposed effects, as it appears in both sides of Equation (IV.9). This is because the shear rate flux is the sum of two fluxes (see Equation (IV.4)). The first implies the migration of the particles even where there is no gradient in volume fraction. This flux arises from the higher number of interparticle interactions on the side of the solution experiencing higher shear rates. The second flux, however, arises from the higher frequency of interactions in the zones of higher concentrations. For these reasons, when a suspension with constant Φ is sheared, the first term in Equation (IV.4) gives rise to a flux, which in turn causes a concentration gradient, enabling the second term to induce another flux in the opposite direction[175].

Brownian motions can also participate in the redistribution of the particles. Indeed, these motions lead to the collision of the particles, especially at zones of higher concentrations, resulting in the migration of the particles to zones of lower concentrations.

From the description above, the redistribution of the particles is induced by shear-rate and Brownian fluxes. The difference between these two fluxes relies in their dependence on shear rate. While the collisions caused by shear-rate flux are cancelled when the rheometer is stopped, those induced by

[I] In literature, the effect of particles concentration is supposed to modify the viscosity of the solution. However, we saw that the viscosity of the solvent is very close to the viscosity of the suspension with the very low concentrations examined in the dynamic study (Figure IV.1). The temperature gradient induced by radius-dependent shear-heating is introduced as a possible origin of viscosity gradient.

self-diffusion persist. For the same reason, when shear rate is very high, the contribution of self-diffusion to particle migration becomes negligible, and the particles behave as they were non-Brownian. In this case, Equation (IV.9) reduces to:

$$K_{\dot{\gamma}}\,\dot{\gamma}\frac{1}{\Phi}\frac{\partial\Phi}{\partial l}=K_C\dot{\gamma}\frac{1}{l}-K_{\dot{\gamma}}\frac{\partial\dot{\gamma}}{\partial l}-K_\eta\frac{\dot{\gamma}}{\eta}\frac{\partial\eta}{\partial(\delta T)}\frac{\partial(\delta T)}{\partial\dot{\gamma}}\frac{\partial\dot{\gamma}}{\partial l} \qquad (IV.10)$$

Now, if we consider parallel-plates geometry, equation (IV.9) yields:

$$\left(K_{\dot{\gamma}}\frac{\omega l}{H_0}\frac{1}{\Phi}+\frac{k_BT}{6\pi\eta r^4}\frac{1}{\Phi^2}\right)\frac{\partial\Phi}{\partial l}=\left(K_C-K_{\dot{\gamma}}\right)\frac{\omega}{H_0}-K_\eta\left(\frac{\omega}{H_0}\right)^2 l\frac{1}{\eta}\frac{\partial\eta}{\partial(\delta T)}\frac{\partial(\delta T)}{\partial\dot{\gamma}} \qquad (IV.11)$$

Or:

$$\left(K_{\dot{\gamma}}\,l\frac{1}{\Phi}+\frac{H_0}{\omega}\frac{k_BT}{6\pi\eta r^4}\frac{1}{\Phi^2}\right)\frac{\partial\Phi}{\partial l}=K_C-K_{\dot{\gamma}}-K_\eta\frac{\omega l}{H_0}\frac{1}{\eta}\frac{\partial\eta}{\partial(\delta T)}\frac{\partial(\delta T)}{\partial\dot{\gamma}} \qquad (IV.12)$$

Three particular cases can be distinguished:

- **Case n°1**: Zero angular velocity ($\omega = 0$):

$$\frac{\partial\Phi}{\partial l}=0 \qquad (IV.13)$$

- **Case n°2**: Very high angular velocity ($\omega \to \infty$):

$$\frac{\partial\Phi}{\partial l}=-\frac{K_\eta}{K_{\dot{\gamma}}}\frac{\omega}{H_0}\Phi\left(\frac{1}{\eta}\frac{\partial\eta}{\partial(\delta T)}\frac{\partial(\delta T)}{\partial\dot{\gamma}}\right) \qquad (IV.14)$$

- **Case n°3**: Negligible shear-heating ($\delta T = 0$) :

$$\left(K_{\dot{\gamma}}\,l\frac{1}{\Phi}+\frac{H_0}{\omega}\frac{k_BT}{6\pi\eta r^4}\frac{1}{\Phi^2}\right)\frac{\partial\Phi}{\partial l}=K_C-K_{\dot{\gamma}} \qquad (IV.15)$$

The equation obtained in case n°1 results in a uniform volume fraction. In case n°2, an inward migration is expected. The case n°3 represents for instance particle migration in squalane at high temperatures. Indeed, due to the low viscosity of the liquid, the shear-induced heating is negligible. In this case, the term $K_C - K_{\dot{\gamma}}$ determines whereas the outward migration or the inward migration is dominant. When $K_C > K_{\dot{\gamma}}$, an outward migration is expected, and an inward migration is expected in the opposite case. For all the other cases, the direction and the magnitude of particles migration is determined by the values of different flux constants ($K_{\dot{\gamma}}$, K_η, K_C and K_B

[*]), as well as the angular velocity ω, the gap H_0, the self-diffusion D of the particles, and the concentration C (or volume fraction Φ) of the particles.

As one can notice, the four mechanisms of particle migration can compete with each other, and their corresponding contributions depend considerably on the sample temperature[†] and the value of the shear rate. More importantly, they can induce a gradient in the volume fraction and consequently fluctuations in the local concentration. These fluctuations may explain the different, and sometimes opposite, variations of the emission energy with shear rate. Namely, when the local concentration is decreased, the emission shifts to higher values, and the opposite happens when the local concentration is increased (as a result of the dependence of the efficiency of energy transfer on the concentration of the particles).

Of course, more experimental tests and quantitative analysis are needed to confirm the existence of such migrations during the different tests. Fluorescence microscope can be used to measure the gradient of the concentration along the distance l from the rotating axis (by simply observing the variation in brightness). Other tests will be proposed in paragraph IV.4.1.3 to verify the existence of such migration and, more generally, to quantify the contribution of the different interaction-related parameters responsible of the influence of shear rate.

IV.4.1.2. Shear rate indirect influence on the emission energy

In this paragraph, a qualitative analysis will be presented on the indirect influence of shear rate on the emission energy. These effects, as described above, can be induced by:

- The shear-heating of the solution;
- Two possible mechanisms affecting the interactions between QDs (*i.e.* flow-enhanced energy transfer and particle migration).

In order to account for these different effects, we can write:

$$E_g\left(T,\dot{\gamma}\right)=E_g^B\left(V_{Crystal}\left(T,\dot{\gamma}\right),r^*\left(T,\dot{\gamma}\right)\right)+E_g^Q\left(r^*\left(T,\dot{\gamma}\right)\right) \qquad (IV.16)$$

Or:

$$E_g\left(T,\dot{\gamma}\right)=E_g^B\left(0\right)+E_g^Q\left(r^*\left(T,\dot{\gamma}\right)\right) - \frac{\left(\alpha_1+\delta\alpha_1\left(r^*\left(T,\dot{\gamma}\right)\right)\right)\left(T+\delta T\left(T,\dot{\gamma}\right)\right)^2}{\left(T+\delta T\left(T,\dot{\gamma}\right)\right)+\beta_1+\delta\beta_1\left(r^*\right)} \qquad (IV.17)$$

[*] These constants need to be determined through comparison between theoretical predictions (diffusion equation applied to a given system, for example plate-plate geometry or cone-plate geometry) with experimental concentration profiles (measured by fluorescence imaging for instance).

[†] For instance, the contribution of Brownian motion increases with increasing temperature and the resulting viscosity drop. The contribution of the viscosity gradient induced by shear-heating depends, as mentioned above, on the viscosity of the sample (and thus on its temperature).

The emission energy depends on the apparent radius r^*. This radius accounts, as shown in the previous chapter, for the thermal expansion of the QDs and the energy transfer between them:

$$r^*\left(T,\dot{\gamma}\right)=r\left(T,\dot{\gamma}\right)+\delta r\left(T,\dot{\gamma}\right) \qquad (IV.18)$$

Where:

$$r\left(T,\dot{\gamma}\right)=r_0+\Delta r\left(T+\delta T\left(T,\dot{\gamma}\right)\right) \qquad (IV.19)$$

$$\delta r\left(T,\dot{\gamma}\right)=\delta r\left(\omega,C\pm\delta C\left(J\left(T,\dot{\gamma}\right)\right)\right) \qquad (IV.20)$$

Where Δr is the thermal expansion of the QDs, and δr is the shift in radius induced by energy transfer from smaller to bigger QDs. Figure IV.6 illustrates the influence of the different terms in Equations (IV.17) to (IV.20) on emission energy *versus* viscosity plots.

The term $\delta T(T,\dot{\gamma})$ is the shear-heating and it induces:

- A decrease of both the bulk ($E_g^B - \delta E_g^B$) and the quantum confinement ($E_g^Q - \delta E_g^Q$) contributions, and thus a decrease of the total emission energy;
- A viscosity drop ($\eta - \delta\eta$);

Shear-heating is significant at low temperatures, and it explains why some points (E_g,η) measured at $T = 293\ K$ and high shear rates were found to be spaced from the other points measured at the same temperature but at lower shear rates (see Figure IV.6 (a)).

The shift δr, which expresses the efficiency of energy transfer, depends on the flow induced by the angular velocity ω. This shift is enhanced when ω is increased, resulting in a lower emission energy, sensitivity to temperature variations $S_T^B - S_T^{B\text{-}ET}$ (lower $\delta\alpha_1$ value) and sensitivity to size variations $S_r^Q - S_r^{Q\text{-}ET}$ [*]. This effect can thus explain partly the decrease of the emission energy with increasing shear rate observed at $T = 293\ K$. The observed energy increase found at $T = 373\ K$ may arise partly from the lower sensitivity at high shear rates (see Figure IV.6 (b)).

[*] Based on the analysis, the effect of the flow induced by the angular velocity ω is similar to the effect of the concentration *C* presented in the previous chapter.

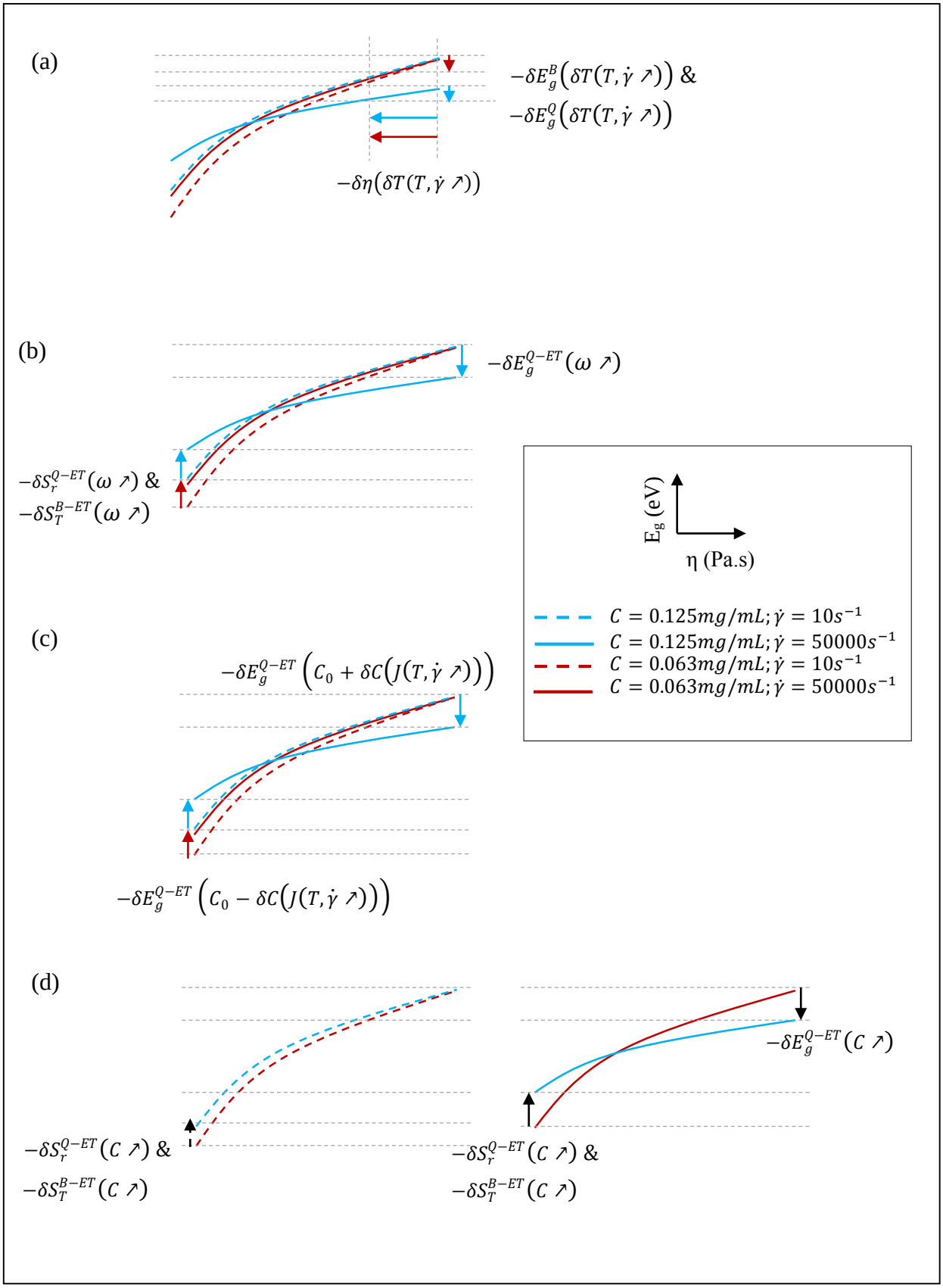

Figure IV.6. Illustration of the different terms in Equations (IV.16)to (IV.20), namely the shifts induced by (a) shear-heating; (b) shear-induced flow; (c) concentration fluctuation due to particle migration and (d) the decrease of the mean concentration.

The term $\delta C(J(T, \dot{\gamma}))$ represents the fluctuation in the local concentration of the QDs due to their migration *via* different competing fluxes. This fluctuation can be positive or negative depending on which flux term is dominant at a given temperature and shear rate, and it leads to a decrease of the emission energy in the first case and an increase in the second case. The fluctuation of the concentration may thus explain partly the decrease of emission energy observed at $T = 293\ K$ and the increase found at $T = 293\ K$ (see Figure IV.6 (c)). The consequences of concentration fluctuations and flow-enhanced energy transfer can be similar. Some complementary tests will be proposed in the paragraph IV.4.1.3 in order to evaluate the contribution of each mechanism (see paragraph IV.4.1.3).

When the mean concentration C is decreased from 0.125 to 0.063 mg/mL, the efficiency of energy transfer decreases, resulting in an enhanced sensitivity to temperature variations $S_T^{B\text{-}ET}$ and size variations $S_r^{Q\text{-}ET}$. Moreover, the sensitivity of the QDs to flow and concentration fluctuations becomes smaller which may explain the lower dispersion of the emission energy at isoviscous (isothermal) conditions with decreasing concentrations (see Figure IV.6 (d)).

IV.4.1.3. Complementary tests

It should be noticed however that further experiments would be needed in order to confirm the existence and the contribution of each one of the above-mentioned parameters, including:

- Measurements at lower concentrations in order to verify if the emission energy and the sensitivity of the QDs to viscosity (or actually temperature) variations becomes independent of shear rate and concentration;
- Measurements in a cone-plate geometry, in which shear-rate remains constant across the radius of the rotating disc, in order to estimate the significance of particle migration and its influence on the local concentration;
- Comparison of the QDs emission in a parallel-plates geometry at different radii on one hand, and the emission in a cone-plate geometry at different radii at the other hand. While film thickness is constant in the parallel-plates geometry, many other parameters are variable in the radial direction, such as shear rate, shear-heating, viscosity. In the cone-plate geometry, the variation of the film thickness in the radial direction keeps the other parameters constant in this direction. This comparisons would allow for a better estimation of the contribution of the different factors influencing the QDs response.

IV.4.1.4. Evaluation of the temperature elevation at high shear rates

As mentioned above, at high shear rates (30000 s^{-1} and 50000 s^{-1}) and when working at ambient temperature, a viscosity and an energy drop is observed due to the elevation of the temperature δT. This temperature rise can be evaluated by two independent ways:

- By using the models for viscosity-temperature dependence (WLF model presented in Appendix B).
- By using the calibration curves of the response of the QDs to temperature variations obtained in the static study (presented in the previous chapter).

Using the viscosity drop, the temperature elevation is estimated to be of about 3 and 8 K, for the shear rates 30000 s^{-1} and 50000 s^{-1}, respectively.

The value of the temperature sensitivity of -0.31 meV/K is used to deduce the temperature rise from the energy decrease. The variations of emission energy as illustrated in Figure IV.6 (a) have to be taken into account for this estimation (downward red arrow for 0.063 mg/mL, and downward blue arrow for 0.125 mg/mL). This is actually necessary in order to account only for emission energy decrease induced by heating (and not the one induced by shearing under isothermal conditions).

The lowest concentration, i.e. *C = 0.063 mg/mL*, yields a temperature rise of 4 and 9.5 K for the shear rates 30000 s^{-1} and 50000 s^{-1}, respectively. The concentration *C = 0.125 mg/mL* yields however a higher estimation: 2.9 and 9.1 K for the shear rates 30000 s^{-1} and 50000 s^{-1}, respectively.

The similarity of the estimations of temperature elevation obtained from the two approaches demonstrates the potential of these QDs for temperature probing in various applications.

IV.4.2. Stability under long periods of shearing

In this paragraph the stability of the QDs response under long periods of shear rate is verified. Experiments were performed in the following conditions:

- The QDs were dispersed in squalane with the lower of the two concentrations (0.063 mg/mL) in order to reduce interaction- and apparatus-related effects;
- Cone-plate geometry was used to insure constant radial shear rate and to minimize possible particle migrations;
- The shear rate and the temperature were fixed at 19000 s^{-1} (corresponding to an angular velocity $\omega = 331\ rad/s$) and 333 K, respectively;
- Another test under the same temperature was performed in a parallel-plates geometry for comparison.

In both tests, the PL of the QDs was collected at three radii *l* from the axis of rotation: $l_1 = 8.33\ mm$, $l_2 = 13.33\ mm$ and $l_3 = 18.33\ mm$. The measurements at different radii were carried out in order to study the contribution of the different mechanisms listed in paragraph IV.4.1.1 leading to the variation of the response of the QDs with shear rate under isothermal conditions.

The different operating conditions are summarized Table IV.2.

Geometry	Radius (mm)	Film thickness (mm)	Angular velocity (rad/s)	Shear rate (s^{-1})
Parallel-plates	8.3	0.04	150	12500
	13.3	=	=	20000
	18.3	=	=	27500
Cone-plate	8.3	0.15	331	19000
	13.3	0.23	=	=
	18.3	0.32	=	=

Table IV.2. Comparison between the operating conditions in the parallel-plates geometry and cone-plate geometry.

Figure IV.7 shows the measurements obtained with the two geometries. As one can notice, the response of the QDs is very stable in the cone-plate geometry, and is virtually independent of the radius *l*. In the parallel-plates geometry, however, the radius seems to have some influence on the response of the QDs, especially when comparing the emission energy obtained at *l = 18.3 mm* with the two other radii.

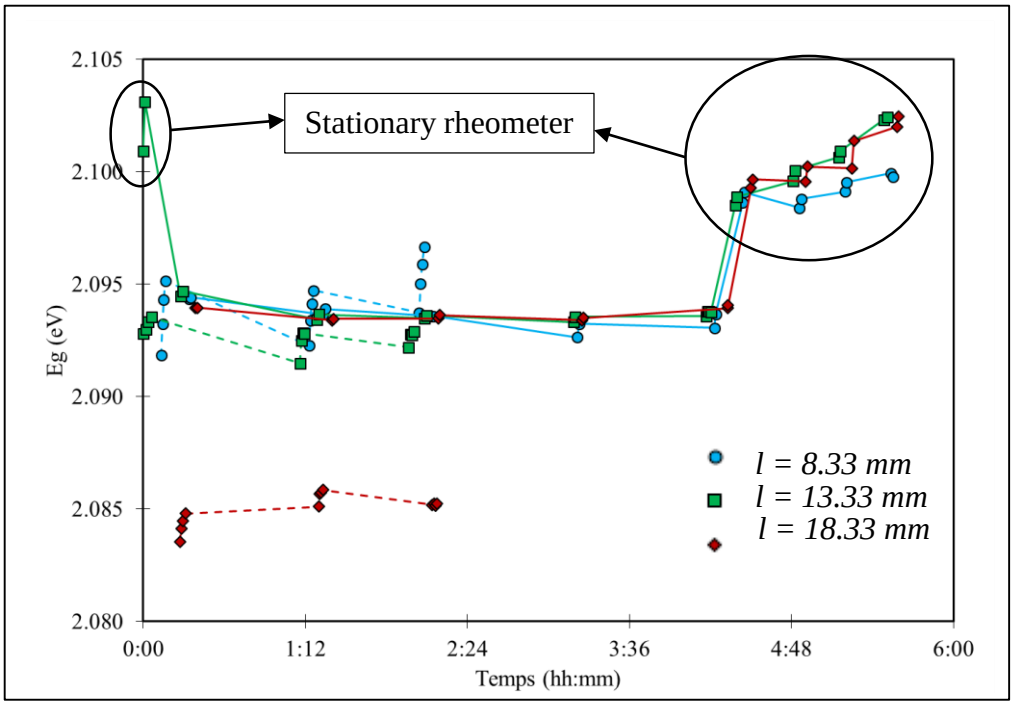

Figure IV.7. Emission energy stability with shear rate under long periods of shear stress obtained with (Continuous lines) Cone-plate geometry and (Dashed lines) parallel-plates geometry.

The constant value of emission energy with cone-plate geometry demonstrates that there is no significant concentration gradient along the three tested radii. In this geometry, and under steady-state conditions, the diffusion equation (Equation (IV.9)) yields:

$$\left(K_{\dot{\gamma}}\frac{\omega}{\tan\varphi}\frac{1}{\Phi}+\frac{k_BT}{6\pi\eta r^4}\frac{1}{\Phi^2}\right)l\frac{\partial\Phi}{\partial l}=K_C\frac{\omega}{\tan\varphi} \qquad (IV.21)$$

In contrary to the parallel-plates geometry, there is no flux induced by viscosity gradient. Such is the case because of the constant value of shear rate in cone-pate geometry (Equation (IV.2))*. This may explain the constant emission energy between *l = 8.33* and *l = 18.33* mm.

The variable emission energy in parallel-plates geometry can be explained in three possible ways:

- The radial gradient of shear rate;
- The radial gradient in temperature rise and/or viscosity drop due to self-heating;

* Despite the zero shear gradient, the coefficient $K_{\dot{\gamma}}$ is found on the left of the equation (IV.21). This is because, the collision of the particles induced by shearing results in the redistribution of the particles.

– The radial gradient in concentration due to particles migration.

The variation of the emission energy as a function of shear rate at *333 K* and with *C = 0.063 mg/mL* showed a weak increase of emission energy (Figure IV.5). The radial gradient of shear rate cannot thus explain the observations here. Based on viscosity measurements (Figure IV.3), temperature rise or viscosity drop due to shear-heating are not significant at *333 K*, especially for shear rates below 30000 s^{-1}. Therefore, the only possible explanation (among those mentioned above) of the emission energy decrease with the distance *l* (observed at 333 K) can be a concentration gradient induced by the migration of the particles. If this migration leads to a concentration increase between *l = 8.33* and *l = 18.33* mm, the interaction between QDs increases, and their emission energy shifts to lower values.

The points at the beginning and end of shearing with the cone-plate geometry and which are located at higher energies, were measured in the rheometer with zero angular velocity (*cf.* stationary rheometer in Figure IV.7). In contrary to the fast increase found at the beginning of the experiment, the return to the initial state seems to be rather slow.

An explanation of this observation is the eventual concentration gradient induced by particle migration, and the time needed for the Brownian motion to redistribute the QDs within the solvent. Indeed, when the rheometer is stopped, the total flux is equal to:

$$\boldsymbol{J} = \boldsymbol{J}_B = -\frac{k_B T}{6\pi\eta r^2}\nabla\Phi \qquad (IV.22)$$

Therefore:

$$\frac{\partial\Phi}{\partial t} = -\nabla\left(-\frac{k_B T}{6\pi\eta r^2}\nabla\Phi\right) = \frac{k_B T}{6\pi\eta r^2}\nabla.\nabla\Phi \qquad (IV.23)$$

In a rotational symmetry, the previous equation reduces to:

$$\frac{\partial\Phi}{\partial t} = \frac{k_B T}{6\pi\eta r^2}\frac{\partial^2\Phi}{\partial l^2} \qquad (IV.24)$$

With:

$$\Phi\left(l, t=0\right) = \Phi_0\left(l\right) \qquad (IV.25)$$

$\Phi_0(l)$ is the volume fraction distribution of the particles just after stopping the rheometer. It can be taken as the solution of the steady-state equation obtained after a sufficiently long period of shearing (solution of the equation (IV.9)).

The solution of the Equation (IV.24), with the initial condition (IV.25) and the boundary condition expressed by a constant number of particles in the solvent (within the range between *l = 0* to *l = L*), implies the gradual redistribution of the particles with time. This process becomes slower and slower with time, in agreement with the observation on emission energy (the variation is rather fast just after

stopping the rheometer and becomes slower afterward). This time-dependent redistribution is illustrated in Figure IV.8 for particles initially distributed *via* an outward migration.

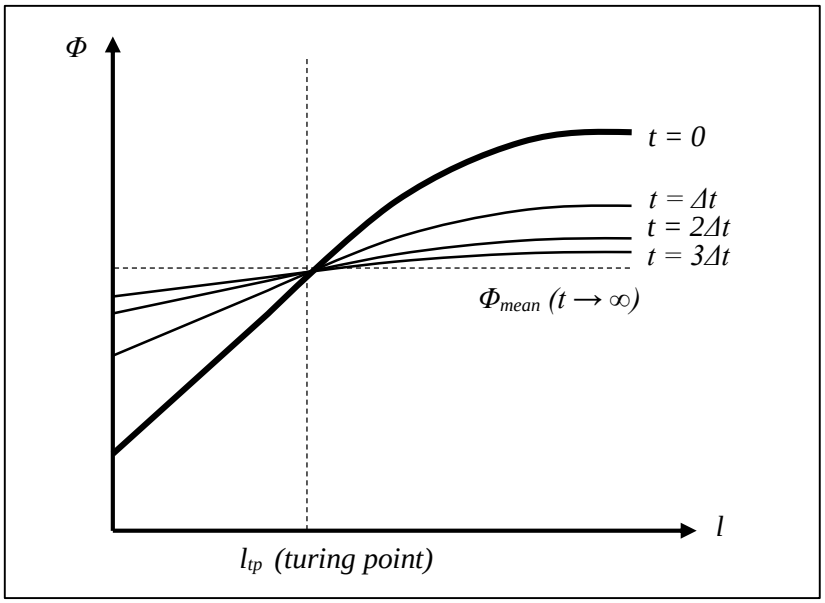

Figure IV.8. The influence of diffusion on the volume fraction initially distributed via an outward migration.

Now, the fast transition in the emission energy when the rheometer starts may be explained with the negligible contribution of the Brownian motion at high shear rates (Equation (IV.10)). The other mechanisms of particle migration are much faster than the one induce by the self-diffusion of the particles. Consequently, the transition takes place much more rapidly when the rheometer starts to rotate than when the rheometer is stopped.

The other possible explanation to the slow transition observed when the rheometer is stopped is that dynamic conditions improve thermal regulation and induce a more uniform temperature distribution throughout the sample. When the rheometer is stopped, the temperature distribution returns to the non-uniform distribution gradually with time.

The tests performed here cannot exclude the influence of the angular velocity on the emission energy or temperature sensitivity rate. To do so, the comparative study presented here has thus to be extended to various shear rates.

IV.5. Conclusion on the dynamic study

In summary, low concentrations (0.125 and 0.063 mg/mL) were used to perform dynamic studies on the CdSe/CdS/ZnS QDs, under controlled conditions of temperature and shear rate. Rheological study showed that with such concentrations, the viscosity of the solvent is almost unchanged with the presence of the QDs. Slight deviations from measurements performed in a SPSP (steel plate against steel plate) geometry were found in the geometries with one of the surfaces made from glass, because of the poor thermal conductivity of the latter.

The optical system was coupled with the rheometer in order to study the influence of the shear rate-induced flow on the response of the QDs. Measurements showed that, with low concentrations, the effect is very small. Despite the small influence of shear rate, some correlation between its magnitude and the emission energy was found. On the other hand, the dependence on shear rate was found to decrease with decreasing concentration. Based on these observations, the shear rate can be classified as an interaction-related parameter. Two mechanisms were proposed to explain the influence of shear rate, namely: (i) the enhancement of the energy transfer efficiency with the flow of the solution (induced by the angular velocity) and (ii) the migration of the particles due to the various radial gradients present within the system (shear rate, viscosity, streamline curvature and concentration). Additional experiments are however needed to elucidate further the contribution of each one of these mechanisms. The fact that the influence of shear rate is enhanced with increasing concentration demonstrates the importance of the concentration minimization presented in the previous chapter. It shows the necessity of studying even lower concentrations (in order to eliminate the residual interaction effect responsible of the small influence of shear rate).

Furthermore, some shear-heating was observed at 293 K and under high shear rates (30000 and $50000 s^{-1}$) through the PL measurements. Such finding demonstrates again the potential of these QDs for temperature probing in various applications.

Other tests were performed in order to verify the stability of the QDs response under long periods of shearing. The QDs were found to yield almost unchanged emission during the shearing. These tests were carried out in parallel-plates and cone-plate geometry. Some differences were observed between the results obtained with these two geometries, as well as between the emission energies with rotating and stationary rheometer. Particle migration and/or the difficulties in thermal regulation encountered with geometry used for PL study were proposed as possible explanations for such differences.

Conclusions

This thesis was a first step toward to the development of a new *in situ* technique allowing for instantaneous temperature and pressure measurements in elastohydrodynamic (EHD) contacts.

The technique exploits the sensitivity of the photoluminescence (PL) of some nanosized semiconductor crystals, or quantum dots (QDs), to these two parameters. The investigations were performed in two main parts. The first part, aimed at calibrating the response of CdSe/CdS/ZnS QDs to temperature/pressure variations under static conditions, while in the second part, the influence of dynamic conditions on these QDs was examined but limited to temperature and shear rate variations only. A comprehensive study was performed in order to identify the different parameters capable of affecting the PL of the QDs. They were classified, as shown in the following figure, in two main groups:

- Intrinsic parameters, in the sense that they arise from the structure and the properties of the sample under investigation. They are divided in dimension-related and interaction-related parameters;
- External parameters, in the sense that they depend upon the measurement system.

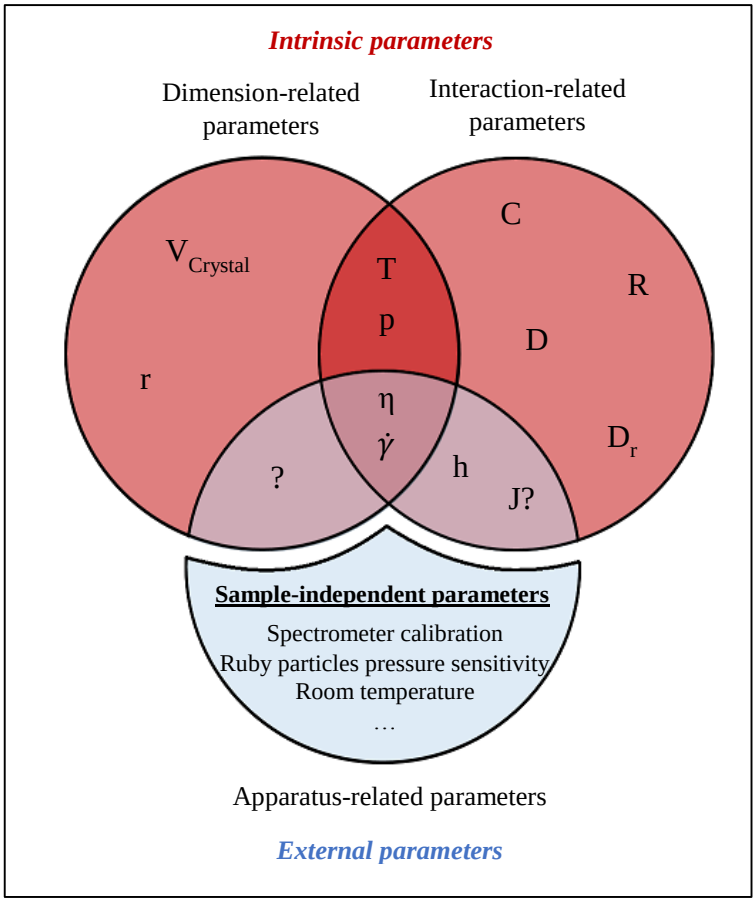

Classification of the influencing parameters in the characterization of the QDs.

The two substantial dimension-related parameters are the crystalline structure (V_{Cryst}) and the size (r) of the QDs. Their dependence on temperature (T) and pressure (p) was the reason why these nanoparticles were chosen as sensors in our study.

Interaction effects emerge whenever an assembly of QDs is considered. The efficiency of these effects depend naturally on the QDs concentration (C), the distances between them (R), and their movement relative to each other. Such movements can be induced by the diffusion of the QD due to Brownian motions (D), the flow of the solvent induced by shearing ($\dot{\gamma}$), and the

migration of the particles (J) induced by the different gradients (temperature, pressure, viscosity, shear rate, etc.) existing within the sample. These latter parameters depend on the viscosity (η) of the solvent, itself depending on the temperature and the pressure. The interaction between QDs can be affected also by the thickness of the sample (h), especially for radiative energy transfer. QDs can also interact with the surrounding solvent molecules. Such interactions can be of physical and even chemical origin. Chemical effects are not a concern in our study, but physical effects can be induced for example when using polar lubricants (or additives). Polarity effect depends itself on the rotational diffusion (D_r) of the solvent molecules around the QDs.

Apparatus-related effects exist in all experimental measurements. Some of them are independent from the sample under consideration (see the figure, the part of the circle below). Some of them however arise from the dependence of the intrinsic parameters on the apparatus characteristics.

No doubt, a particular attention has to be paid to the first type of apparatus-related effects in order ensure the performance and the accuracy of the measuring system. For instance, the diffraction gratings, used in the spectrometers to separate light of different wavelengths (or energies) with high resolution, are sensitive to the room temperature. Therefore, room temperature has to be well controlled. Some corrections are even needed in some cases, as for example when ruby microparticles are used for pressure calibrations (correction with spectral lamps).

What is more critical is the parameters affecting the properties of the sample. The influence of some of these parameters was demonstrated in this study. In the measurements conducted with the rheometer, a glass surface was used for observations. Due to poor thermal conductivity of glass, shear-heating was induced within the solution. We saw also that the film thickness, which can vary considerably from one apparatus to another (to reach extreme reduced values in EHD contacts), can affect the interaction between the QDs. Particle migration is suspected to be possible, but its extent depends on the experimental conditions. For example, the gradient of shear rate existing in parallel-plates geometry can favor inward migration of the particles, whereas in cone-plate geometry, the shear rate remains constant along the radius of the rotating disc.

Now, since the long term aim of this project is to perform accurate temperature and pressure measurements, all the parasitic effects, arising from interaction or apparatus-related parameters, have to be identified and then minimized or quantified (for corrections). Our choice was to minimize these effects by reducing the concentration of the QDs. We showed in the static study that the sensitivity of the QDs to temperature and pressure variations becomes independent from the interaction-related parameters (concentration and the diffusion of the QDs) in highly diluted suspensions.

Some residual interaction-related effects were observed under dynamic study. Indeed, as mentioned above, flowing conditions can enhance the interaction between QDs. This finding suggests the necessity of working with even lower concentrations. It should be noted here that at this stage, the understanding results obtained under dynamic conditions is less developed due to the complexity of the problem and the numerous parameters involved. Further experiments are thus needed to clarify the observations and to verify the interpretations.

Although the aim of the current work is to isolate temperature and pressure effects, we should say that the existence of interaction-related effects may be considered as an opportunity for probing other relevant parameters in EHD contacts. Examples are the local viscosity and shear stress which have not yet been measured reliably, and which have a crucial influence in film and friction generation in EHD contacts.

A last question that we should raise here is how to uncouple temperature and pressure effects. Two approaches can be considered. The first consists of using all the characteristics of the steady-state emission spectrum, namely the energy at maximum emission and the FWHM. The second approach is to prepare a mixture of two types of QDs of distinguishable emission spectra and different *T/p* sensitivities. These two approaches can obviously be applied together for gaining in precision and/or for taking into account the influence of persisting parasitic parameters. This problem has to be addressed in subsequent studies..

References

1. Stribeck R. Characteristics of plain and roller bearings. *Zeit VDI.* 1902;46.
2. Habchi W, Bair S, Vergne P. On friction regimes in quantitative elastohydrodynamics. *Tribol Int.* 2013 Feb;58:107–117.
3. Czichos H. Tribology. A systems approach to the science and technology of friction, lubrication and wear. *Elsevier Sci Publ Co, 1978,.* 1978;414.
4. Spikes HA. Sixty years of EHL. *Lubr Sci.* 2006;18(4):265–291.
5. Hamrock BJ, Dowson D. Minimum film thickness in elliptical contacts for different regimes of fluid-film lubrication. In: Dowson, D., Taylot, C.M., Godet, M., Berthe D, editor. Proc. 5th Leeds-Lyon Symp. on Tribology, Elastohydrodynamics and Related Topics. London: Mechanical Engineering Publications Ltd.tran; 1979. p. 22–27.
6. Spikes H, Jie Z. History, Origins and Prediction of Elastohydrodynamic Friction. *Tribol Lett.* 2014;56(1):1–25.
7. Bair S, Vergne P, Kumar P, Poll G, Krupka I, Hartl M, et al. Comment on "History, Origins and Prediction of Elastohydrodynamic Friction" by Spikes and Jie. *Tribol Lett.* 2015;58(1):1–8.
8. Dowson D, Ehret P. Past, present and future studies in elastohydrodynamics. *J Eng Tribol.* 1999;213:317–333.
9. Petrusevich AI. Principal Conclusions from Contact-hydrodynamic Theory of Lubrication. *Izv Akad Nauk SSSR, Otd Tekh Nauk.* 1951;2(2):209–23.
10. Bair SS. High Pressure Rheology for Quantitative Elastohydrodynamics. Elsevier Science; 2007.
11. Hertz H. Uber den kontakt elastischer körper. *J Reine Angew Math.* 1881;92:156.
12. Reynolds O. On the Theory of Lubrication and Its Application to Mr. Beauchamp Tower's Experiments, Including an Experimental Determination of the Viscosity of Olive Oil. *Proc R Soc London.* 1886;40(242-245):191–203.
13. Tower B. First report on friction experiments. *Proc Inst Mech Eng.* 1883;34(1):632–659.
14. Zhu D, Wang Q. J. Elastohydrodynamic Lubrication: A Gateway to Interfacial Mechanics - Review and Prospect. *J Tribol.* 2011;133(4):41001.
15. Martin HM. Lubrication of Gear Teeth. *Engineering.* 1916;102:119–121.
16. Peppler W. Druckübertragung an geschmiert zylindrischen Gleit und Walzflächen. 1938;VDI Verlag.

17. Gatcombe EK. Lubrication characteristics of involute spur-gears—a theoretical investigation,. *Trans Am Soc Mech Eng.* 1945;67:177–181.

18. Ertel AM. Hydrodynamic Calculation of Lubrication of Curved Surfaces (Gears, Rolling Bearings, Highly Loaded Journal Bearings etc.). *Akad Nauk Moscow.* 64AD;1945.

19. Dowson D, Higginson GR. A Numerical Solution to the Elasto-Hydrodynamic Problem. *J Mech Eng Sci.* 1959;1:6–15.

20. Mohrenstein-Ertel A. Die Berechnung der hydrodynamischen Schmierung gekrümmter Oberflächen unter hoher Belastung und Relativbewegung. *Fortschrittsberichte VDI.* 1984;1.

21. Gohar R. Elastohydrodynamics. Imperial College Press; 2001.

22. Lugt PM, Morales-Espejel GE. A Review of Elasto-Hydrodynamic Lubrication Theory. *Tribol Trans.* 2011;54(3):470–496.

23. Gohar R, Cameron A. Optical Measurement of Oil Film Thickness under Elasto-hydrodynamic Lubrication. *Nature.* 1963 Nov 2;200(4905):458–459.

24. Cameron A, Gohar R. Theoretical and Experimental Studies of the Oil Film in Lubricated Point Contact. *Proc R Soc A Math Phys Eng Sci.* 1966 Apr 26;291(1427):520–536.

25. Crook AW. The Lubrication of Rollers II. Film Thickness with Relation to Viscosity and Speed. *Philos Trans R Soc London A Math Phys Eng Sci.* 1961 Dec 21;254(1040):223–236.

26. Archard JF, Kirk MT. Lubrication at Point Contacts. *Proc R Soc London A Math Phys Eng Sci.* 1961 May 23;261(1307):532–550.

27. Hamilton GM, Moore SL. Deformation and Pressure in an Elastohydrodynamic Contact. *Proc R Soc A Math Phys Eng Sci.* 1971 May 4;322(1550):313–330.

28. Albahrani SMB, Philippon D, Vergne P, Bluet JM. A review of in situ methodologies for studying elastohydrodynamic lubrication. *Proc Inst Mech Eng Part J J Eng Tribol.* 2015 Jun 17;

29. Smith FW. Lubricant behaviour in concentrated contact systems — the castor oil-steel system. *Wear.* 1959 May;2(4):250–263.

30. Bair S, Winer WO. Shear Strength Measurements of Lubricants at High Pressure. *J Lubr Technol.* 1979 Jul 1;101(3):251–257.

31. Clyens S, Evans CR, Johnson KL. Measurement of the Viscosity of Supercooled Liquids at High Shear Rates with a Hopkinson Torsion Bar. *Proc R Soc London A Math Phys Eng Sci.* 1982 May 8;381(1780):195–214.

32. Ramesh KT, Clifton RJ. A Pressure-Shear Plate Impact Experiment for Studying the Rheology of Lubricants at High Pressures and High Shearing Rates. *J Tribol.* 1987 Apr

1;109(2):215–222.

33. Feng R, Ramesh KT. The Rheology of Lubricants at High Shear Rates. *J Tribol.* 1993 Oct 1;115(4):640–647.

34. Jacobson B. A High Pressure-Short Time Shear Strength Analyzer for Lubricants. *J Tribol.* 1985 Apr 1;107(2):220–223.

35. Johnson KL, Roberts AD. Observations of Viscoelastic Behaviour of an Elastohydrodynamic Lubricant Film. *Proc R Soc London A Math Phys Eng Sci.* 1974 Mar 19;337(1609):217–242.

36. Bair S, McCabe C. A study of mechanical shear bands in liquids at high pressure. *Tribol Int.* 2004;37(10):783–789.

37. Evans CR, Johnson KL. The Rheological Properties of Elastohydrodynamic Lubricants. *Proc Inst Mech Eng Part C J Mech Eng Sci.* 1986 Sep 1;200(5):303–312.

38. Kaneta M, Nishikawa H, Kameishi K. Observation of Wall Slip in Elastohydrodynamic Lubrication. *J Tribol.* 1990 Jul 1;112(3):447–452.

39. Ehret P, Dowson D, Taylor CM. On lubricant transport conditions in elastohydrodynamic conjuctions. *Proc R Soc London A Math Phys Eng Sci.* 1998 Mar 8;454(1971):763–787.

40. Ponjavic A, Chennaoui M, Wong JSS. Through-Thickness Velocity Profile Measurements in an Elastohydrodynamic Contact. *Tribol Lett.* 2013 Mar 2;50(2):261–277.

41. Spikes HA, Anghel V, Glovnea R. Measurement of the Rheology of Lubricant Films Within Elastohydrodynamic Contacts. *Tribol Lett.* 2004 Oct;17(3):593–605.

42. Cheng HS, Sternlicht B. A numerical solution for the pressure, temperature, and film thickness between two infinitely long, lubricated rolling and sliding cylinders, under heavy loads. *J Fluids Eng.* 1965;87(3):695–704.

43. Dowson D, Whitaker A V. A Numerical Procedure for the Solution of the Elastohydrodynamic Problem of Rolling and Sliding Contacts Lubricated by a Newtonian Fluid. In: Proceedings of the Institution of Mechanical Engineers, Conference Proceedings. SAGE Publications; 1965. p. 57–71.

44. Guo F, Yang P, Qu S. On the Theory of Thermal Elastohydrodynamic Lubrication at High Slide-Roll Ratios—Circular Glass-Steel Contact Solution at Opposite Sliding. *J Tribol.* 2000 Sep 14;123(4):816–821.

45. Björling M, Habchi W, Bair S, Larsson R, Marklund P. Towards the true prediction of EHL friction. *Tribol Int.* 2013 Oct;66:19–26.

46. Habchi W, Vergne P, Bair S, Andersson O, Eyheramendy D, Morales-Espejel GE. Influence of pressure and temperature dependence of thermal properties of a lubricant

on the behaviour of circular {TEHD} contacts. *Tribol Int.* 2010;43(10):1842–1850.

47. Cameron A. Hydrodynamic Lubrication of Rotating Disks in Pure Sliding. A New Type of Oil Film Formation,. *J Inst Pet.* 1951;37:471–486.

48. El-Sisi SI, Shawki GSA. Measurement of Oil-Film Thickness Between Disks by Electrical Conductivity. *J Basic Eng.* 1960 Mar 1;82(1):12–16.

49. El-Sisi SI, Shawki GSA. Performance Characteristics of Lubricating Oil Film Between Rotating Disks. *J Basic Eng.* 1960 Mar 1;82(1):19–28.

50. Dyson A, Wilson AR. Film Thicknesses in Elastohydrodynamic Lubrication at High Slide/Roll Ratios. *Proc Inst Mech Eng Conf Proc.* 1968 Sep 1;183(16):81–97.

51. Kaneta M, Nishikawa H, Kameishi K, Sakai T, Ohno N. Effects of Elastic Moduli of Contact Surfaces in Elastohydrodynamic Lubrication. *J Tribol.* 1992 Jan 1;114(1):75.

52. Kaneta M, Nishikawa H, Kanada T, Matsuda K. Abnormal Phenomena Appearing in EHL Contacts. *J Tribol.* 1996 Oct 1;118(4):886–892.

53. Kaneta M. For the Establishment of a New EHL Theory. In: D. Dowson C.M. Taylor, P. Ehret, T.H.C. Childs, G. Dalmaz, Y. Berthier, L. Flamand, J.-M. Georges and A.A. Lubrecht BT - Tribology Series MP, editor. Lubrication at the FrontierThe Role of the Interface and Surface Layers in the Thin Film and Boundary RegimeProceedings of the 25th Leeds-Lyon Symposium on Tribology. Elsevier; 1999. p. 25–36.

54. Zhang Y, Wen S. An Analysis of Elastohydrodynamic Lubrication with Limiting Shear Stress: Part I—Theory and Solutions. *Tribol Trans.* 2002 Jan 1;45(2):135–144.

55. Yagi K, Kyogoku K, Nakahara T. Relationship Between Temperature Distribution in EHL Film and Dimple Formation. *J Tribol.* 2005;127(3):658.

56. Guo F, Li XM, Wong PL. A novel approach to measure slip-length of thin lubricant films under high pressures. *Tribol Int.* 2012;46(1):22–29.

57. Long DA. Raman spectroscopy. *New York.* 1977;1–12.

58. Ferraro JR. Introductory raman spectroscopy. Academic press; 2003.

59. Stuart B. Infrared spectroscopy. Wiley Online Library; 2005.

60. Dowson D. Elastohydrodynamic and micro-elastohydrodynamic lubrication. *Wear.* 1995;190(2):125–138.

61. Guangteng G, Cann PM, Olver A V, Spikes HA. An experimental study of film thickness between rough surfaces in EHD contacts. *Tribol Int.* 2000 Apr;33(3–4):183–189.

62. Křupka I, Hartl M. The effect of surface texturing on thin EHD lubrication films. *Tribol Int.* 2007 Jul;40(7):1100–1110.

63. Höhn B-R, Michaelis K, Kreil O. Influence of Surface Roughness on Pressure Distribution and Film Thickness in EHL-Contacts. *Tribol Int.* 2006;39(12):1719–1725.

64. Christensen H. The Oil Film in a Closing Gap. *Proc R Soc London A Math Phys Eng Sci.* 1962 Mar 20;266(1326):312–328.

65. Dowson D, Jones DA. Lubricant entrapment between approaching elastic solids. *Nature.* 1967;214:947–948.

66. Guo F, Kaneta M, Wang J, Nishikawa H, Yang P. Occurrence of a Noncentral Dimple in Squeezing EHL Contacts. *J Tribol.* 2006 Mar 19;128(3):632–640.

67. Safa MMA, Gohar R. Pressure Distribution Under a Ball Impacting a Thin Lubricant Layer. *J Tribol.* 1986 Jul 1;108(3):372–376.

68. Dowson D, Wang D. Impact elastohydrodynamics. In: D. Dowson T.H.C. Childs and G. Dalmaz BT - Tribology Series CMT, editor. Lubricants and LubricationProceedings of the 21th leeds-Lyon Symposium on Tribology. Elsevier; 1995. p. 565–582.

69. Glovnea RP, Spikes H a. Elastohydrodynamic film formation at the start-up of the motion. *Proc Inst Mech Eng Part J J Eng Tribol.* 2001;215(2):125–138.

70. Glovnea RP, Section H a ST, Jones WR, Nasa J. Behaviour of Several Lubricants for Space Applications under Transient Speed Conditions. *J Synth Lubr.* 2002;19(3):191–211.

71. Sugimura J, Spikes HA. Technique for measuring EHD film thickness in non-steady state contact conditions. In: D. Dowson T.H.C. Childs, G. Dalmaz, Y. Berthier, L. Flamand, J.-M. Georges and A.A. Lubrecht BT - Tribology Series CMT, editor. Elastohydrodynamics - ’96 Fundamentals and Applications in Lubrication and TractionProceedings of the 23rd Leeds-Lyon Symposium on Tribology held in the Institute of Tribology, Department of Mechanical Engineering. Elsevier; 1997. p. 91–100.

72. Hooke CJ. The Minimum Film Thickness in Lubricated Line Contacts during a Reversal of Entrainment—General Solution and the Development of a Design Chart. *Proc Inst Mech Eng Part J J Eng Tribol.* 1994 Mar 1;208(1):53–64.

73. Glovnea RP, Spikes H a. Behavior of EHD Films During Reversal of Entrainment in Cyclically Accelerated/Decelerated Motion. *Tribol Trans.* 2002;45(2):177–184.

74. Spikes HA. Thin Films in Elastohydrodynamic Lubrication: the Contribution of Experiment. *Proc Inst Mech Eng Part J J Eng Tribol.* 1999;213(J5):335–352.

75. Siripongse C, Rogers PR, Cameron A. Discharge through Oil Films. *Engineering.* 1958;186:146–147.

76. I. O. MacConochie AC. The Measurement of Oil-Film Thickness in Gear Teeth. *J Fluids Eng.* 1960;82(1):29–34.

77. Lane TB, Hughes JR. A Study of the Oil-Film Formation in Gears by Electrical Resistance Measurements. *Br J Appl Phys.* 1952 Oct 20;3(10):315–318.

78. Dwyer-Joyce RS, Drinkwater BW, Donohoe CJ. The Measurement of Lubricant-Film Thickness Using Ultrasound. *Proc R Soc A Math Phys Eng Sci.* 2003 Apr 8;459(2032):957–976.

79. Gardiner DJ, Baird EM, Craggs C, Dare-Edwards MP, Bell JC. Raman Microspectroscopy of a Working Elastohydrodynamic Contact. *Lubr Sci.* 1989 Jul 1;1(4):301–313.

80. Jubault I, Mansot JL, Vergne P, Mazuyer D. In-situ Pressure Measurements Using Raman Microspectroscopy in a Rolling Elastohydrodynamic Contact. *J Tribol.* 2002;124(1):114.

81. Miyata S, Höhn B-R, Michaelis K, Kreil O. Experimental Investigation of Temperature Rise in Elliptical EHL Contacts. *Tribol Int.* 2008 Nov;41(11):1074–1082.

82. Reddyhoff T, Spikes HA, Olver A V. Improved Infrared Temperature Mapping of Elastohydrodynamic Contacts. *Proc Inst Mech Eng Part J J Eng Tribol.* 2009 Dec 1;223(8):1165–1177.

83. Bair S, Qureshi F, Winer WO. Observations of Shear Localization in Liquid Lubricants Under Pressure. *J Tribol.* 1993 Jul 1;115(3):507–513.

84. Reddyhoff T, Choo JH, Spikes HA, Glovnea RP. Lubricant Flow in an Elastohydrodynamic Contact Using Fluorescence. *Tribol Lett.* 2010 Mar 24;38(3):207–215.

85. Wong PL, Li XM, Guo F. Evidence of lubricant slip on steel surface in EHL contact. *Tribol Int.* 2013;61:116–119.

86. Yagi K, Kyogoku K, Nakahara T. Mechanism of dimple formation under elastohydrodynamic conditions. In: D. Dowson G. Dalmaz and A.A Lubrecht BT - Tribology Series MP, editor. Tribological Research and Design for Engineering SystemsProceedings of the 29th Leeds-Lyon Symposium on Tribology. Elsevier; 2003. p. 111–120.

87. Roco M. The long view of nanotechnology development: the National Nanotechnology Initiative at 10 years. *J Nanoparticle Res.* 2011;13(2):427–445.

88. Royal Society, Royal Academy of Engineering GB. Nanoscience and Nanotechnologies: Opportunities and Uncertainties. Royal Society; 2004.

89. Drexler KE. Radical Abundance: How a Revolution in Nanotechnology Will Change Civilization. PublicAffairs; 2013.

90. Wolf EL, Medikonda M. Understanding the Nanotechnology Revolution. Wiley; 2012.

91. Jaque D, Vetrone F. Luminescence Nanothermometry. *Nanoscale.* 2012 Aug 7;4(15):4301–26.

92. Lee J, Kotov NA. Thermometer design at the nanoscale. *Nano Today.* 2007;2(1):48–51.

93. Wang S, Westcott S, Chen W. Nanoparticle Luminescence Thermometry. *J Phys Chem B.* 2002;106(43):11203–11209.

94. Caillier C, Ayari A, Gouttenoire V, San Miguel A, Jourdain V, Picher M, et al. Gold contact to individual metallic carbon nanotubes: A sensitive nanosensor for high-pressure. *Appl Phys Lett.* 2010;97(17):173111.

95. Sorkin V, Zhang Y. Graphene-based pressure nano-sensors. *J Mol Model.* 2011;17(11):2825–2830.

96. Hajjaji H. Nanosondes fluorescentes pour l'exploration des pressions et des températures dans les films lubrifiants. 2014;

97. Jabłoński A. Über den Mechanismus der Photolumineszenz von Farbstoffphosphoren. *Zeitschrift für Phys.* 1935 Jan;94(1-2):38–46.

98. Lakowicz JR. Principles of fluorescence spectroscopy. Springer Science & Business Media; 2007.

99. Kasha M. Characterization of electronic transitions in complex molecules. *Discuss Faraday Soc.* 1950;9(0):14–19.

100. Stokes GG. On the Change of Refrangibility of Light. *Philos Trans R Soc London.* 1852;142.

101. Valeur B, Berberan-Santos MN. Molecular Fluorescence: Principles and Applications. Wiley; 2013.

102. Berlman I. Handbook of florescence spectra of aromatic molecules. Elsevier; 2012.

103. Horiba Scientific. Time-resolved emission spectra / decay associated spectra [Internet]. Available from: http://www.horiba.com/fileadmin/uploads/Scientific/Documents/Fluorescence/Tech_Note4_-_TRES-DAS.pdf

104. Lin SH, Villaeys AA, Fujimura Y. Advances in Multi-Photon Processes and Spectroscopy. World Scientific; 1996.

105. Niebling T, Zhang F, Ali Z, Parak WJ, Heimbrodt W. Excitation dynamics in polymer-coated semiconductor quantum dots with integrated dye molecules: The role of reabsorption. *J Appl Phys.* 2009;106(10):-.

106. Förster T. Zwischenmolekulare energiewanderung und fluoreszenz (Intermolecular energy migration and fluorescence). *Ann Phys.* 437(1-2):55–75.

107. Clegg RM. Fluorescence resonance energy transfer. *Curr Opin Biotechnol.* 1995;6(1):103–110.

108. Dexter DL. A Theory of Sensitized Luminescence in Solids. *J Chem Phys.* 1953;21(5).

109. Lyo SK. Energy transfer of excitons between quantum wells separated by a wide barrier.

Phys Rev B. 2000 Nov 15;62(20):13641–13656.

110. Medintz I, Hildebrandt N. FRET-Förster Resonance Energy Transfer: From Theory to Applications. John Wiley & Sons; 2013.

111. Lippert E. Spektroskopische Bestimmung des Dipolmomentes aromatischer Verbindungen im ersten angeregten Singulettzustand. *Zeitschrift für Elektrochemie, Berichte der Bunsengesellschaft für Phys Chemie.* 1957;61(8):962–975.

112. Mataga N, Kaifu Y, Koizumi M. Solvent Effects upon Fluorescence Spectra and the Dipolemoments of Excited Molecules. *Bull Chem Soc Jpn.* 1956;29(4):465–470.

113. Stryer L. Fluorescence energy transfer as a spectroscopic ruler. *Annu Rev Biochem.* 1978;47(1):819–846.

114. Steinberg IZ. Long-range nonradiative transfer of electronic excitation energy in proteins and polypeptides. *Annu Rev Biochem.* 1971;40(1):83–114.

115. Lakowicz JR, Gryczynski I, Wiczk W, Laczko G, Prendergast FC, Johnson ML. Conformational distributions of melittin in water/methanol mixtures from frequency-domain measurements of nonradiative energy transfer. *Biophys Chem.* 1990;36(2):99–115.

116. Parkhurst KM, Parkhurst LJ. Detection of point mutations in DNA by fluorescence energy transfer. *J Biomed Opt.* 1996;1(4):435–441.

117. Ohkuma S, Poole B. Fluorescence probe measurement of the intralysosomal pH in living cells and the perturbation of pH by various agents. *Proc Natl Acad Sci.* 1978;75(7):3327–3331.

118. Demas JN, DeGraff BA, Coleman PB. Peer Reviewed: Oxygen Sensors Based on Luminescence Quenching. *Anal Chem.* 1999 Dec 1;71(23):793A–800A.

119. Rigler R, Elson ES. Fluorescence correlation spectroscopy: theory and applications. Springer Science & Business Media; 2012.

120. Chandezon F, Reiss P. Nanocristaux semi-conducteurs fluorescents. *Tech l'ingénieur Nanotechnologies pour l'électronique, l'optique la photonique.* 2004 Oct 10;base docum(ref. article : nm2030).

121. Varshni YP. Temperature dependence of the energy gap in semiconductors. *Physica.* 1967;34(1):149–154.

122. Murnaghan FD. The Compressibility of Media under Extreme Pressures. *Proc Natl Acad Sci U S A.* 1944 Sep 15;30(9):244–247.

123. Mei JR, Lemos V. Photoluminescence on CdSe and CdTe under hydrostatic pressure. *Solid State Commun.* 1984 Dec;52(9):785–788.

124. Prins AD, Sly JL, Dunstan DJ. Determination of the Linear Pressure Coefficients of Semiconductor Bandgaps. *Phys status solidi.* 1996 Nov 1;198(1):57–60.

125. Kobayashi T, Tei T, Aoki K, Yamamoto K, Abe K. Pressure dependence of photoluminescence of n-InP. *J Lumin.* 1981 Nov;24–25, Par:347–350.

126. Ekimov AI, Onushchenko AA. Quantum size effect in three-dimensional microscopic semiconductor crystals. *ZhETF Pisma Redaktsiiu.* 1981;34:363.

127. De Kergommeaux A, Fiore A, Bruyant N, Chandezon F, Reiss P, Pron A, et al. Synthesis of colloidal CuInSe 2 nanocrystals films for photovoltaic applications. *Sol Energy Mater Sol Cells.* 2011;95:S39–S43.

128. Coe-Sullivan S. Optoelectronics: Quantum dot developments. *Nat Photonics.* 2009;3(6):315–316.

129. Caruge JM, Halpert JE, Wood V, Bulović V, Bawendi MG. Colloidal quantum-dot light-emitting diodes with metal-oxide charge transport layers. *Nat Photonics.* 2008;2(4):247–250.

130. Klimov VI, Mikhailovsky AA, Xu S, Malko A, Hollingsworth JA, Leatherdale CA, et al. Optical gain and stimulated emission in nanocrystal quantum dots. *Science (80-).* 2000;290(5490):314–317.

131. Bruchez M, Moronne M, Gin P, Weiss S, Alivisatos AP. Semiconductor nanocrystals as fluorescent biological labels. *Science (80-).* 1998;281(5385):2013–2016.

132. Dubertret B, Skourides P, Norris DJ, Noireaux V, Brivanlou AH, Libchaber A. In vivo imaging of quantum dots encapsulated in phospholipid micelles. *Science (80-).* 2002;298(5599):1759–1762.

133. Walker GW, Sundar VC, Rudzinski CM, Wun AW, Bawendi MG, Nocera DG. Quantum-dot optical temperature probes. *Appl Phys Lett.* 2003;83(17):3555–3557.

134. Hajjaji H, Alekseev S, Guillot G, Blanchard NP, Monnier V, Chevolot Y, et al. Luminescence nanothermometry with alkyl-capped silicon nanoparticles dispersed in nonpolar liquids. *Nanoscale Res Lett.* 2014;9(1):1–6.

135. Choi CL, Koski KJ, Sivasankar S, Alivisatos AP. Strain-Dependent Photoluminescence Behavior of CdSe/CdS Nanocrystals with Spherical, Linear, and Branched Topologies. *Nano Lett.* 2009 Oct;9(10):3544–9.

136. Efros AL. Interband absorption of light in a semiconductor sphere. *Sov Phys Semicond.* 1982;16(7):772–775.

137. Brus LE. A simple model for the ionization potential, electron affinity, and aqueous redox potentials of small semiconductor crystallites. *J Chem Phys.* 1983;79(11).

138. Valerini D, Creti A, Lomascolo M, Manna L, Cingolani R, Anni M. Temperature dependence of the photoluminescence properties of colloidal CdSe/ZnS core/shell quantum dots embedded in a polystyrene matrix. *Phys Rev B.* 2005;71(23):235409–.

139. Fan HM, Ni ZH, Feng YP, Fan XF, Kuo JL, Shen ZX, et al. High pressure

photoluminescence and Raman investigations of CdSe/ZnS core/shell quantum dots. *Appl Phys Lett.* 2007;90:21921.

140. Kusova K, OndiC L, Klimesova E, Herynkova K, Pelant I, Danis S, et al. Luminescence of free-standing versus matrix-embedded oxide-passivated silicon nanocrystals: The role of matrix-induced strain. *Appl Phys Lett.* 2012;101(14):143101–143105.

141. Trallero-Giner ESFN and NOD and SW da S and PCM and MAP-S and AJDM and VL-R and GEM and C. Temperature-dependent Raman study of thermal parameters in CdS quantum dots. *Nanotechnology.* 2012;23(12):125701.

142. Klein MC, Hache F, Ricard D, Flytzanis C. Size dependence of electron-phonon coupling in semiconductor nanospheres: The case of CdSe. *Phys Rev B.* 1990 Dec 15;42(17):11123–11132.

143. Nomura S, Kobayashi T. Exciton–LO-phonon couplings in spherical semiconductor microcrystallites. *Phys Rev B.* 1992 Jan 15;45(3):1305–1316.

144. Olkhovets A, Hsu R-C, Lipovskii A, Wise FW. Size-Dependent Temperature Variation of the Energy Gap in Lead-Salt Quantum Dots. *Phys Rev Lett.* 1998 Oct 19;81(16):3539–3542.

145. Meulenberg RW, Strouse GF. Pressure-induced electronic coupling in CdSe semiconductor quantum dots. *Phys Rev B.* 2002 Jul 17;66(3):35317.

146. Joshi A, Narsingi KY, Manasreh MO, Davis E a., Weaver BD. Temperature dependence of the band gap of colloidal CdSe/ZnS core/shell nanocrystals embedded into an ultraviolet curable resin. *Appl Phys Lett.* 2006;89(13):2006–2008.

147. Maestro LM, Rodríguez EM, Rodríguez FS, la Cruz MCI, Juarranz A, Naccache R, et al. CdSe Quantum Dots for Two-Photon Fluorescence Thermal Imaging. *Nano Lett.* 2010;10(12):5109–5115.

148. Rudin S, Reinecke TL, Segall B. Temperature-dependent exciton linewidths in semiconductors. *Phys Rev B.* 1990 Dec 15;42(17):11218–11231.

149. Ji C, Zhang Y, Zhang T, Liu W, Zhang X, Shen H, et al. Temperature-Dependent Photoluminescence of Ag2Se Quantum Dots. *J Phys Chem C.* 2015 Jun 18;119(24):13841–13846.

150. Talapin D V, Mekis I, Götzinger S, Kornowski A, Benson O, Weller H. CdSe/CdS/ZnS and CdSe/ZnSe/ZnS Core−Shell−Shell Nanocrystals. *J Phys Chem B.* 2004 Nov 12;108(49):18826–18831.

151. Protière M, Nerambourg N, Renard O, Reiss P. Rational design of the gram-scale synthesis of nearly monodisperse semiconductor nanocrystals. *Nanoscale Res Lett.* 2011;6(1):1–14.

152. Bimberg D. Landolt-Börnstein series : Crystal and solid state physics – Physics of group

IV elements and III-V compounds et Physics of II-VI and I-VII compounds. *Cryst Res Technol.* 1982;3.

153. Kittel C. Physique de l'état solide, Dunod Université. ISBN 2-04-010611-1; 1983.

154. Neumann H. No Title. *Krist Tech.* 1980;15:849.

155. Deuschle G, Howard J, Fischer H. Landolt-Bvrnstein: Numerical Data and Functional Relationships in Science and Technology - New Series Gruppe/Group 2 Molecules and Radicals Volume 17 Magnetic Properties of Free Radicals / Magnetische Eigenschaften Freier Radikale Radicals Centered. Springer; 1988.

156. Edwards AL, Drickamer HG. Effect of Pressure on the Absorption Edges of Some III-V, II-VI, and I-VII Compounds. *Phys Rev.* 1961 May 15;122(4):1149–1157.

157. Li J, Li G-H, Xia J-B, Zhang J, Lin Y, Xiao X. Optical spectra of CdSe nanocrystals under hydrostatic pressure. *J Phys Condens Matter.* 2001;13(9):2033.

158. Oliveira CAD and NP-M and ZB and MP and LE. Effects of applied magnetic fields and hydrostatic pressure on the optical transitions in self-assembled InAs/GaAs quantum dots. *J Phys Condens Matter.* 2006;18(6):1877.

159. Wei S-H, Zunger A. Predicted band-gap pressure coefficients of all diamond and zinc-blende semiconductors: Chemical trends. *Phys Rev B.* 1999 Aug 15;60(8):5404–5411.

160. Zhang W, Dai D, Chen X, Guo X, Fan J. Red shift in the photoluminescence of colloidal carbon quantum dots induced by photon reabsorption. *Appl Phys Lett.* 2014;104(9):-.

161. Zhang N, Dai D, Zhang W, Fan J. Photoluminescence and light reabsorption in SiC quantum dots embedded in binary-polyelectrolyte solid matrix. *J Appl Phys.* 2012;112(9):-.

162. Azevedo G, Monte AFG, Reis AF, Messias DN. Fluorescence resonance energy transfer measured by spatial photon migration in CdSe-ZnS quantum dots colloidal systems as a function of concentration. *Appl Phys Lett.* 2014;105(20):203108.

163. Kagan CR, Murray CB, Bawendi MG. Long-range resonance transfer of electronic excitations in close-packed CdSe quantum-dot solids. *Phys Rev B.* 1996;54(12):8633.

164. Kagan CR, Murray CB, Nirmal M, Bawendi MG. Electronic Energy Transfer in CdSe Quantum Dot Solids. *Phys Rev Lett.* 1996 Feb 26;76(9):1517–1520.

165. Mork AJ, Weidman MC, Prins F, Tisdale WA. Magnitude of the Forster Radius in Colloidal Quantum Dot Solids. *J Phys Chem C.* 2014;118(25):13920–13928.

166. Lakowicz JR, Gryczynski I, Kuśba J, Wiczk W, Szmacinski H, Johnson ML. Site-to-site diffusion in proteins as observed by energy transfer and frequency-domain fluorometry. *Photochem Photobiol.* 1994;59(1):16–29.

167. Jacob MH, Dsouza RN, Ghosh I, Norouzy A, Schwarzlose T, Nau WM. Diffusion-enhanced Förster resonance energy transfer and the effects of external quenchers and the

donor quantum yield. *J Phys Chem B.* 2013 Jan 10;117(1):185–98.

168. Lakowicz JR, Wiczk WM, Gryczynski I, Szmacinski H, Johnson ML. Influence of end-to-end diffusion on intramolecular energy transfer as observed by frequency-domain fluorometry. 1990. p. 554–569.

169. Maliwal BP, Kuśba J, Lakowicz JR. Fluorescence energy transfer in one dimension: Frequency-domain fluorescence study of DNA–fluorophore complexes. *Biopolymers.* 1995;35(2):245–255.

170. Lakowicz J, Kuśba J, Shen Y, Malicka J, D'Auria S, Gryczynski Z, et al. Effects of Metallic Silver Particles on Resonance Energy Transfer Between Fluorophores Bound to DNA. *J Fluoresc.* 2003;13(1):69–77.

171. Zhang J, Fu Y, Lakowicz JR. Enhanced Förster resonance energy transfer (FRET) on a single metal particle. *J Phys Chem C.* 2007;111(1):50–56.

172. Hamza H, Albahrani SMB, Guillot G, Maillard M, Philippon D, Vergne P, et al. Temperature and Viscosity Effects on the Photoluminescence Properties of Alkyl-Capped Silicon Nanoparticles Dispersed in Nonpolar Liquids. *J Phys Chem C.* 2015 Jul 23;119(29):16897–16904.

173. Chandrasekhar S. Stochastic Problems in Physics and Astronomy. *Rev Mod Phys.* 1943 Jan 1;15(1):1–89.

174. Crooker SA, Hollingsworth JA, Tretiak S, Klimov VI. Spectrally resolved dynamics of energy transfer in quantum-dot assemblies: Towards engineered energy flows in artificial materials. *Phys Rev Lett.* 2002;89(18):186802.

175. Phillips RJ, Armstrong RC, Brown RA, Graham AL, Abbott JR. A constitutive equation for concentrated suspensions that accounts for shear-induced particle migration. *Phys Fluids A.* 1992;4(1).

176. Merhi D, Lemaire E, Bossis G, Moukalled F. Particle migration in a concentrated suspension flowing between rotating parallel plates: Investigation of diffusion flux coefficients. *J Rheol (N Y N Y).* 2005;49(6).

177. Ding Y, Wen D. Particle migration in a flow of nanoparticle suspensions. *Powder Technol.* 2005 Jan 3;149(2–3):84–92.

178. Daniel I, Oger P, Picard A, Cardon H, Couzinet B, Chervin J-C. A diamond anvil cell adapted for low-pressure high-resolution investigations. In: Book of Abstracts. Citeseer; 2006. p. 228.

179. Mao HK, Xu J, Bell PM. Calibration of the ruby pressure gauge to 800 kbar under quasi-hydrostatic conditions. *J Geophys Res.* 1986;91(B5):4673–4676.

180. Datchi F, LeToullec R, Loubeyre P. Improved calibration of the SrBO:Sm optical pressure gauge: Advantages at very high pressures and high temperatures. *J Appl Phys.*

1997;81(8):3333–3339.

181. Gaponenko S V. Optical properties of semiconductor nanocrystals. Cambridge University Press; 1998.

182. Reiss P, Carayon S, Bleuse J, Pron A. Low polydispersity core/shell nanocrystals of CdSe/ZnSe and CdSe/ZnSe/ZnS type: preparation and optical studies. *Synth Met.* 2003;139(3):649–652.

Appendices

Appendix A. Energy, wavelength, frequency and wavenumber

Light energy *E*, wavelength λ, frequency *v*, and wavenumber *k* can be converted from one to another using the following formula:

$$E = h\nu \Rightarrow \nu = \frac{E}{h} \quad (1)$$

$$\lambda = \frac{c}{\nu} = \frac{hc}{E} \quad (2)$$

$$k = \frac{1}{\lambda} = \frac{E}{hc} \quad (3)$$

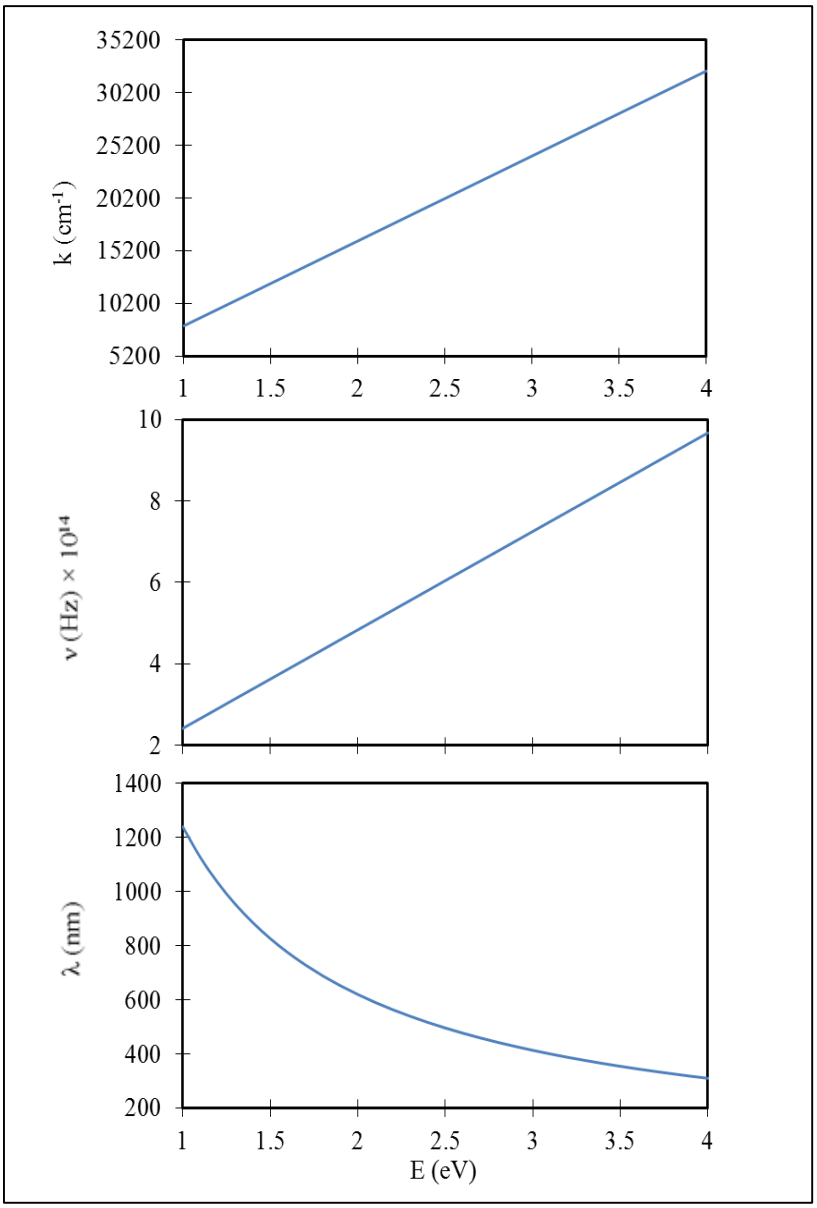

Conversion between the different units between energy *E*, wavelength λ, frequency *v*, and wavenumber *k*

Appendix B. Properties of the lubricants used in the study

B.I. Squalane

Chemical structure: $C_{30}H_{62}$

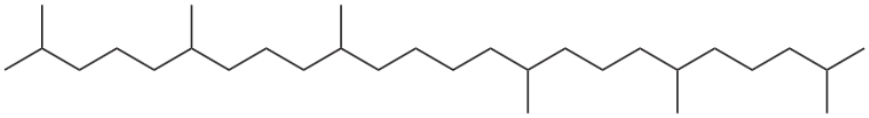

Boiling point: 350 °C (623 K) at ambient pressure.

Density

Tait's model was used to estimate the dependence of the density on temperature and pressure:

$$\frac{\rho(p,T)}{\rho(p_0,T_0)}=\frac{V(p_0,T_0)}{V(p,T)}=\frac{V(p_0,T_0)}{V(p_0,T)}\times\frac{V(p_0,T)}{V(p,T)} \quad (4)$$

with:

$$\frac{V(p_0,T)}{V(p_0,T_0)}=1+a_v(T-T_0) \quad (5)$$

$$\frac{V(p,T)}{V(p_0,T)}=1-\frac{1}{1+K_0'}\ln\left[1+\left(\frac{1+K_0'}{K_{00}}\exp(-\beta_K\,\mathrm{T})\right)(p-p_0)\right] \quad (6)$$

Good estimations are obtained for hydrocarbons with $a_v = 0.0008\ K^{-1}$, $\beta_K = -0.0065\ K^{-1}$, $K_{0R} = 9\ GPa$ and $K_0' = 11$.

Viscosity

Modified WLF-Yasutomi model was used to estimate the dependence of the viscosity on temperature and pressure:

$$\eta(p,T)=\eta_g\exp\left(\ln(10)\frac{-C_1(T-T_g(p))F(p)}{C_2+(T-T_g(p))F(p)}\right) \quad (7)$$

with:

$$T_g(p) = T_g(p_{atm}) + A_1 \ln(1 + A_2 p) \quad (8)$$

$$F(p) = (1 + B_1 p)^{B_2} \quad (9)$$

where A_1, A_2, B_1, B_2, C_1 *and* C_2 are parameters that have to be determined by fitting the experimental data to the model, $F(p)$ is the relative thermal expansion of the free volume, η_g is a viscosity signaling the glass transition at atmospheric pressure p_{atm} (and it is assumed to be equal to 10^{12} Pa.s).

The following values were used for squalane:

C_1	16.38
C_2	25.22 (°C)
A_1	270.50 (°C)
A_2	0.00024 (MPa^{-1})
B_1	0.010 (MPa^{-1})
B_2	-0.4151
T_g^0	-96.60 (°C)
η_g	10^{12} (Pa.s)

B.II. Cyclopentane

Chemical structure: C_5H_{10}

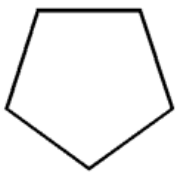

Density

Tait's model was used to estimate the dependence of the density on temperature and pressure.

Boiling point: 49.3 °C (322.3 K) at ambient pressure.

Viscosity

The dependence of the viscosity on pressure was measured using a falling Ball Viscometer in the range between ambient to 500 MPa. For higher pressure values, Barus law with the asymptotic pressure coefficient α^* was used:

$$\eta(p) = \eta_0 \exp(\alpha^* p) \quad (10)$$

With:

$$\alpha^* = \frac{1}{\int_0^{\infty} \frac{\eta_0}{\eta(p)} dp} \approx \frac{1}{\int_0^{500MPa} \frac{\eta_0}{\eta(p)} dp} \quad (11)$$

Mixture: Squalane (30 vol %) + Cyclopentane (70 vol %)

Density

Tait's law was used to estimate of the dependence of the density of the mixture on pressure.

Viscosity

Logarithmic mixture law was used to estimate the dependence of the viscosity of the mixture on pressure:

$$\ln(\eta) = X_{Squalane} \ln(\eta_{Squalane}) + (1 - X_{Squalane}) \ln(\eta_{Cyclopentane}) \quad (12)$$

With $X_{Squalane} = 0.3$.

Appendix C. Apparatus

C.I. General description

In all the tests, a setup simulating the experimental conditions (temperature, pressure, shear rate, etc.) was combined with an optical system comprising a fluorescence microscope and a spectrometer, as well as an acquisition system:

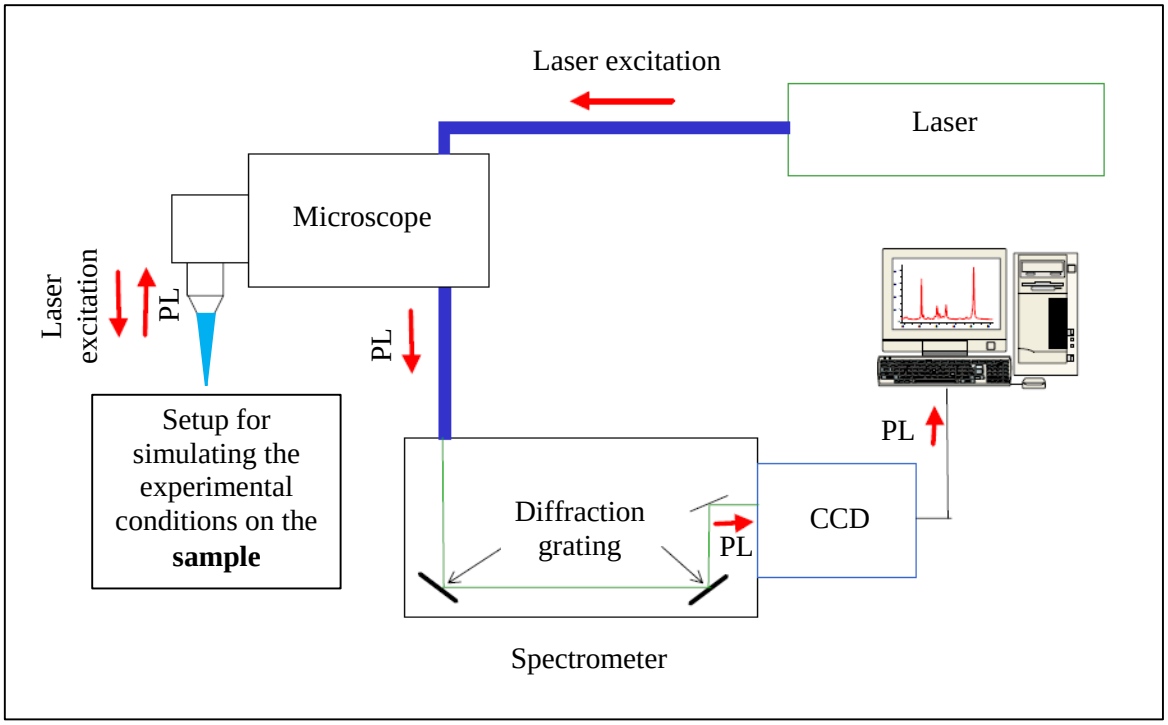

Coupling between the setup simulating the experimental conditions with the optical and the acquisition system.

C.II. Optical system: Spectrometer – Microscope – Laser

Steady-state PL measurements were carried out with either an U1000 Jobin-Yvon spectrometer (at LaMCoS – INSA de Lyon) or a LabRam HR800 spectrometer (at LGLTPE – ENS).

- In the first spectrometer, the light emission is dispersed, via a double monochromator with 100 gr/mm gratings, and a resolution of 0.07 nm/pixel (0.20 meV/pixel) is obtained. A continuous argon-ion laser with an excitation wavelength of 488 nm, and a 20× objective were used with this spectrometer, yielding a laser spot of 20 µm diameter on the sample. The tests were performed with a laser power of about 1 mW, which corresponds to a power density of 318 W/cm^2.
- In the second spectrometer, a 150 gr/mm grating was used, and a resolution of 0.21 nm/pixel (1.06 meV/pixel) is obtained. A continuous Nd:YAG laser with an excitation wavelength of 532 nm was used with this spectrometer together with a 50× objective, yielding a laser spot

of about 4 µm diameter. The tests were performed with a laser power of 20 µW, which corresponds to a power density of 159 W/cm^2.

Practical reasons were behind the choice of using different optical systems. Pressure calibrations on CdSe/CdS/ZnS QDs dispersed with a concentration of 5 mg/mL of QDs (in squalane at 298, 323 or 373 K, as well as in the mixture of squalane (30 vol%) and cyclopentane (70 vol%) at 298 K) were conducted with the LabRam HR800 spectrometer at at LGLTPE – ENS. All the other measurements were carried out with the U1000 Jobin-Yvon spectrometer at LaMCoS.

In all the systems, no specific confocal system was used. The confocality is of some tens of µm (a 300 µm diameter optical fiber was used with U1000 Jobin-Yvon spectrometer, and no optical fiber was used with LabRam HR800 spectrometer).

C.III. Sample holder for concentration effect study

10 µL of each sample was deposited on an aluminum holder and covered with a cover-glass plate. The cover-glass plate was itself glued on the aluminum holder. The sample forms a capillary bridge between the two surfaces, which ensures a constant film thickness of 1 mm in all the samples.

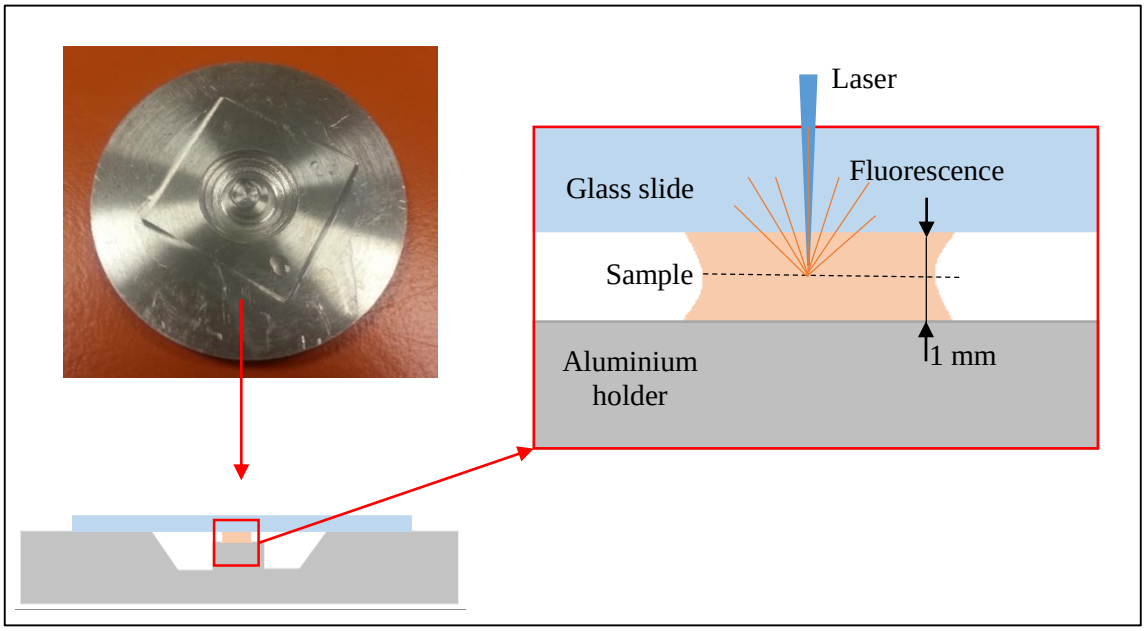

Sample holder for concentration effect study

C.IV. Cell for temperature sensitivity

The same holder presented above was used for temperature calibrations. The sample holder was put inside a heating ring, itself connected to a voltage source. Teflon insulators were used to enclose the system and improve the thermal regulation. A thermocouple was used to measure the temperature close to the sample. Temperature was regulated with a precision of 0.1 °C.

The following figure shows the schematic of the cell and its coupling with the optical system:

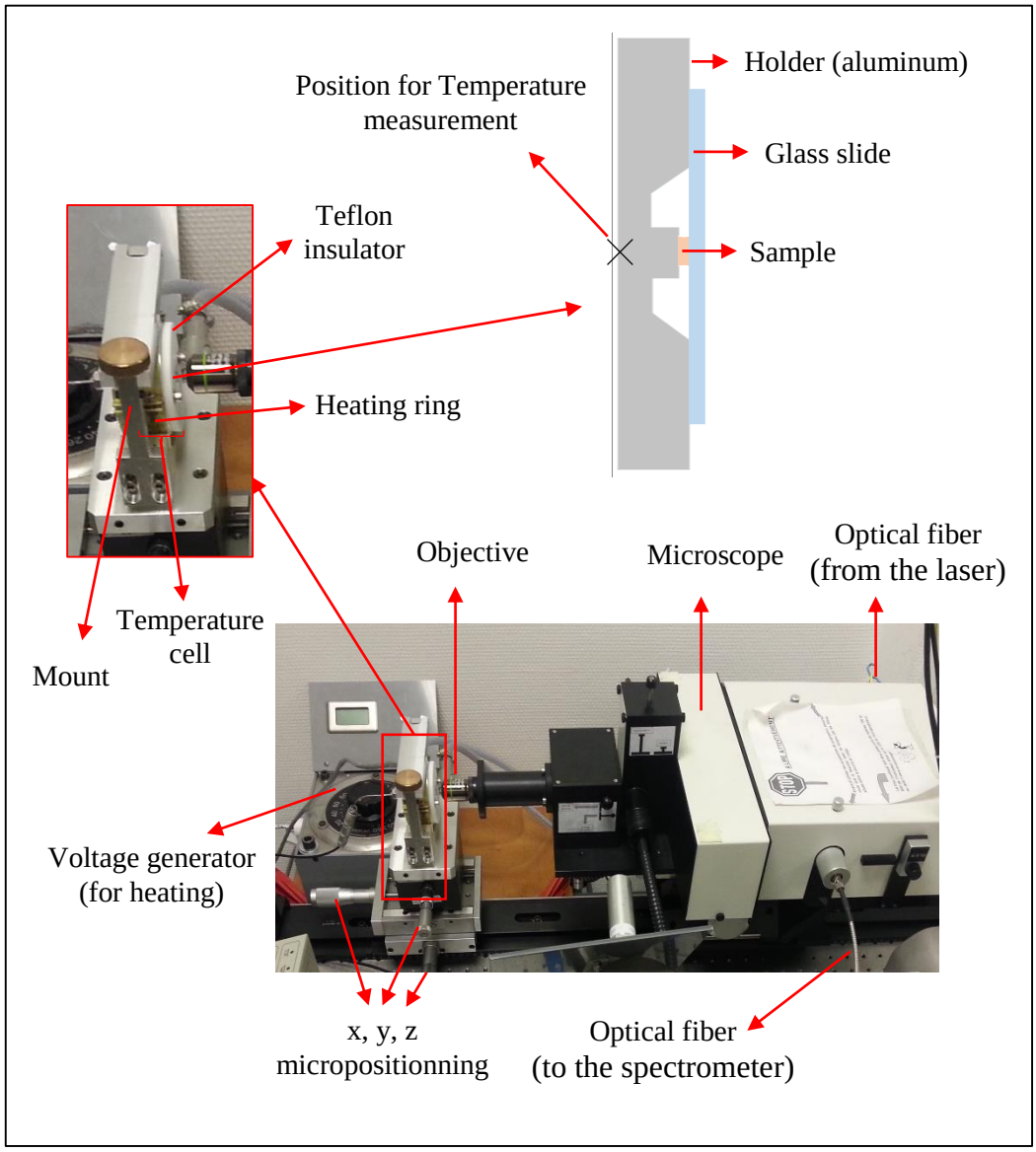

Temperature cell.

C.V. High pressure diamond cell

Pressure calibrations were conducted using a thermally regulated high pressure diamond cell. In this cell, the sample is deposited inside a nickel gasket. The nickel gasket thickness was about 0.2 mm, and its hole was 0.5 mm in diameter. Hydrostatic pressure conditions were maintained by compressing the gasket between a diamond anvil and a thin diamond window. The cell was put inside a heating ring, itself connected to a heating system ensuring a thermal regulation with a precision of 0.1 °C. A thermocouple was used to measure the temperature close to the sample. The following figure shows the schematic of this cell, and the coupling of the cell with the optical system:

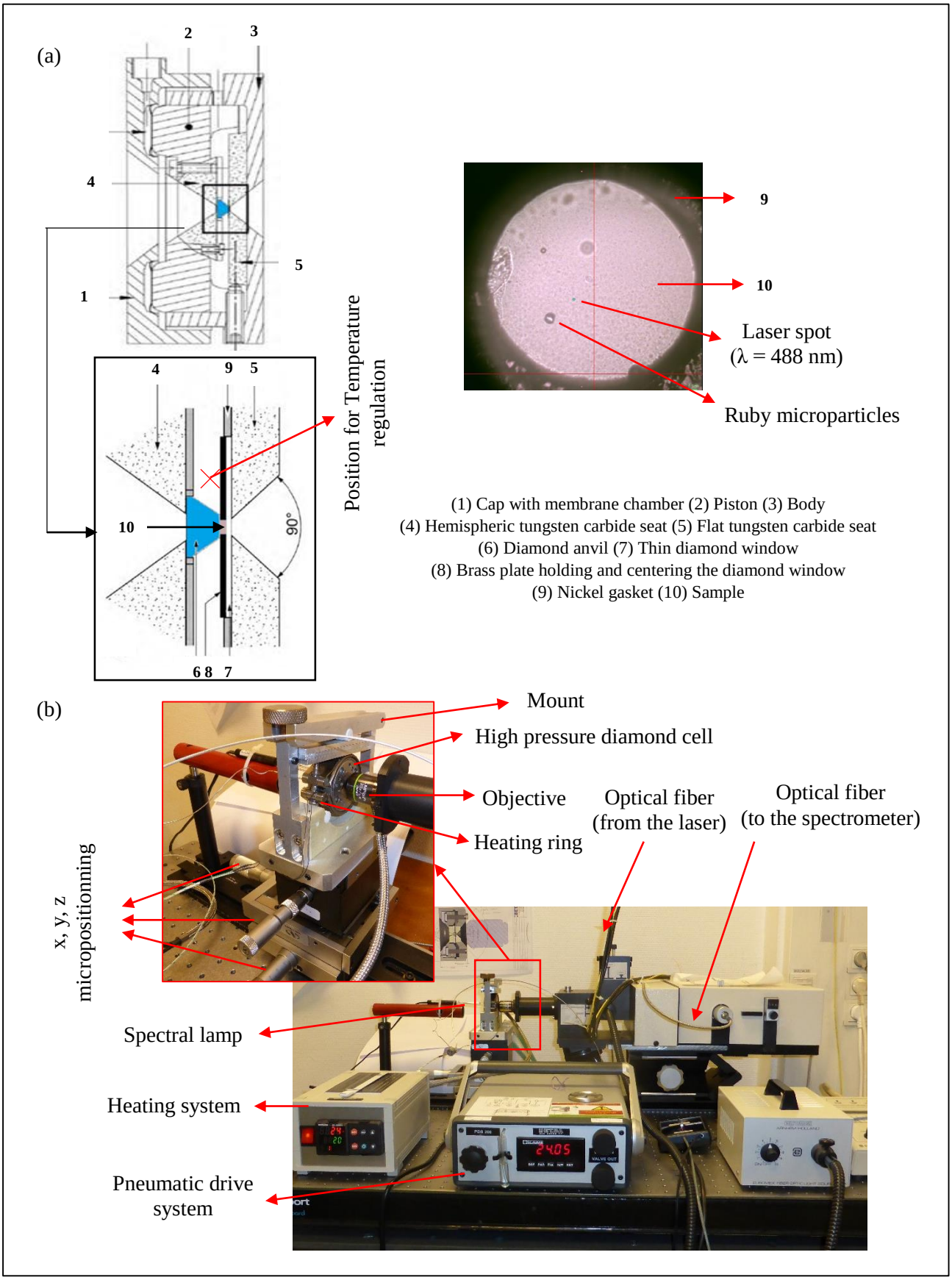

(a) The different parts of the high pressure diamond cell, (b) The coupling of the high pressure cell with the optical system (microscope and spectrometer).

More details on the principle of this type of diamond cells can be found elsewhere[178]. Several ruby micro-particles were deposited into the lubricant, and the well-established shift with pressure of the R1 line in ruby's PL spectrum with pressure[179,180] was used to measure the latter during the tests. Ruby suffers however from limited sensitivity in the range of pressure under investigation (≤ 2000 MPa), and even small errors in spectroscopic measurements induced by fluctuations of room temperature can result in relatively big errors in pressure readings. A neon spectral lamp was therefore used throughout the tests in order to measure and then compensate such undesirable effects in the determination of ruby's line position. With such precautions, pressures are estimated with an uncertainty of 50 MPa.

C.VI. Rheometer

Two geometries were used: parallel-plates and cone-plate. In both cases, the glass disc was fixed, and the steel (plate or cone) disc was rotating. For reinforcement purpose, a steel plate with a slotted hole was placed beneath the glass plate. The slotted hole was used for observation and spectroscopic measurements. Peltier devices were used for heating and cooling the sample, and a platinum sensor allows the thermal regulation and the temperature measurement with a precision of 0.03 °C.

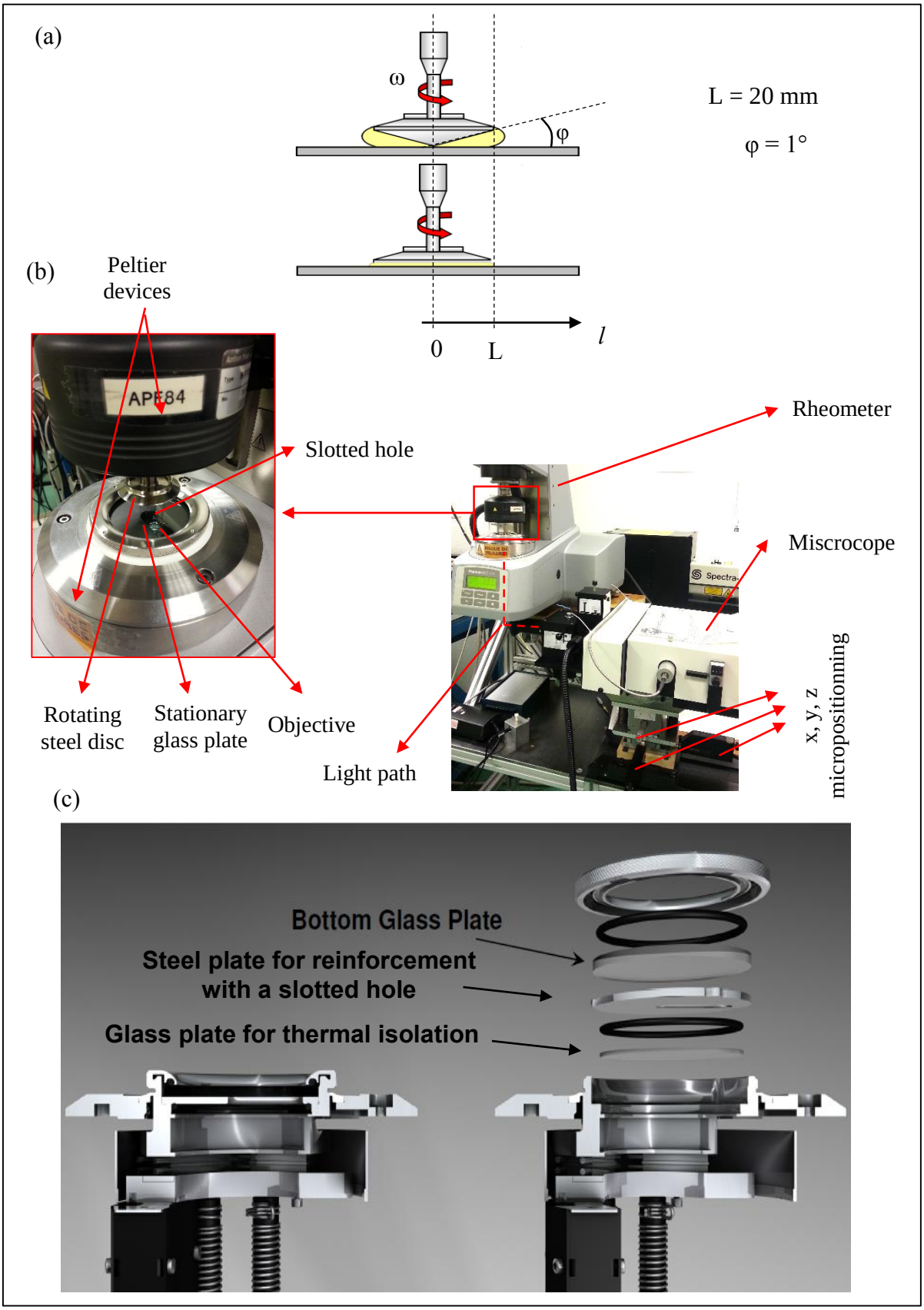

(a) Cone-plate and parallel-plates geometries, (b) Coupling of the rheometer with the optical system, (c) Exploded-view drawing of the rheometer used for PL study.

Appendix D. Complementary tests in a fluorimeter

Description of the Apparatus

Some measurements were performed with a fluorimeter (FLS920 series spectrometer) in which the sample is put in a cuvette of a light path of 10 × 10 mm. A steady state Xenon lamp was used as light source, and a wavelength of 488 nm was selected with an excitation monochromator. The temperature can be controlled with a precision of 0.02 °C.

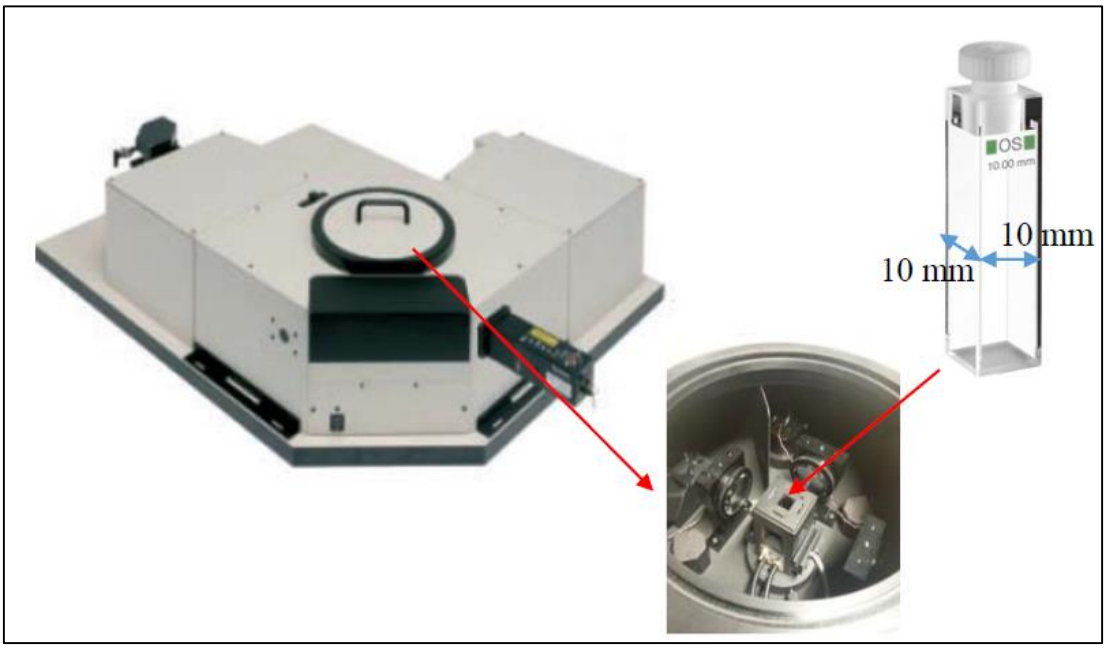

Hysteresis test

In order to investigate the hysteresis of the QDs response with pressure variations, a cycle of heating (298 → 373 K), cooling (373 → 298 K) and a second heating (28 → 373 K) was performed on a mixture of squalane (83%) and cyclopentane (17%) with 5 mg/mL of CdSe/CdS/ZnS QDs.

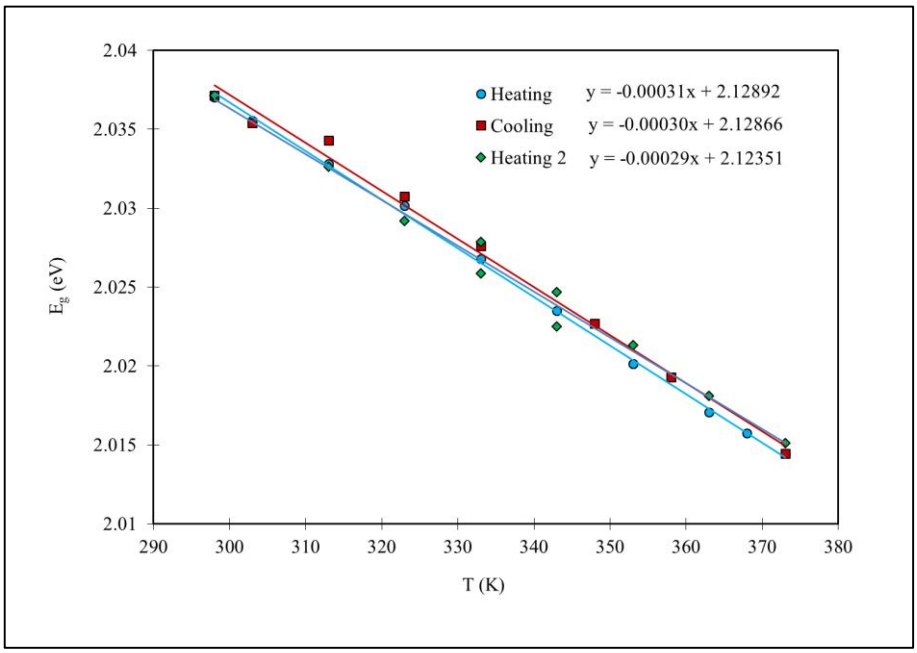

Influence of the viscosity of the solvent

The influence of the viscosity of the solvent on the response of the QDs was examined by studying mixtures of different volume fractions of squalane (X_{sq}) and cyclopentane ($X_{cyc} = 1 - X_{sq}$). The concentration of the QDs was fixed at 5 mg/mL.The following sensitivities were obtained:

Xsq (%)	Temperature sensitivity (meV/K)
100	-0.25 ± 0.01
83	-0.31 ± 0.01
50	-0.33 ± 0.01
17	-0.37 ± 0.01
0	-0.34 ± 0.01

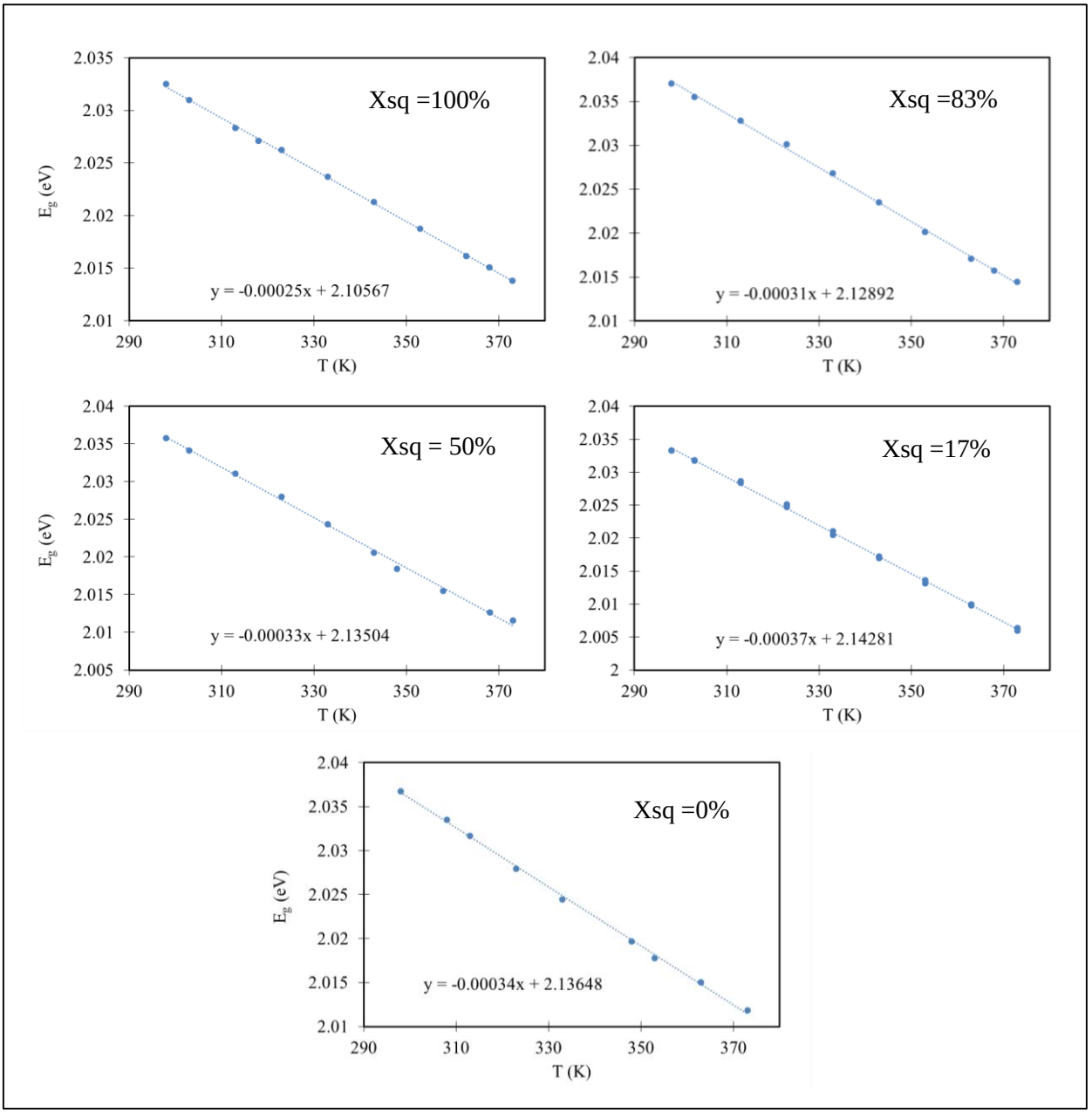

The variation of the diffusion of the QDs and their Mean Free Path (MFP) with temperature are given by:

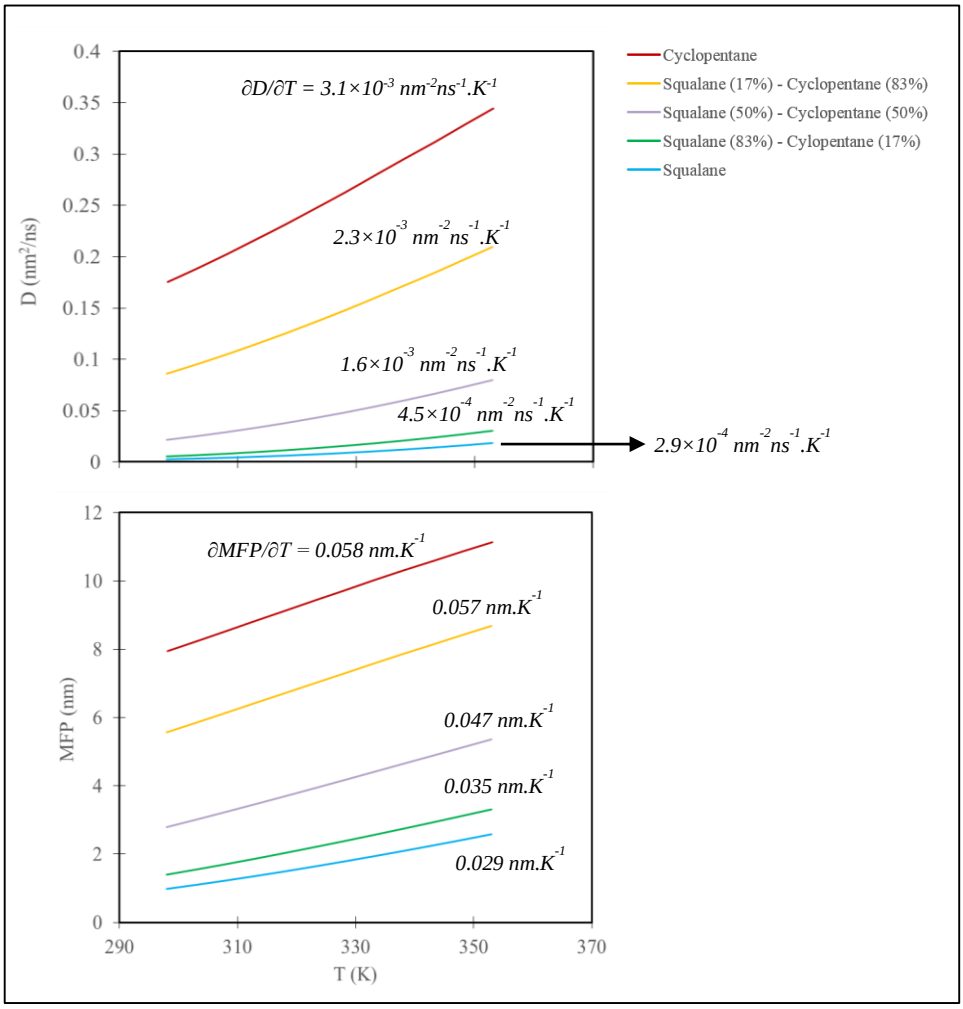

The model presented in chapter 3 (Equation (III.29)), based on the notion of apparent radius, predicts an increase of temperature sensitivity with increasing $\partial D/\partial T$. As one can notice, the same trend is observed experimentally.

The observed emission energies are lower than in other experiments due to higher internal filter effect caused by the cuvette dimension (10 mm × 10 mm).

Appendix E. Density of the CdSe/CdS/ZnS QDs

The density of the QDs can be estimated from the density and the volume fraction *X* of its constituents[34]:

$$\rho_{QDs} = X_{CdSe}\rho_{CdSe} + X_{CdS}\rho_{CdS} + X_{ZnS}\rho_{ZnS} \qquad (13)$$

The volume of a QD and the volume of its constituents are given by:

$$V_{QD} = \frac{4\pi}{3}\left(r_{CdSe} + e_{CdS} + e_{ZnS}\right)^3 \qquad (14)$$

$$V_{CdSe} = \frac{4\pi}{3} r_{CdSe}^3 \qquad (15)$$

$$V_{CdS} = \frac{4\pi}{3}\left(r_{CdSe} + e_{CdS}\right)^3 - \frac{4\pi}{3} r_{CdSe}^3 \qquad (16)$$

$$V_{ZnS} = \frac{4\pi}{3}\left(r_{CdSe} + e_{CdS} + e_{ZnS}\right)^3 - \frac{4\pi}{3}\left(r_{CdSe} + e_{CdS}\right)^3 \qquad (17)$$

Where r_{CdSe} is the radius of the CdSe core, e_{CdS} and e_{ZnS} are the thickness of the CdS and ZnS shells, respectively. Hence:

$$\begin{aligned}\rho_{QDs} = {} & \frac{r_{CdSe}^3}{\left(r_{CdSe} + e_{CdS} + e_{ZnS}\right)^3}\rho_{CdSe} \\ & + \frac{\left(r_{CdSe} + e_{CdS}\right)^3 - r_{CdSe}^3}{\left(r_{CdSe} + e_{CdS} + e_{ZnS}\right)^3}\rho_{CdS} \\ & + \frac{\left(r_{CdSe} + e_{CdS} + e_{ZnS}\right)^3 - \left(r_{CdSe} + e_{CdS}\right)^3}{\left(r_{CdSe} + e_{CdS} + e_{ZnS}\right)^3}\rho_{ZnS}\end{aligned} \qquad (18)$$

By substituting with numerical values for the density of the constituents (ρ_{CdSe} = 5816 mg/mL, ρ_{CdS} = 4090 mg/mL, ρ_{ZnS} = 4826 mg/mL), the Equation *(18)* yields ρ_{QDs} = 4911 mg/mL.

[34] The influence of the ligands on the volume fraction can be neglected.

Appendix F. Temperature sensitivity expression accounting for energy transfer effect

For interacting QDs, the expression of the temperature sensitivity is given by:

$$S_T(T) = S_T^B\left(V_{Crystal}(T), r^*(T)\right) + S_{r^*}^Q\left(r^*(T)\right)\frac{\partial r^*}{\partial T} \qquad (19)$$

The quantum sensitivity to size variations of interacting and non-interacting QDs ($S_{r^*}^Q$ and S_r^Q, respectively) can be related using Taylor expansion to the first order, the previous equation becomes:

$$S_{r^*}^Q(r,\delta r) \approx S_r^Q(r) - \delta S_r^{Q-ET}(r,\delta r) \qquad (20)$$

$\delta S_r^{Q\text{-}ET}$ is a correcting term taking into account the interaction between QDs given by:

$$\delta S_r^{Q-ET}(r,\delta r) = \left(2\left(\frac{\nu^Q}{r^2}\right) - 3\left(\frac{2\gamma^Q}{r^3}\right)\right)\frac{\delta r}{r} \qquad (21)$$

The results in literature show that the temperature sensitivity increases with decreasing size (see Chapter 2). Therefore, we can write:

$$S_T^B\left(V_{Crystal}, r, \delta r\right) \approx S_r^B\left(V_{Crystal}, r\right) - \delta S_r^{B-ET}(r,\delta r) \qquad (22)$$

The mean thermal expansion of active QDs can be related to the mean thermal expansion of the all the QDs (active and inactive) in the following way:

$$\frac{\partial r^*}{\partial T} = \frac{\partial r\left(\alpha_T^Q\right)}{\partial T} + \frac{\partial(\delta r)}{\partial T} \qquad (23)$$

However, the influence of the temperature on δr arises from (i) its influence on the concentration of the QDs and their diffusion and (ii) the influence of these two parameters on energy transfer efficiency. Therefore, one can write:

$$\frac{\partial\left(\delta r(T)\right)}{\partial T} = \frac{\partial(\delta r)}{\partial E^{ET}}\frac{\partial E^{ET}}{\partial T} = \frac{\partial(\delta r)}{\partial E^{ET}}\left(\frac{\partial E^{ET}}{\partial C}\frac{\partial C}{\partial T} + \frac{\partial E^{ET}}{\partial D}\frac{\partial D}{\partial T}\right) \qquad (24)$$

The term $\partial C/\partial T$ is thus zero, since the variation of the concentration with temperature is almost negligible ($C(T) = C_0$). On the other hand, the influence of diffusion is limited by the concentration, as illustrated in Figure III.14. Therefore, the $\partial E^{ET}/\partial D$ depends on the concentration C_0 of the QDs in the solvent, and it approaches zero in highly diluted solutions.

Based on the previous considerations, the expression of the temperature sensitivity S_T can be written as following:

$$
\begin{aligned}
S_T = {} & S_T^B\left(V_{Crystal}, r\right) - \delta S_T^{B-ET}\left(V_{Crystal}, \delta r\left(C_0, D\right)\right) \\
& + \left[S_r\left(r\right) - \delta S_r^{Q-ET}\left(r, \delta r\left(C_0, D\right)\right)\right] \\
& \times \left[\frac{\partial r}{\partial T} + \frac{\partial\left(\delta r\right)}{\partial E^{ET}} \frac{\partial E^{ET}\left(C_0, D\right)}{\partial D} \frac{\partial D}{\partial T}\right]
\end{aligned}
\qquad (25)
$$